UNIVERSITEIT ANTWERPEN

UNIVERSITAIRE INSTELLING ANTWERPEN

Departement Scheikunde

APPLICATIONS OF LASER MICROPROBE MASS ANALYSIS IN AEROSOL RESEARCH

Proefschrift ter verkrijging van de graad van Doctor in de Wetenschappen aan de Universitaire Instelling Antwerpen te verdedigen door Frank BRUYNSEELS

Promotor :

Prof. Dr. R. Van Grieken

Antwerpen, 1987

Instituut voor Zeewetenschappelijk onderzoek
Institute for Marine Scientific Research
Prinses Elisabethlaan 69
8401 Bredene - Belgium - Tel. 059/80 37 15

UNIVERSITEIT ANTWERPEN
UNIVERSITAIRE INSTELLING ANTWERPEN
Departement Scheikunde

APPLICATIONS OF LASER MICROPROBE MASS ANALYSIS IN AEROSOL RESEARCH

Proefschrift ter verkrijging van de graad van Doctor in de Wetenschappen aan de Universitaire Instelling Antwerpen te verdedigen door Frank BRUYNSEELS

Promotor :

Prof. Dr. R. Van Grieken

Antwerpen, 1987

DANKWOORD

Bij de voltooiing van dit proefschrift had ik graag mijn erkentelijkheid betuigt aan allen die hebben bijgedragen tot de realisatie van dit werk.

In eerste instantie dank ik mijn ouders voor de morele steun en de kansen die ze mij hebben geboden om mijn studies te volbrengen, wat me in de mogelijkheid stelde dit proefschrift voor te bereiden.

Bijzondere erkentelijkheid ben ik verschuldigd aan mijn promotor Prof. Dr. R. Van Grieken, voor zijn permanente wetenschappelijke interesse en de konstruktieve raadgevingen, die in belangrijke mate hebben bijgedragen tot de realisatie van dit werk.

Prof. Dr. R. Niessner (Universität Dortmund, Dortmund, BRD), Prof. Dr. M.O. Andreae (Florida State University, Tallahassee, USA), Prof. Dr. P. Artaxo (Universidade de Sao Paulo, Brazil) en Prof. Dr. R.W. Linton (University of North Carolina at Chapel Hill, Chapel Hill, USA) ben ik erkentelijk voor de interessante wetenschappelijke discussies en de mogelijkheid die ze mij hebben gegeven om aan verschillende onderzoeksprojecten deel te nemen.

Ik dank alle collega's van de groep analytische scheikunde voor de aangename werksfeer. Ph. Otten en H. Storms dank ik voor de vlotte samenwerking en de interessante wetenschapellijke konversaties.

R. Saelens, R. Nullens en L. Van't Dack dank ik voor hun deskundige assistentie bij het gebruik van het analytisch instrumentarium.

Het Instituut tot Aanmoediging van het Wetenschappelijk Onderzoek in Nijverheid en Landbouw (IWONL), de Geconcerteerde Actie Noordzee van het Ministerie van Wetenschapsbeleid en de Universitaire Instelling Antwerpen, dank ik voor hun financiële steun.

TABLE OF CONTENTS

CHAPTER 1 INTRODUCTION

In analytical chemistry there is a growing interest for the chemical characterization of individual micrometer-size particles in a variety of research fields, including atmospheric chemistry to deal with questions about aerosol formation and reactivity, and in particle technology for industrial applications. A solution to specific problems and new insights on the chemical composition of a sample of particulates has often to be sought on the microscopic level. Knowledge about the external and internal heterogeneity of particulates in a sample can provide important clues about their chemical history, as well as for the prediction of their future behaviour in well defined chemical environments such as a suspension or an aerosol phase.

Therefore, in recent years a considerable effort has been put in the development and improvement of microanalytical techniques that can potentially be invoked in this challenging research topic of individual particle analysis. Laser microprobe mass analysis (LAMMA) is a new and promising technique in this context. In LAMMA, a high power laser pulse is used to evaporate and ionize microvolumina of a sample. By coupling the ion source to a mass spectrometer a complete mass spectrum can be recorded for each micrometer-size particle. Considerable improvement with respect to the instrumental performance in comparison to the earliest mass spectrometeric designs was gained by reducing the laser pulse lengths (by Q-switching) and spot diameters (by focusing the laser beam and reducing its wavelength). With the introduction of a light microscope for further focusing of the laser beam down to a diffraction-limited spot size of about 0.5 μm, a time-of-flight mass spectrometer allowing a high ion transmission, and a time-focusing ion reflector in the TOF-drift tube to improve the the mass resolution, laser microprobe mass spectrometry reached a level of sophistication that made its commmercial introduction possible.

The goal of the present study was to develop laser microprobe mass spectrometry for the qualitative and quantitative analysis of individual aerosol particulates. Already in an early stage of the work, much attention was paid to the cluster ion patterns observed for both inorganic and organic compounds and the research focused on the potential of LAMMA for the localized determination of the speciation of compounds on a microscopic scale.

Since LAMMA is a destructive analysis technique causing decomposition of the sample by partial fragmentation of the original chemical bonds, recombination reactions between the generated atoms, clusters and molecules limit the amount of unbiased information that can be gained from the spectra. Hence, a fundamental study was undertaken to investigate to what extent recombination reactions can influence the final composition of the charged clusters ions as detected in the spectrum of the LAMMA-500 instrument (Chapter 4). The cluster ion distributions of a series of inorganic compounds relevant to atmospheric chemistry (especially sulfur and nitrogen salts) was studied in some detail to describe the systematic trends that can be observed with respect to valence states and anion stoichiometry (Chapter 5). A method for inorganic salt speciation with high lateral resolution allowing individual aerosol particle analysis in a heterogeneous particle population was judged to be relevant for studying the anthropogenic impact on the global atmospheric sulfur and nitrogen cycles.

Another interesting feature of LAMMA is the surface selectivity of the measurement at low laser power irradiation (in general for excitation energies close to the threshold that allows the recording of a spectrum). The validity of the method was tested on three laboratory generated aerosol systems in order to learn more about the reliability of the method (Chapter 6). The determination of the surface composition of microparticlulates is of considerable importance because the fate and reactivity of an aerosol is largely controlled by the structure and chemical characteristics of the gas-particle interface. Standard aerosol samples were artificially

coated in their airborne state by a gas phase condensation technique with organic compounds such as n-hexadecanol and polynuclear aromatic hydrocarbons (PAH). For the PAH an orienting study was done to investigate the applicability of LAMMA for the identification of chemical transformation products as a result of heterogeneous reactions between PAH-coated aerosols and possibly reactive trace gases such as O_3, NO_2, Cl_2 and Br_2. Also the interaction beween HNO_3 and the natural seasalt aerosol was studied in some detail.

The knowledge gained by the more fundamentally inspired experiments was applied to three case studies that deal with the chemical characterization of airborne particulate matter based on individual particle analysis measurements (Chapter 7). The first study concerns the analysis of aerosol samples collected in Salvador (Brazil), at rather unpolluted beach and inland sites, and in a heavily polluted industrial area. The second study was carried out on North Sea aerosol samples, collected on board the research vessel Belgica as part of the North Sea project of the Belgian Ministry for Science Policy. The third set of samples was collected during the Amazone Boundary Layer Experiment (ABLE-2A) as a part of the Global Tropospheric Experiment (GTE) of the US National Aeronautics and Space Administration (NASA).

Finally, the general conclusions that can be drawn from the present work are resumed and some suggestions for future developments that could contribute to a further improvement of laser microprobe mass spectrometry as an analytical tool are made.

CHAPTER 2 THE LAMMA-500 INSTRUMENT

The principle of the laser microprobe mass analyzer LAMMA-500, (Leybold-Heraeus, Köln. FRG) is based on the excitation of a microvolume of the sample to an ionized state by a focused laser beam. The analytical information is derived from mass spectrometry of these ions. The special feature of LAMMA is that the analysis is performed under microscopical observation so that a well defined area of the sample can be selected.

A schematic diagram of the system is shown in Figure 2.1 (1). The sample is mounted in vacuum at an operating pressure of usually 10^{-4} Pa on a movable x-y stage; it can be observed in a binocular microscope through a thin quartz glass window (0.2-0.3 mm), which simultaneously serves as a vacuum seal. Either transmitted or reflected light illumination can be chosen for the observation of the sample. The optical microscope (magnifications of 100X up to 1250X) is equipped with UV-transparent immersion (glycerol) objectives and is simultaneously used for focusing the red spot of a continuous low-powered (2 mW) pilot He-Ne laser onto the region of analytical interest (e.g. a single micrometer-size particle).

The vaporization and ionization of the selected sample volume is accomplished by a single pulse (τ = 15 ns) of a high-power Q-switched and frequency-quadrupled Nd:YAG laser (System 2000, J.K. Lasers Ltd., Rugby, Warwickshire, U.K.) that is collinear with the visible He-Ne search laser. The laser intensity (λ = 266 nm, power density in the range of 10^{7}-10^{11} W/cm^2 for a 1 μm laser focus) can be attenuated to 2 % of its initial value by a 25-step UV-absorbing filter system. The energy of each laser pulse is monitored and displayed directly for reference purposes. The laser generated ions are almost exclusively of unit charge. They are accelerated and collimated by an Einzel-type ion lens into the drift tube of a 1.8 m TOF-mass spectrometer with a high ion extraction and transmission efficiency (up to 50 %, within a limited kinetic energy range). The

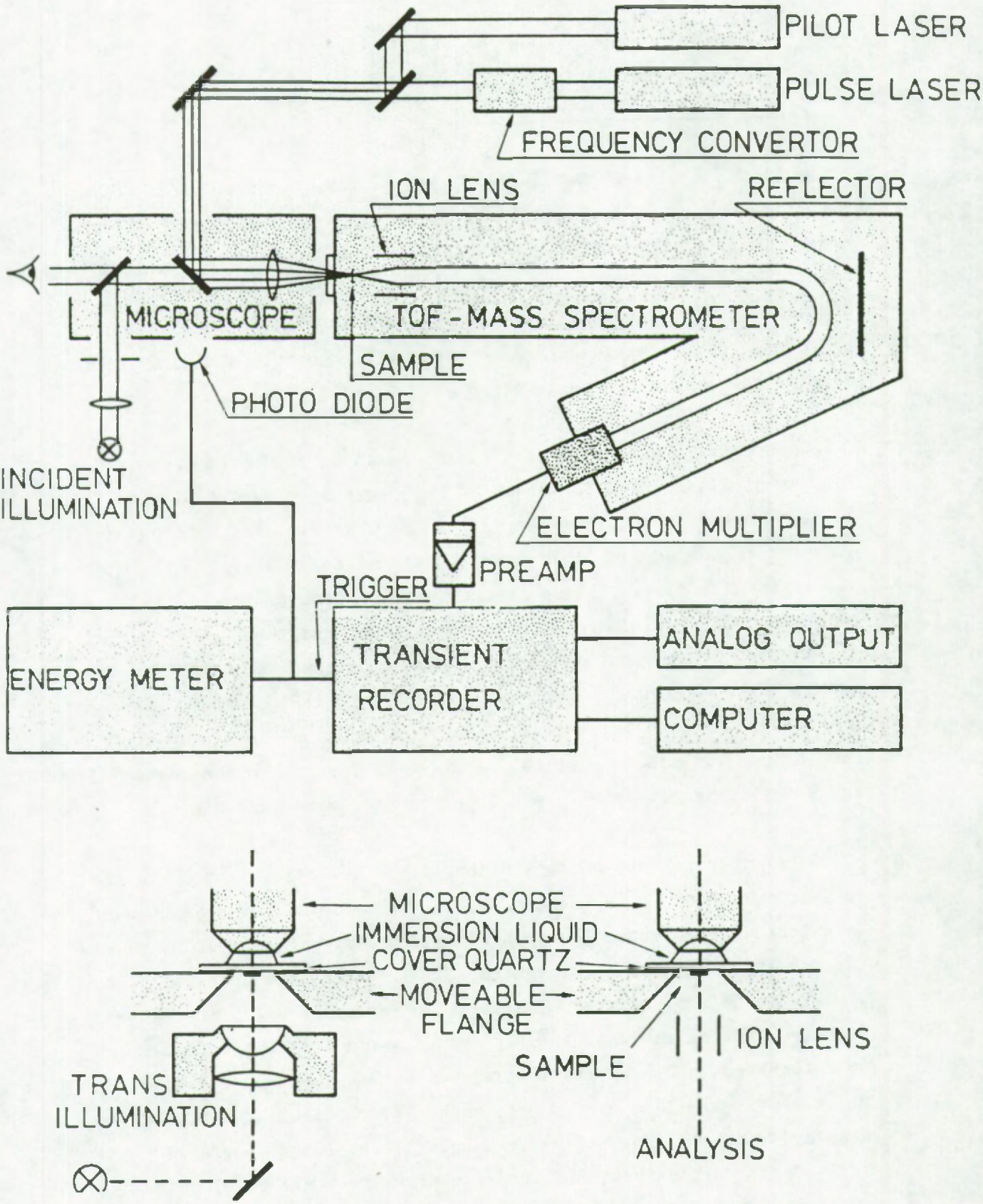

Figure 2.1: Schematic diagram of the LAMMA-500 system (1)

initial kinetic energy spread of the extracted ions is further strongly reduced by passing through a time-focusing electrostatic reflector (ion mirror) in the folded flight path (2). This ion reflecting element thus allows to bunch ions of the same mass but with different velocities, and thereby considerably improves the attainable mass resolution of the instrument. The ions are post-accelerated towards the first dynode of an open secondary electron multiplier with 17 Cu-Be dynodes and a gain of about 10^6. The output signal is stored in a fast 2048-channel and 100 MHz transient waveform recorder of 8-bit resolution. The recorded spectrum is displayed on a screen. It can be plotted as hard-copy output by a strip-chart recorder or transferred to a computer for data processing, e.g. mass scale calibration, ion signal integration, spectral averaging and further statistical data treatment.

The microplasma produced by the interaction of the focused laser beam with the sample contains electrically neutral atoms and molecular fragments, as well as atomic and molecular ions of either charge, which are all derived from the constituents of the analyzed volume. The TOF-mass spectrometer can be used for the detection of negative as well as positive ions by simply switching the polarity of the electric fields. In this way a broad mass range spectrum can be recorded for each single laser pulse. Table 2.1 summarizes some technical data and specifications of the apparatus.

Since the LAMMA-500 instrument operates in the transmission mode (ion extraction at 180° relative to the incident laser beam), the sample usually consists of a thin polymeric supporting foil loaded with micrometer-size particles, a thin specimen ($\leq 2\ \mu m$) as e.g. a standard metal or semiconductor foil or a biological microtome section.

A detailed study of the most important instrumental components of the LAMMA-500 instrument was carried out by Mauney (3). He investigated the performance characteristics of the instrumental

Table 2.1: Summary of technical data and specifications of the LAMMA-500 instrument.

Microscope	eyepiece 10 x objectives 10x, 32x, 100x (UV objectives) incident and transmitted light illumination
Laser	pilot laser : He-Ne, 2mW high power : Nd : YAG, TEM_{00}, Q-switch energy : 80 mJoule at λ = 1060 nm, τ = 15 ns
Time-of-flight mass spectrometer	length of the drift tube: 1.8 m including the ion reflector drift voltage 0 ± 5 kV
electronics	open 17-dynode Cu-Be multiplier, preamplifier 100 MHz (10x) transient recorder (2048 channels, 100 MHz, 8 bit resolution, sensitivity range 100mV -
vacuum system - sample stage - mass spectrometer	 forepump D 16 A, turbomolecular pump ion getter pump
Mass range	0 - 100 amu, 100 - 400 amu, 400 - 1000 amu with 0.02 μs sampling time, depending on delay of transient recorder (2048 channels, min. sampling time 0.01 μs)
Laser energy	20 μJ on entrance aperture of the microscope objective with 100 % filter transmission, λ = 265 nm

components such as the ion lens the drift tube, the ion reflector, and the ion detection system. For the sake of completeness a short description of the instrumental set-up will be outlined below.

2.1 IONIZATION SOURCE

2.1.1 Description of the laser system

The LAMMA-500 instrument (3,4) employs a Nd:YAG solid state laser in an oscillator-amplifier combination. A schematic representation of the laser system is shown in Figure 2.2. The laser medium consists of a crystalline YAG-host of high thermal conductivity (YAG represents yttrium aluminium garnet or $Y_3Al_5O_{12}$) doped with Nd^{3+}, as the paramagnetic lasing ion in a concentration or ion density of about 10^{20} cm^{-3}. The selected laser transition is from the $^4F_{3/2}$ state to $^4I_{11/2}$ giving 1064 nm laser light. The laser rod is located at one focus of an elliptical cavity (reflecting Au-plated elliptic cylinder as a common pumping geometry), where a linear flashlamp (xenon-filled) centered at the conjugate focus efficiently provides the optical pumping. Energy stored in a capacitor bank (high voltage around 1 kV) is dumped into the flashlamps of the pumping chamber, hereby exciting a broad range of Nd^{3+} electronic states. This discharge is triggered by the release of the laser-firing pushbutton of the LAMMA apparatus. Cooling of the laser material, which is in general necessary for a high repetition rate laser operation, is provided by a self-contained closed loop of circulating distilled water containing 8 % $NaNO_2$. The oscillator, in LAMMA, has a stable-resonator design (4). Its primary function is to provide the optical feedback mechanism needed to return the radiation emitted by the laser medium back to it (gain medium) for repeated amplification. In the LAMMA-apparatus, a concave rear mirror (totally reflecting) and a plane, partially reflecting output mirror are used. Also included in the cavity is a mode selecting aperture (1.8 mm diameter) in order to restrict the

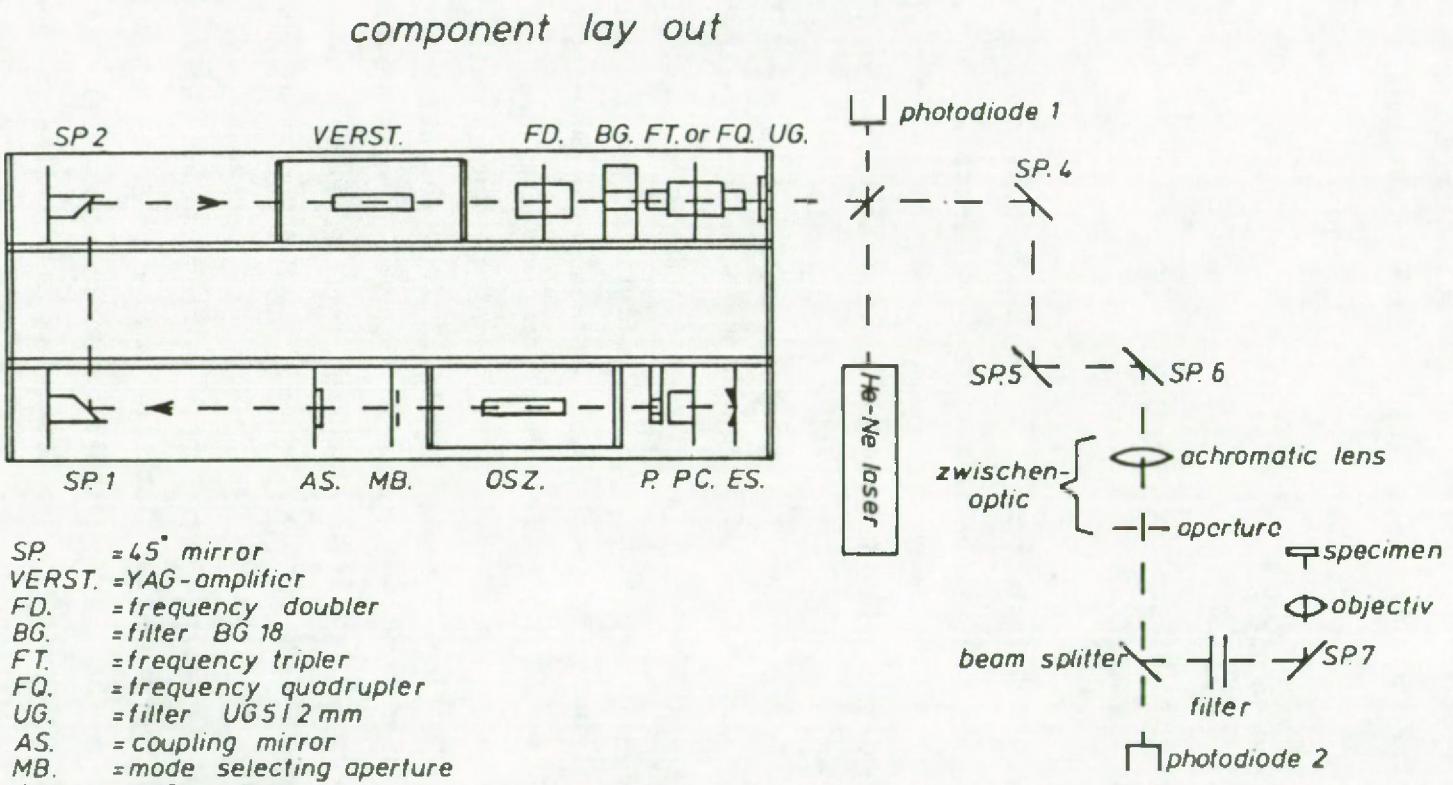

Figure 2.2: Schematic diagram of the laser system showing the pathway followed by the laser beam.

laser output to a single transverse mode, namely the fundamental TEM_{00} mode. The intensity profile of such a laser beam is shown to follow a Gaussian distribution (4). The exclusion of the higher order transverse modes is necessary to finally achieve diffraction limited focusing of the laser beam.

In order to control the laser output and to concentrate all of the available energy into a single, intense, and short pulse (down to the ns range), the oscillator is Q-switched (5). In this way, high and reproducible peak powers can be obtained that may subsequently be doubled and quadrupled in frequency (the frequency doubling process requires a high intensity of the incoming light). The Q-switching technique is thus often introduced whenever analytical methods are considered which utilize short laser pulses with high output intensities. In LAMMA, a very fast Q-switch is provided by an electro-optical shutter employing a combination of a Pockels cell and a thin associated polarizer positioned in the optical cavity. The light emitted from the laser rod becomes linearly polarized in passing the plane polarizer. The electro-optic crystal (KDP: potassium dihydrogen phosphate) or Pockels cell is maintained at such a voltage (ca. 3.5 kV) that the plane polarized light incident on the crystal is converted into circularly polarized light by transmission through the crystal. The induced phase shift in the Pockels cell depends directly on the high voltage applied, hence the effect is often referred to as the linear electro-optic effect. The laser mirror at the back reflects this circularly polarized light and in doing so it reverses the direction of polarization. Hence, on re-emerging from the Pockels cell the light is again plane polarized but now oriented at 90° to its original direction and therefore not transmitted by the polarizer. As a consequence, the shutter is closed and laser action will not occur; hence the population inversion can reach large values. By reducing the bias voltage to zero, the electro-optic crystal will have no effect other than a small source of transmission loss within the cavity (minimized by index-matching fluid), as it does no longer interfere with the polarization state of the light. When the shutter

is suddenly opened, the laser will have a high net gain and the stored energy is released in the form of a short (about 15 ns) and intense light pulse. The change in voltage is synchronized with the optical pumping and is triggered at a suitable delay time (ca. 280 μs) after the ignition of the flashlamp.

By a set of external non-linear crystals (two thermostated frequency doubling crystals) the original frequency is quadrupled to the UV-wavelength of 266 nm (providing 0.400 - 2 mJ of laser energy). The unconverted lower harmonics of the laser beam are filtered out each time from the output by an absorbing-glass wavelength separator. At this stage, the beam of a continuous He-Ne laser (red light with λ = 632.8 nm; typical power of 0.5-5 mW) is introduced in the optical pathway and is alligned collinearly with the UV-beam of the high power Nd:YAG laser. This red pilot laser eases the alignment of the laser beam optics and serves for aiming and focusing at a selected area of the sample. In essence, a quartz plate acts as a beam combiner. Additional mirrors (prisms) are required for correct alignment of both laser beams relative to the optical axis of the microscope.

An intermediate optical system is used to demagnify the laser beam waist to the useful aperture of the objectives of the light microscope, and to focus the laser exactly onto the intermediate image plane of the microscope objective. It consists of an achromatic lens with a circular pinhole in its focus. This small aperture is used as a spatial filter to eliminate higher order contributions, yielding a more homogeneous and circular intensity distribution. The system lens-pinhole is axially adjustable for correct focusing of both laser beams onto the sample. Hereafter, a constant fraction of the UV-laser light is transmitted through a beam splitter and is detected by a calibrated photodiode meter for laser energy monitoring. The splitter reflects part of the incident laser light and introduces it onto the optical microscope. Before the light enters the microscope, a set of in tandem UV-absorbing filters can be used to reduce the laser intensity. A folding mirror

inside the microscope nosepiece reflects the laser beam and orients it into the selected objective lens (Zeiss Ultrafluar 100X or 32X, both of the oil immersion type, and the 10X objective for the use at longer working distance). These UV-transmitting objectives are thus used to focus the laser beam onto the particle and simultaneously they serve for the light microscope observation of the sample with either incident or transmitted light (total magnification up to 1250X).

2.1.2 Laser power at the sample

In general, for multimode beams, as for pulsed solid-state lasers, the approximation (6):

$$D = f.Q_o \qquad \text{(eq. 2.1)}$$

is used, where D is the diameter of the focused spot and Q_o the divergence angle of the beam approaching the lens (with focal length f). If the power in the beam is W watts ($W = P/\tau$; P is the measured quantity of energy delivered during the laser pulse of duration τ, defined as the full width at half maximum, which equals 15 ns) then the power density E at the focused spot is given by:

$$E = \frac{4.W}{\pi\, f^2\, Q_o^2} \qquad \text{(eq. 2.2)}$$

For a beam of uniform intensity distribution and radius R, one has:

$$Q_o = \frac{1.22\ \lambda}{R} \qquad \text{(eq. 2.3)}$$

Hence,

$$E = \frac{0.86\ WR^2}{f^2\ \lambda^2} \qquad \text{(eq. 2.4)}$$

In the equations cited above, the power densities are derived on the assumption that the light is concentrated uniformly over the focused spot. In practice, however, the intensity at the center will be greater than at the edge; the beam produced by the resonator operated in the TEM_{00} mode has a radial amplitude profile, which is Gausssian, and a characteristic diameter at which the amplitude is 1/e times the maximum, and with an intensity $1/e^2$ times the maximum. If the laser is operating, as we have seen above, in the uniphase mode and if only light of intensities higher than $1/e^2$ that at the center are included, then

$$Q_O = \frac{2\ \lambda}{\pi\ R} \qquad \text{(eq. 2.5)}$$

And so in this case:

$$E = \frac{\pi\ WR^2}{f^2\lambda^2} \qquad \text{(eq. 2.6)}$$

Calculations based on idealisation and geometrical approximation readily provide approximate values of laser intensity, focal diameter and energy available at the sample. With commercially available equipment, it is possible to achieve focusing of the laser beam to nearly the limit imposed by the laws of optical diffraction. As a first approximation, the diffraction-limited spot size may be used, and the radial amplitude profile estimated as Gaussian. Estimates of the minimal laser-induced perforation radii are 0.2 - 0.3 and 0.3 - 0.5 μm at 100X and 32X objectives, respectively, in polymer films (4) and 1.8 μm in silver foils (7), comparable to 0.48 μm with the 100X objective as derived from diffraction theory and

geometrical optics (3).

The energy actually deposited in the sample, being the time integral of the power available at the sample and the absorbance of sample and plasma, is not directly measurable. The energy delivered is estimated by integration of the current through a photodiode which, via a beam splitter, measures part of the laser beam. The fraction absorbed is not directly known.

A pulse of 15 ns delivering 1 μJ to a spot with a Gaussian profile and a radius parameter of 1 μm would have a peak intensity of 1.06×10^9 W/cm^2. In practice, absolute laser energies between about 0.001 and 10 μJ may be available at the sample surface, leaving a power density in the range of 10^7-10^{11} W/cm^2 for a spot of about 1 μm diameter. The latter figure is subjected to considerable uncertainty as an absolute power density range and the pulse energies stated by different laboratories are not strictly comparable. Indeed, interlaboratory standardization is uncommon in LAMMA , nor has the method of calculating focal intensities been agreed upon. Uncertainty in estimates of power density at the sample is aggravated by chromatic aberration of the microscope between the UV-focus of the pulsed laser, the red laser for sampling and the visual focus which may easily differ from each other by a few μm. The shot-to-shot variability of the laser energy output is estimated to be 8-15 % (8).

The mean energy available to the sample molecules is the time integrated laser intensity, corrected for reflection and transmission losses in sample and plasma. Intensity, transmittance and reflectance are not constant over time or space, nor from sample to sample. This energy is partitioned into vaporization, ionization and plasma expansion. Hence, inevitable variations in laser intensity or laser focusing conditions will lead to differences in the volume analyzed, the degree of molecular fragmentation and the ionization efficiency. The influence of the focusing condition on the spectral intensity was studied for a multilayered sample built

up in the geometry as shown below:

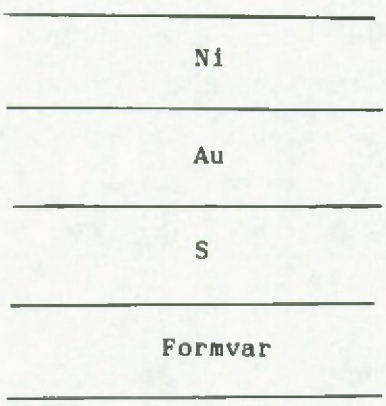

The overall thickness of the sample (prepared by I. Musselman) was smaller than 1 μm. The measurements were carried out in cooperation with Prof. R. Linton. The Ni-layer was positioned towards the extraction lens. The focusing position was shifted between -10 and +20 μm in steps of 5 μm. A sharp view of the perforations in the sample as observed in the optical microscope was defined as the 0 or in focus condition. For each focusing condition an average spectrum was recorded by the addition of 10 individual spectra and the standard deviation on the intensities is about 10 %. The intensities for the Ni_2^+ and the NiS_2^+ clusters are plotted as a function of the focus in Figure 2.3 It is clear that the Ni_2^+-cluster has a broader range for detection ranging from -5 to +20 μm, whereas for the NiS_2^+ a narrow distribution from 0 to 15 is observed. It should also be noticed that the maximum intensity is found for +5 or +10 μm and not for 0 μm. The appearance of higher intensities for the clusters at a so-called prefocused condition was also observed for other inorganic compounds.

Samples of uniform thickness as e.g. metal and carbon foils or biological microtome sections generally offer a better shot-to-shot reproducibility compared to particles spread on a thin film. Differences in reflection and light transmittance of the individual particles highly influence the efficiency of particle destruction i.e. the possibility to analyse particles in a single laser shot.

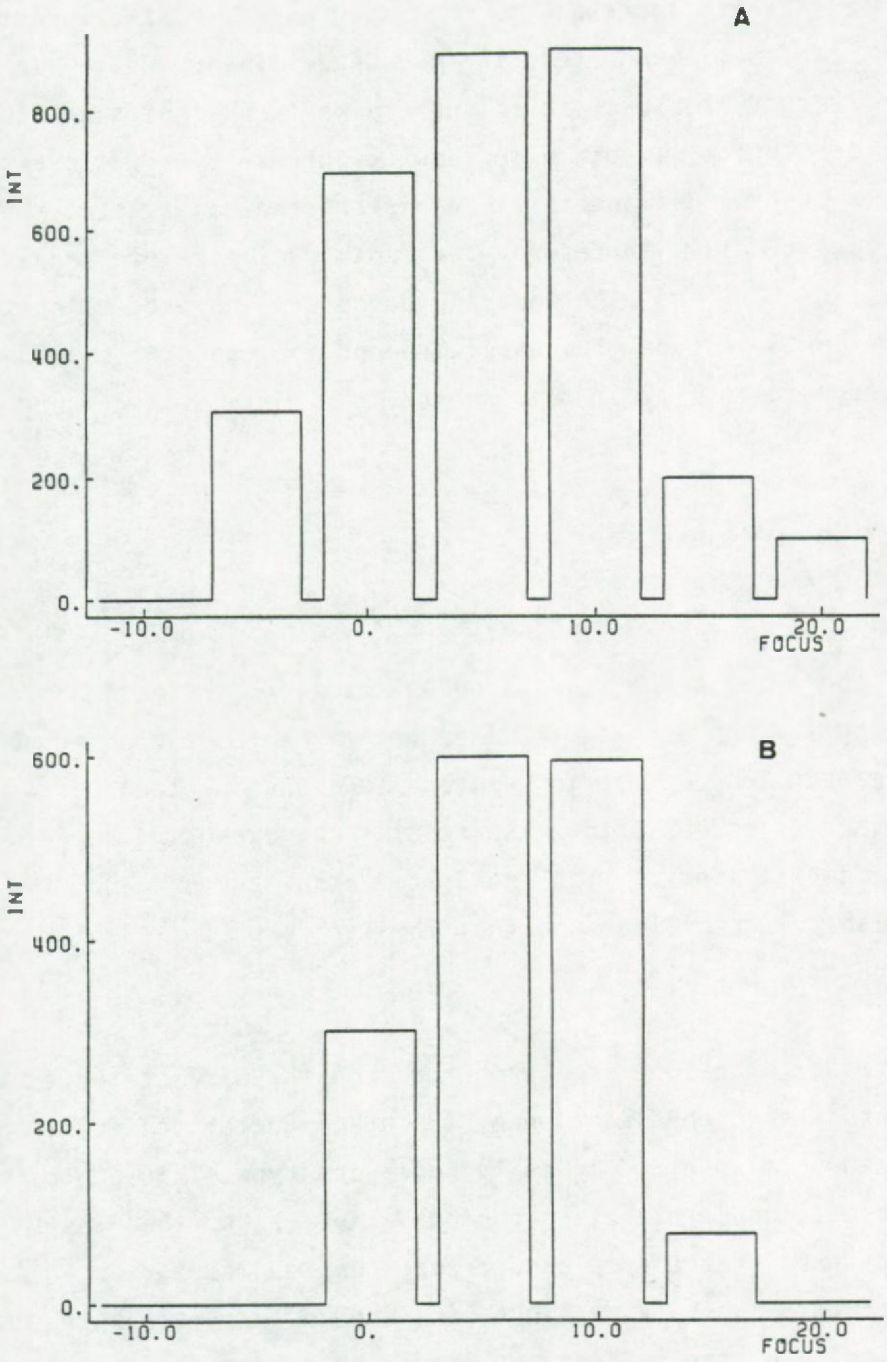

Figure 2.3: Intensity of the Ni_2^+ (a) and NiS_2^+ (b) clusters for the Ni/Au/S/Formvar multilayered sample recorded for different focusing conditions ranging from -10 to 20 μm.

A significant increase in the laser energy to increase the volume that can be evaporated in a single laser pulse is seldomly satisfactory because it often results in a significant loss of the mass resolution. It can also lead to intense overflow peaks for the matrix components, and this can distort the baseline of the spectrum very drastically. Therefore, for individual particle analysis, the laser energy and the focusing conditions have to be optimized for every particle type. The experience of the operator can thus improve the reproducibility of the spectra.

2.2 MASS SPECTROMETER

The microprobe is based on the timed ionization of solids by the application of a short laser pulse. Hence, a continuous instead of gated ion extraction into a TOF-mass spectrometer is allowed. However, as a result the mass resolution directly depends on the time definition of the generated ion bunch. For the sake of simplicity, we will assume that the ion formation follows a pulse shaped time profile.

Since the ions are extracted from the side of the sample which is opposite to the laser beam, the spectrometer configuration of the LAMMA-500 is referred to as transmission type. This contrasts to the frequently used reflection geometry, in which the laser and ion optics are at the same side of the sample. The latter configuration is utilized in the LAMMA-1000, introduced in 1982, which has been developed for the analysis of larger bulk samples.

2.2.1 Ion extraction and mass separation

The ions formed upon laser impact are extracted from the source to the drift tube by a potential difference of typically 3000 V, and then they pass through an ion lens which focuses them toward the

detector. The ions are thus accelerated toward the drift region of the TOF-mass spectrometer by an electrostatic field formed between the sample itself and the entrance electrode of the spectrometer (since the gap covers a distance of 5.75 mm, the electric field is about 5200 V/cm). The LAMMA-500 can be used to analyse negative as well as positive ions, depending on the polarity of the potentials applied to the electrodes. In the drift region of the TOF-tube the ions separate according to their different velocities. The principle is outlined in Figure 2.4. The mass discrimination and dispersion of a TOF-mass spectrometer is derived from the classical energy-velocity relationship $E_K = 1/2\ mv^2$, or $v = (2E_K/m)^{\frac{1}{2}}$, where v represents the velocity of the ion, m its mass, and E_K the respective kinetic energy. In the first part of the mass spectrometer the bunch of ions has been accelerated over a short distance in order to gain sufficient kinetic energy. Let us assume that the contribution of any initial kinetic energy E_0 due to the laser ionization process can be neglected. The kinetic energy obtained by the ions after passing the whole acceleration region equals the potential difference (u_{TOF}) multiplied by the charge of the ion (q). So, we obtain

$$v = (2q\ U_{TOF}/m)^{\frac{1}{2}} \qquad \text{(eq. 2.7)}$$

The ion mass can be expressed in atomic mass units (1.6604×10^{-27} kg) and its charge by z times the electron elementary charge (1.6021×10^{-19} C), so that

$$v = 1.39 \times 10^4 \frac{(U_{TOF})^{\frac{1}{2}}}{(m/z)^{\frac{1}{2}}} \qquad \text{(eq. 2.8)}$$

From this point on, the ions are allowed to drift for a distance L sufficient for the velocity differences to separate the various mass species from each other spatially. These spatially resolved groups of ions arrive in succession at the detector, presenting a series of ion pulses with specific arrival times indicative of their mass-to-charge ratios. As a first approximation

the arrival time t of the ions will then be:

$$t = L\ (m/2q\ U_{TOF})^{\frac{1}{2}} \qquad \text{(eq. 2.9)}$$

$$= \frac{7.2\ 10^{-5}\ L\ (m)^{\frac{1}{2}}}{(U_{TOF})^{\frac{1}{2}}} \qquad \text{(eq. 2.10)}$$

$$= C\ (m)^{\frac{1}{2}} \qquad \text{(eq. 2.11)}$$

where L represents the length (in meters) of the effective drift region, implied mainly by the geometry of the instrument. The proportionality of time versus $(m)^{\frac{1}{2}}$ is a crucial property for the mass calibration of time-of-flight spectra (see further below). The constant C can be calculated from the geometry and the electric potentials of the TOF-mass spectrometer. For practical use it is easier to derive the value of C by identifying several mass peaks of the spectra obtained from reference samples.

A practical TOF-spectrometer will not merely have a field-free drift region, but also accelerating and decelerating regions whose transit time will contribute to the total flight time. In the LAMMA-500, an ion lens of the immersion type is introduced to increase the acceptance of the spectrometer and to collimate and focus the ion beam. Furthermore, a time-compensating ion reflector system and a post-accelerating region near the detector cathode supply additional electric fields which influence the velocity and the pathway of the ions. A thorough calculation of the ion flight time for mass calibration purposes will have to deal with all these contributions.

In general, the resolving power of a mass spectrometer will be better if the components of the ion beam are simultaneously well separated in space and well focused to small images. The spectrometer completely resolves adjacent masses if the spread of flight times for ions of a single mass does not exceed $(t_{M+1} - t_M)$. If the spectrometer just resolves an ion bunch of mass M from

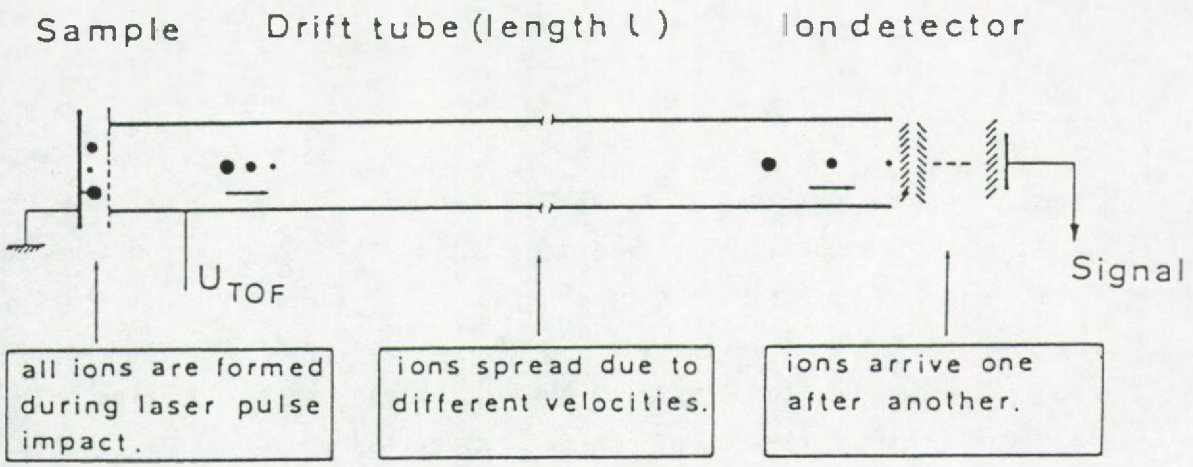

Figure 2.4: Schematic representation of the principle of time-of flight mass spectrometry. A bunch of ions, generated in a very short time interval, is accelerated and proceeds its way in the drift tube towards the detector. The flight time for each ion is a function of its mass, so the detector receives a series of consecutive ion bunches. A mass spectrum is obtained by recording the detector current versus time (4).

another differing in mass by ΔM, the mass resolution (R) of the instrument is defined as:

$$R = \frac{M}{\Delta M} \qquad \text{(eq. 2.12)}$$

Two ion types are just resolved when the interval Δt between their centers becomes equal to their mean width W. Hence, the following expression for the resolving power (RP), as stated by Vogt et al. (4) is obtained:

$$RP = \frac{\Delta t \; M}{W \quad \Delta M} \qquad \text{(eq. 2.13)}$$

For a good estimation, Δt may be considered to be proportional to $L/(U_{TOF}.M)^{\frac{1}{2}}$, as obtained by differentiation of Equation 2.9. The peak width W is influenced by a number of factors: the distribution of the initial kinetic energies E_o of the ions, differences in ion optical pathways, the length of the ion acceleration and drift path, and the response time C_A of the ion detection system. The initial energy E_o results from the laser ionization process itself and is depending on the excitation state of the sample, which in turn is influenced by the applied laser intensity and the absorption characteristics of the irradiated sample area. Due to the insertion of the ion reflector, the resolution of the TOF-mass spectrometer is considerably improved by eliminating the ΔE_o-effect to a first order approximation. In this way, the possible dependence of the mass resolution on the sample excitation conditions is strongly reduced. Eventually, the contributions from the instrumental response time C_A, essentially determined by the transit-time spread of the electron multiplier, the frequency-bandwidth of the preamplifier and transient recorder (typically around 10^{-8} s) (4), become dominant and lead to the formula:

$$RP = C.\sqrt{\frac{M}{U_{TOF}} \cdot \frac{1}{C_A}} \qquad \text{(eq. 2.14)}$$

with C as aconstant. Kaufmann et al.(2) improved the mass resolution to about 850 by inserting an ion reflector in the TOF-mass spectrometer to compensate for the spread of initial ion energies. This value is certainly sufficient for the identification and measurement of elemental ions. In particular at the high mass range, any deterioration of the performance of the istrument will have a pronounced effect on the spectral quality and the obtainable mass resolution. It is difficult to accomplish a base line separation of full scale peaks at adjacent masses in the range from m/z = 600 onwards (Van Vaeck, personal commucication). Moreover, comparison of instruments with and without ion reflector reveals that this element reduces the peak width by overlapping several possible contributions from isobaric ions with different initial velocities. As a result, the reflector allows for a better peak shape at the expense of some specific information, that can be useful in fundamental studies on the ion formation mechanism.

An electostatic TOF-mass spectrometer provides some particular advantage over other types of mass analysers. Since there are no dead times of scanning, a whole mass spectrum of one polarity can be recorded from a single laser pulse. Since the TOF-mass spectrometer essentially consists of cylindrical tube electrodes, a high transmittance of the ions is obtained, leading to a high intrinsic ion detection capability. The latter is also determined by the ion extraction efficiency. The quality of the ion extraction will depend on both the geometry of the system (design of the instrument and applied voltages) and the specific distribution of radial ion velocities. Despite its importance, a fully quantitative treatment of the extraction efficiency as a function of general physical parameters is not available. The fraction of ions that can be extracted effiently will thus be characterized by the distribution in space of the ions and the radial distribution of their respective

velocity vectors. If such distributional differences would occur in single or sequential measurements, then ion discrimination during the extraction process is to be expected (9). It has been suggested that atomic ions are mainly formed in the central core region (of a higher ionic temperature) of the laser-induced microplasma, while molecular ions may be formed by a so-called laser desorption process in the lower intensity fringe of the beam. During the ion formation, initial kinetic energy distributions may be generated which differ from species to species (10). The geometry and position of the sample, the laser beam intensity profile and focus, as well as the deposited laser energy, can vary, being either changed by the operator or by random shot-to-shot variation. All these factors may have a pronounced influence on the extraction efficiency and as a consequence also on the experimental signal variability.

2.2.2 Ion lens

In the LAMMA-500 mass spectrometer an ion lens is positioned in the drift tube, centered at about 2 cm behind the accelerating electrode. It consists of a tubular, three element (with the same radius R), constant voltage, immersion ion lens. The central segment is held at a different and lower potential (U_{lens}), in absolute value, with respect to the two outer electrodes which are kept at the same potential (U_{TOF}). Such an ion lens is classified as an Einzel (single) lens. The lens length (L) is 13 mm and its geometrical parameters are L/R = 2.6 and D/R = 0.4, where D represents the spacing between the segments. It serves to collimate the ion beam (Figure 2.5) and thereby to improve the transmittance of the ions through the spectrometer by focusing them onto the detector surface. Otherwise, most of the ions would be lost due to collision with the tube walls. An ion beam crossing a potential discontinuity suffers a change of its normal velocity component, while its velocity parallel to the equipotential surface remains

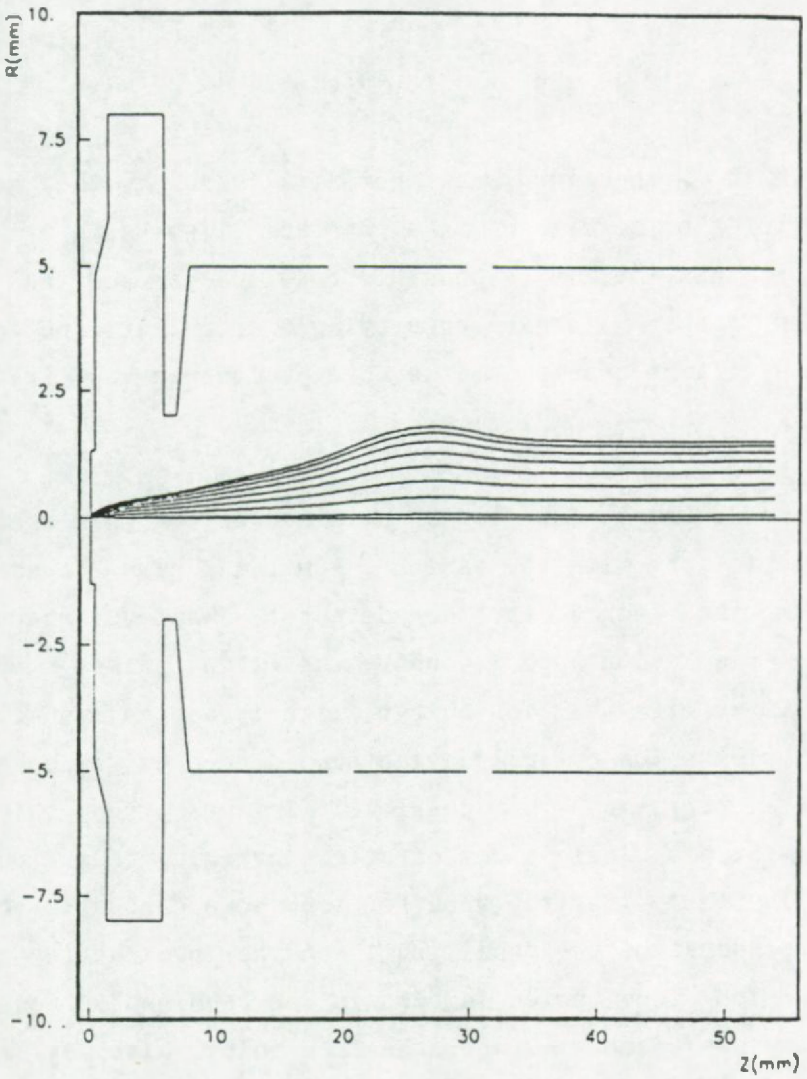

Figure 2.5: Focusing effect of the ion lens on the ion trajectories: U_{TOF} = 3000 V, U_{lens} = 900 V for ions with an initial kinetic energy of 5 eV, starting from the sample surface on the optical axis and for specific angles (2.5°, 12.5°, 22.5°, 32.5°, 42.5°, 52.5°, 62.5°, 72.5°) (11).

constant. Since the velocity of the ions is proportional to the square root of their energy which in turn is determined by the focal potential, an equation is obtained similar to the ordinary law of optical refraction:

$$(U_1)^{\frac{1}{2}} \sin i_1 = (U_2)^{\frac{1}{2}} \sin i_2 \qquad \text{(eq. 2.15)}$$

where U is the respective local potential and i the angle with respect to the normal of the surface line separating the two regions. In this way, it is possible to visualize how the ion beam is traced across a region of varying electrostatic potential. The higher the voltage change is, the more pronounced is its focusing effect.

Two objectives are to be attained in TOF-mass spectrometry. Monoenergetic ions with the same mass must all have the same flight time from the source to the detector, whatever the angles and positions of emission are. Secondly, the flight times must remain constant even if the ion energy slightly varies around a central value. Thus, the ion optical design should have as few spherical and chromatic aberrations as possible. In practice, this is not achievable with a single electrostatic converging lens. Ion lenses, as used in LAMMA, inevitably suffer from some chromatic aberration, i.e. a dependence of the focal length on the ion kinetic energy. A different ion lens potential would be required to focus ions of different kinetic energies onto the same point. Also, at a certain voltage setting of U_{lens}, a varying transmittance is observed for ion species with different kinetic energy distributions. It has been shown that, in LAMMA, ions of different chemical origin show different distributions of initial ion kinetic energies (3,8,11).

For optimal ion transmission, the zone of ion formation has to be imaged onto the sensitive diameter of the detector. So, any defocusing condition of the ion lens will influence the spectral intensity. Not only the total spectral intensity may vary, but also the relative signal intensities of the different chemical species.

Variation in sample position and ionization conditions may require optimizing of the ion lens potential for each specimen. Degradation of spectral information and even masking of peaks can occur due to incorrect selection of the ion lens potential.

The ability to essentially extinguish the ion beam by overfocusing the ion lens was used by Mauney (3) to estimate the chromatic aberration of the ion lens. The lens potential was varied until the ion signal sharply decreased with increasing lens voltage differential $U_{TOF} - U_{lens}$. Thus, at the low voltage side (low U_{lens}) a threshold lens potential (threshold for overfocus) was defined and measured as a function of ion kinetic energy determined by the ion accelerating potential. Based on the negative-ion spectra of carbon foil the potential required to focus ions was shown to be proportional to the ion kinetic energy (the threshold lens potential to TOF-potential was measured to be 0.327). In practice, a ratio U_{lens}/U_{TOF} close to 1/3 is used for proper focusing of the lens. The exact ion lens voltage for the maximum detected signal will however be dependent on the specific kinetic energy and the spatial position of the emission of the ions.

2.2.3 Ion reflector

The LAMMA-500 design includes a single stage, electrostatic ion reflector which compensates for possible differences in the ion flight times resulting from different ion kinetic energy to be retarded by their longer flight into the retarding field, and so their arrival time at the detector can be matched with that of the slower ions of the same mass. The principle is outlined in Figure 2.6. The ion transmittance of the reflector has been studied by Mauney and Adams (12) by means of a simple thermal ion source which emits Na^+ ions from a tungsten filament.

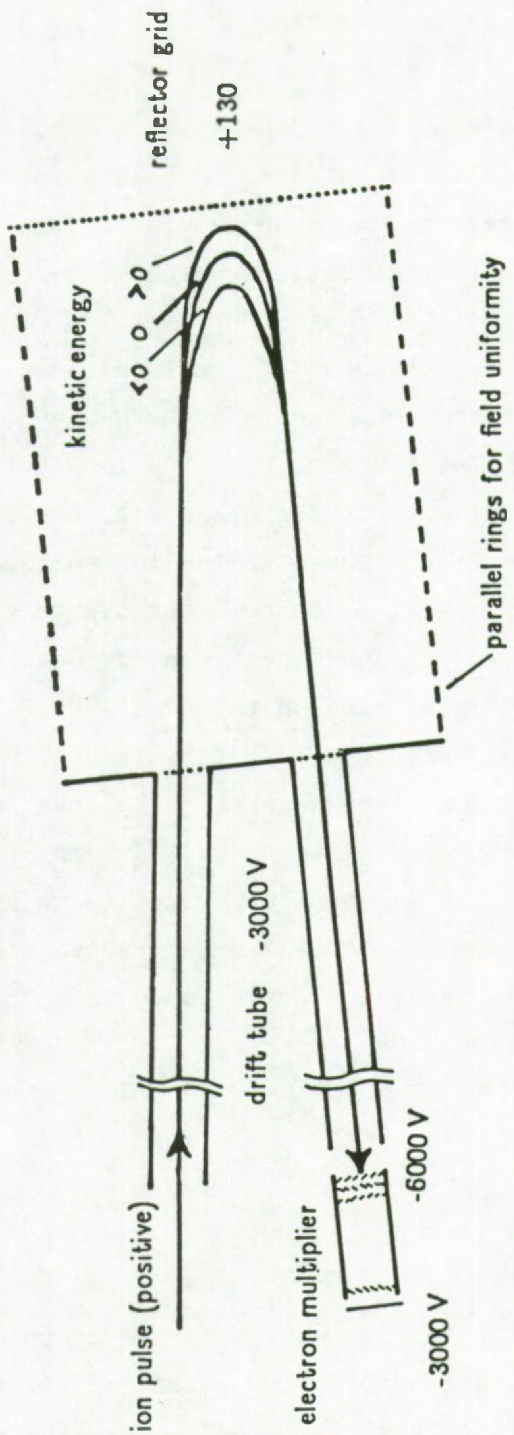

Figure 2.6: Ion reflector of the type employed in the LAMMA-500 instrument. Ions of higher kinetic energy penetrate more deeply into the reflecting field and are delayed with respect to ions of lower kinetic energy. The delay compensates for differences in transit time in the field free region. (Differences in trajectory are exaggerated for clarity.)

As stated above, the mass resolution of the TOF-mass spectrometer is considerably improved by employing the ion reflector system in the drift path. This is not only due to its energy-time focusing action but also because it simultaneously enlarges the effective drift path (and thus the mass separation). Compared to a linear TOF-mass spectrometer, the folded drift tube nearly doubles the available length of flight path without consuming much more room space. On the other hand, it can influence the relative signal intensities in the spectrum by acting as a filter which cuts off all ions having more kinetic energy than $(U_{TOF} - U_{refl}).\cos^2\theta$, with θ being the reflector incidence angle. It also attenuates ions when the reflected image is not well centered on the detector (3).

The influence of the reflector as an instrumental parameter is not important when applied in the normal working range around a reflector voltage of 125 V, where all signal intensities have reached a plateau. However, its energy cutoff property may be utilized in order to obtain cumulative ion kinetic energy distributions (8-14). Such an operation requires the recording of repetitive spectra from homogeneous samples under uniform ionization conditions, while stepping of the cutoff level across the energy range is provided by adjusting the reflector potential.

2.2.4 Mass calibration

For the LAMMA-500 spectrometer, the following experimental flight time equation is established:

$$t = \alpha + \beta\,(m/z)^{1/2} \qquad \text{(eq. 2.16)}$$

The parameter α represents the time delay between the nominal starting time of the experiment and the actual time of ion emission. It implies the delays in the propagation of the electronic signals, the various triggering events and the ion production process itself which is induced within a time interval of the order of the laser

pulse duration (10 ns). The value for the parameter α was determined experimentally by Mauney (3) to be about 3.0 μs. The coefficient β is comprised of the flight equation coefficients for all of the various regions of the spectrometer. Its value can be calculated from the instrumental geometry and electronic parameters, and it can be compared to the value obtained experimentally.

The apparatus can be divided into the following regions: acceleration region, ion lens, drift tube 1, reflector, drift tube 2, and postacceleration at the cathode. The latter region refers to a gap of about 3 cm between drift tube 2 and the electron multiplier cathode in which the ions receive an additional acceleration in order to minimize mass discrimination of the detection efficiency. Thus,

$$t_{flight} = t_{accel} + t_{drift} + t_{lens} + t_{refl} + t_{cath} \quad \text{(eq. 2.17)}$$

Using some geometrical approximations and basic assumptions on the electrostatic potentials along the spectrometer axis in order to simplify the calculations, the coefficient β can be expressed by (3):

$$\beta = 1.972\ 10^{-6} + \frac{6.42 \times 10^{-3}}{\left|U_{TOF} - U_{refl}\right|} \quad \text{(eq. 2.18)}$$

$$(U_{lens} = 1/3\ U_{TOF} \text{ and } U_{cath} = 2\ U_{TOF})$$

for an acceleration voltage (U_{TOF}) of 3000 V and with time t expressed in seconds. Variation of the ion reflector potential thus changes the drift time for ions of a particular mass and energy: ion signals are shifted to shorter delay times (lower b) at higher (more repulsive) reflector voltages due to a decreased effective drift length. As an example, the flight time of $^{208}Pb^{+}$ ions under routine conditions (U_{TOF} = -3000 V; U_{refl} = 125 V) is calculated to be 58 μs. The relative contribution of the time, in seconds, spent by

the ions in the first acceleration region, for U_{TOF} = -3000 V, is given by:

$$t_{accel} = 15.1 \times 10^{-9} \, (m/z)^{\frac{1}{2}} \qquad \text{(eq. 2.19)}$$

For the $^{208}Pb^{+}$ ions this would be 0.218 μs, which is indeed small compared to the actual ion drift time

Mauney (3) demonstrated a good correspondence between the calculated flight-time coefficients and the experimental calibration coefficients obtained by making two-point evaluations of sets of mass spectra. The relative discrepancy between both values was not statistically significant.

2.3 ION DETECTION

Since ions striking metal surfaces cause the emission of secondary electrons, open electron multipliers are often used in mass spectrometers to detect small ion currents. The ion current is converted to an electron current at the first dynode of the multiplier and is magnified by further dynodes, the total amplification or gain being given by:

$$G = G_1 \cdot G_2^{m} \qquad \text{(eq. 2.20)}$$

where G_1 is the ion-electron conversion coefficient (number of secondary electrons released per incident ion at the conversion dynode) and G_2 the multiplication factor of each of the m remaining dynodes (at each of the multiplier stages, further secondary electrons are emitted). Understanding of the ion-induced electron emission at the first dynode is important for the use of an open electron multiplier in mass spectrometry, because at this particular stage, mass discrimination complicates the measurements; i.e. isotopes of smaller mass bombarding the metal surface produce a

heavier emission of electrons than do isotopes of greater mass with equal kinetic energy. In general, the ion-electron emission parameter G_1 is dependent on the composition and purity of the target dynode, the relative angle of ion impact, the charge and polarity of the ions, their electronic configuration, and the ion kinetic energy. Discrepancies in ion detection occur as a function of the chemical nature and structure of composite ion species and, mostly, of the ion mass (13-18). In practice, it is often assumed that ions with the same velocity also produce the same number of secondary electrons. For a constant ion kinetic energy, the detector response will then decrease with the square root of the ion mass. However, Fehn (15) established the relationship:

$$G_1 \sim v^b \qquad \text{(eq. 2.21)}$$

where the exponent b decreases with increasing ion kinetic energy, and increases in a nonmonotonous periodic way with increasing atomic number of the impacting ions. In particular for the heavier elements, a simple signal correction by a factor proportional to the inverse square root of the isotope mass is no longer valid. Molecular and cluster ions have been studied less extensively than atomic ions (17,18). Positively charged dimers M_2^+ and monoxide MO^+ result in a higher ion-electron conversion coefficient than the corresponding elemental ion M^+. Also, the conversion efficiency appears to be a factor of 2 higher for positive ions than for negative ions. The average secondary electron yield increases with the number of atoms per ion and, for constant mass, it is larger for polyatomic ions than for single atomic ions. The difference in yield between cluster ions in homologous series (of the type M_{n+1}^+, M_n^+) decreases for larger values of n. The conversion efficiency of the cathode also depends on the type, age and previous history, and the experimental conditions of the electron multiplier.

At the end of the drift tube the ion bunch is post-accelerated towards the first dynode (cathode) of the detector (U_{cath} is usually - 6000 V for positive ion detection). The non-linear field near the

cathode induces a slight lens effect which tightens the ion beam and minimizes angular losses due to collisions outside the sensitive area of the detector. The detector consists of an open 17-stage CuBe venetian blind secondary electron multiplier (Model 9643/4B, EMI, Middlesex, U.K.), which provides a gain of about 10^6 (for a multiplier voltage U_{mult} = 3000-3250V). The spectrum may be recorded after an additional preamplification (10X) of the output of the electron multiplier. Signal pich-up can be performed at the 6th, 12th or 17th (last) dynode. By using these different outlet connections and by varying the respective voltages U_{mult}, the signal amplification can be varied over a wide range and adapted to the signal intensities. This is particulary useful to reduce the overall spectral intensity and to avoid overloading of intense peaks (see further below). A maximal voltage of 3.5 kV is recommended when using the total dynode series. This value has to be lowered when a smaller number of dynodes is used.

An important property of the detector, in particular for quantitative measurements such as isotope ratio determinations, is the experimental linearity of response, i.e. the proportionality between the input ion current and the signal output. Substantial non-linearity for output peaks greater than 0.2-0.3 V has been observed by Simons (19) for ion detection in LAMMA. A decrease in gain of the electron multiplier with increasing output pulse amplitude restricts the analytical accuracy. Whithin the experimental error, a simple saturation model fits the response curve, so that its effect can be calibrated and corrected. In case of large ion currents, for which saturation of the last electron multiplier stages would distort the spectra, the signal can be tapped at the 6th or 12th dynode stage. In the low amplitude signal regime, the statistical nature of the ion counting process becomes important and needs consideration.

2.4 SPECTRUM RECORDING

In any form of TOF-mass spectrometry, the time-dependent ion signal must be recorded as the series of masses arrive over a short period of usually microseconds.

In the original design the pulsed ion signal from the detector is fed into a fast transient recorder (Model B-8100, Gould-Biomation, Cupertino, California, U.S.A.) which incorporates a 100 MHz, 8-bit resolution analog-to-digital convertor, and a total of 2048 memory channels (2 kbyte). The input sensitivity of the transient recorder (TR) ranges from 50 mV to 5 V and allows matching of the signal peak heights according to the nominal "8-bit" dynamics of the TR. Digitizing of the signals is usually performed in sample intervals of 10, 20 or 50 ns. The selected delay time and sampling rate determine the recorded mass range and to some degree the mass resolution achieved. Using an acceleration voltage of 3000 V, the principal portion of the mass spectrum, between 20 and 200 mass units, arrives in the time interval from 20 to 60 μs after the laser pulse. The TR is triggered by the Pockels cell controller when releasing the Q-switched laser pulse. For adequate representation of the peak shape, several time intervals should be sampled within each peak profile. If the routinely used sampling interval of 20 ns is selected, about 7 measurements points are made for each mass peak in the lower mass range (below m/z = 120, at U_{TOF} = 3 kV).

The dynamic range of the TR are limited by the 8-bit word size (static resolution). At high signal slew rates the precision of digitization decreases and the resolution of measurement is severely reduced for large peaks. The resolution of the TR is limited by the aperture uncertainty and the signal frequency. Simons (19) stressed the importance of this decrease in resolution, from nominally 1 in 256 down to about 1 part in 5 (2.3 bits) for large mass spectral peaks at 10 MHz, which deteriorates the precision of the measurement. Solutions to minimize this problem are based on the use

of transient recorders of a higher performance such as the TR 8818 B from LeCroy (LeCroy Research Systems Co., New York, U.S.A.), of which the hybrid circuitry allows for an aperture uncertainty of only 25 ps. It allows to retain 8 significant bits at 100 MHz signal frequency. According to Simons (19), an effective dynamic range of 6.5 bits (1 part in 90) is achievable in practice. An additional advantage is the memory size of 32 kbyte allowing to record a properly resolved mass spectrum up to m/z = 600 on each laser shot. A LeCroy TR 8818 B-MM 8103/8 transient recorder was recently installed on the LAMMA-500 instument of our lab and it has been equiped with a very efficient and userfriendly software package running on a IBM PC-AT (20).

By installing two separate recorders operating at different signal attenuations, either working in one and the same mass range or in two sequential possibly overlapping mass regions, one can attempt to overcome the limitations imposed by the preset input range. Nevertheless, in addition to the digitization errors, the non-linearity of the electron multiplier has to be considered when large relative abundance ratios have to be measured accurately, e.g. for quantitative isotope ratio measurements.

2.5 SPECTRAL DATA PROCESSING

The nature of the instrument allows the acquisition of a complete mass spectrum in less than a millisecond and the complete cycle of selecting a target, focusing the laser, acquiring and displaying the spectrum, can be completed in less than a minute for simple samples. Hence, the use of a computer to rapidly store the spectra considerably simplifies the overall operation. Further, a computer can conveniently perform many tasks which are slow and tedious if done manually.

The program LAM, written by Mauney (3,21), is used for data processing of the spectra recorded with the B-8100 Gould-Biomation transient recorder. It readily allows calibration of the mass spectra, integration of the ion signals, logging of specific instrumental parameters and of informative comments, and the calculation of the laser energy available at the sample. It also gives a record of the details of calibration of the TOF-mass spectra (the calibration coefficients are reported and can be checked). A particularly interesting feature of the program is the possibility to perform a channel-per-channel averaging of the spectral data over a large set of spectra recorded under identical conditions, so that an averaged mass spectrum is obtained that can provide a representative mean. In conjunction with the program LAM, an additional program for simple statistical analysis and tabulation can be used to process the output from LAM, e.g. to select sets of spectral data which can subsequently be averaged and/or ratioed with respect to a specified reference mass signal. Together, these programs allow to acquire, store, integrate, report and process a large number of mass spectra per day.

The instrument, in the experimental set-up outlined above, was used for the present work on laser microprobe mass analysis of individual particles.

2.6 REFERENCES

1. E. Denoyer, R. Van Grieken, F. Adams, and D.F.S. Natusch, Anal. Chem., 54, 26A (1982).

2. R.L. Kaufmann, H.J. Heinen, M.W. Schürmann and R.W. Wechsung, in Microbeam Analysis-1979, ed. by D.E. Newbury, San Francisco Press, San Francisco, 1979, p.63

3. T. Mauney, Ph.D. thesis, Colorado State University, Fort Collins, U.S.A., 1984.

4. H. Vogt, H.J. Heinen, S. Meier, and R. Wechsung, Fres. Z. Anal. Chem., 308, 195 (1981).

5. M.J. Beesly, Lasers and their Applications, Taylor and Francis Ltd., London, 1972.

6. M.I. Cohen, in Laser Handbook, ed. by F.T. Arecchi and E.O. Schulz-Dubois, Vol.2, North-Holland Publ. Co., Amsterdam, 1972, p.1599.

7. R. Wurster, U. Haas, and P. Wieser, Fres. Z. Anal. Chem., 308, 206 (1981).

8. A. Verbueken, Ph.D. Thesis, University of Antwerp (UIA), Antwerp, Belgium, 1985.

9. E. Michiels, M. De Wolf, and R. Gijbels, Scanning Electron Microsc., III, 947 (1985).

10. T. Mauney and F. Adams, in Microbeam Analysis-1984, ed. by A.D. Romig Jr. and J.I. Goldstein, San Francisco Press, San Francisco, 1984, p.19

11. E. Michiels, Ph.D. Thesis, University of Antwerp (UIA), Antwerp,Belgium, 1985.

12. T. Mauney and F. Adams, Int. J. Mass Spectrom. Ion Proc., 63, 201 (1985).

13. T. Mauney and F. Adams, Int. J. Mass Spectrom. Ion Proc., 59, 103 (1984).

14. E. Michiels, T. Mauney, F. Adams, and R. Gijbels, Int. J. Mass Spectrom. Ion Proc., 61, 231 (1984).

15. U. Fehn, Int. J. Mass Spectrom. Ion Phys., 15, 391 (1974).

16. U. Fehn, Int. J. Mass Spectrom. Ion Phys., 21, 1 (1976).

17. M.A. Rudat and G.H. Morrison, Int. J. Mass Spectrom. Ion Phys., 27, 249 (1978).

18. M.A. Rudat and G.H. Morrison, Int. J. Mass Spectrom. Ion Phys., 29, 1 (1979).

19. D.S. Simons, Int. J. Mass Spectrom. Ion Proc., 55, 15 (1983/1984).

20. P. Van Espen, L. Van Vaeck and F. Adams, in Third International Laser Microprobe Mass Spectrometry Workshop 1986, 26-27 August, 1986, Antwerp, Belgium, p. 195.

21. T. Mauney and P. Van Espen, in Microbeam Analysis-1984, ed. by A.D. Romig Jr. and J.I. Goldstein, San Francisco Press, San Francisco Press, 1984, p. 295.

CHAPTER 3. ANALYTICAL CHARACTERISTICS OF THE LAMMA TECHNIQUE

The LAMMA technique was originally developed for highly sensitive microanalysis of thin histological sections in applications of a biological an medical relevance (1). In particular, it was intended to be a complementary method to other existing microanalytical techniques such as electron probe X-ray microanalysis (EPMA), secondary-ion mass spectrometry (SIMS) and Raman microprobe analysis, for determining the intracellular distribution of physiological cations like Na^+, K^+ and Ca^{2+}, as well as toxic constituents, in biological tissues. During the last years it has increasingly been applied in other research fields including atmospheric chemistry, geology and mineralogy, forensic science, material research, and general chemistry (2-4). The main advantage of LAMMA is its ability to perform a rapid and highly sensitive mass analysis of both atomic and molecular species present in a micro-region of the sample, in either positive or negative ion detection modes.

3.1 SAMPLE REQUIREMENTS

Inherently limited by its transmission geometry, the LAMMA-500 requires samples such as thin sections (usually 0.1-2 μm thick) or small particles (0.5-5 μm) that can be perforated or vaporized by laser impact. In particular cases, however, some ingenuity may circumvent this obvious limitation. For specific applications in thick specimens may even be of some advantage (5,6).

Also, the sample should necessarily be stable in the vacuum of the mass spectrometer (ca 10^{-4}-10^{-5} Pa). Only a special technique allows compounds of high volatility to be analyzed under normal atmospheric conditions (7,8): in this procedure the vacuum seal of the LAMMA-500 is not a quartz window, but a thin polymer film which carries the deposited material to be analyzed at its atmospheric

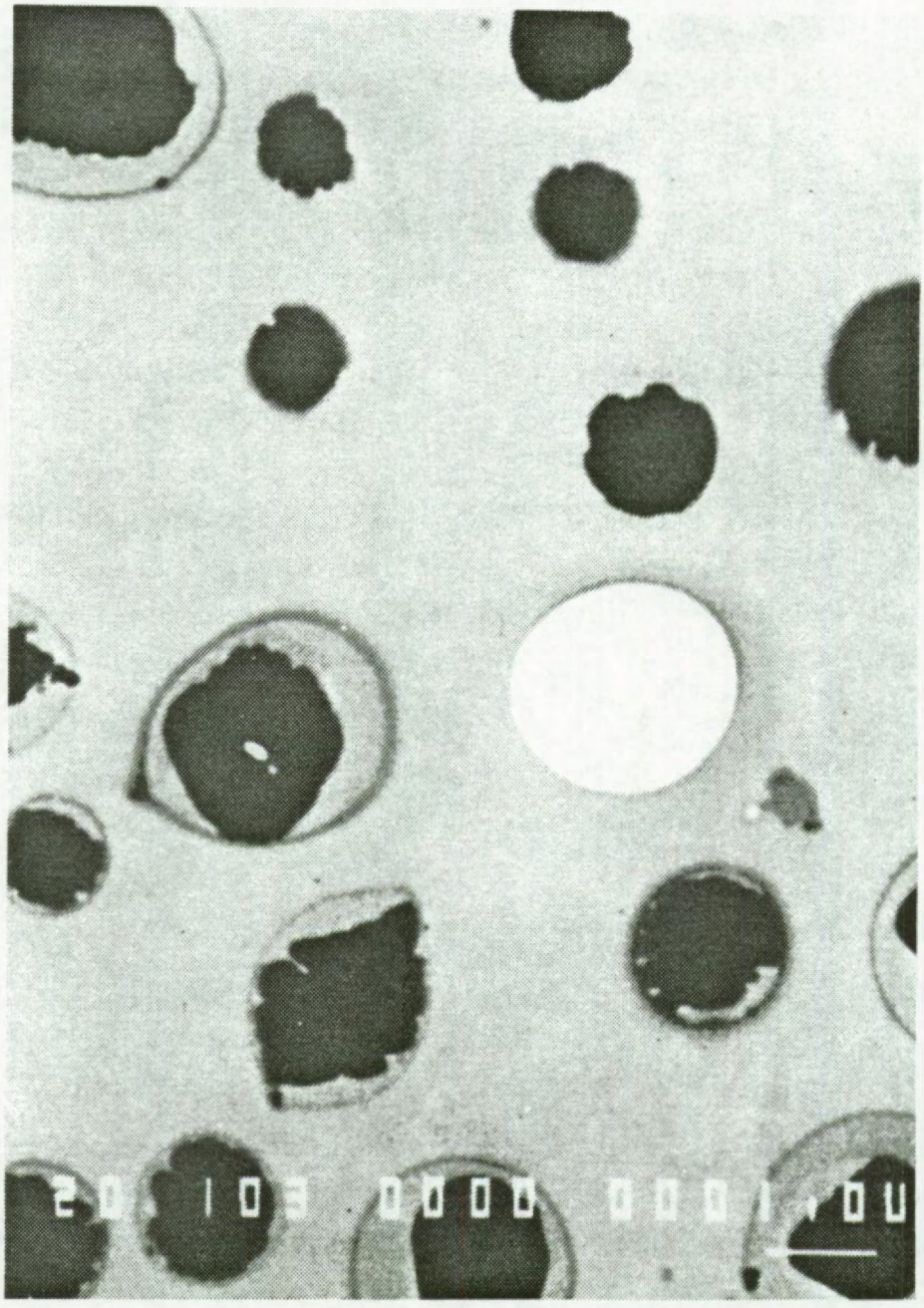

Figure 3.1: Electron micrograph (original magnification 10,000X, bar represents 1 μm) illustrating atmospheric aerosol particles directly impacted on a thin Formvar foil. In the center of the picture a hole is shown originating from the pulsed laser interaction

side. The laser pulse will then generate tiny perforations in the vacuum seal, through which the ions from the analytes formed under atmospheric conditions can enter the instrument. The spectra were found to be identical with those obtained from the same compounds by ionization in the conventional way inside the vacuum chamber (7,8). Although this mounting procedure has the potential to create new opportunities for mass spectrometric microanalysis, further experiments are needed to demonstrate its practical applicability in the study of e.g. aerosols and biological material at ambient pressure and relative humidity. A serious practical limitation is that only the 10X lens objective can be used because of the long working distance. For each sample only very few particles can be analyzed before the vacuum in the sample chamber worsens too much so that the pendulum valve between the drift tube and the sample chamber has to be closed to prevent damage to the mass spectrometric system.

Thin sections of materials can also be mounted directly provided that they have sufficient mechanical stability. Microtome sections of biological and clinical samples (9), thin foils of metals and semiconducters (10-12), thin sections of soils (13-15) and very thin sheets of minerals (mica) (16) can be studied. An advantage of LAMMA (and of laser mass spectrometry in general) is that electrically non-conducting samples may be analyzed.

A common approach in LAMMA of particles is to mount the particulate matter on a TEM-grid coated with a thin organic or metal supporting foil ($\leq$ 0.1 μm thick). This can be done by bringing small particles, fibers or finely pulverized material into close contact with a Formvar-coated electron microscope grid to allow the particles to adhere sufficiently. Aerosols can also be collected by direct impaction in a number of current collector devices, with or without size classification (Figure 3.1) (17-20). Larger particles or fibers may sometimes be attached to the metal grid bars without any film coating, though such samples are usually mechanically unstable. Particles with larger diameter (0.1-0.5 mm) may well be

mounted in so-called sandwich grids, while macroscopic samples up to some millimeters in size can be clamped in a modified sample holder, which keeps the particle by a special tweezer on the rear side. In such a case, one should pay attention to the orientation of the sample and make sure that the interesting areas lie near the edges visible in the light microscope, so that they can be analyzed with laser light at grazing incidence (21-24). In principle, this allows to record mass spectra free from any additional background. Another approach is to use multiple laser shots until complete perforation is reached, producing a mass spectrum from the final shot. However, preferential vaporization and migration of some species may occur and lead to non-representative analytical results. This laser drilling on e.g. a multi-layered sandwich of different materials deteriorates the obtainable lateral resolution of analysis by irreproducible crater shape formation (1, 25). Large bulky specimens may also be analyzed in a "two-step" procedure in which regions of the sample are vaporized by laser impact in the absence of the accelerating electric field. Under these conditions the evaporated material is recondensed and deposited on the quartz window vacuum seal; it is reionized by subsequent laser shots and further analyzed in the normal way (18). This procedure is applicable only for those specimen that can recondense from the plasma state without change of composition. If the sample is transparent to the laser wavelength and suitable for use as a vacuum seal of the mass spectrometer, it is sometimes possible to focus the laser beam onto the back-side of the specimen and produce ionization from that surface. This method was for instance applied by Michiels et al. (26) to mineral quartz samples.

Soluble compounds or suspensions may also be investigated. A microliter droplet of a dilute solution is brought onto a thin film suspended on a grid. After evaporation of the solvent, small crystallites or particulate residues remain on the foil which can then be visualized in the microscope and analyzed (27). In some special cases, as for anionic surfactants (wetted with e.g. chloroform) or viscous fluids, the material can be prepared directly

for analysis by simply dipping a grid into the sample (28).

3.2 INSTRUMENTAL FEATURES

The intensity of the UV-laser will influence both the elemental detection efficiency and the spatial resolution of the analysis. It can be controlled to a certain extent by using the set of filters situated at the entrance of the light microscope. In this way, the laser power can be attenuated to provide relatively low laser energies which will produce sufficiently small perforation diameters. In aerosol research, particles as small as 0.5 μm may be spotted and analyzed. Although in this case an increased background contribution of the supporting foil has to be expected, in practice it is most of the time very small compared to the overall spectral intensity. Formvar (commonly used as a particle support) is the trade name for an organic polymer with a polyvinylformaldehyde structure. The major fingerprint peaks in the negative mode spectrum include m/z = 45 ($C_2H_5O^-$), m/z = 59 ($C_3H_7O^-$) and m/z = 97 ($C_5H_7O_2^-$). The peaks are of comparable intensity. Under normal operational conditions and for the foil thickness currently used for aerosol sampling, no significant positive mode peaks are of practical concern. The use of a polymer surface for aerosol particle collection with impactors is very convenient due to their elastic properties. The particles are efficiently immobilized upon impaction and they can even slightly penetrate the foil if they have sharp edges.

The actual analytical volume (usually around 10^{-13} cm^3) is a function of laser focusing, morphology, local mass density and chemical composition of the sample, which influence the relative absorption and dissipation of the laser energy. For particulate matter, also individual particle size and geometry are important. For thicker samples, higher laser power is required for perforation, which will affect the perforation diameter and ionization efficiency.

With every laser shot a complete mass spectrum (positive or negative ion mode) is recorded with a mass resolution of $M/\Delta M$ = 850 at m/z = 208 (25). Under these conditions unit mass identification is clearly feasible, and individual isotopes can be detected and discriminated. LAMMA is thus capable of providing isotopic information for tracer experiments using stable isotopes (isotope dilution) or radionuclides. The mass resolution in LAMMA is, however, insufficient to avoid mass interference between elemental signals and contributions from both organic fragments or inorganic cluster ions.

One major advantage of LAMMA is the short analysis time in which the multi-element spectra can be obtained. A sample can easily be mounted and the appropriate vacuum conditions are established within minutes. Detailed analysis often requires initial optimization of instrumental settings, such as the selection of laser power and ion lens voltage. Moreover, the sample should sometimes be analyzed in both positive and negative ion modes using different laser powers and multiple mass spectra recorded for signal averaging. The shot-to-shot spectral reproducibility is limited by variations in instrumental parameters and specimen properties. The former concern the laser energy output, focusing conditions, ion extraction and ion detection. Inherent chemical or physical inhomogeneities of the sample as well as the sample preparation itself may influence the overall analytical reproducibility. Since the LAMMA technique is destructive, for submicron aerosols it is obviously impossible to record both positive and negative ion spectra from a single particle. Moreover, a number of possibly interesting particles are destroyed while optimizing the operational conditions.

The high speed at which spectra can be acquired and transferred to a computer for storage and further data processing permits to analyze relatively large populations of individual particles for the compilation of a data base that can be used for classification and source identification studies.

3.3 DETECTION LIMITS AND SENSITIVITY

As in any microprobe technique, the detection limits of LAMMA depend on operational conditions as well as on properties of the sample under investigation. A number of factors need to be considered: the first ionization potential for the formation of positive ions and the electron affinity for negative ions, the binding state of the elements with the surrounding matrix, the stability of the generated ions, the probability of recombination processes in the laser-induced microplasma. In addition, instrumental parameters such as laser wavelength, pulse duration and irradiance in the focus, as well as specific ion optical properties, will affect the overall analytical sensitivity.

The high overall ion transmission through the TOF-mass spectrometer of the LAMMA instrument enables very low detection limits for a wide range of elements (1,18,25,29,30-38). LAMMA is particularly sensitive for those elements with a low first ionization potential, e.g. physiological cations. It has been stated that absolute amounts down to about 10^{-20} g are detectable in the microvolume analyzed, resulting in relative detection limits in the ppm range (Table 3.1). On the other hand, some elements such as Zn, Cl, P, S and N, and toxic heavy metals such as Hg, Cd, Pt, and Au, show poor detection limits in the positive-ion mode LAMMA spectra. All these elements share the property of having high ionization energies. LAMMA can easily be operated to detect negatively charged ions. In the negative-ion mode, non metallic elements such as the halogens with high affinities for electron capture can be detected with high sensitivity, either as their elemental anions or as cluster ions, e.g. of the type XO^-_n(X=P,S,N).

Table 3.1: Relative detection limits (ppmw) for elemental analysis (positive ions).

Element	Glass Matrices (a)	Organic matrices (b)	Element	Glass matrices (a)	Organic matrices (b)
Li	3	0.4 1.6(c)	Nb	7	
Be	25		Ag		1
B	9		Cd		20
Na		0.2	In	7	
Mg	8	0.4	Cs	6	0.5
Al		0.3 5(d) 4(g)	Ba	6	0.5 2.5(c)
Si	10		La	4	10(c)
K	0.8	0.1	Ce	5	
Ca		1 1.6(c)	Pr	3	
		0.4(e)	Ho	14	
Ti	1		Tm	11	
V		0.5	Lu	6	
Co		10	Ta	6	
Cu		15	Pt		20(d)
Rb		0.5	Pb	10	0.4 10(c) 5(f)
Sr		0.5 2.5(c)	Th	6	
Y	4		U	6	2.0

(a) NBS Standard Reference Materials of the SMR 610-616 series. Limits defined by mass signal exceeding 3 times standard deviation of the background noise (31).
(b) Epoxy resin (Spurr's low viscosity medium) standards containing trace amounts of organometallic complexes (10^{-13}g evaporated material, irradiance set at 5 times the damaging threshold, signal intensities averaged over 5 analyses must exceed 3 times the background noise) (18).
(c) Data obtained in either natural pigment granula or epoxy resin matrices (0.3 μm thick sections) (30).
(d) Metal loaded Chelex-100 beads embedded in Epon resin (0.2 μm thick sections) (34).
(e) Standard specimen of CaF_2 deposited on a 0.3 μm epoxy resin section (30).
(f) Epoxy resin (Epon) thin section (0.5 μm) doped with known concentrations of lead acetate (35).
(g) Lyophilized serum (36,37).

A detailed comparative study of laser and ion microprobe sensitivities for the detection of Pb in biological material has been made by Linton et al. (35). At a comparable lateral resolution of analysis of about 1 μm, a relative detection limit of 5 μg/g was found in LAMMA, which is superior by 2 orders of magnitude to that obtained with the Cameca IMS-3F ion microscope. Also, the useful ion yield for Pb was 2 orders of magnitude better in LAMMA compared to the IMS-3F value ($3x10^{-3}$ versus $5x10^{-5}$). Although sensitivity factors for the alkali and alkaline earth metals show trends similar in SIMS and LAMMA, the sensitivity factor for Pb is orders of magnitude lower (0.5 in LAMMA versus $3x10^{-4}$ in SIMS when normalized to K). Other LAMMA studies also showed an enhanced Pb sensitivity when compared with local thermal equilibrium (LTE) calculations (33). A specific reason for the large enhancement of the Pb ion yield in LAMMA was not given, but it could be caused by resonance absorption of lead for the 265 nm laser light.

Krier et al. (39) reported the coupling of a tunable dye laser to a LAMMA-500 instrument and found that, when the wavelength of the laser beam corresponds to a particular electron transition of the element being analyzed, resonance absorption phenomena may be observed: the detection thresholds fell from 50 ppm at 266 nm to 1 ppm at 228.80 nm for Cd and from 20 ppm at 266 nm to 0.050 ppm at 324.75 nm for Cu. The irradiation wavelength at the lowest detection threshold corresponds to an electronic transition of the metal with a high transition momentum. The same authors also reported that the energy required to ionize anthracene is 100 nJ at 286.5 nm, 50 nJ at 266 nm and only 3 nJ at 225.7 nm.

In LAMMA, polyatomic ions are produced by fragmentation and/or recombination processes. Organic ions and major inorganic cluster ions can interfere with the atomic mass signals to be measured. For this reason the detection limit of the element of interest may be worse in practical analysis. In "real" specimens, the majority of potentially interfering background peaks appear in the mass range m/z = 20-140, with maximum ion intensities near the lower mass end;

the spectral pattern of these background peaks is strongly influenced by the laser power used. This may create a problem when analyzing trace amounts of the transition metals whose atomic weights fall in this mass range. Small ion signals from Fe or Cu, for example, may be hidden by larger peaks of organic fragments with the same nominal m/z number. Only if these background mass peaks are reproducible and result in typical fingerprint spectra, background subtraction procedures by computer may become applicable to some extent on the extra condition that the ion formation for the total sample and for the background alone is the same. The laser power density at the focus of the sample plays a crucial role in the process of matrix fragmentation and ion formation. Therefore, the power has to be controlled in order to avoid excessive spectral background. Since the transmission of the TOF-mass spectrometer for complex molecular ions may be lower than for simpler atomic ions, due to differences in the initial kinetic energy distributions, appropriate selection of ion optical parameters has been able to suppress part of the mass spectral interferences (9,41,42).

3.4 IONIZATION CHARACTERISTICS AND SPECIATION CAPABILITIES

A considerable advantage of the laser ion source is the fact that the laser intensity can easily be varied to provide a wide range of ionization conditions (43). Experience has shown that irradiances close to the threshold of ion formation at low laser power (laser desorption) will preferentially desorb ions from the target surface facing the spectrometer (surface characterization) and promote parent ion formation (44, chapter 4 and 6). On the other hand, laser irradiances 3-10 fold above this threshold will lead to evaporation of the full target volume and yield information on the bulk composition. In the latter mode, the high-power ionization causes extensive fragmentation (laser pyrolysis) and molecular rearrangement. Exploiting these special features of LAMMA, a two-step procedure can be applied for the analysis of micrometer size particles:

1. a laser shot at low irradiance with a slightly defocused beam is aimed at the particle surface facing the mass spectrometer. A selective evaporation of the surface material is obtained, while the particle appears to remain intact and no gross morphological changes are observed.

2. a second laser shot with a focused laser beam is aimed at the center of the particle; this results in a complete destruction of the particle and the registration of the fragmentation spectrum.

This procedure has proven to be very useful for the surface characterization of e.g. aerosols (45,46) and asbestos fibres (47).

Lindner and Seydel (5) showed that laser irradiation of a thick sample (ca. 20 μm) which does not lead to perforation, also offers soft ionization conditions. They described a desorption mechanism based on a non-thermal, shock-wave driven process, leading to the release of mainly intact molecules from the solid sample surface.

An interesting feature of LAMMA is its ability to produce molecular ions (e.g. for aromatic compounds) or quasi-molecular peaks (e.g. for polysaccharides) from non-volatile and/or thermally unstable compounds. Frequently, in LAMMA, a cationization or simple protonation of non-ionic molecules occurs, i.e. attachment of a metal, alkali ion or proton to a neutral organic molecule. In this way, molecular information is obtained from labile species that may be difficult or impossible to obtain by conventional mass spectrometry with an electron impact source. Moreover, organic salts and acids, free organic bases, organometallic complexes, organic polymers, and inorganic compounds ranging from simple halides or oxides to complex inorganic salts, all give typical mass spectra suitable for identification of molecular species (48-58). In addition to the signals that are characteristic of molecular structure and functional groups (quasi-molecular ions and counter-ions in salts), typical cluster ions are also observed, which are formed by fragmentation and/or recombination. Cluster ions

show characteristic intensity distributions that can be described by theoretical or by empirical models of ion formation such as the "valence model" of Plog (10-12,26,43,57-61, section 5.2 and 5.3).

For single particle analysis purposes, fingerprint mass spectra of individual aerosol particulates can be obtained. This can be done either at low laser power, to produce specific molecular fragment ions, or at high laser power, comparable to laser pyrolysis ionization mass spectrometry. This approach can be used to deal with chemically complex particulate matter in classification studies (20, chapter 7).

Valuable information on inorganic species and organic components may thus be extracted from the LAMMA spectra, albeit hitherto only for the major constituents within the sampled area.

3.5 IN-DEPTH RESOLUTION OF THE LAMMA-500 INSTRUMENT

An important instrumental feature for LAMMA-500 is the surface selectivity of the measurements. Since the LAMMA-500 instrument operates in the transmission mode the laser beam passes through the whole sample thickness so that the reliability of the measurements in terms of the sample surface composition is not straightforward. One could even interpret the results as preferential evaporation and ionization from the total sample rather than as selective excitation of the surface layers. Several experiments have been designed to solve the dilemma between the two adverse hypotheses. From their study of the ion formation from alkali halide solids, Jöst et al. (59) made an estimation of the depth from which the detected ions are generated: for a laser irradiance of 3 times the threshold, leading to a 50 % probability for ion detection, they found an upper limit of 300 atomic layers being involved in the ion formation process and proposed a more realistic value in the order of ten monolayers. This corresponds to an upper limit for the depth

resolution of about 80 nm. In a study involving $^{12}C/^{13}C$-bilayers (see chapter 4), we pointed out that at the threshold laser irradiance for sample perforation, 97 % of the ionized material originates from the top 20 nm of the sample. If the laser irradiance is increased the surface sensitivity is deteriorated and the spectrum becomes representative for the chemical composition of the overall thickness of the sample. For thin samples (i.e. ≤ μm) the surface sensitivity is highest for the lowest possible laser irradiances. The speciation of the inorganic and especially organic substances requires minimum laser energy deposition onto the sample to prevent extensive fragmentation of the original compounds, so that in practical applications LAMMA allows the surface selective speciation of the sample surfaces, provided that the surface component yields a typical fingerprint spectrum.

The same conclusions were drawn from the study by Van Vaeck et al. (63). The in depth limitation of LAMMA for organic microprobing in the perforation mode was clearly illustrated. Several samples were analyzed consisting of an Epon matrix and pure organic compounds where the organic product was either on the Epon surface or squeezed between two Epon layers. Organic molecular information could only be obtained from targets in the upper-surface layer i.e. 20-50 nm for a 1 μm thick sample.

Another interesting approach to laser desorption mass spectrometry was reported by Lindner and Seydel (5). Sugar layers on Formvar foil with an overall thickness of about 20 μm were analyzed. The quasi-molecular signals detected after full laser power irradiation (ca. 10^{11} W/cm^2) of the 20 μm thick sample, without perforating it, were explained by a non-thermal shock-wave driven desorption process followed by a gas-phase reaction between neutral intactly desorbed molecules and co-desorbed alkali ions (64-67).

Fletcher et al. (68) reported that they were able to detect a monolayer of paranitrobenzoic acid, deposited onto a 5 nm silver layer that was evaporated onto a quartz substrate. The sample was

irradiated with a 14 μm diameter spot at a laser irradiance of about 10^7 W/cm^2. The remarkable sensitivity and the selectivity was attributed to the surface microstructure of the silver foil that should aid in the absorption of a significant fraction of the laser radiation which can lead to a relatively gentle thermal desorption of molecular monolayers.

Although evidence on the surface selectivity of LAMMA exists, it is highly recommended not to interpret the data in terms of the surface composition of the sample without a prior investigation of a representative model system (see chapter 6). The LAMMA-data cannot as such be considered as a proof, without the backup from the results of these model systems. Certainly in the case where multiple laser shots are fired onto the same sample area (so-called depth profiling), homogenisation and recondensation of the sample material can result in erroneous interpretations.

3.6 QUANTIFICATION

In the present state of the LAMMA technique, accurate quantification is still problematic. Absolute quantitative analysis requires data concerning the ion yield, the evaporated volume, the overall ion transmission, the ion-electron conversion efficiency (dependent on ion mass, structure and energy) of the secondary electron multiplier. Since no theoretical model at the moment can predict the ion yield for a specific specimen as a function of the target and laser beam parameters, empirical procedures must be applied for quantification.

One such an approach is the use of suitable calibration standards. Such homogeneous standards are necessary, not only to be compared directly with a variety of samples but also to be used as simple model systems to study the general analytical features of the laser microprobe. Ideal elemental calibration standards should fulfil the following requirements (34):

(1) well-defined chemical composition and structure
(2) similar matrix composition as the unknown sample
(3) homogeneous at the level of spatial resolution
(4) controllable doping for a wide variety of elements and compounds must be feasible
(5) the concentrations must be adjustable within a range typical for the unknown sample to be analyzed
(6) the concentrations of the dopant must be assessable by other analytical techniques

In LAMMA, additional properties should be similar for standards and specimens:

(1) target geometry
(2) matrix mass density
(3) optical characteristics and surface texture, as well as the instrumental conditions used

In practice it can be extremely difficult to fulfil all these requirements at the same time for the standards that are needed in quantification studies. Most efforts for element quantification were done for biological and medical specimens and a wide variety of standards has been proposed:

- dissolving metal containing organic compounds such as crown ethers into epoxy resins (1, 25, 33, 38, 70)
- thin films of metals or dielectrical materials vacuum deposited onto the surface of the specimen (70, 71)
- proteinaceous standards consisting of an organic matrix (gelatin or albumin) doped with a variety of elements (72, 73)
- anionic surfactant films containing several metal cations (28)

- ion-chelating resin beads homogeneously loaded with

the ions of interest (34, 74, 75)

Another approach could be the use of a thin coating of a stable isotope of the element of interest itself as an internal standard, thus providing the possibility of the quantitative application of "isotope dilution" analysis. However, instrumental effects of LAMMA have to be considered carefully to allow a meaningful interpretation of the results for quantitative purposes, because of the inhomogeneous distribution over the sample thickness of the analyte. One has to take into account the geometric effect of ion extraction: it favours the detection of ions generated from the side of the sample that is faced toward the extraction lens of the TOF-mass spectrometer (see chapter 4). Moreover, the coated element is present in a different chemical environment than the analyte in the specimen, so that differences in sensitivity factors as a result of matrix effects are to be expected.

Methods for incorporating internal standards into thin sections for quantitative analysis of organic compounds have only scarcely been reported (63). Interesting approaches include the dissolution of pure organic compounds (e.g. aromatic monomers or polar molecules) in polyethylene (3 % w/w) or in polymeric resin, for the identification of molecular or quasi-molecular mass signals by selective laser desorption (30,76).

The LAMMA analysis of particulate matter obviously requires another type of calibration, i.e. particle standards. For this purpose micrometer size particles may be synthesized directly in the suitable dimension. The generation of particles with a well-defined size and chemical composition by atomization of liquid solutions with the desired particulate material as the solute, provides a suitable way for the calibration of LAMMA in e.g. aerosol research and fundamental studies (77,78). This method was used by Kaufmann et al. (18) to calibrate the dependence of the ion signal on the particle size for NaCl-particulates. In our laboratory a Collison-type nebulizer is used for the dispersion of aqueous

solutions what enables the preparation of a wide variety of multi-element salt standards that are useful for quantification studies in environmental applications (79). As an illustration of the nebulization method for aerosol standard preparation, the detection limit and sensitivity of Pb in mixed NH_4/Na-sulfate particles (a particle type currently found in airborne particulate matter sampled in polluted marine environments) will be discussed. Standard samples containing 3, 10, 30, 100, and 250 ppm of Pb were prepared from an aqueous solution of $(NH_4)_2SO_4$ and Na_2SO_4 of 0.05 and 0.025 molar concentrations, respectively, and a 500 ppm Pb standard solution. The ppm-values refer to the Pb-concentrations of the dry mixture of sulfate salts. The standard solutions were atomized by a Collison-type nebulizer and the generated aerosols were collected on filmed grids positioned on the impaction surfaces of a low volume cascade impactor. The LAMMA-measurements were performed on 1 μm diameter aerosols. For the 10 ppm Pb standard, the Pb-signal could not systematically be detected and therefore this concentration is considered to fall bellow the practical detection limit. A linear plot for the Pb-concentration versus the number of counts in the integrated mass peak at m/z = 208 for the other standards of 30, 100 and 250 ppm is show in Figure 3.2. For the 30 ppm standard the following values concerning the sampled material can be given:

volume analyzed : 0.5 μm^3
weight analyzed : 1.3 pg
relative detection limit: 30 ppm
absolute detection limit: 4×10^{-17} g

A detection limit of 8 ppm is obtained by taken 3 times the background noise of the ^{208}Pb-isotope. This is comparable to the extrapolated detection limit for Pb in glass microspheres (see Table 3.1). For this low signal intensities the noise for the other Pb-isotopes at m/z = 206 and 207 is too high so that the isotopic pattern of Pb cannot be recognized. This is confirmed by the fact that for the 10 ppm Pb standard, Pb could not systematically be detected.

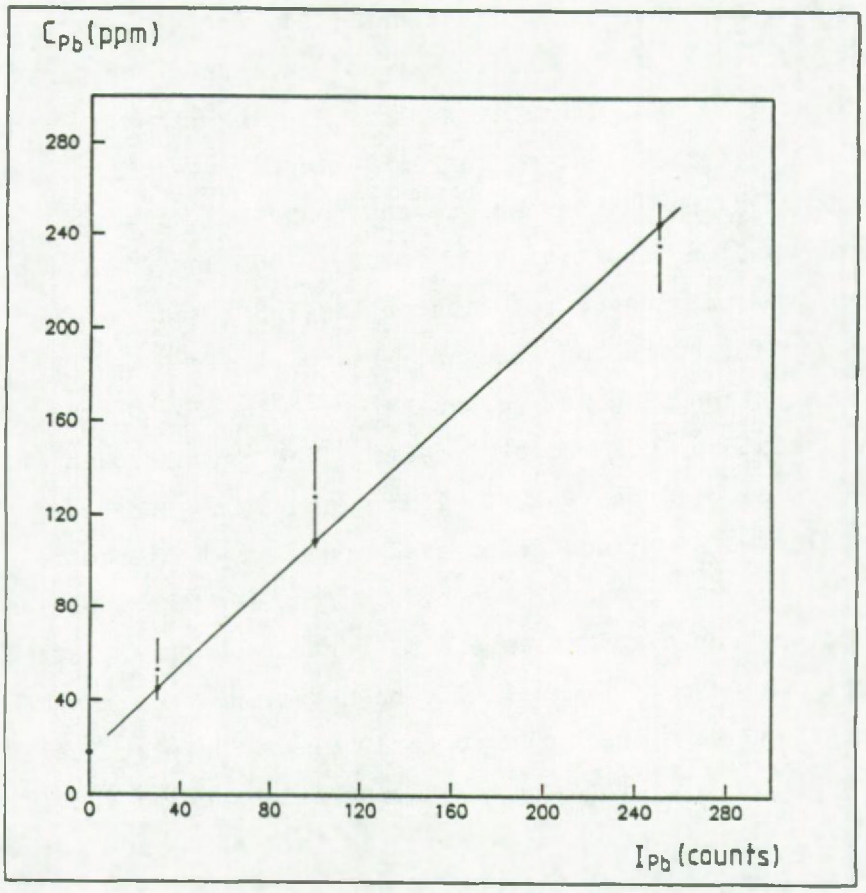

Figure 3.2: Plot (calcutated by linear regression) of the Pb-concentrations in the mixed NH_4/Na-sulfate standard particles, versus the number of counts in the integrated mass peak at m/z = 208.

Heavy metal doped organic particulate matter has also been proposed as a standard (32,80): flat particles were produced by nebulizing aqueous solutions of sucrose containing known amounts of metal salts and subsequent drying of the generated droplets. For the preparation of the salt aerosols coated with polynuclear aromatic hydrocarbons (PAH), Niessner et al. (81) used a gas phase condensation apparatus coupled to the outlet of a Collison nebulizer, equipped with a diffusion dryer. For the preparation of

multi-element salt standards, mixtures of inorganic salts can also be dissolved in water with some ethanol added, pipetted onto a supporting film, rapidily frozen and finally freeze-dried, to obtain a structure of small granules in the dimension of less than 1 μm (82).

Bulk homogeneous material can be crushed to micrometer size particles and serve as standard reference samples. They include silicate minerals (augite, hornblende, lepidolite) (83), silicate glass microspheres and glass fibers composed of various element oxides (18,31,83-86), and glass films and uranium oxide microspheres (21,87).

Another approach is the use of large carrier particles consisting of a polymer matrix (88) or synthetic highly porous silica spheres (spherisorb particles), about 3 μm in diameter, which can be loaded by soaking with solutions of various salts (89). Submicrometer size polybead polymeric spheres, i.e. monodisperse latex particles available with carboxy, hydroxy, or amino functionality (Polysciences Inc., Warrington, Pa., U.S.A.) may provide an alternative means for standardization (9). It has also been reported that the spark of the emission spectrometer may be a suitable and efficient source for the production of metal and metal alloy particle standards in the 5 nm - 10 μm range (90). Several hydrous metal oxide sols consisting of spherical particles with narrow size distribution have also been described (91); they might be useful as a uniform calibration system.

A basic prerequisite to quantify LAMMA results is that a straightforward relation can be established between the ion signal intensity and the local concentration of the analyte. Using different types of standard specimens, linear calibration curves over a broad range, even up to 3 orders of magnitude, have been experimentally obtained with a fair reproducibility of meaurement (10-30 % RSD, in practice, for homogeneous thin sections) (28,32,34,36,92-94). These calibration curves represent absolute

signal intensities or show relative data with respect to a reference mass peak.

The amplitude of the ion signal is susceptible to a number of sources of variability which influence the ion yiels and the evaporated volume. This includes laser intensity fluctuations, differences in target geometry, local mass density, physical and microchemical properties of the particulate matter to be analyzed. Correction for variation in e.g. the evaporated volume can be obtained by normalizing the signals to one or several suitable internal reference mass peaks. Reference candidates include an element with known and homogeneous concentration, e.g. a matrix element, a doped element, or an inorganic or organic mass fragment. Only under carefully controlled conditions, a direct sample-to-standard comparison may provide successful quantification.

In practice, element-specific relative sensitivity coefficients (RSC) obtained from multi-element standards may empirically permit quantification (18,25,30-35,72,83,84). As an example the relative sensitivity factors for Na, K ,Br and Cl in NaCl/KBr mixed salts will be briefly outlined. Three aqueous standard solutions of NaCl and KBr mixtures, with concentrations as shown in Table 3.2, were pneumatically nebulized and the aerosols were collected on Formvar-coated electron microscope grids.

Table 3.2: Molar concentration of standard solutions used for aerosol generation by pneumatic nebulization.

	C_{NaCl}	C_{KBr}	C_{NaCl}/C_{KBr}
Standard #1	0.0379	0.0270	1.404
Standard #2	0.0213	0.0200	1.064
Standard #3	0.0214	0.0348	0.615

The relative sensitivity factors were calculated according to the formula given below and are listed in Table 3.3:

$$ {}_{X}R_{Y} = \frac{C_X/C_Y}{I_X/I_Y} \qquad \text{(eq. 3.1)} $$

with ${}_{X}R_{Y}$: relative sensitivity factor of element X to element Y

X, Y : Na,K,Cl,Br

C_X and C_Y : molar concentration of element X and Y, respectively, in the sample

I_X and I_Y : mass peak intensities of element X and Y, respectively in the LAMMA-spectra

Table 3.3: Intensity ratios of the mass peaks in the positive and negative ion mode spectra of the three standards

	Intensity ratio ± S.D.		
Peak intensity ratio	Standard #1	Standard #2	Standard #3
$^{23}Na/^{39}K$	1.1 ± 0.1	0.50 ± 0.06	0.69 ± 0.08
$^{23}Na/^{41}K$	8.6 ± 2.4	3.8 ± 0.7	3.7 ± 0.7
$^{35}Cl/^{79}Br$	0.55 ± 0.15	0.62 ± 0.16	0.37 ± 0.09
$^{35}Cl/^{81}Br$	0.60 ± 0.15	0.64 ± 0.16	0.37 ± 0.09
$^{37}Cl/^{79}Br$	0.24 ± 0.08	0.28 ± 0.10	0.15 ± 0.03
$^{37}Cl/^{81}Br$	0.26 ± 0.07	0.28 ± 0.11	0.16 ± 0.04
$^{39}K/^{41}K$	9.2 ± 1.8	6.0 ± 1.1	7.4 ± 1.5
$^{35}Cl/^{37}Cl$	2.2 ± 0.2	2.3 ± 0.4	2.4 ± 0.4
$^{79}Br/^{81}Cl$	1.1 ± 0.1	1.00 ± 0.04	1.02 ± 0.04

Table 3.4: Relative sensitivity factors for Na, K, Cl and Br in NaCl/KBr.

X_RY	Standard #1	Standard #2	Standard #3	X ± S.D.	S.D. (%)
$Na^{23}{}_R K^{39}$	1.37 ± 0.14	1.66 ± 0.18	1.48 ± 0.19	1.50 ± 0.15	10
$Na^{23}{}_R K^{41}$	2.38 ± 0.66	4.1 ± 0.7	2.42 ± 0.44	2.97 ± 0.98	33
$Cl^{35}{}_R Br^{79}$	3.8 ± 1.1	2.56 ± 0.59	2.49 ± 0.60	2.95 ± 0.74	25
$Cl^{35}{}_R Br^{81}$	3.6 ± 0.9	2.54 ± 0.63	2.54 ± 0.60	2.89 ± 0.61	21
$Cl^{37}{}_R Br^{79}$	2.83 ± 0.94	1.84 ± 0.66	1.94 ± 0.45	2.20 ± 0.55	25
$Cl^{37}{}_R Br^{81}$	2.68 ± 0.88	1.88 ± 0.68	1.94 ± 0.45	2.17 ± 0.45	21

The X_RY -values are listed in Table 3.4. The relative sensivity factors range from 1.5 to 3 and have relative standard deviations from 10 to 33 %.

To illustrate the reliability of the isotope ratio measurements, analogous calculations were done for the isotopes of the elements K, Cl and Br (Table 3.5). The R-ratios calculated for the isotopes clearly illustrate the limited dynamic range of the ion detection system as outlined above: the value deviates more from unity when the abundances of the two isotopes of the same element differ more.

Table 3.5: R-values calculated for the isotopes ^{39}K and ^{41}K, ^{35}Cl and ^{37}Cl, ^{79}Br and ^{81}Br.

R	Standard #1	Standard #2	Standard #3	X ± S.D.	S.D.(%)
$^{39}R^{41}$	1.47 ± 0.29	2.26 ± 0.43	1.83 ± 0.37	1.85 ± 0.40	21
$^{35}R^{37}$	1.42 ± 0.14	1.32 ± 0.20	1.28 ± 0.19	1.34 ± 0.07	5
$^{79}R^{81}$	0.91 ± 0.09	1.00 ± 0.04	1.00 ± 0.04	0.97 ± 0.04	4

The success of relative sensitivity factors for standardization largely depends on the similarity between the standars and the unknown sample with respect to matrix composition and sample geometry.

A theoretical approach to quantification is to apply the LTE-model in order to interpret the relative sensitivity factors of the ion emission. Satisfactory analytical results have been shown to ensue from this model in SIMS for a variety of materials (95,96). With the assumption that a local thermal equilibrium exists in the laser-induced microplasma, the degree of ionization of an element may be estimated to a first approximation provided that realistic estimates can be made of the relevant parameters of the model such as electronic partition functions, electron density and plasma temperature.

Phenomenological laws such as the Saha-Eggert ionization equation have been applied to some extent to metal alloy (30) or sandwich foils (11), glass particles (31,83), anionic surfactant films (28), sucrose particulate matter (32) and doped epoxy resins (33). The calculated parametric temperature values have been shown to range from about 5,000 K to 13,000 K. The LTE-model applied to homogeneous silicate minerals was tested in a comparative study of SIMS and LAMMA, using the transmission as well as the reflection type instrument (83). The relative intensities of the positive ions in the LAMMA spectra followed a similar dependence with ionization potential as observed in SIMS, as illustrated in Figure 3.3. In the case of the transmission type LAMMA-500 instrument, considerably larger deviations from the Saha-Eggert ionization equation were noted. This deviation might be associated with the inherent lack of reproducibility of the method for these samples compared to SIMS, rather than with the unapplicability of the LTE-approach, since excellent results were obtained with the reflection type LAMMA-1000 instrument (Figure 3.3). The SIMS and LAMMA-1000 measurements were carried out on a polished flat surface, while the LAMMA-500 measurements were performed on crushed material prepared by grinding the hornblende in an agate mortar to micrometer-size particles. Ion signal discrimination in the mass spectrometer and mass interference should be avoided or at least corrected in order to allow a better estimation of the relative ion concentrations as produced by laser impact.

The analytical characteristics of the LAMMA-500 instrument, as presented in this chapter, will be demonstrated in some specific applications in the later sections.

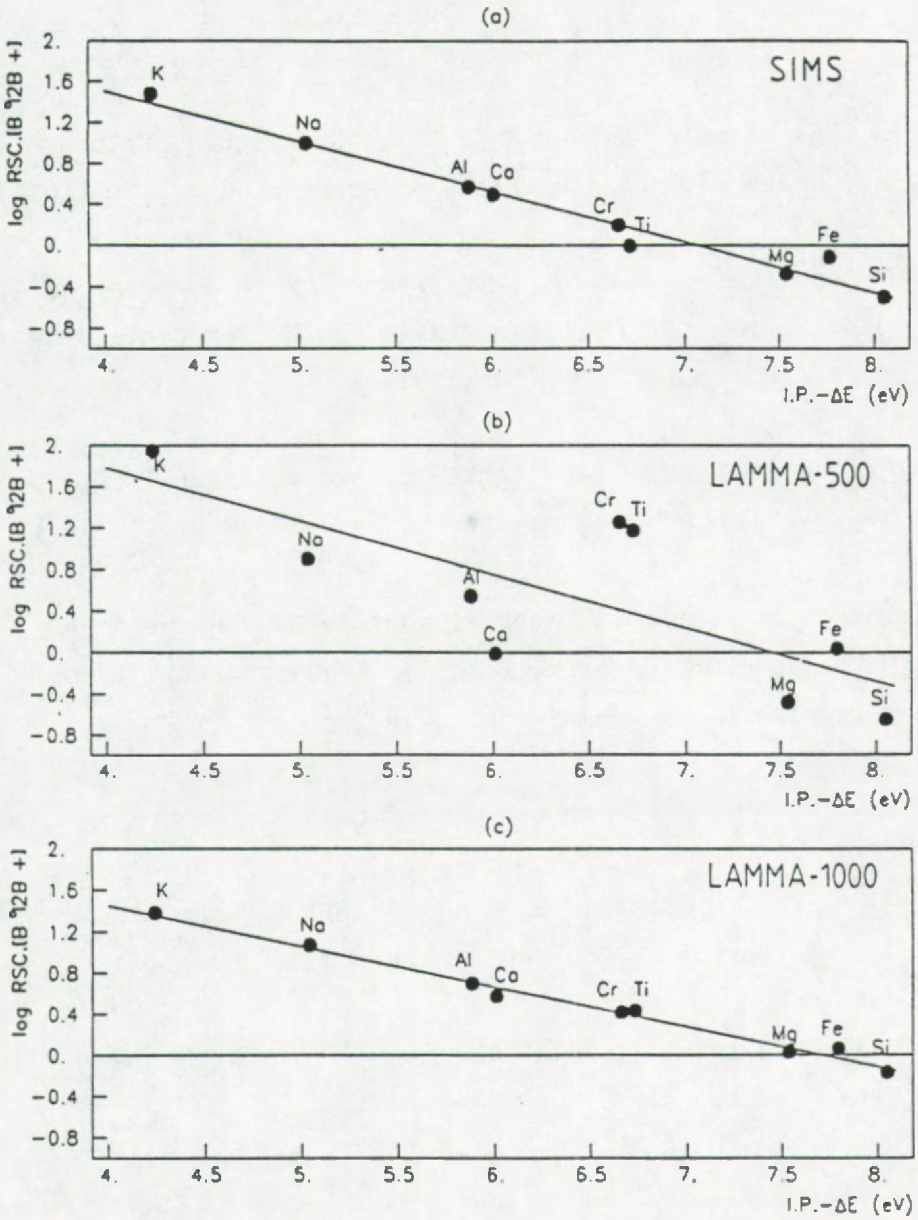

Figure 3.3: Fitting of the Saha-Eggert ionization equation for positive ions obtained from a hornblende sample (83). RSC = $(I_M^+/C_M)/(I_{Al}^+/C_{Al})$, B = internal partition function, IP = ionization potential (eV), ΔE = ionization potential depression (eV) due to Coulomb interactions of the charged particles.

a) SIMS, O^- bombardment, 0 - 20 eV secondary ions

b) LAMMA-500

c) LAMMA-1000

3.7 REFERENCES

1. R. Kaufmann, F. Hillenkamp, R. Wechsung, H.J. Heinen, and M. Schürmann, Scanning Electron Microsc., II, 279 (1979).

2. Proceedings of the 1st LAMMA-Symposium, Dusseldorf, F.R.G., Oct. 8-10, 1980 (Organizers: F. Hillenkamp and R. Kaufmann) Fres.Z.Anal.Chem., 308193 (1981).

3. Proceedings of the 2nd LAMMA-Symposium, Borstel, F.R.G., Sept. 1-2, 1983 (Organizers: U. Seydel and B. Lindner).

4. Third International Laser Microprobe Mass Spectrometry Workshop 1986, Antwerp, Belgium, August. 26-27, 1986 (Organizers: F. Adams and L. Van Vaeck)

5. B. Lindner and U. Seydel, Anal.Chem., 57, 895 (1985).

6. P. Moesta, U. Seydel, B. Lindner, and H. Grisebach, Z. Naturforsch., 37c, 748 (1982).

7. H.J. Heinen ans R. Holm, Scanning Electron Microsc., III, 1129 (1984).

8. R. Holm, G. Kampf, D. Kirchner, H.J. Heinen, and S. Meier, Anal. Chem., 56, 690 (1984).

9. A. Verbeuken, Ph. D. Thesis, University of Antwerp (UIA), Antwerp, Belgium, 1985.

10. N. Fürstenau, F. Hillenkamp, and R. Nitsche, Int. J. Mass Spectrom. Ion Phys. , 31, 85 (1979).

11. N. Fürstenau, Fres. Z. Anal. Chem., 308,201 (1981).

12. N. Fürstenau and F. Hillenkamp, Int J. Mass Spectrom. Ion Phys., 37, 135 (1981).

13. S. Henstra, E.B.A. Bisdom, A. Jongerius, H.J. Heinen, and S. Meier, Beitr. Electronmikroskop. Direktabb. Oberfl., 13, 63 (1980).

14. E.B.A. Bisdom, S. Henstra, A. Jongerius, H.J. Heinen, and S. Meier, Neth. J. Agric. Sci., 29, 23 (1981).

15. S. Henstra, E.B.A. Bisdom, A. Jongerius, H.J. Heinen and S. Meier, Fres. Z. Anal. Chem., 308, 280 (1981).

16. J.M. Beusen, L. Van't dack, and R. Gijbels, in Extended Summaries (EUR 8853 EN) Third International Seminar "European Geothermal Update", Munich, F.R.G., Nov. 29 - Dec. 1, 1983. p.370.

17. P. Weiser, R. Wurster, and H. Seiler, Atmos. Environ, 14, 485 (1980).

18. R. Kaufmann, P. Weiser, and R. Wurster, Scanning Electron Microsc., II, 607 (1980).

19. F. Bruynseels, H. Storms, and R. Van Grieken, J. Physique, 45, C2-785 (1984).

20. F. Bruynseels, H. Storms, T. Tavares, and R. Van Grieken, Int. J. Environ. Anal. Chem., 23, 1 (1985).

21. D.S. Simons, Int. J. Mass Spectrom. Ion Proc., 55 15 (1983/1984).

22. F. Freund, H. Kathrein, H. Wengeler, R. Knobel, and H.J. Heinen, Geochim. Cosmochim. Acta, 44 1319 (1980).

23. P.K. Dutta and Y. Talmi, Fuel, 61, 1241 (1982).

24. N.E. Vanderborgh and C.E.R. Jones, Anal. Chem., 55, 527 (1983).

25. R.L. Kaufmann, H.J. Heinen, M.W. Schurmann, and R.M. Wechsung in Microbeam Analysis 1979, ed. by D. E. Newbury, San Francisco Press, San Francisco, 1979, p. 63.

26. E. Michiels, A. Celis, and R. Gijbels, in Microbeam Analysis-1982, ed. by K. F. J. Heinrich, San Francisco Press, San Francisco, 1982, p. 383.

27. R. Kaufmann and P. Wieser, in Characterization of Particles, ed. by K.F.J. Heinrich, NBS Spec. Publ. 533, Washington, 1980, p.199.

28. R. Gijbels, P. Verlodt, and S. Tavernier, in Microbeam analysis-1982, ed. by K.F.J. Heinrich, san Francisco Press, San Francisco, 1982, p.378.

29. P. Wieser, R. Wurster, and H. Seiler, J. de Physique, 45, C2-261 (1984).

30. R. Kaufmann, in Microbeam Analysis - 1982, ed. by K. F. J. Heinrich, San Francisco press, San Francisco, 1982, p. 341.

31. P. Surkyn and F. Adams, J. Trace Microprobe Techn., 1, 79 (1982).

32. P. Wieser, R, Wurster, and H. Seiler, Scanning Electron Microsc., III, 1035 (1983).

33. P. Wieser, R. Wurster, and H. Seiler, Scanning Electron Microsc., IV, 1435 (1982).

34. A.H. Verbueken, R.E. Van Grieken, G.J. Paulus, and W.C. de Bruijn, Anal. Chem., 56, 1362 (1984).

35. R.W. Linton, S.R, Bryan, P.F. Schmidt, and D.P. Griffis, Anal. Chem., 57, 440 (1984).

36. J.F. Muller, M.A. Gelot, P. Netter, and R. Kaufmann, Biomedicine, 36, 380 (1982).

37. A.H. Verbueken, F.L. Van de Vyver, W.J. Visser, F. Roels, R.E. Van Grieken, and M.E. De Broe, Biol. Trace Elem. Res., in press.

38. R. Kaufmann, F. Hillenkamp, and R. Wechsung, Med. Progr. Technol., 6, 109 (1979).

39. G. Krier, F. Verdun, and J.F. Muller, Fres. Z. Anal. Chem., 322, 379 (1985).

40. E. Michiels, M. De Wolf, and R. Gijbels, Scanning Electron Microsc., III, 947 (1985).

41. T. Mauney, Ph.D. Thesis, Colorado State University, Fort Collins, U.S.A., 1984.

42. E. Michiels and R. Gijbels, Spectrochim. Acta, 38b, 1347 (1983).

43. F. Hillenkamp, in Ion Formation from Organic Solids, ed. by A. Benninghoven, Springer-Verlag, berlin, 1983, p. 190.

44. D.M. Hercules, R.J. Day, K. Balasanmugam, T.A. Dang, and C.P. Li, Anal. Chem., 54, 280A (1982).

45. F. Bruynseels and R. Van Grieken, Atmos. Environ., 19, 1969 (1985).

46. Ph. Otten, F. Bruynseels, and R. Van Grieken, Bull. Soc. Chim. Belg., 95, 447 (1986).

47. J.K. De Waele and F.C. Adams, Scanning Electron Microsc., III, 935 (1985).

48. H.J. Heinen, Int. J. Mass Spectrom. Ion Phys., 38, 309 (1981).

49. L. Van Vaeck, J. Claereboudt, J. De Waele, E. Esmans, and R. Gijbels, Anal. Chem. 57, 2944 (1985).

50. H.J. Heinen, S. Meier, H. Vogt, and R. Wechsung, Adv. Mass Spectrom., 8, 942 (1980).

51. P.K. Dutta and Y. Talmi, Anal. Chem., 132, 111 (1981).

52. L. Van Vaeck, J. De Waele, and R. Gijbels, Mikrochim. Acta., III, 237 (1984).

53. C.D. Parker and D.M. Hercules, Anal. Chem., 57, 698 (1985).

54. J.F. Muller, C. Berthé, and J.M. Magar, Fres. Z. Anal. Chem., 308, 297 (1981).

55. J.A. Gardella, Jr., D.M. Hercules, and H.J. Heinen, Spectrosc. Lett., 13, 347 (1980)

56. J.A. Gardella, Jr. amd D.M. Hercules, Fres. Z. Anal. Chem., 308, 297 (1981).

57. F.J. Bruynseels and R.E. Van Grieken, Spectrochim. Acta, 38B, 853 (1983).

58. F.J. Bruynseels and R.E. Van Grieken, Anal. Chem., 56, 871 (1984).

59. B. Jöst, B. Schüler, and F.R. Krüger, Z. Naturforsch., 37A, 18 (1982).

60. E. Michiels, A. Celis, and R. Gijbels, Int. J. Mass Spectrom. Ion Phys., 47,23 (1983).

61. E. Michiels, and R. Gijbels, Anal. Chem., 56, 1115 (1984)

62. F. Bruynseels and R. Van Grieken, Int. J. Mass Spectrom. Ion Proc., 1987, in press.

63. L. Van Vaeck, J. Claereboudt, S. De Nollin, W. Jacob, F. Adams, R. Gijbels, and W. Cautreels, Proceedings of the 10th Int. Mass Spectrom. Conference, 9-13 Sept. 1985, Swansea, UK, p.1249.

64. F. Heresch, in Ion Formation from Organic Solids, ed. by A. Benninghoven, Springer-Verlag, Berlin, 1983, p 240.

65. G.L.Q. Van der Peyl, K. Isa, J. Haverkamp, and P.G. Kistemaker, Nucl. Instrum. Methods, 198, 125 (1982).

66. R. Stoll and F.W. Röllgen, Z. Naturforsch, 37a, 9 (1982).

67. R.J. Cotter, M. Snow, M. Colvin, in Ion Formation from Organic Solids, ed. by A. Benninghoven, Springer-Verlag, Berlin, 1983, p.

68. R.A. Fletcher, I. Chabay, D.A. Weitz and J.C. Chung, Chem. Phys. Letters, 106, 615 (1984).

69. E. Weber and F.Vögtle, Chem Ber., 109,1803 (1976).

70. W.H. Schröder, Fres. Z. Anal. Chem., 308, 212 (1981).

71. W. Schröder, D. Frings, and H. Stieve, Scanning Electron Microsc., II, 647 (1980).

72. A.H. Verbueken, W.A. Jacob, P.M. Frederik, W.M. Busing, R.C. Hertsens, and R.E. Van Grieken, J. Physique, 45, C2-561 (1984).

73. L. Edelmann, Fres. Z. Anal. Chem., 308, 218 (1981).

74. A.H. Verbueken, R.E. Van Grieken, G.J. Paulus, G.A. Verpooten, and M.E. De Broe, Biomed. Mass Spectrom., 159 (1984).

75. A. H. Verbueken, G. Paulus, F. Van de Vijver, G. Verpooten, M. De Broe, and R. Van Grieken, in Proceedings of the 31st Annual Conference on Mass Spectrometry and Allied Topics, Boston, Ma., May 8-13, 1983, p. 67.

76. H.J. Heinen, Int. J. Mass Spectrom. Ion Phys., 38, 309 (1981).

77. P. Wieser, R. Wurster, and U. Haas, Fres. Z. Anal. Chem., 308, 260 (1981).

78. H.G. Fromme, M. Grote, J. Schaffstein, W. Hollaender, and B. Bechtloff, J. Physique, 45, C2-389 (1984).

79. Ph. Otten, F. Bruynseels, and R.E. Van Grieken, in Third International Laser Microprobe Mass Spectrometry Workshop 1986, 26-27 August, Antwerp-Wilrijk, Belgium, p.159.

80. P. Wieser, R. Wurster, and H. Seiler, J. Physique, 45, C2-261 (1984).

81. R. Niessner, D. Klockow, F. Bruynseels, and R. Van Grieken, Int. J. Environ. Anal. Chem., 22, 281 (1985).

82. E.-R. Krefting, G. Lissner, and H.J. Hoehling, Scanning Electron. Microsc., II, 369 (1981).

83. J.M. Beusen, P. Surkyn, R. Gijbels, and F. Adams, Spectrochim. Acta, 38B, 843 (1983).

84. U. Haas, P. Wieser, and R. Wurster, Fres. Z. Anal. Chem., 308,270 (1981).

85. D.S. Simons, in Microbeam Analysis-1980, ed by D.B. Wittry, San Francisco Press, San Francisco, 1980, p. 178.

86. K.R. Spurny, J. Schoermann, and R. Kaufmann, Fres. Z. Anal. Chem., 308, 270 (1981).

87. D.S. Simons, in Microbeam Analysis-1982, ed by K.F.J. Heinrich, San Francisco Press, San Francisco, 1982, p. 390.

88. R.A. Fletcher and A.J. Fatiadi, in Microbeam Analysis-1984, ed. by A.D. Romig, Jr. ,and J.I. Goldstein, San Francisco Press, San Francisco, 1984, p. 14

89. P. Wieser, R. Wurster, and L. Phillips, in Aerosols in the Mining and Industrial Work Environments, Vol 3, ed by V.A. Marple and B.Y.H. Liu, Ann Arbor Science, Michigan, 1983, p. 1169.

90. J.A. Small, J.A. Norris, and R.L. McKenzie, in Microbeam Analysis-1983, ed. by R. Gooley, San Francisco Press, San Francisco, 1983, p. 209.

91. R. Brace and E. Matijevic, J. Inorg Nucl. Chem., 35, 3691 (1973).

92. R. Wechsung, F. Hillenkamp, R. Kaufmann, R. Nitsche, E. Unsöld, and H. Vogt, Microsc. Acta., Suppl. 2, 281 (1978).

93. P.F. Schmidt, H.G. Fromme, and G. Pfefferkorn, Scanning Electron Microsc., II, 623 (1980).

94. P.F. Schmidt and K. Ilsemann, Scanning Electron Microsc., I, 77 (1984).

95. C.A. Andersen and J.R. Hinthorne, Anal. Chem., 45, 1421 (1973).

96. A.E. Morgan and H.W. Werner, Mikrochim. Acta, II, 31 (1978).

CHAPTER 4 RECOMBINATION REACTIONS AND GEOMETRY EFFECTS IN LAMMA STUDIES WITH $^{12}C/^{13}C$ BILAYERS

4.1 INTRODUCTION

To improve the practical applicability of laser microprobe mass spectrometry to the structural analysis of organic and inorganic compounds, further research about the mechanism of laser induced ion formation is needed.

For the LAMMA-500 instrument in particular, studies on the ion formation mechanism and on the modelling by empirical formula of the cluster ion distribution were performed on carbon, metal (Al, Fe, Ag, Au) and semiconductor foils (1-4), oxides (5-7), salts (8-11) and organic compounds (12-14).

Foils of carbon are very suitable for fundamental studies, because the features of its cluster ion distribution have extensively been studied with a variety of spectrometric techniques using different excitation sources, and a theoretical explanation based on molecular orbital theory has been developed (3,15). The present chapter reports on the study of a carbon bilayer that consists of a layer of natural carbon and a second one enriched in ^{13}C. When such a bilayer is perforated by the laser beam in the transmission geometry of the LAMMA-500 instrument, comparable areas of both foils can be ionized and recombination reactions during laser induced ionization can straightforwardly be studied.

4.2 EXPERIMENTAL

A chemically pure carbon foil of 99.73 % ^{13}C and a thickness of 25 nm (type ICH-5, Atomic Energy of Canada, Ottawa, Canada) was floated off from its supporting objective glass onto a surface of

demineralized bidistilled water. The foil was picked up on a 300 mesh electron microscope (EM) grid. A 20 nm thick natural carbon layer (98.89 % ^{12}C) was then evaporated on top of the ^{13}C foil to form a $^{12}C/^{13}C$ bilayer.

Also by the same floating-off procedure, an EM-grid was covered at one side with a 25 nm natural carbon foil (type TCF-5, Atomic Energy of Canada, Ottawa, Canada) and at the other side by a 25 nm ^{13}C foil. In this sample, the two carbon foils are spatially separated by the thickness of the grid.

4.3 RESULTS AND DISCUSSION

4.3.1 Positive and negative clusters generated by a single laser shot perforation of a carbon foil

Single laser shot perforation of a carbon foil yields cluster ions of the type C_n^+ and C_n^- (n is a whole number), in the positive and negative ion mode respectively (Figure 4.1). The principal features of the cluster ion intensity distributions are the following (1,2),

for $n \leq 9$: - odd-even rule with periodicity $\Delta n = 2$
- positive ion mode : relative maxima for odd n
- negative ion mode : relative maxima for even n

$n > 9$: - periodicity $\Delta n = 4$ for positive ions
- negative ion intensities are rapidly decreasing

The results for $n \leq 9$ are in qualitative agreement with the calculations of Pitzer and Clementi (15). They used the molecular orbital theory to calculate the partial pressure of the various vapour species C_n in equilibrium with graphite. They found that odd species have closed shell structures and lower energies than the even species but that the even species show greater electron affinity. The absolute maximum of the distributions shifts to lower

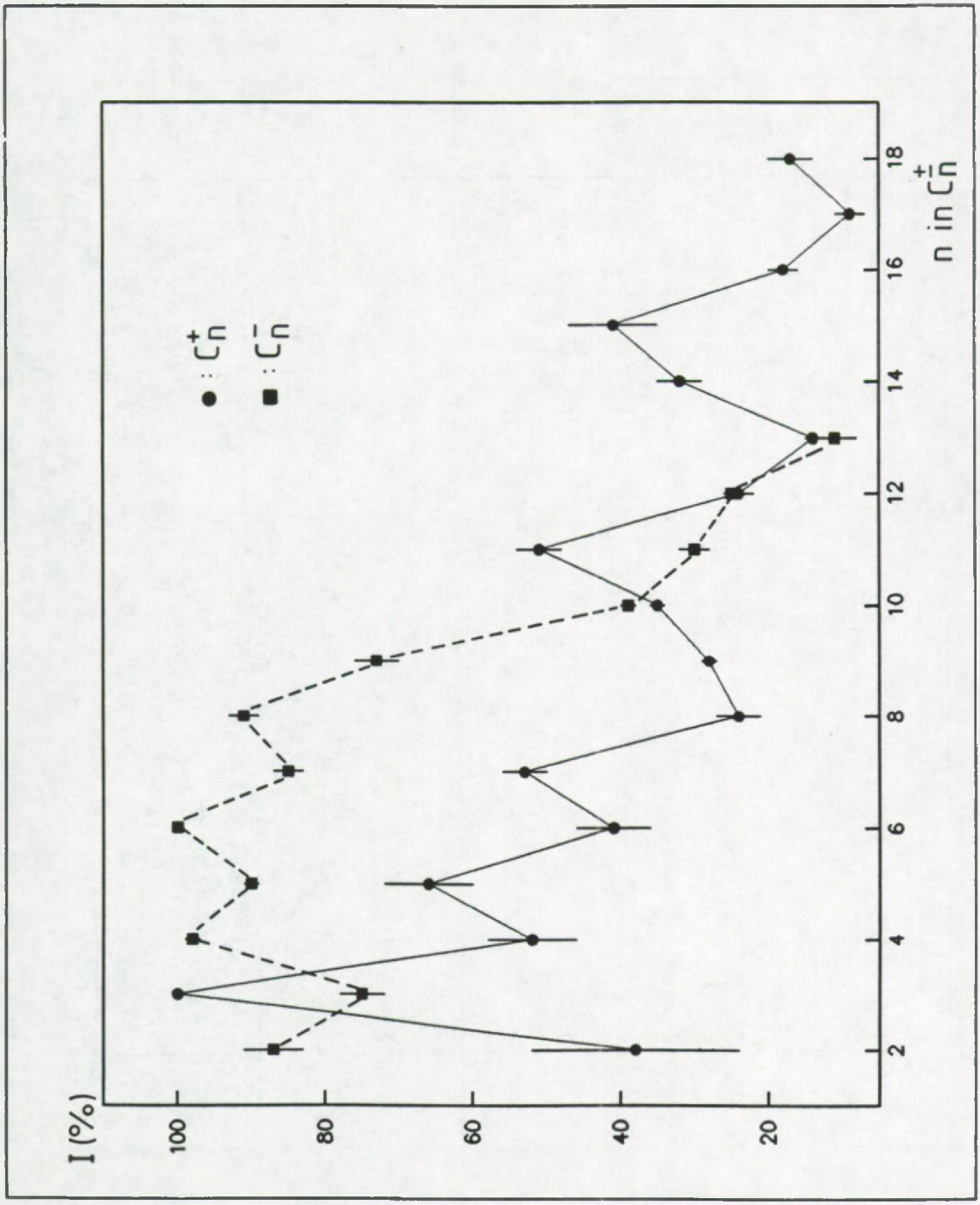

Figure 4.1: Mass peak intensities as a function of the number of C-atoms in the C_n^+- and C_n^--clusters ,respectively, for single laser shot perforation of a carbon foil.

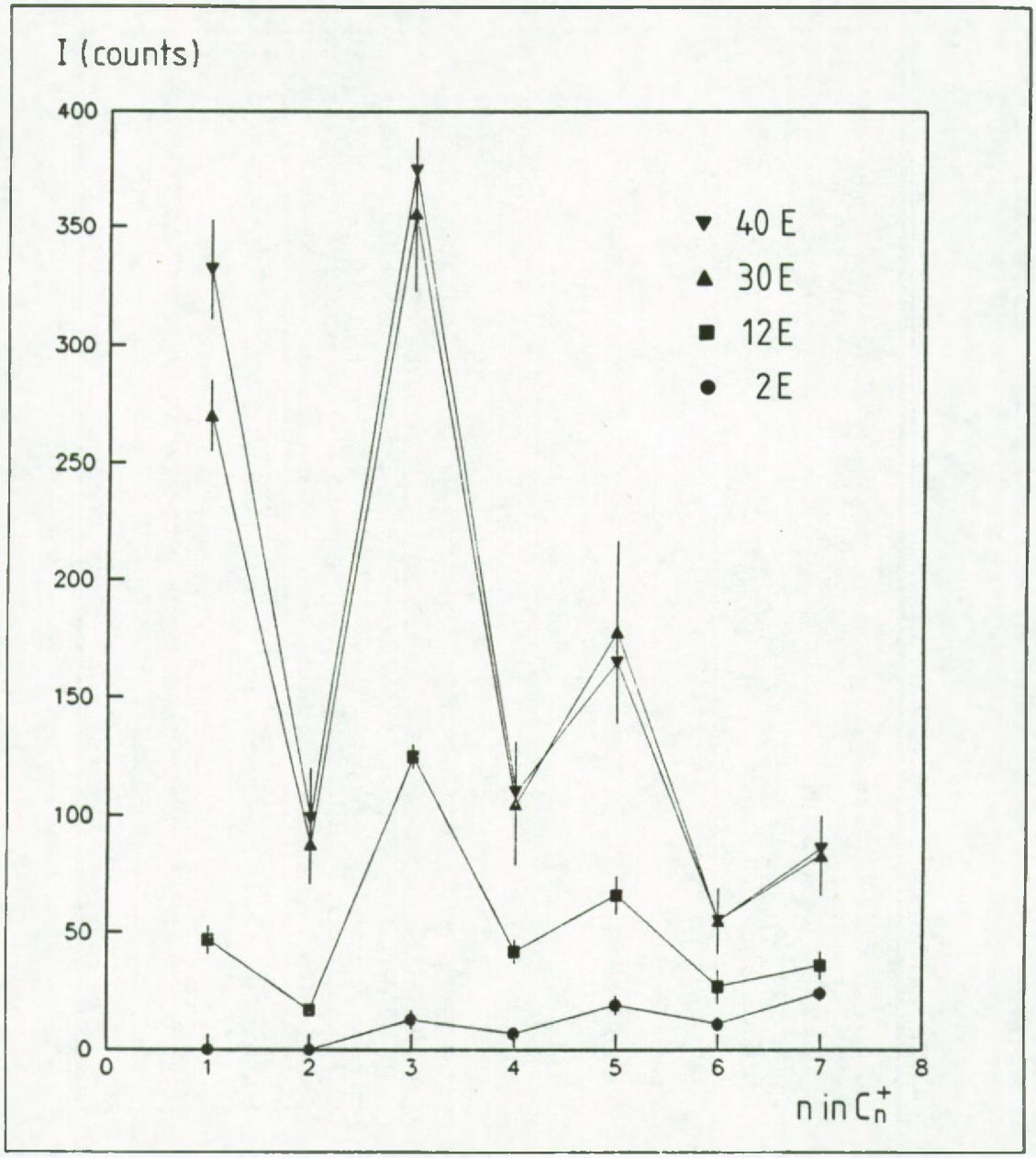

Figure 4.2: Absolute intensity distributions of the C_n^+-cluster ions for 4 different laser irradiances ranging from 2E to 40E, with E = minimal energy needed for sample perforation in a single laser pulse.

n-values with increasing laser irradiance (Figure 4.2) (Irradiance refers to the actually applied laser output. The irradiance is correlated to the energy denisty by the material that is consumed (see also below). For practical purposos, this relationship is not taken into account in the discussion). The absolute maximum is situated at n = 3 for energies ≥ 12E (E is the minimal energy needed for the perforation of the sample). For energies close to the threshold for perforation, the maximum shifts towards higher n-values, and the C_1^-- and C_2^--clusters are not detected.

4.3.2 Single laser shot perforation of a $^{12}C/^{13}C$-bilayer

When a carbon foil that consists of a ^{12}C and a ^{13}C layer is perforated by a laser beam, comparable amounts of ^{12}C and ^{13}C are evaporated (as seen in Figure 4.3) and partly ionized, so that clusters of the type C_n^+ and C_n^- (with n as whole number), as described above, show up in the positive and negative mode mass spectra, respectively. A typical mass spectrum for the negative ion mode is shown in Figure 4.4. If the detected clusters were directly desorbed fragments of the solid structure, the spectra would only show mass peaks at m/z = 12n and m/z = 13n of the $^{12}C_n^{\pm}$- and $^{13}C_n^{\pm}$-clusters. If, however, the solid material would become homogeneously mixed as a consequence of complete disintegration of the carbon bonds, followed by random recombination into clusters of size n, the ^{12}C and ^{13}C atoms would be binomially distributed within every cluster. Figure 4.4 and the experimental data below will show that both ion formation mechanisms have to be considered.

Another mechanism that can result in the formation of mixed isotope clusters is the metastable decay of large size clusters containing C-atoms of both foils that can possibly be formed during laser irradiation. In this context it is worthwile to note that Ens et al. (16) pointed out that in a SIMS study of $(CsI)_nCs^+$-clusters, parent ion fragmentation significantly increases for clusters with n > 4 and for n > 7 only fragments of the parent ions could be

detected 70 μs after emission. Also experiments with a modified LAMMA-500 instrument that allows the simultaneous detection of ions as well as neutral species originating from metastable decay processes, showed that C_nH_m-cluster ions (n > 5) generated from aromatic organic compounds are less stable than smaller ones (17).

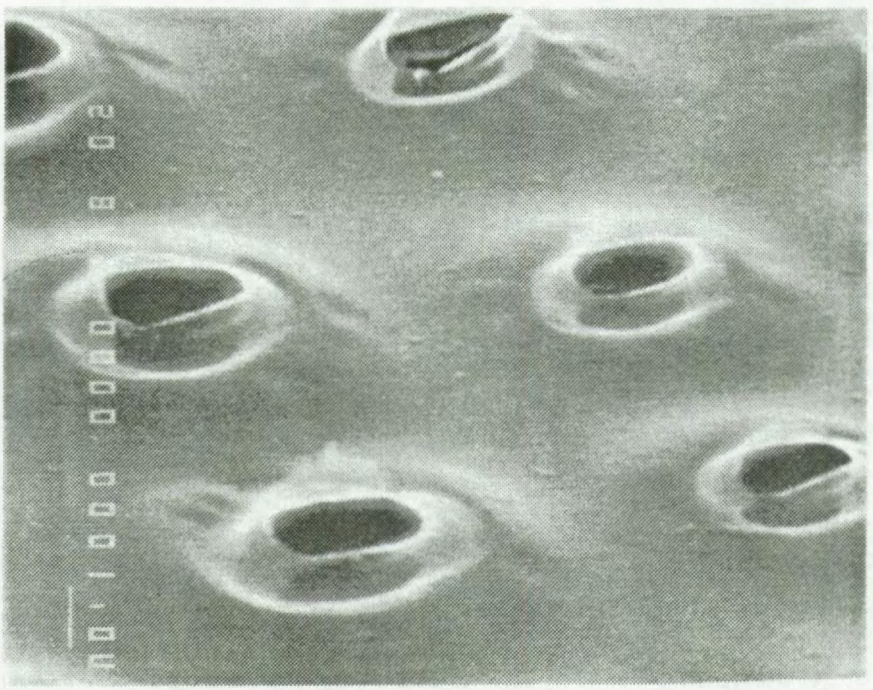

Figure 4.3: Electron micrograph of laser induced perforations in the carbon double-layer. The perforations in the top layer (^{12}C) and underlying layer (^{13}C) are discernible and of comparable size.

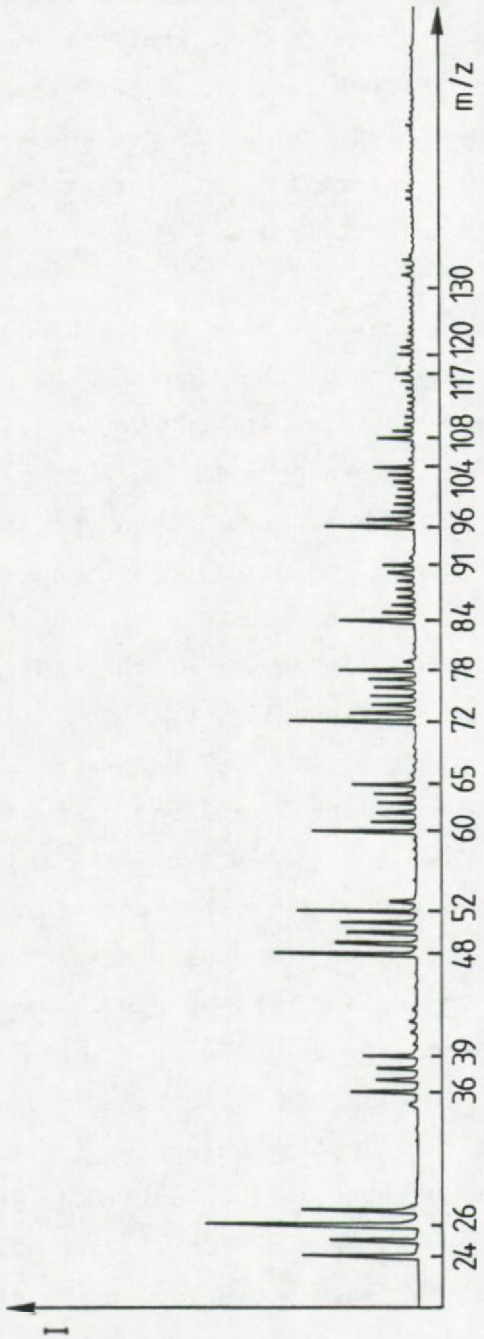

Figure 4.4: Typical negative mode LAMMA-spectrum of a $^{12}C/^{13}C$ bilayer, for a laser energy of 14E, with E = minimal energy needed for sample perforation in a single pulse.

This could be inferred from a shift of the C_nH_m-distribution in the spectrum of neutral species to higher masses relative to the negative ion spectrum. The question to what extent the metastable decay of large size clusters influences the mixed isotope cluster intensities remains unanswered, but it is reminded that also this mechanism assumes prior formation of larger size clusters by recombining fragments from both layers.

Before discussing the results more thoroughly, two remarks are to be made. First, because of the limited mass resolution of the TOF-mass spectrometer, the association of hydrogen to the $C_n^{\pm}$-clusters can cause interference with the pure carbon clusters of nearly equal m/z-value. Hydrogen association predominantly occurs with the even n clusters in the negative ion mode and with the odd n-clusters in the positive ion mode. Measurements on the pure ^{13}C-foil pointed out that the intensity of the C_nH^- can be estimated to be around 10 % of the corresponding C_n^--peak intensity for the even n-clusters, except for the C_2^--clusters where the C_2H^--intensity amounted to 50 % of the C_2^--signal. The mass peak at m/z = 26 can also suffer from the interference of CN^-. This cluster ion is frequently seen in mass spectra of carbon containing samples. The nitrogen can originate from N_2 residual gas that enters the sample chamber either during the venting procedure with N_2 or from ambient air during sample exchange. For the C_n^--clusters with odd n the hydrogen contribution is negligible. Therefore the result of the odd, C_n^--clusters are the most indicative for the occurrence of recombination reactions in the negative ion mode spectra, whereas for the positive ion mode the even n-clusters are more favourable in this respect. Second, in the interpretation of the results one must consider the contribution to the mixed isotopic mass peaks of the 1.112 % ^{13}C in the natural carbon layer and 0.27 % ^{12}C in the ^{13}C-layer. The intensities of the mass peaks, used in the following discussion were corrected for these isotopic contributions. All the results given below are averages of ten measurements at every considered energy.

Negative cluster ions, generated by a single laser shot perforation of the bilayer

Table 4.1 lists the relative intensities of the C_3^--cluster ions, generated from a bilayer of ^{12}C and ^{13}C for 5 different laser excitation energies ranging from minimal energy E needed for the perforation of the sample in a single laser pulse, to 28E. The ^{12}C-side was facing towards the extraction potential of the mass spectrometer. The presence of the mixed isotopic clusters at m/z = 37 and 38 clearly demonstrates that recombination reactions between atoms that were spatially separated in the sample do occur. At the minimal energy needed for perforation of the sample, 97 % of the material found in the spectrum originates from the top 20 nm of the sample. The results also indicate that the total contribution of the ^{13}C to the C_3^--clusters increases with increasing laser irradiance to reach 48 % of ^{13}C as calculated from the spectra while the sample (20 nm layer of ^{12}C and 25 nm of ^{13}C) consists of 56 % ^{13}C, assuming that the evaporated volumes of both layers are identical. This implies that the geometry effect for ion extraction decreases with increasing laser irradiance or, otherwise stated, laser irradiances close to the threshold of perforation of the sample promote ion extraction from that side of the sample that is faced towards the mass spectrometer (see also below). This effect has to be taken into account in the analysis of inhomogeneous samples. Moreover, it can facilitate the use of LAMMA-500 as a quasi surface selective analysis technique, certainly in these cases where the threshold for sample perforation is not exceeded.

Figure 4.5 represents the absolute intensity distribution for the C_n^--cluster ions for n = 2 to 9 at the 5 different laser energies, ranging from E to 28E. The material consumption (in picograms) was calculated from the amount of carbon evaporated as inferred from the dimensions of the perforations in the foil. The results are plotted as a function of the laser energy in Figure 4.6. The relative maxima are situated at the even n-clusters, because of their higher electron affinity (2). The absolute maximum of the

Table 4.1: Relative intensities of the C_3^--clusters, generated from a $^{12}C/^{13}C$ bilayer at 5 different laser excitation energies.

	Average relative intensity * of the C_3^--clusters ± Stand. Dev.				
Energy	E**	2E	6E	14E	28E
m/z					
36($^{12}C_3$)	91 ± 6	56 ± 3	50 ± 4	39 ± 3	31 ± 3
37($^{12}C_2{}^{13}C$)	9 ± 2	21 ± 3	23 ± 4	20 ± 3	21 ± 2
38($^{12}C{}^{13}C_2$)	0	13 ± 2	16 ± 2	17 ± 2	21 ± 3
39($^{13}C_3$)	0	10 ± 2	11 ± 2	24 ± 3	28 ± 3
Percent of ^{13}C in the C_3^--clusters	3	26	29	42	48

* Average of 10 spectra, normalized to the sum of the intensities at m/z = 36 through 39 as 100 %.

** E is the minimal energy needed for the perforation of the sample in a single laser pulse.

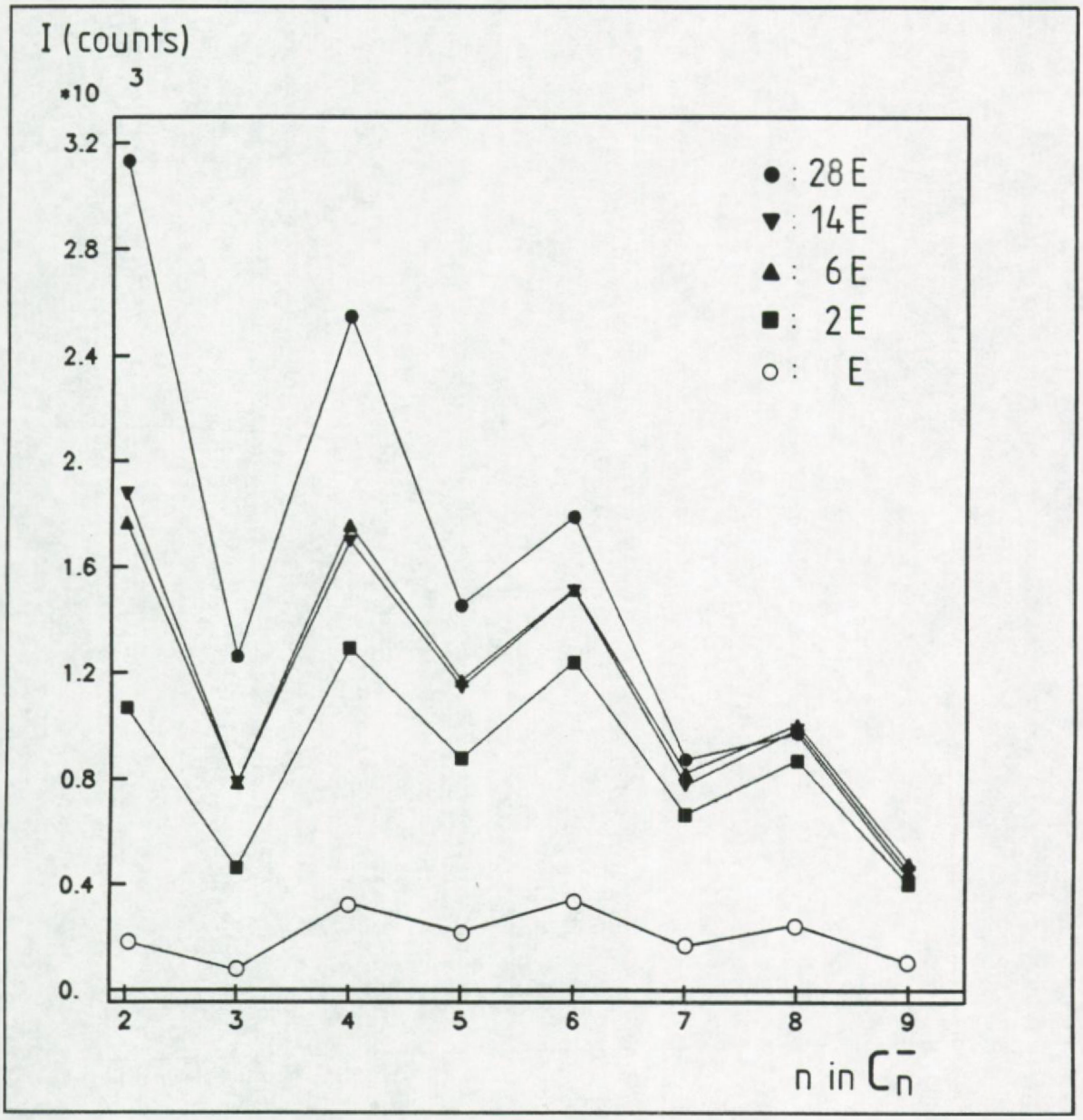

Figure 4.5: Absolute intensity distributions of C_n^--cluster ions at 5 different laser irradiances, from E to 28 E, with E = minimal energy needed for sample perforation in a single laser pulse.

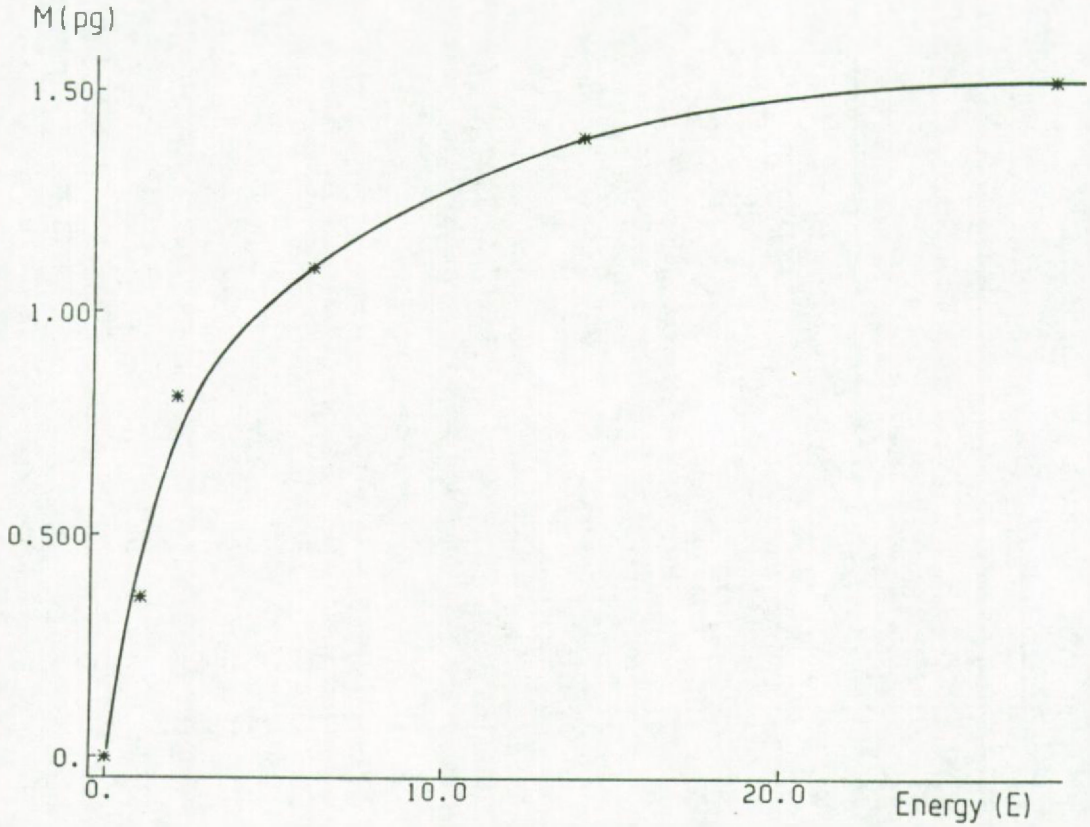

Figure 4.6: Amount of carbon (in picograms), evaporated from the $^{12}C/^{13}C$ bilayer in a single laser shot perforation of the sample, as a function of the laser energy E to 28E, with E = minimal energy needed for sample perforation.

distribution shifts from n = 6 at energy E to n = 4 at energies of 2E and 6E, and finaly to n = 2 for 14E and 28E. Hence for the negatively charged clusters, increasing laser irradiances promote the formation of lower size clusters while the alternating effect in the intensity of the odd and even n-clusters remains unchanged, even at the lowest laser irradiances, in contrast to what has been found for the positive clusters (19), that show a single maximum for n < 9 at n = 6 for a laser irradiance of 1.5E.

Figure 4.7 shows the percentatage ^{13}C in the C_n^--clusters generated at the different laser energies from a $^{12}C/^{13}C$ bilayer with the ^{12}C-side facing the mass spectrometer. For the clusters with n-values ranging from 3 to 8, the ^{13}C contribution decreases slightly with growing cluster size. Relative maxima are seen for the odd n-clusters at energy E, but for the even n-clusters at an energy 28E, with a smoothing of the odd-even effect for the intermediate energies, resulting e.g. in an approximately linear relationship for the clusters with $3 \leq n \leq 8$ at an energy of 14E. Figure 4.7 also shows the progressive increase in ^{13}C with increasing laser energy (at the expense of the ^{12}C-contribution) as a result from the geometry effect, as discussed earlier.

The relative intensity of the mixed-isotope clusters (denoted % R) of given size n, normalized to all clusters of that size, is plotted in Figure 4.8a. As mentioned earlier, the relative intensities of these mixed-isotope clusters are a measure for the degree to which recombination reactions occur between spatially separated atoms or lattice fragments. In Figure 4.8a, a slight increase of the mixed-isotope cluster intensities with increasing cluster size, is seen. This increase can almost entirely be attributed to the statistically lower probability of obtaining pure-isotope clusters with increasing number of atoms in case of complete degradation and recombination (namely 50 %, 25 %, 12.5 %, etc., for n = 2, 3, 4, etc., respectively, according to a binomial law with p = q = 0.5). Indeed, when the % R-values in Figure 4.8a. are divided by the hypothetical intensity of the mixed-isotope

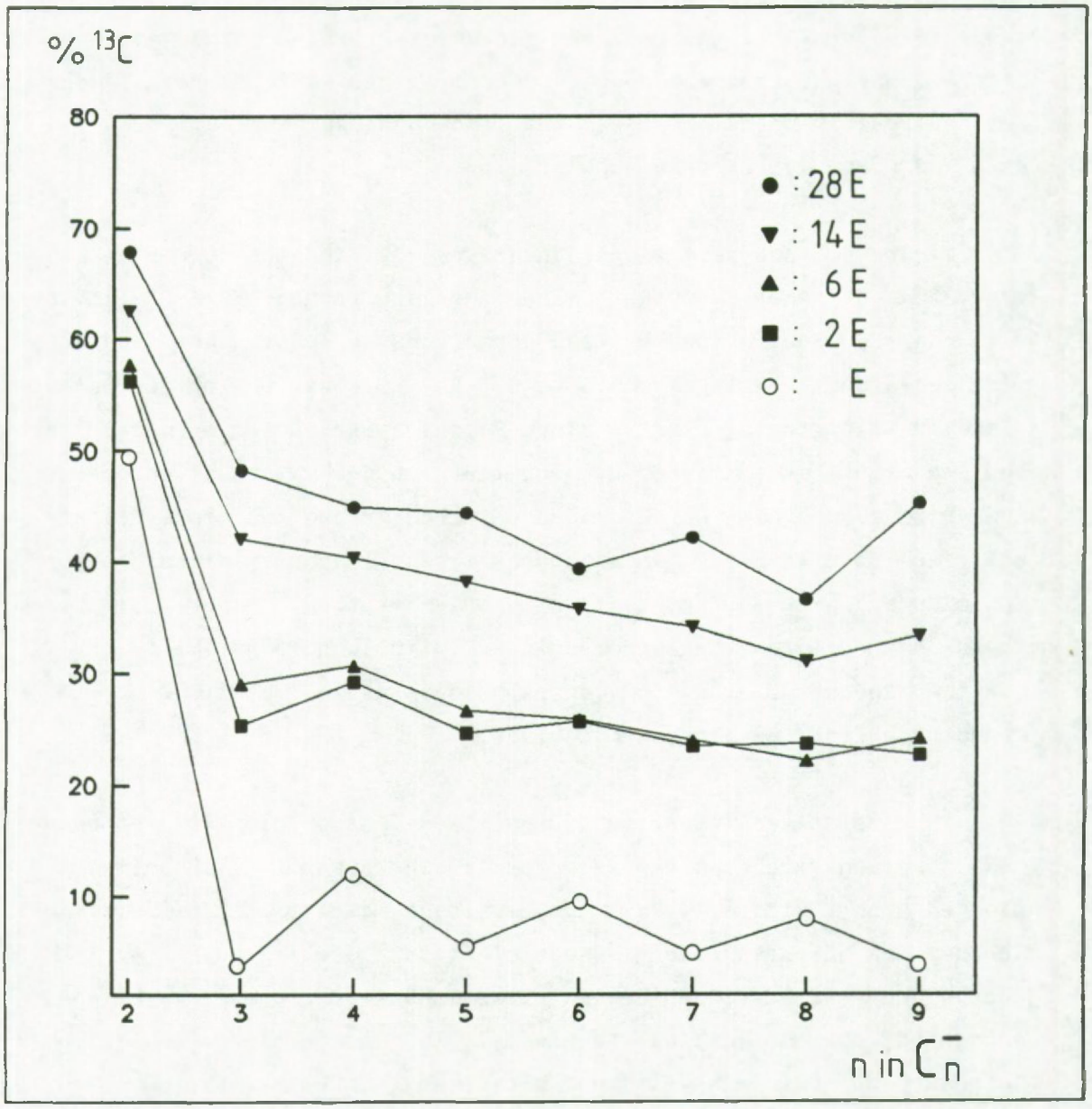

Figure 4.7: Percent ^{13}C in C_n^--clusters generated at five laser energies from a $^{12}C/^{13}C$ bilayer with the ^{12}C-side facing the mass spectrometer.

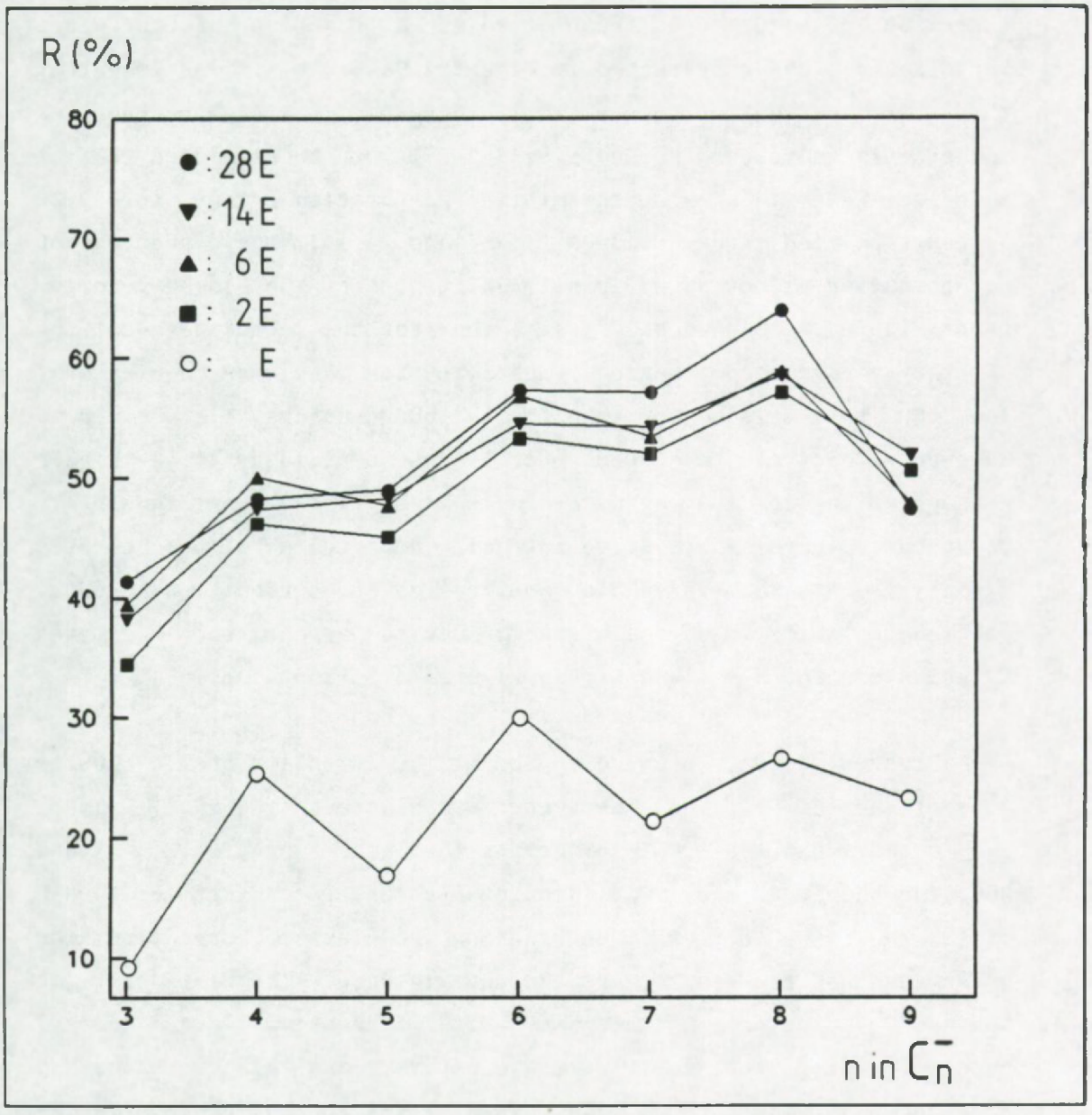

Figure 4.8a: Percent abundance of mixed-isotope clusters (% R) as a function of the cluster size, at 5 different laser irradiances, from E to 28E, with E = minimal energy needed for sample perforation in a single laser pulse

clusters, as calculated for a binomial distribution, the increasing trend disappears. This can be seen in Figure 4.8b. When the % R-values of Figure 4.8a are plotted as a function of the laser irradiances, as represented in Figure 4.9a and b, it is clear that the % R is constant or only slightly increasing for higher energies and steeply increases for energies ≤ 2E. It can be concluded that at energies higher than twice the minimal perforation energy (or 2.2E as extrapolated from Figures 4.9a and 4.9b), the percentage of recombination is not significantly influenced by the laser energy. From Figure 4.8b one could assume that for the irradiances up from 2E, the average recombination probability for the even n-clusters, i.e. 60 ± 1 % is higher than for the odd clusters, i.e. 54 ± 3 %. However, this can at least partly be explained by a higher H-association in the even n-clusters and it does not necessarily point to an increased relative intensity due to a higher cluster stability. At the threshold laser energy for perforation however, pronounced maxima in degree of recombination appear for the even C_n^--clusters for n = 4 and 6 (see Figures 4.8a and 4.8b).

Figures 4.10a, b and c represent the intensity of the cluster ions of the $^{12}C_n^-$-series, the recombined clusters $^{12}C_n{}^{13}C_{n-m}$ with $1 \leq m \leq n-1$ and the $^{13}C_n^-$-series for the laser energy of E, 6E, and 28E. For energy E, the $^{13}C_n^-$ intenisty is very low, exept for $^{13}C_2^-$ while the $^{12}C_n^-$-series, representing the clusters formed from the upper 20 nm of the sample, are the most intense. The intensity of the $^{13}C_n^-$-clusters, increases with increasing laser energy, especially for the lower size clusters, and always shows a pronounced maximum for the mass peak at m/z = 26 that represents the $^{13}C_2^-$-cluster. Interference of this mass peak by CN^- cannot be excluded as mentioned earlier. The overall intensity of the recombinated peaks $^{12}C_m{}^{13}C_{n-m}^-$ increases as the laser energy increases, to exceed the intensity of the corresponding $^{12}C_n^-$-clusters. Progressive shifts of the cluster ion intensities towards the lower cluster sizes can be observed for both the $^{12}C_m{}^{13}C_{n-m}^-$- and $^{12}C_n^-$-clusters. If the $^{13}C_2^-$ is left out of the

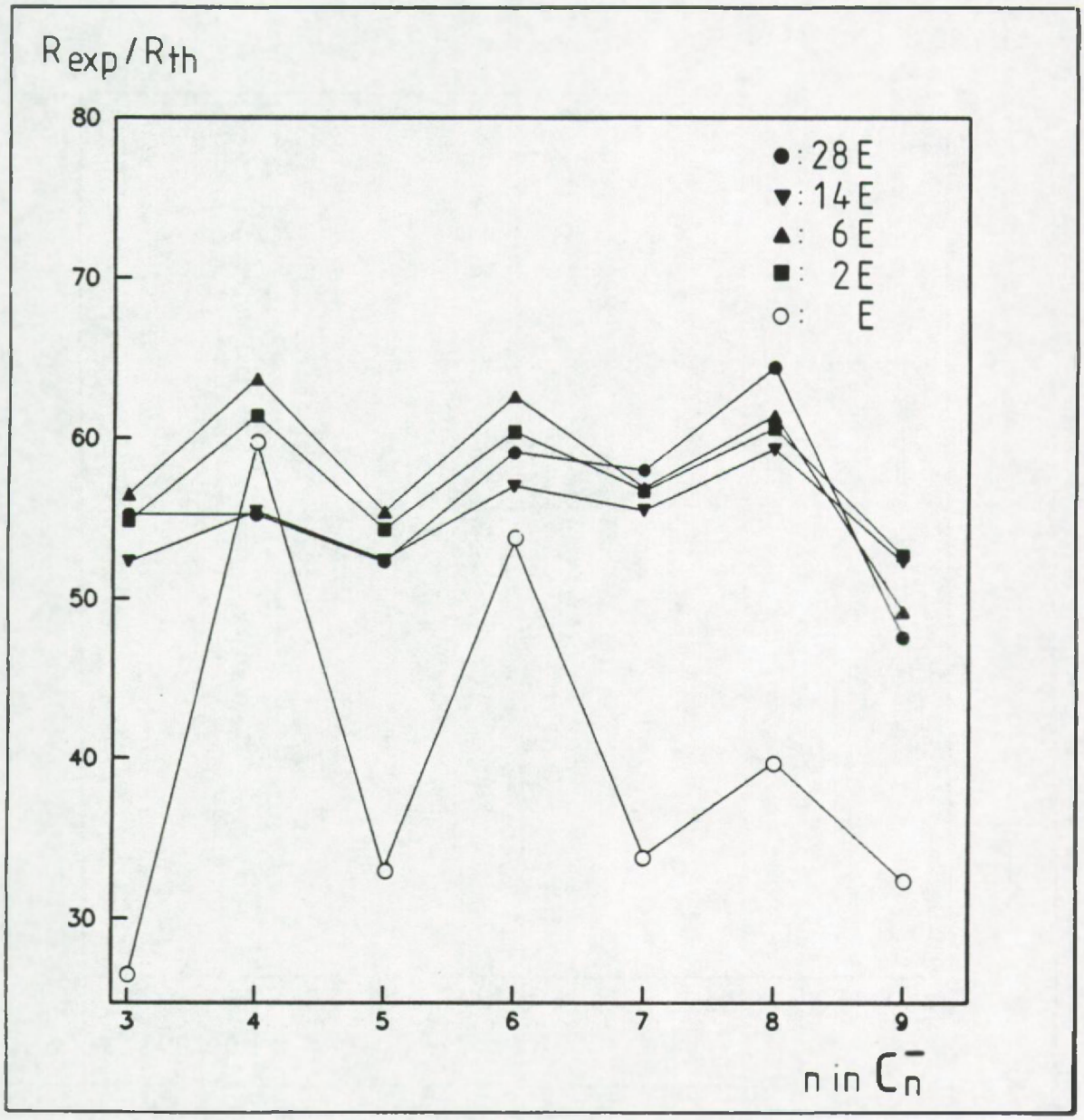

Figure 4.8b: Percent abundance of mixed-isotope clusters (% R) normalized to the probability for obtaining mixed isotope recombinations according to a binomial law

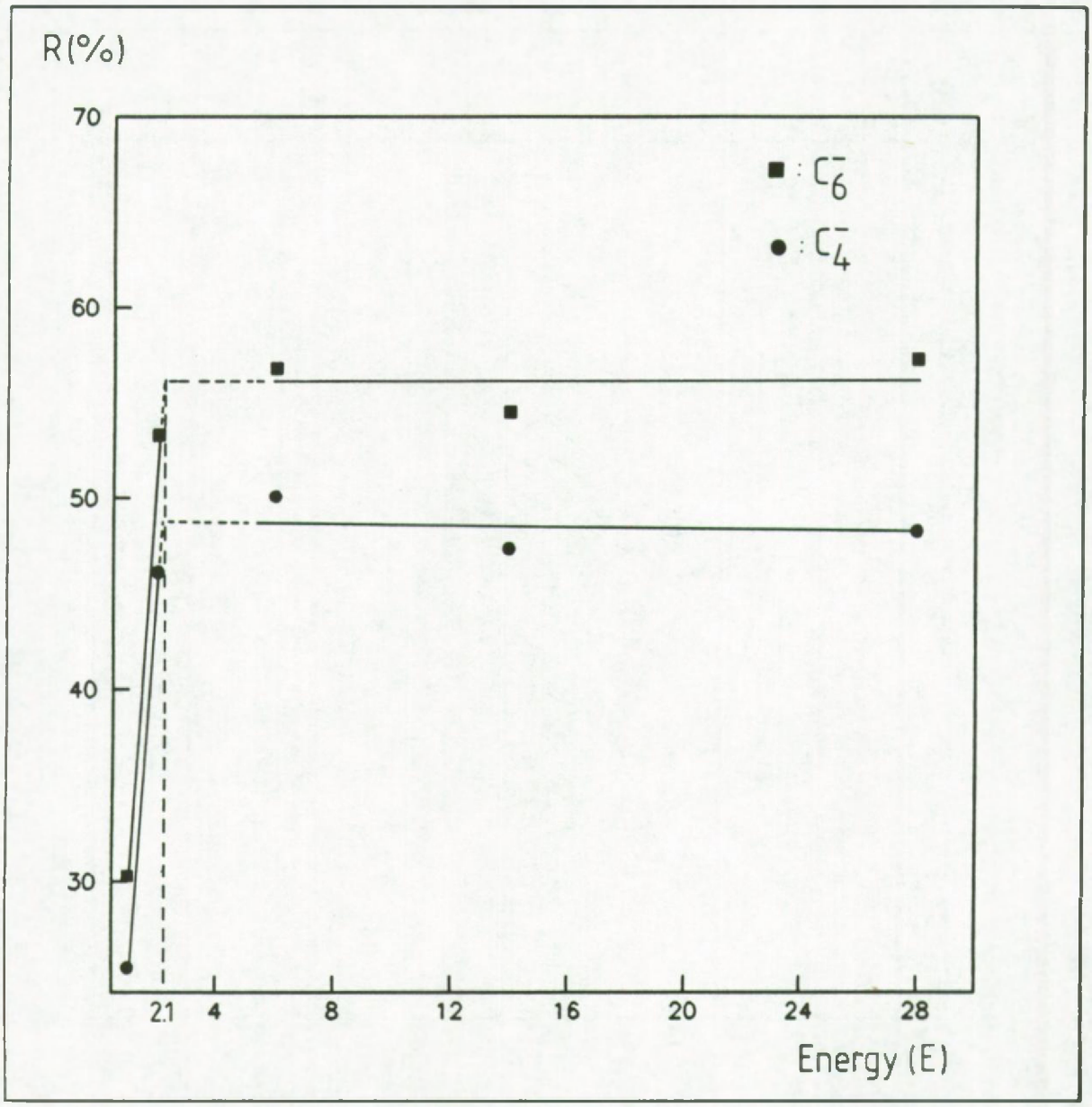

Figure 4.9a: Percent abundance of the mixed-isotope clusters (% R) for C_4^- and C_6^-, as a function of the laser irradiance, from E to 28E, with E = minimal energy needed for sample perforation in a single laser pulse.

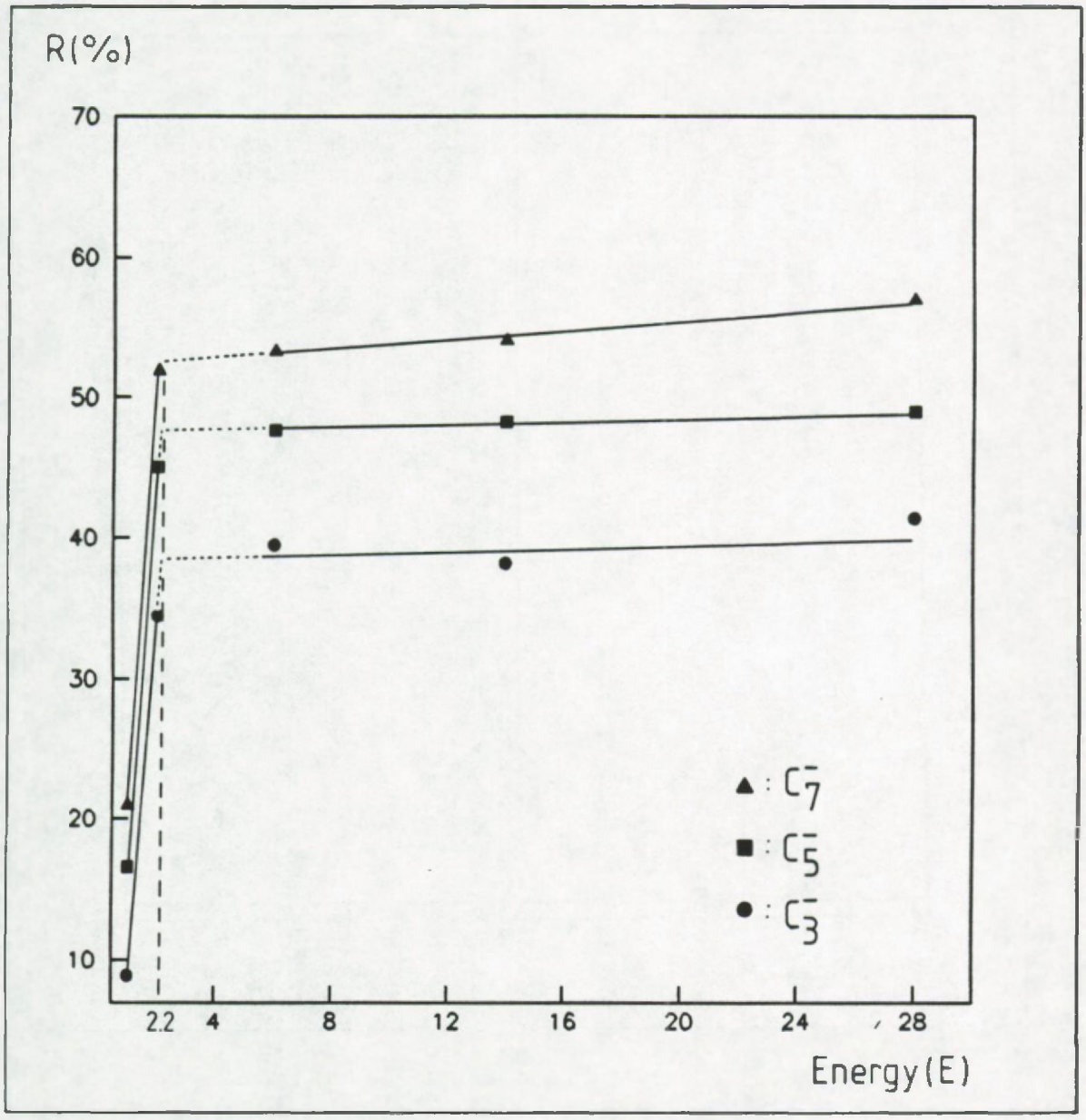

Figure 4.9b: Percent abundance of the mixed-isotope clusters (% R) for C_3^-, C_5^- and C_7^-, as a function of the laser irradiance, from E to 28E, with E = minimal energy needed for sample perforation in a single laser pulse.

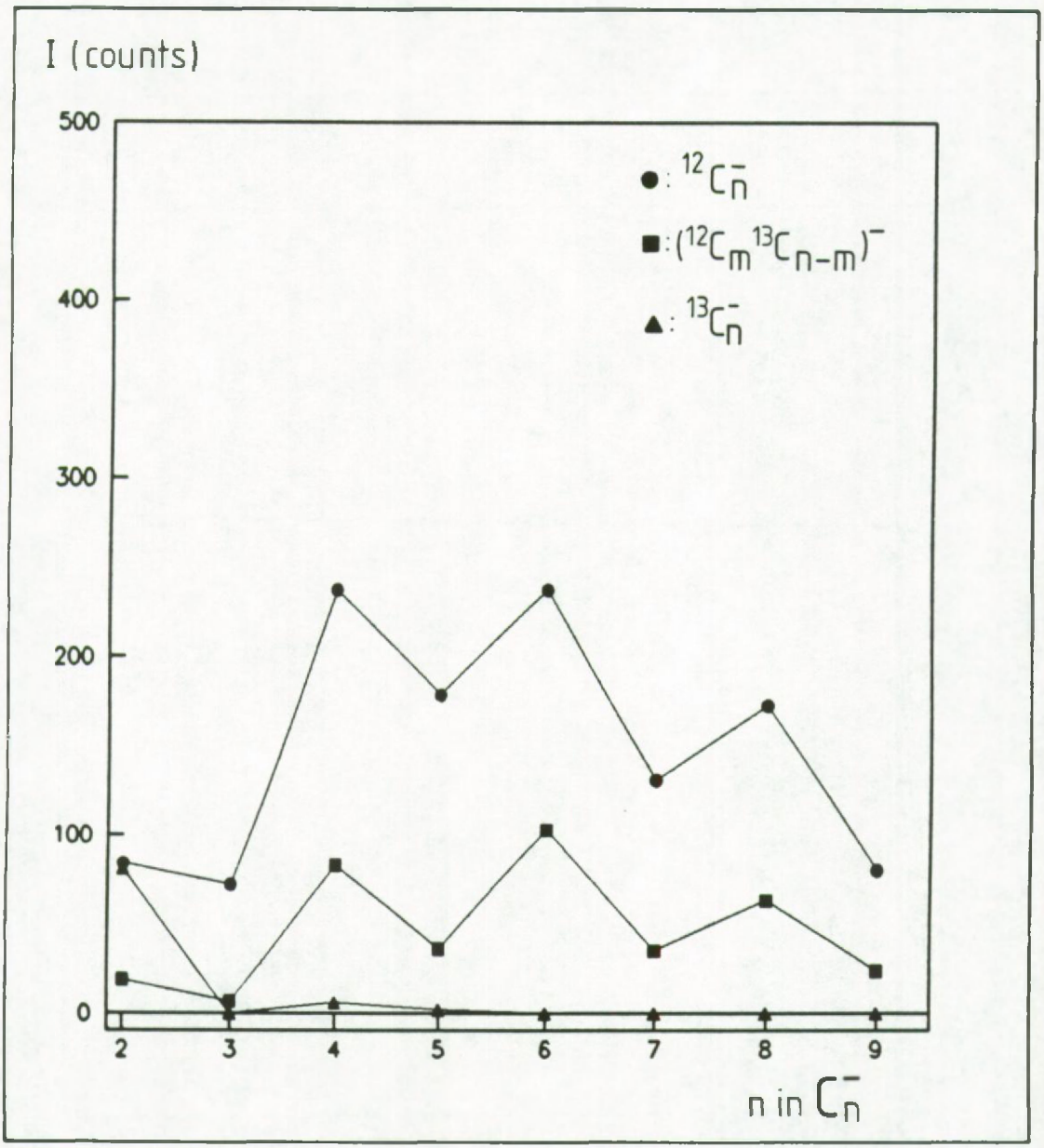

Figure 4.10a: Absolute intensity distribution of $^{12}C_n^-$, $^{13}C_n^-$ and mixed isotope clusters, $^{12}C_mC_{n-m}^-$ ($1 \leq m \leq n-1$) as a function of the cluster size for a laser irradiance of E, with E = the minimal energy needed for the perforation of the sample in a single laser pulse

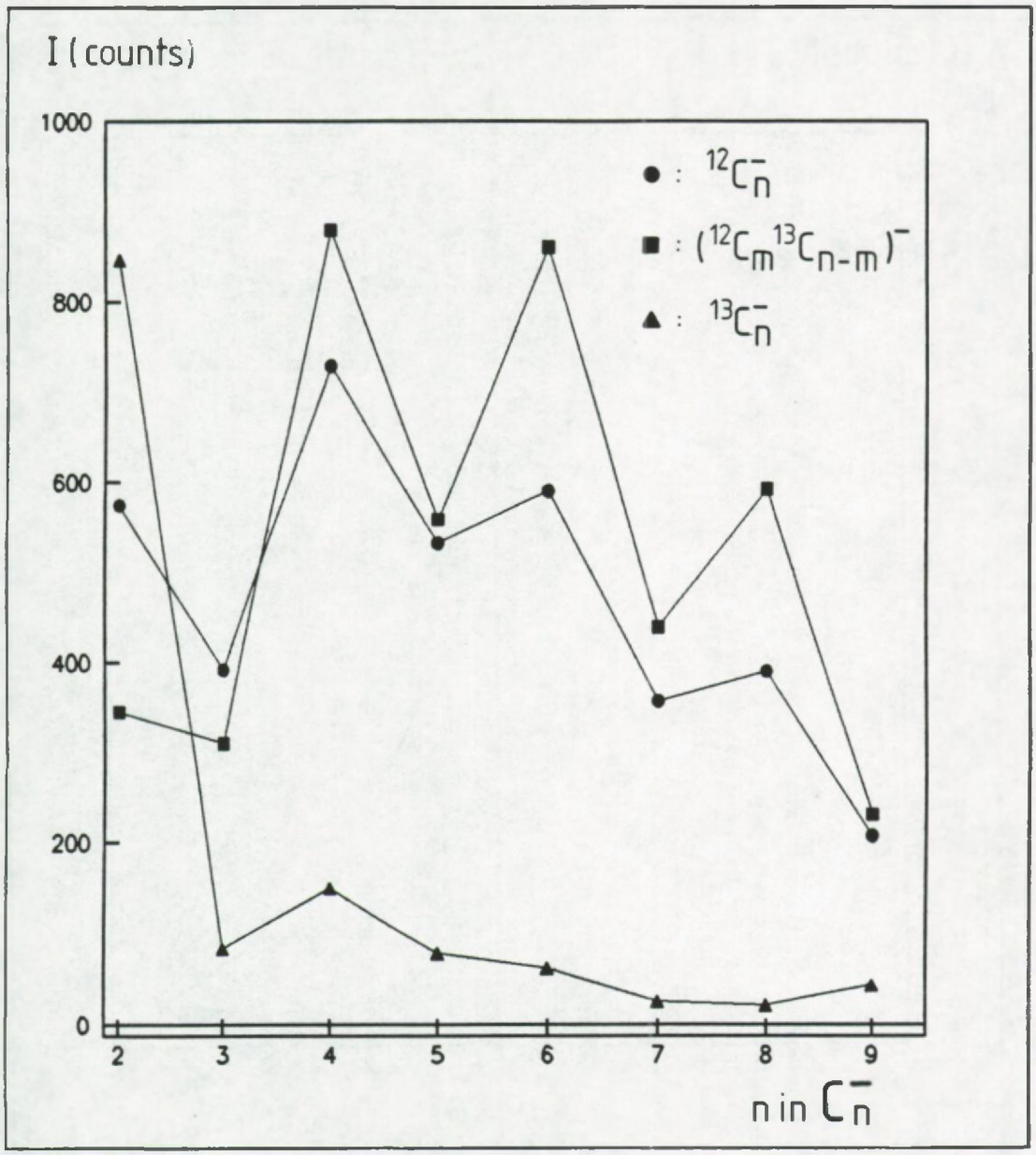

Figure 4.10b.: Absolute intensity distributions of $^{12}C_n^-$, $^{13}C_n^-$ and mixed isotope clusters, $^{12}C_m{}^{13}C_{n-m}^-$ ($1 \leq m \leq n-1$) as a function of the cluster size, for a laser irradiance of 6E, with E = minimal energy needed for the perforation of the sample in a single laser pulse.

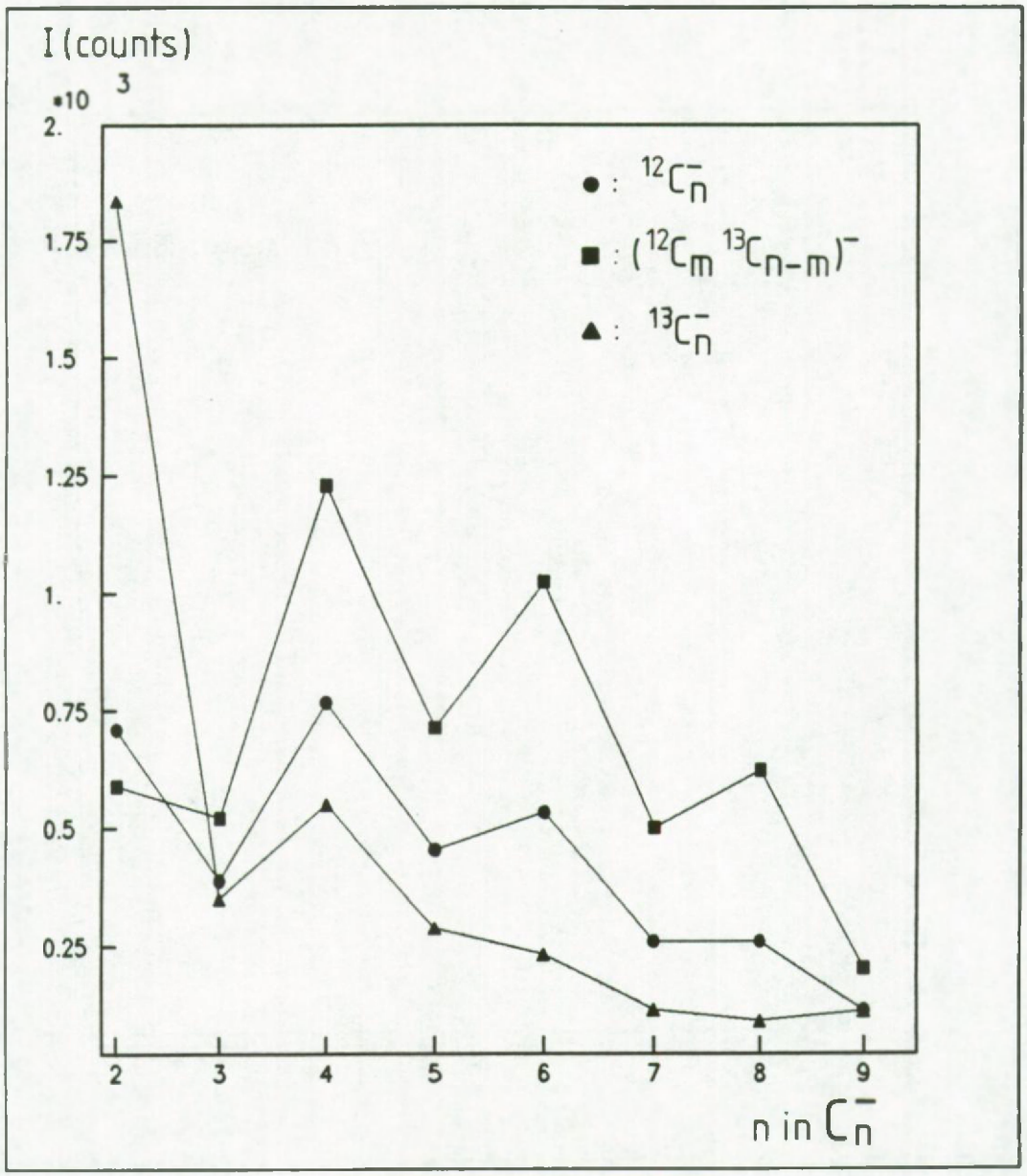

Figure 4.10c: Absolute intensity distributions of $^{12}C_n^-$, $^{13}C_n^-$ and mixed isotope clusters, $^{12}C_m{}^{13}C_{n-m}^-$ ($1 \leq m \leq n-1$) as a function of the cluster size for a laser irradiance of 28E, with E = minimal energy needed for the perforation of the sample in a single pulse.

discussion because of the possible CN^--interference, the $^{13}C_n^-$-distribution always shows a maximum at $^{13}C_4^-$. It can also be observed that the ^{13}C is always largely associated to the recombined clusters and that the intensity distribution of the $^{13}C_n^-$ (with n > 2) is always lower than the $^{12}C_n^-$-distribution for all laser irradiances. It was not possible to prepare a bilayer in exactly the reverse geometry. However, spectra recorded after the present sample was reversed, so that the ^{13}C layer faces the mass spectrometer, yielded mass spectra that were dominated by the $^{13}C_n^-$-clusters as expected from the current observations.

In an attempt to interpret the data in a more quantitative way and to correlate them with the probability for recombination for the individual $^{12}C_m{}^{13}C_{n-m}^-$-clusters, the intensities of the cluster ions were normalized to their intensity distribution resulting from a pure recombination of individual ^{12}C and ^{13}C-atoms, i.e. a binomial distribution calculated by using the abundance of ^{12}C relative to ^{13}C in these specific mass peaks and the cluster size as parameters. The normalized intensities for the measurements at laser energies of 2E and 28E are shown in Table 4.2. The highest intensity ratios are situated at the monoisotopic clusters of ^{12}C and ^{13}C; this can be explained by the fact that their intensity in the mass spectra is largely dominated by a mechanism of direct fragment emission from the two foils; nevertheless also recombination reactions are of considerable importance. The values for mixed-isotope clusters of the same cluster size are not constant, as would be the case for indirect recombination of individual ^{12}C and ^{13}C atoms. The minimum of the ratios for a cluster ion of size n is located at the cluster that has one or two ^{13}C-atoms in the cluster.

Table 4.2: Ratios of the experimental mass peak intensities versus the intensity calculated for a binomial distribution with the relative abundance ^{12}C in a given cluster series and the cluster size as parameters of the distribution.

Cluster	Ion mass	Energy 2E		Energy 28E	
		% ^{12}C	Intensity ratio	% ^{12}C	Intensity ratio
C_3^-	36	74.6	1.34	51.7	2.24
	37		0.51		0.54
	38		0.90		0.56
	39		6.06		2.45
C_4^-	48	70.7	1.80	55.0	3.27
	49		0.50		0.59
	50		0.59		0.45
	51		1.42		0.72
	52		12.7		5.3
C_5^-	60	75.3	1.96	55.5	5.89
	61		0.44		0.62
	62		0.47		0.32
	63		1.05		0.42
	64		4.50		1.25
	65		65		11.7
C_6^-	72	74.3	2.52	60.6	5.94
	73		0.52		0.79
	74		0.43		0.38
	75		0.70		0.39
	76		1.97		0.74
	77		10.4		2.74
	78		147		32.5

Positive cluster ions, generated after a two step laser perforation of the bilayer sample

Mass interferences caused by elements as e.g. Mg and K in the positive ion mode spectra prevented a straightforward interpretation of the results, because homogenization and recombination can occur during and shortly after the first laser shot. However, spectra recorded after two consecutive laser shots had been fired into the same sample area, yielded interference free spectra, that showed the same general features as reported for the negative ions e.g., the overall intensity of the mixed isotope clusters $^{12}C_{n-m}{}^{13}C_m^+$ (with $1 \leq m \leq n-1$) increased with increasing cluster size n.

4.3.3 Single laser shot perforation of spatially separated foils.

For the measurements on the spatially separated foils, the ^{13}C-layer was mounted toward the acceleration potential of the mass spectrometer. The laser beam was focused on the ^{13}C-layer. This resulted in a large perforation in the carbon ^{12}C-foil and a small perforation in the ^{13}C-foil. The ions generated from the ^{12}C-foil, had to pass through the 2 μm diameter perforation in the ^{13}C-foil in order to get into the mass spectrometer. Figures 11. a and b show typical spectra, recorded under these conditions. The mass resolution in these spectra is very poor because the ions are generated from areas with a different distance from the accelerating voltage. These spectra also show clusters with mixed isotopic composition as a result of recombination between atoms from the two spatially separated foils. Hence, it can be concluded that direct contact between the two foils is not a prerequisite for the formation of recombination clusters what leads to the conclusion that interaction in the gas phase can also play a determining role for the final isotopic composition of the clusters.

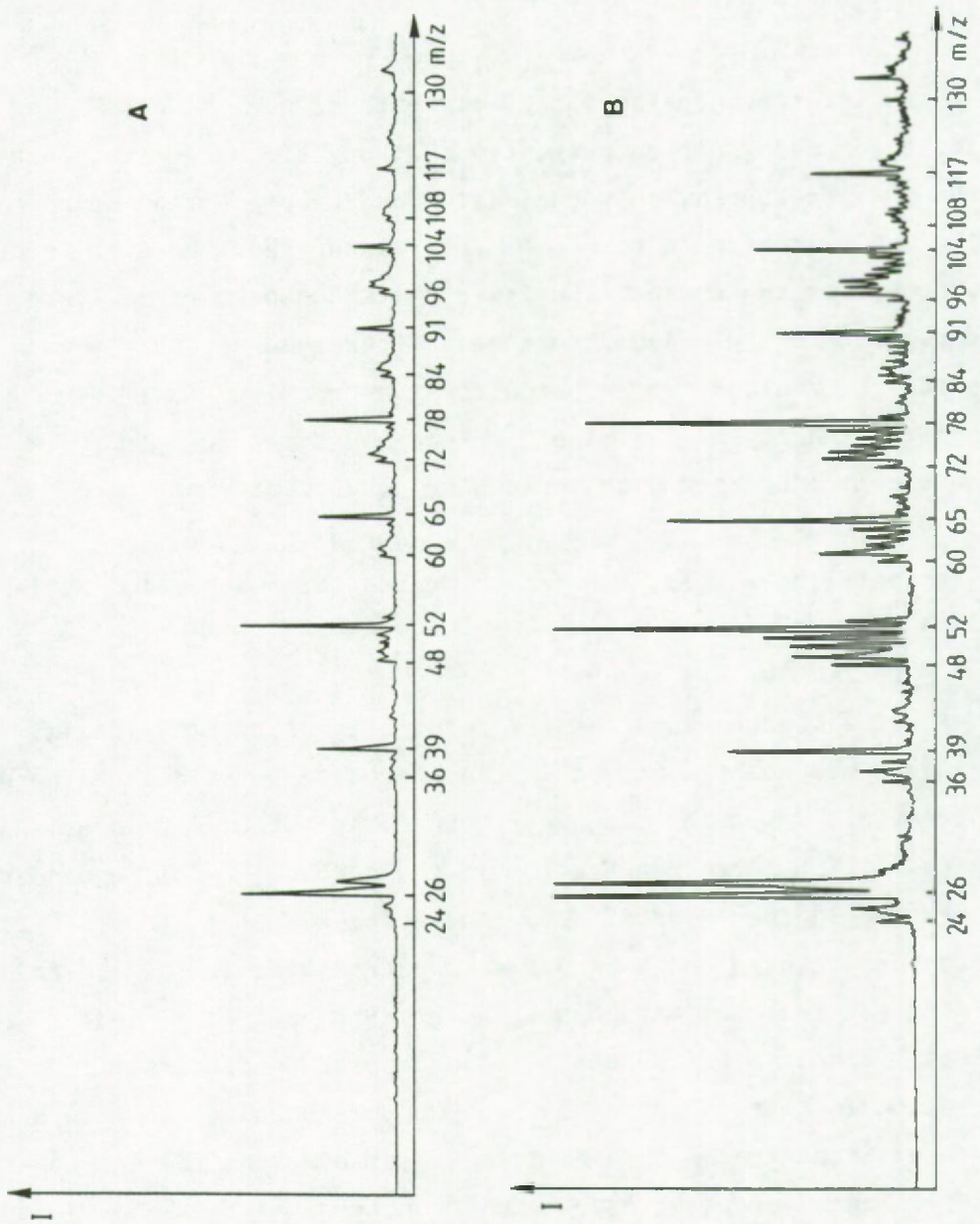

Figure 4.11a and b: Typical negative mode LAMMA-spectra from spatially separated ^{12}C and ^{13}C-foils, recorded with different sensitivity, namely with input ranges of 0.5 V and 0.1 V, respectively (in the second spectrum, the largest mass peaks are in overflow).

4.4 REFERENCES

1. N. Fürstenau, F. Hillenkamp, and R. Nitsche, Int. J. Mass Spectrom. Ion Phys., 31, 85 (1979).

2. N. Fürstenau and F. Hillenkamp, Int. J. Mass Spectrom. Ion Phys., 37, 137 (1981).

3. N. Fürstenau, Fres. Z. Anal. Chem., 308, 201 (1981).

4. T. Mauney and F. Adams, Int. J. Mass Spectrom. Ion Proc., 59, 103 (1984).

5. E. Michiels, A. Celis, and R. Gijbels, Int. J. Mass Spectrom. Ion Phys., 47, 23 (1983).

6. E. Michiels and R. Gijbels, Spectochim. Acta. 38B, 1347 (1983).

7. E. Michiels and R. Gijbels, Anal. Chem., 56, 1115 (1984).

8. B. Shüler, F.R. Krüger, and P.Feigl, Int. J. Mass Spectrom Ion Phys., 47, 3 (1983).

9. E. Michiels and R. Gijbels, Mikrochim. Acta, III, 277 (1983).

10. F. Bruynseels and R. Van Grieken, Spectrochim. Acta, 38B, 853 (1983)

11. F. Bruynseels and R. Van Grieken, Anal. Chem., 56 ,871 (1984).

12. H.J. Heinen, Int. J. Mass Spectrom. Ion Phys., 38, 309 (1981).

13. D.M. Hercules, Pure & Appl. Chem., 55, 1869 (1983).

14. L. Van Vaeck, J. Claereboudt, J. De Waele, E. Esmans, and R. Gijbels, Anal. Chem., 57, 2944 (1985).

15. K.S. Pitzer and E. Clementi, J. Am. Chem. Soc., 81, 4477 (1959).

16. W. Ens, R. Beavis, and K.G. Standing, Phys. Rev. Lett., 50, 27 (1983)

17. J. Rosmarinowsky, M. Karas, and F. Hillenkamp, Int. J. Mass Spectrom. Ion Proc., 67, 109 (1985).

18. R.L. Kaufmann, H.J. Heinen, M.W. Shurmann, and R.M. Wechsung, in Microbeam Analysis-1979, ed. by D.E.Newbury, San Francisco Press, San Francisco, 1979, p.63.

19. N. Fürstenau, Ph.D. Thesis, J.W Goethe Universität, Frankfurt-am-Main, B.R.D. (1981).

CHAPTER 5. LASER MICROPROBE MASS SPECTROMETRY OF INORGANIC SALT PARTICULATES

5.1 INTRODUCTION

The chemical characterization of individual particles is important in a variety of fields, in aerosol chemistry and geochemical research on sediments and suspensions as well as for industrial applications. Most of the conventional analytical techniques provide information about the bulk elemental composition of a particulate sample, but not about the distribution of the elements over and within the particles, nor about the stoichiometry of the compounds present. This information is fundamental to assess the origin of a particle and the physico-chemical transformations it has gone through.

Laser microprobe mass analysis is one of the novel techniques that allow analysis of single particles or microscopic samples with a favourable sensitivity. LAMMA can be used for structural analysis, since in addition to the atomic mass peaks, many cluster ions appear in the mass spectrum that could be useful for structural identification of compounds at a microscopic size level. Table 5.1 gives an overview of the other analytical techniques that can be applied in the field of individual particle analysis.

Qualitatively LAMMA-spectra are very similar to static SIMS-spectra (1.2). Since in static SIMS (the mode normally used to gain structural information) use is made of a defocused low ion dose beam, LAMMA has a superior lateral resolution (0.5-1.0 μm). Also the high speed of analysis makes it potentially more interesting for single particle characterization. Also the ease of sample preparation and the possibility to use electrically non-conductive samples is a major advantage of LAMMA compared to SIMS. XPS and Auger electron spectroscopy (AES) could be regarded as a good

alternative to gain chemical state information, but for these techniques the depth resolution is so high that minor changes in the outer atomic layers of the particles, possibly caused by e.g. sample storage and sample preparation will lead to different results. Also the lateral resolution of XPS is poor compared to LAMMA. AES has also the disadvantage to require thermally stable samples, and long data acquisition times so that the surface can be altered

Table 5.1: Analytical techniques for particle microanalysis
(R.W. Linton, personal communication)

MICROPROBE TECHNIQUE	LATERAL RESOL.[a]	DEPTH RESOL.[b]	ELEMENT CONC. DETECTION LIMITS	CHEMICAL STATE INF.	ISOTOPIC INF.
XPS (small spot)	-	+	-	+	-
Auger	+	+	-	0	-
Electron	0	-	+/-	-	-
Laser	0	0	+	0	+
keV Ion (SIMS)	0	+	+	0	+
MeV Ion:					
- RBS	0	+	+/-	-	-
- NRA	0	-	+/-	-	+
- PIXE	0	-	+/-	-	-
Raman	0	*	-	+	-

[a]scale: + ≈ 0.1 μm; 0 ≈ 1 μm; - ≈ 100 μm

[b]scale: + ≈ 0.01 μm; 0 ≈ 0.1 μm; - > 1 μm

*: highly dependenant on the transparency of the matrix

during irradiation. Also the high vacuum in the sample chamber can result in the loss of many volatile compounds. Compared to the Raman probe, LAMMA has the advantage to give simultaneously information about the speciation of the matrix as well as about the trace

elements associated with this particle. However because of the destructive nature of the LAMMA-technique, the interpretation of the spectra is not always straightforward because every particle, that can be regarded as unique can only be analyzed once. Therefore, for clearcut problem solving none of these techniques is capable of providing all the information that is needed and a combined study with several instruments is mostly indispensible. The major drawback of individual particle analysis in general is the difficulty to obtain statistically meaningful results within a reasonable period of time, that can be extrapolated to the whole particle population. This can be done by automated electron probe X-ray microanalysis (EPMA). Therefore because of their complementary features combination of LAMMA with EPMA offers a powerful tool to analyse particulate matter on an individual particle basis.

5.2 CLUSTER ION DISTRIBUTION OF CALCIUM OXIDE AND CALCIUM SALTS

In this section LAMMA-spectra of calcium-oxy-salts and CaO will be discussed. Ca-compounds are frequently detected in aerosol samples and they can originate from both continental, marine as well as anthropogenic sources.

The composition and relative intensities of these cluster ions are examined in order to find the relationship between the mass spectral pattern and the original compound stoichiometry, and to contribute to the understanding of the laws that govern ion formation by laser irradiation of solids.

5.2.1 Sample preparation

Analytical grade powders of $CaSO_4$, $CaCO_3$, $CaSO_4.2H_2O$ and CaO were ground with an agate mortar and pestle to particles of micrometer-size. The sample was prepared by contacting the fine powder with a Formvar coated grid. The measurements were performed

on particles of about 2 μm diameter.

5.2.2 Results and discussion

Figure 5.1a shows the negative cluster ions emitted by $CaSO_4$ particles under pulsed laser irradiation (energy = 1μJ). The characteristic mass peaks are O^-, OH^- (m/z = 16, 17), S^- and O_2^- (m/z = 32), SO^-, SO_2^-, SO_3^-, SO_4^- (m/z = 48, 64, 80, 96),CaO^- (m/z = 56), CaO_2^-, CaO_2H^- (m/z = 72, 73). The presence of the O_2^- ion is confirmed by its appearance in the negative $CaCO_3$ spectrum (Figure 5.1b). The other cluster ions in the $CaCO_3$ spectrum are C^- (m/z = 12), O^-, OH^- (m/z = 16, 17), C_2^-, C_2H^- (m/z = 24, 25), CaO^-, CaO_2^- (m/z = 56, 72). CaO shows characteristic mass peaks (Figure 5.1c) at O^- (m/z = 16), O_2^- (m/z = 32), CaO^-, CaO_2^- (m/z = 56, 72). Although the presence of a sulfur oxyanion can easily be established, the distinction between $CaCO_3$ and CaO may be difficult: experience has shown that the $C_2H_n^-$-cluster cannot be used as a diagnostic peak since it can easily be formed from a wide variety of carbonaceous compounds. The positive ion spectra of the compounds under examination are qualitatively the same and offer the possibility to make a quantitative comparison of the cluster ion intensities.

As seen in Figure 5.2, three different cluster series are observed: $Ca(CaO)_n^+$, $(CaO)_n^+$ and $(CaO)_nH^+$. The calcium ions appear predominantly in the positive spectrum and they are largely associated with oxygen and other calcium atoms.

The relative intensities of the cluster ions can be evaluated with the empirical model as described by Plog et al. (3) for ions with the general formula $M_mO_n^q$. This model, that was initially developed for the evaluation of static SIMS measurements, is also applicable to laser induced ion emission data: this was for the first time demonstrated via the relative ion distributions of silica samples (4). For describing the cluster ions with different atomic composition by a uniform parameter, the fragment valence K of a

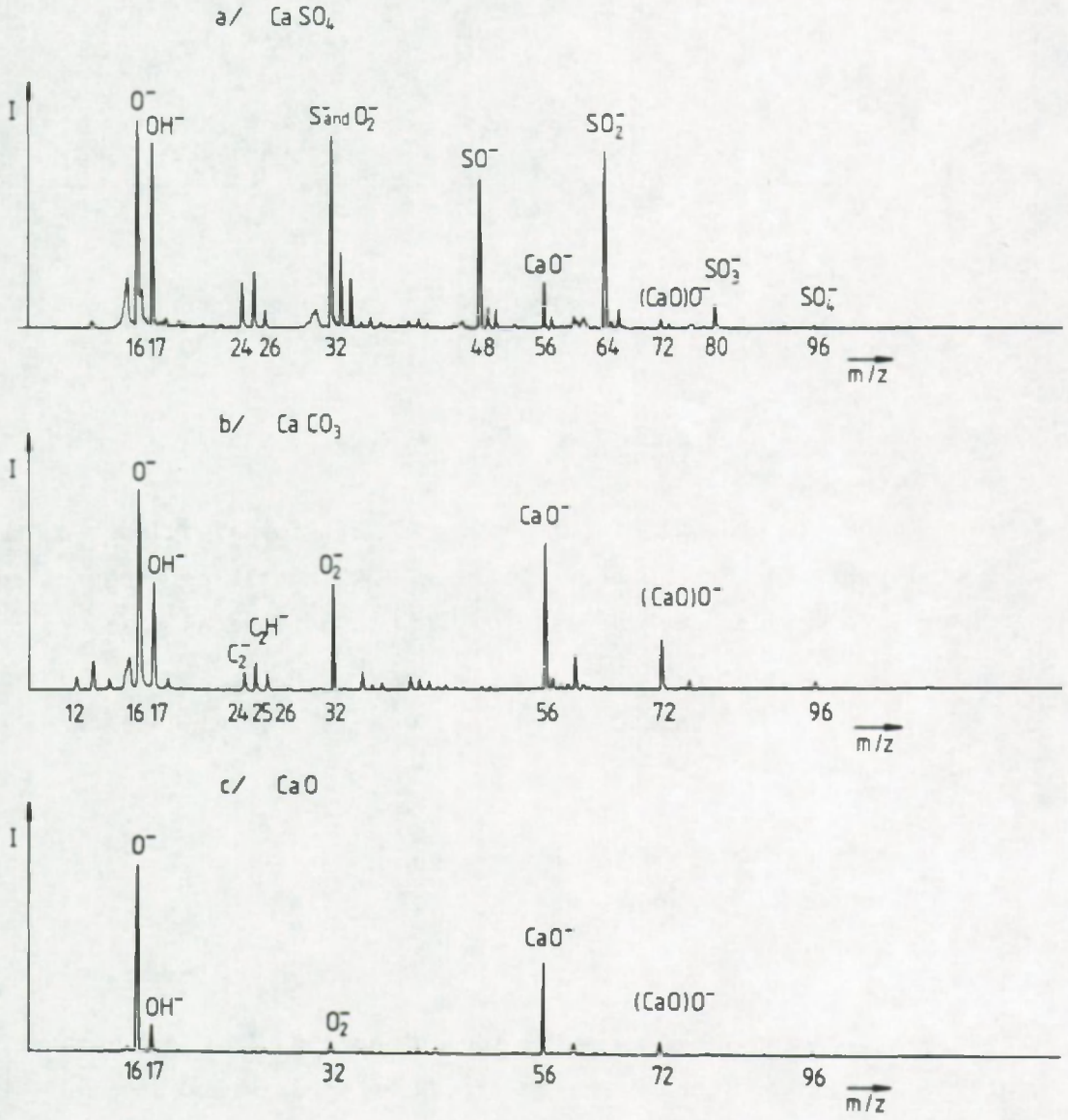

Figure 5.1: Negative mode LAMMA-spectra of

(a) $CaSO_4$

(b) $CaCO_3$

(c) CaO

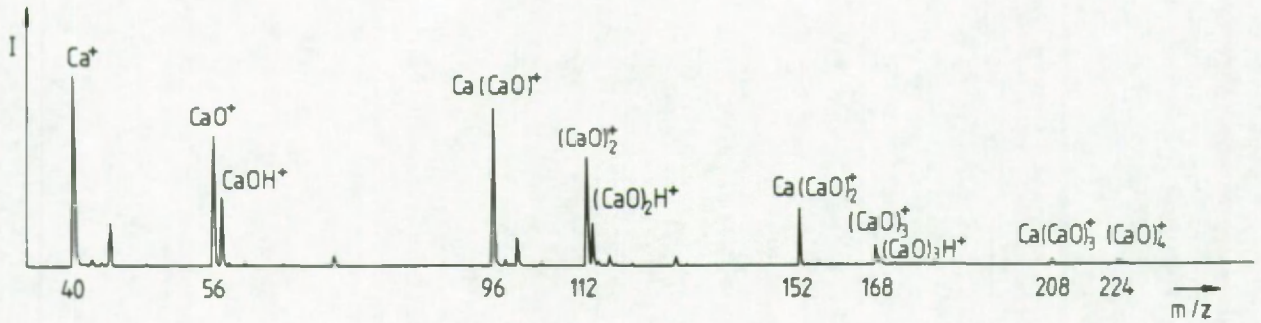

Figure 5.2: Positive ion mode LAMMA-spectrum of $CaSO_4$

metal atom in an emitted fragment, i.e. its formal valence number, is of importance. K can be calculated by ascribing the valence number 2 to oxygen. For the ion $M_mO_n^q$, K is defined as (3):

$$K = \frac{q + 2n}{m} \qquad \text{(eq. 5.1)}$$

with q: total charge of the cluster ion
n: number of oxygen atoms
m: number of metal atoms

For positive ions, the relative ion intensities $I^+(K)$ as a function of the fragment valence K can be fitted by a Gaussian curve of the form (3):

$$I^+(K) = I^+_{max}.\exp\,[-(K-G^+)^2/2\gamma^2] \qquad \text{(eq. 5.2)}$$

with I^+_{max}: maximum of the distribution
G^+: K-value of maximum of the curve
γ^2: variance of the intensities

In the spectra of the calcium compounds under investigation, for a given m number, only 2 cluster ions are present with different n number, namely n = m-1 and n = m, so that a fitting for constant m-value as done for static SIMS-data (3) is not meaningful. However, in LAMMA the m-value varies over a wider range and it becomes clear that the cluster ion distributions of the series $Ca_mO_{m-1}^+$ and $(CaO)_m^+$ are well fitted by a Gaussian curve as a function of K i.e. by a parabola in a semilog plot. M, the mass of the cluster ions is of course, equal to M = 40m + 16n. For the major cluster ion series $Ca_mO_n^q$, the function K can be expressed as:

$$K = \frac{2m - 1}{m} = \frac{2M - 24}{M + 16} \quad \text{for } m = n + 1,\ q = +1 \qquad \text{(eq. 5.3)}$$

$$K = \frac{2m + 1}{m} = \frac{2M + 56}{M} \quad \text{for } m = n,\ q = +1 \qquad \text{(eq. 5.4)}$$

$$K = \frac{2m - 1}{m} = \frac{2M - 56}{M} \quad \text{for } m = n,\ q = -1 \qquad \text{(eq. 5.5)}$$

$$K = \frac{2m + 1}{m} = \frac{2M + 24}{M - 16} \quad \text{for } m = n - 1,\ q = -1 \qquad \text{(eq. 5.6)}$$

For both the series $(CaO)_mH^+$ and $(CaO)_mOH^-$, the fragment valence K is equal to 2, if one ascribes the valence number +1 to hydrogen.

For $(CaO)_m^+$ and $Ca_mO_{m+1}^-$, and for $Ca_mO_{m-1}^+$ and $(CaO)_m^-$, the same functions ,represented in Figure 5.3, are described for equal m-values. In this regard, the two series are equivalent. However, from the experimental data, as shown in Figure 5.1 and 5.2 and Table 5.2, it is seen that higher molecular clusters appear almost exclusively in the positive mode spectrum.

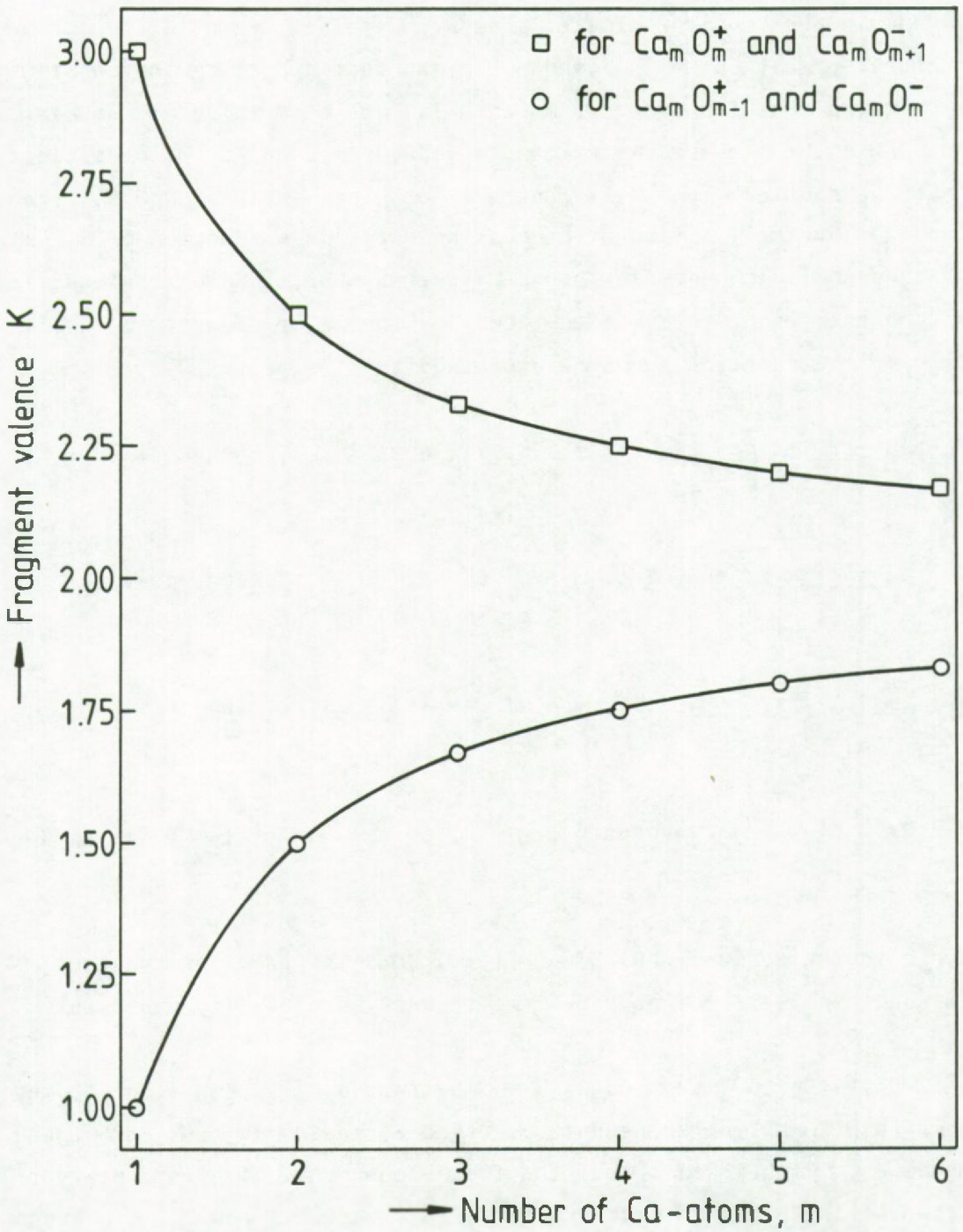

Figure 5.3: Dependence of the fragment valence on the number of calcium atoms in the different cluster ion series.

Table 5.2: Average intensities of the positively charged cluster ions, normalized to the Ca^+-peak.

			Ion intensities from				
Ion	m/z	K	$CaCO_3$	$CaSO_4.2H_2O$	$CaSO_4$	CaO	CaO.anhyd.
Ca^+	40	1.00	$1.0\ 10^{0}$	$1.0\ 10^{0}$	$1.0\ 10^{0}$	$1.0\ 10^{0}$	$1.0\ 10^{0}$
CaO^+	56	3.00	$5.8\ 10^{-1}$	$5.9\ 10^{-1}$	$5.5\ 10^{-1}$	$3.5\ 10^{-1}$	$1.8\ 10^{-1}$
$(CaO)H^+$	57	2.00	$1.7\ 10^{-1}$	$5.4\ 10^{-1}$	$2.2\ 10^{-1}$	$7.1\ 10^{-1}$	$1.0\ 10^{-1}$
$Ca(CaO)^+$	96	1.50	$6.3\ 10^{-1}$	$4.8\ 10^{-1}$	$5.6\ 10^{-1}$	$8.4\ 10^{-1}$	$8.1\ 10^{-1}$
$(CaO)_2^+$	112	2.50	$3.6\ 10^{-1}$	$2.8\ 10^{-1}$	$3.6\ 10^{-1}$	$3.7\ 10^{-1}$	$1.8\ 10^{-1}$
$(CaO)_2H^+$	113	2.00	$6.3\ 10^{-2}$	$4.4\ 10^{-1}$	$1.3\ 10^{-1}$	$6.5\ 10_{-1}$	$7.8\ 10^{-2}$
$Ca(CaO)_2^+$	152	1.67	$1.3\ 10^{-1}$	$6.1\ 10^{-2}$	$1.1\ 10^{-1}$	$2.3\ 10^{-1}$	$1.4\ 10^{-1}$
$(CaO)_3^+$	168	2.33	$3.7\ 10^{-2}$	$2.3\ 10^{-2}$	$3.9\ 10^{-2}$	$6.2\ 10^{-2}$	$1.4\ 10^{-2}$
$(CaO)_3H^+$	169	2.00	-	$9.2\ 10^{-2}$	$1.7\ 10^{-2}$	$2.1\ 10^{-1}$	-
$Ca(CaO)_3^+$	208	1.75	$1.7\ 10^{-2}$	$1.1\ 10^{-2}$	$1.7\ 10^{-2}$	$4.4\ 10^{-2}$	$1.0\ 10^{-2}$
$(CaO)_4^+$	224	2.25	$6.3\ 10^{-3}$	$6.9\ 10^{-3}$	-	$1.8\ 10^{-2}$	$2.0\ 10^{-3}$
$(CaO)_4H^+$	225	2.00	-	$2.3\ 10^{-2}$	-	$3.8\ 10^{-2}$	-
$Ca(CaO)_4^+$	264	1.80	-	$2.8\ 10^{-3}$	-	-	-
$(CaO)_5^+$	280	2.20	-	$1.6\ 10^{-3}$	-	-	-
$(CaO)_5H^+$	281	2.00	-	$4.7\ 10^{-3}$	-	-	-

The experimental data were fitted by polynomial regression analysis with the formula: $\ln I = a_0 + a_1K + a_2K^2$. The resulting parameters of the Gaussian distribution, according to equation 5.2, are given in Table 5.3. A graphical representation of the data for $CaSO_4.2H_2O$ is plotted in Figure 5.4. The values for G_1^+ of the $Ca(CaO)_n^+$ series and G_2^+ of the $(CaO)_n^+$ series are constant for all three calcium salts, namely:

$G_1^+ = 1.227 \pm 0.007$

$G_2^+ = 2.777 \pm 0.009$

The "lattice valence" (3), here defined as $G^0 = (G_1^+ + G_2^+)/2$, is equal to 2.002 ± 0.003 (0.2 %). The displacement parameter α, defined (3) as the difference between G^0 and G_1^+ or G_2^+, equals 0.775 in both cases. It is clear that the parameters of the curves are the same for the $Ca(CaO)_n^+$ and $(CaO)_n^+$ series and that their distributions only differ in the intensity at the maximum, I^+_{max}. The average for the three calcium salts normalized to the Ca^+-intensity amounts to: $I^+_{1max} = 2.56 \pm 0.33$ (13 %) for the $Ca(CaO)_n^+$, and $I_{2max} = 1.50 \pm 0.17$ (11 %) for $(CaO)_n^+$. The spectra of CaO show basically the same features, but the ratio I^+_{1max}/I^+_{2max} is larger than for the salts, especially in the absence of H-atoms, as can be seen in Table 5.2.

For the third series of cluster ions, $(CaO)_mH^+$, the fragment valence is always equal to 2. This K-value is equal to the experimental lattice valence and to the oxidation state of Ca in the considered compounds. The attachment of a proton gives rise to a relatively stable cluster ion that has a significant intensity even in the spectra of oven-dried samples. In the spectrum of $CaSO_4.2H_2O$, the $(CaO)_mH^+$ intensity is higher or equal to the $(CaO)_m^+$ intensity while for the $CaSO_4$ the reverse phenomenon is observed. This means that the hydrogen is predominantly supplied by the water molecules. Also for the $(CaO)_mH^+$ series the cluster ion intensity decreases about exponentially with the cluster ion mass.

Table 5.3: Parameters of the fitting of a Gaussian according to eq.(5.2) through the experimental data of Table 5.2: for the series: 1 = $Ca(CaO)_m^+$ and 2 = $(CaO)_m^+$.

Compound	γ_i^+	G_i^+	I_{imax}^+	r^2
$CaCO_3$	$\gamma 1^+ = 0.166$	$G_1^+ = 1.235$	$I_{1max}^+ = 2.68$	0.987
	$\gamma_2^+ = 0.157$	$G_2^+ = 2.771$	$I_{2max}^+ = 1.69$	0.999
$CaSO_4.2H_2O$	$\gamma_1^+ = 0.158$	$G_1^+ = 1.222$	$I_{1max}^+ = 2.63$	0.997
	$\gamma_2^+ = 0.168$	$G_2^+ = 2.778$	$I_{2max}^+ = 1.39$	0.998
$CaSO_4$	$\gamma_1^+ = 0.171$	$G_1^+ = 1.225$	$I_{1max}^+ = 2.36$	0.999
	$\gamma_2^+ = 0.166$	$G_2^+ = 2.773$	$I_{2max}^+ = 1.41$	= 1
CaO	$\gamma_1^+ = 0.180$	$G_1^+ = 1.248$	$I_{1max}^+ = 2.58$	0.987
	$\gamma_2^+ = 0.175$	$G_2^+ = 2.746$	$I_{2max}^+ = 1.00$	0.999
CaO.anhyd.	$\gamma_1^+ = 0.147$	$G_1^+ = 1.253$	$I_{1max}^+ = 5.48$	0.980
	$\gamma_2^+ = 0.145$	$G_2^+ = 2.748$	$I_{2max}^+ = 0.81$	0.999

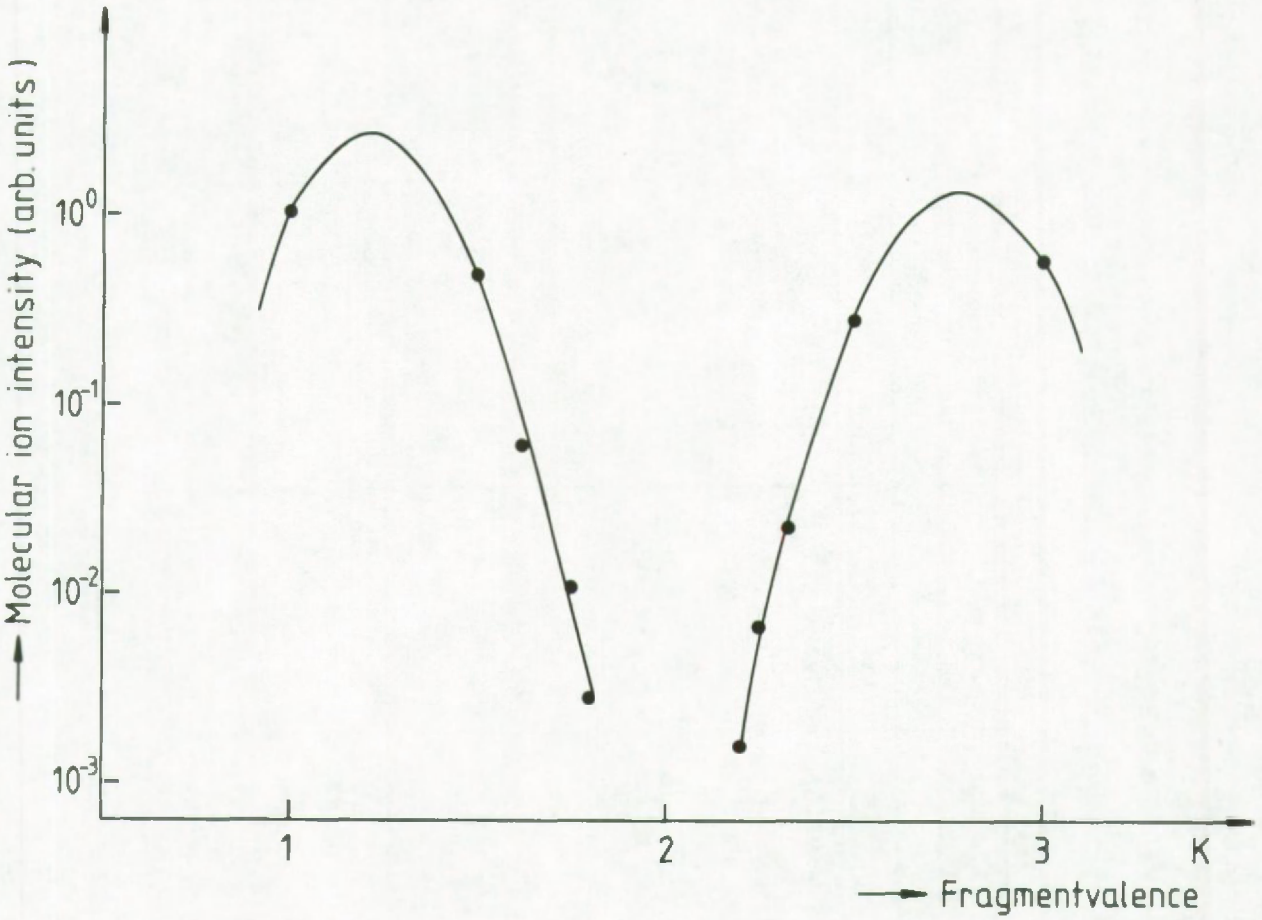

Figure 5.4: Cluster ion intensities for the series $Ca_mO_{m-1}^+$ at left, and $(CaO)_m^+$, at right. as emitted for laser irradiation of $CaSO_4.2H_2O$.

The $(CaO)_m^+/(CaO)_mH^+$ intensity ratio remains essentially constant for the higher m-values and this suggests that there is a correlation between the $(CaO)_m^+$ and the $(CaO)_mH^+$ formation. The high intensities of the $(CaO)_mH^+$-cluster ions in the CaO-spectrum in comparison to the spectrum of anhydric CaO indicate the importance of the hydrogen atoms for the cluster ion distribution and the Ca-to-O ratio of the cluster ions. For increasing m number the K(m) functions approach the fragment valence value of 2 what favours the formation of higher mass cluster ions. These higher mass clusters are not a direct fragment of the original compound but are the results of chemical reactions that take place during the short laser irradiation. The appearance of the same cluster ion series in the spectra of $CaSO_4$, $CaCO_3$ and CaO can be due to the rapid formation of CaO by the following reactions (5):

$CaCO_3 \longrightarrow CaO + CO_2$ T = 990°C, in O_2

$CaSO_4 \longrightarrow CaO + SO_3$ T = 900 - 1034°C, in CO_2

For the negative ions of $CaSO_4$, the following relative intensities were found on the average; S^-: 1.04 (m/z = 32), SO^-: 0.80 (m/z = 48), SO_2^-: 1.00 (m/z = 64), SO_3^-: 0.24 (m/z = 80), and SO_4^-: 0.01 (m/z = 96). The high intensity of the peak with mass 32 can partially be due to the presence of O_2^- (m/z = 32). Applying the model of Plog at al. (3) to the cluster ions of SO_n^-, with n ranging from 1 to 4, yields the following parameters for the Gaussian distribution: $G^- = 2.29$, $\gamma^- = 1.53$, $I^-_{max} = 1.13$ and $r = 0.999$.

5.2.3 CONCLUSION

The model of Plog et al. (3) can be used for describing the cluster ion distribution for constant number of metal ions (6-8), but also for the series $(CaO)_m^+$ and $Ca_mO^+_{m-1}$ with simultaneously varying numbers of metal and oxygen atoms. The series $(CaO)_mH^+$ has a

constant fragment valence value of 2, that is equal to the limit value of the K(m) function, to the lattice valence and to the oxidation state of Ca in the compounds. The intensity of those series is dominated by the H-content of the sample and therefore it is very high for hydrated compounds.

5.3. THE IDENTIFICATION OF SULFUR SPECIES IN SINGLE MICROMETER-SIZE PARTICLES.

Positive and negative mode LAMMA spectra of particles of micrometer-size of sodium-oxy-salts with a different stoichiometric sulfur-to-oxygen ratio, namely sulfate, sulfite and thiosulfate, were examined with the aim of checking whether information about the sulfur speciation can be derived from the LAMMA cluster ion intensity distribution. The fingerprint spectra of other sulfate compounds such as $NaCH_3SO_3$, $CaSO_4$, $MgSO_4$, K_2SO_4, $(NH_4)_2SO_4$ and $CuSO_4$ will also be briefly discussed.

Sulfur compounds are very important atmospheric constituents, since in clean tropospheric air as well as in the stratosphere, the majority of aerosol particles is composed of various types of sulfates. The study of the atmospheric sulfur cycle is a rapidly expanding field because human activity provides an important sulfur dioxide source that can possibly disturbe the natural atmospheric equilibrium. In the atmosphere, SO_2 is converted to sulfate containing aerosol particles which can modify the radiation balance of the earth-atmosphere system, the optical properties and the precipitation forming ability of the air.

Chemical tests have been developed for the determination of sulfate in individual aerosol particles (9-12). However, further research about suitable and sequential tests is needed to reduce ambiguities and to explore the range of interfering substances for each test. Therefore the introduction of novel analytical techniques as the laser microprobe mass analyser for the identification of the

sulfur species in individual micrometer-size particles can contribute to the elucidation of the transformation mechanisms governing the fate of sulfur compounds in the atmosphere.

5.3.1 Results and discussion

Negative ion mode

The major negative ions detected in the LAMMA mass spectrum of Na_2SO_4, Na_2SO_3, $Na_2S_2O_3$ and $NaCH_3SO_3$ are:

O^-, OH^-, O_2^-		m/z = 16, 17, 32
SO_n^-	(n = 0 to 4)	m/z = 32, 48, 64, 80, 96
$NaSO_n^-$	(n = 3,4)	m/z = 103, 119

The relative intensities of the SO_n^- (n = 1 to 4) cluster ions are listed in Table 5.4. Since all these ions appear in the spectra of each of the sulfur-oxy-compounds, their mere presence is no direct indication of the sulfur speciation. The occurrence of SO_n^- ions with different S oxidation states, does not neccesarily reflect the presence of different sulfur-oxy-salts in the sample, in contrast to such suggestions in the literature (13,14). The intensity ratios do not differ very drastically for the three salts. Yet the low SO_4^-/SO_2^- ratio seems to be indicative for Na_2SO_3 while the SO^-/SO_2^- ratio is distinctly higher for $Na_2S_2O_3$.

If one wants to use these criteria for the identification of the sulfur salts, the laser energy has to be carefully controlled because shifts in the SO_n^- intensity distribution can also be caused by differences in the laser energy density used for sample excitation. This is clearly illustrated in Figure 5.5 which shows the negative cluster ion distribution of $MgSO_4$ recorded at 3 different laser excitation energies. Higher laser irradiances give rise to more fragmentation.This results in a lower SO_3^- intensity and increased SO^- and S^- cluster ion intensities.

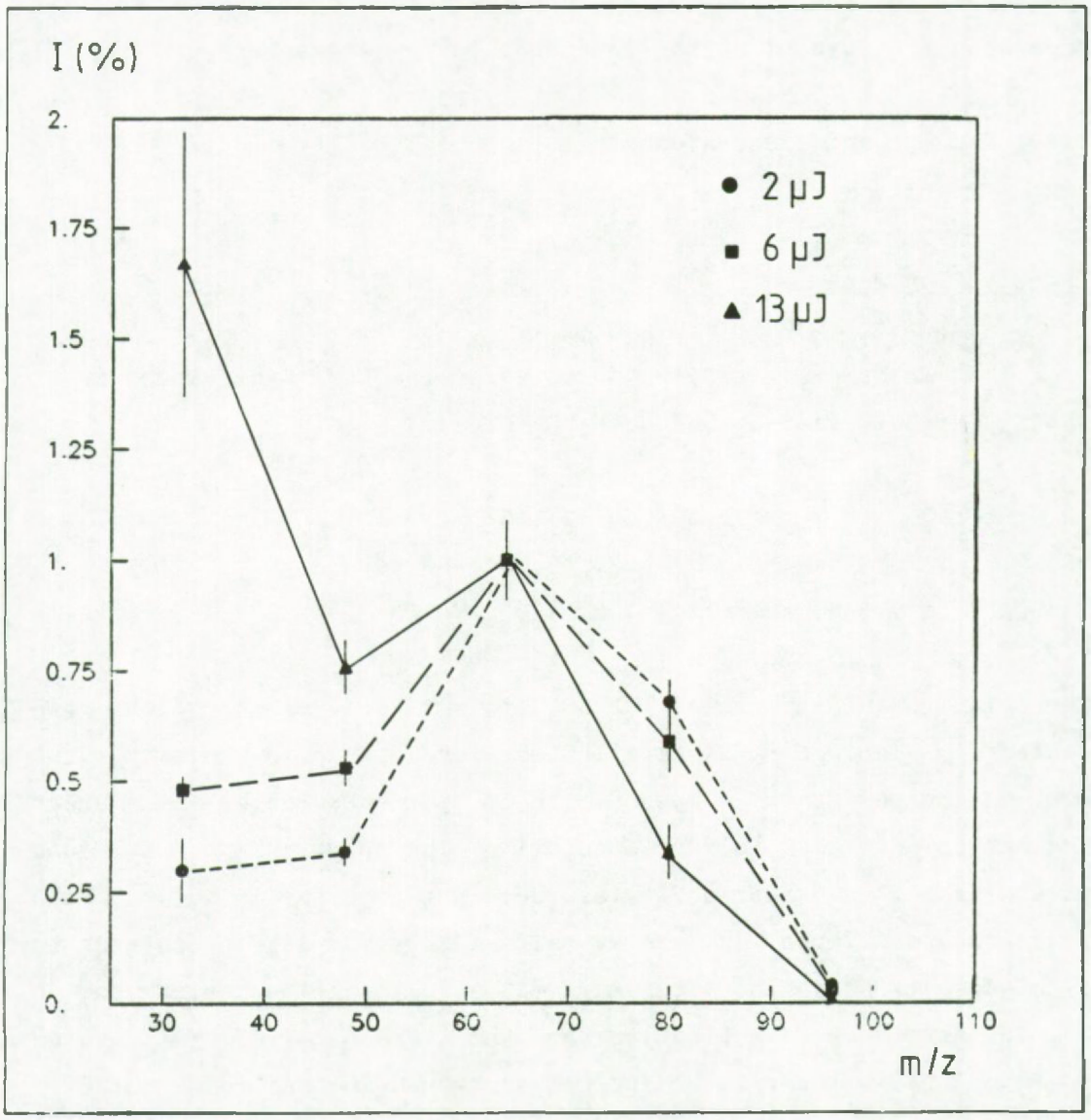

Figure 5.5: Cluster ion intensities as a function of m/z for $MgSO_4$, recorded for 3 different laser irradiances of 2 μJ, 6 μJ and 13 μJ. The intensities are the average of six measurements; they have been normalized to the m/z = 64 mass peak and the error bars represent the standard deviations

Table 5.4: Negative ion intensities. Relative intensities (I_R) of the SO_n^- (n = 1 to 4) cluster ions for Na_2SO_4, Na_2SO_3 and $Na_2S_2O_3$, normalized to the SO_2^--cluster intensity (laser energy = 2 μJ).

m/z	cluster ion	$I_R(Na_2SO_4)$	$I_R(Na_2SO_3)$	$I_R(Na_2S_2O_3)$
48	SO^-	0.32 ± 0.03*	0.23 ± 0.02	0.49 ± 0.04
64	SO_2^-	1.00	1.00	1.00
80	SO_3^-	0.79 ± 0.06	0.67 ± 0.05	0.80 ± 0.07
96	SO_4^-	0.21 ± 0.05	0.06 ± 0.02	0.20 ± 0.05

* standard deviation on the average

For $NaCH_3SO_3$ the identification is facilitated by the presence of the intense $CH_3SO_3^-$-cluster ion at m/z = 95 that represents the intact anion of the salt (see Figure 5.6). An accompanying mass peak at m/z = 94 resulting from the loss of one hydrogen atom is also seen.

In SIMS, the cluster ion intensity distribution can be representative for the sulfur speciation, as was demonstrated by Ganjei et al. (1). Using Plog's empirical model (3), they fitted the distribution of the relative intensities I^- of SO_n^- (n = 1 to 4) cluster ions, as function of the fragment valence K = q + 2n (with q: charge of the ion, n: number of oxygen atoms in the cluster ion) according to equation 5.2(p. 106).

The parameters describing the fitting of the present experimental data for the sulfur-oxy-salts are listed in Table 5.5. The relatively small range of G^- and γ^- values for the SO_n^- distributions of the three compounds, makes a reliable identification by these parameters not straightforward because the differences are within or close to the experimental errors. For the

SIMS measurements G^- = -1.3 for SO_3^{2-} and G = +1 for SO_4^{2-} and γ equals 2.7 ± 0.1 for both anions (1). In LAMMA, the distributions have smaller γ-values (narrower distribution) and higher G-values what reflects a lower degree of fragmentation of the original chemical bounds in LAMMA compared to SIMS. The data for $NaCH_3SO_3$ could not be appropriatly fitted by Plog's model what can be due to the presence of the methyl group in the salt. For $Na_2S_2O_3$ one of the S-atoms is readily lost (see also below) and therefore the Gaussian distribution of the SO_n^--cluster appears in the spectra as it is the case for sodium-sulfur-oxy-salts.

Table 5.5: Parameters of the Gaussian distributions fitting the relative intensities of the SO_n^- (n = 1 to 4) cluster ions as a function of the fragment valence (laser energy = 2 μJ).

Compound	G^-	γ^-
Na_2SO_4	3.7 ± 0.4*	1.8 ± 0.1
Na_2SO_3	3.6 ± 0.3	1.5 ± 0.1
$Na_2S_2O_3$	3.5 ± 0.5	2.0 ± 0.2
$CaSO_4$	2.3 ± 0.2	1.6 ± 0.1
$CuSO_4$	4.8 ± 1.0	3.0 ± 0.6

* standard deviation on the average

It appeared that at constant laser energy of 2 μJ the SO_n^- distribution depends more on the salt cation than on the sulfur speciation, e.g. G^- = 2.3 for $CaSO_4$ (see section 5.2), G^- = 3.7 for Na_2SO_4 and G^- = 4.8 for $CuSO_4$. In the case of $(NH_4)_2SO_4$, the negative mode LAMMA spectrum is completely changed and the predominant peak becomes $(HSO_4)^-$ (m/z = 97), as has already been reported (13,14); this ion has a formal valence, corresponding to the oxidation state of sulfur in the original salt, which provides H-atoms abundantly.

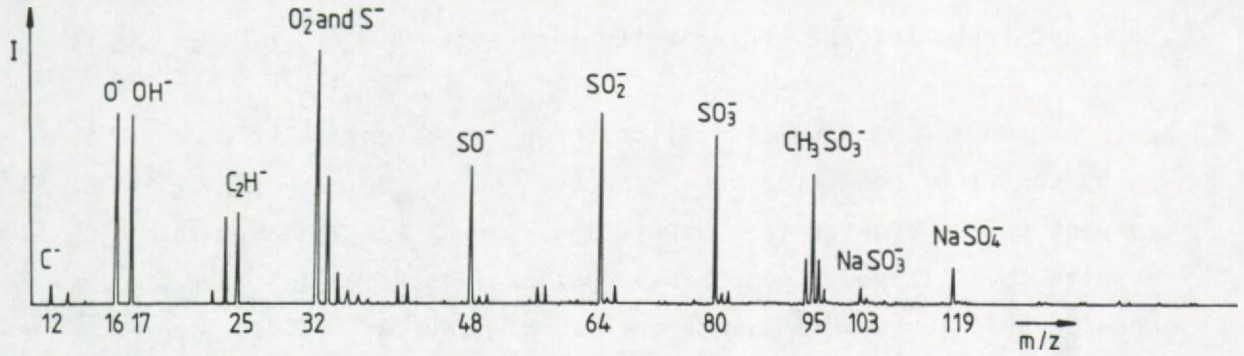

Figure 5.6: Typical negative mode LAMMA-spectrum of $NaCH_3SO_3$.

Positive ion mode

The positive spectra of the sulfur salts show cluster ions with the following composition:

Na_n^+	(n = 1, 2)	m/z = 23, 46
NaO^+		m/z = 39
$Na_2O_n^+$	(n = 1 to 3)	m/z = 62, 78, 94
$Na_3O_n^+$	(n = 1, 2)	m/z = 85, 101
$Na_2SO_n^+$	(n = 0 to 3)	m/z = 78, 94, 110, 126
$Na_3SO_n^+$	(n = 0 to 4)	m/z = 101, 117, 133, 149, 165

In some cases the exact cluster ion identification can be ambiguous. Indeed, the mass resolution of the LAMMA instrument does not allow to separarte an ion containing two oxygen atoms from another with one sulfur atom. The intensity of the corresponding ^{34}S containing cluster ion cannot always be indicative because of its low abundance and the limitations imposed by the transient recorder. Measurements on Na_2CO_3 showed that the dominant clusters in the spectrum are Na_2^+, $Na_2O_n^+$ (n = 1, 2), $Na_3O_n^+$ (n = 1, 2) and $Na_3CO_3^+$, (see section

5.5). In the $NaNO_3$ and $NaNO_2$ spectra, on the other hand, some minor mass peaks at m/z = 124 and m/z = 140 can be detected that were identified as $Na_4O_n^+$ (n = 2, 3) (see section 5.4). These clusters were not found for the sodium-sulfur-oxy-salts.

Marien and De Pauw (15-17) performed an extensive static SIMS study on the positive mode spectra of Na_2SO_4 and Na_2SO_3. With respect to the cluster ion composition, the LAMMA and static SIMS results are largely comparable. Since in static SIMS experiments considerably larger beam diameters (lower lateral resolution) are used, the measurements were done on salts that were compressed into pellets. In our LAMMA-experiments, however, the measurements were done on individual micrometer-size particles.

Also the sodium salt of methylsulfonic acid was studied by LAMMA because it plays an important role in the natural sulfur cycle (18) and its atmospheric behaviour is largely unknown. In the $NaCH_3SO_3$-spectra a mass peak at m/z = 141 appears that is identified as $Na_2CH_3SO_3^+$ and can be regarded as the cationized form of $NaCH_3SO_3$. This is the only mass peak that gives a direct indication of the methylsulfonate structure of the salt under investigation. Since H-atoms can be provided by the methyl group of the anion, the Na_2OH^+-cluster (m/z = 63) is more intense than the Na_2^+-cluster for the $NaCH_3SO_3$-spectra. For the other sulfur-oxy-salts the Na_2O^+-cluster is always more intense than the Na_2OH^--cluster. Typical LAMMA-spectra for Na_2SO_4, Na_2SO_3, $Na_2S_2O_3$ and $NaCH_3SO_3$ are given in Figures 5.7a to d. The relative cluster ion intensities (averages of six measurements) are represented in Figure 5.8a. A plot of the relative cluster ion intensities for $Na_2S_2O_3$ and $Na_2CH_3SO_3$ is shown in Figure 5.8b.

The most intense mass peak in the $Na_2S_2O_3$ spectrum is attributed to Na_3S^+; in view of the low intensity of this mass peak in the Na_2SO_4 and Na_2SO_3 spectra it is suggested that the sulfur atoms in Na_3S^+ are predominantly coming from the low valence sulfur in $Na_2S_2O_3$.

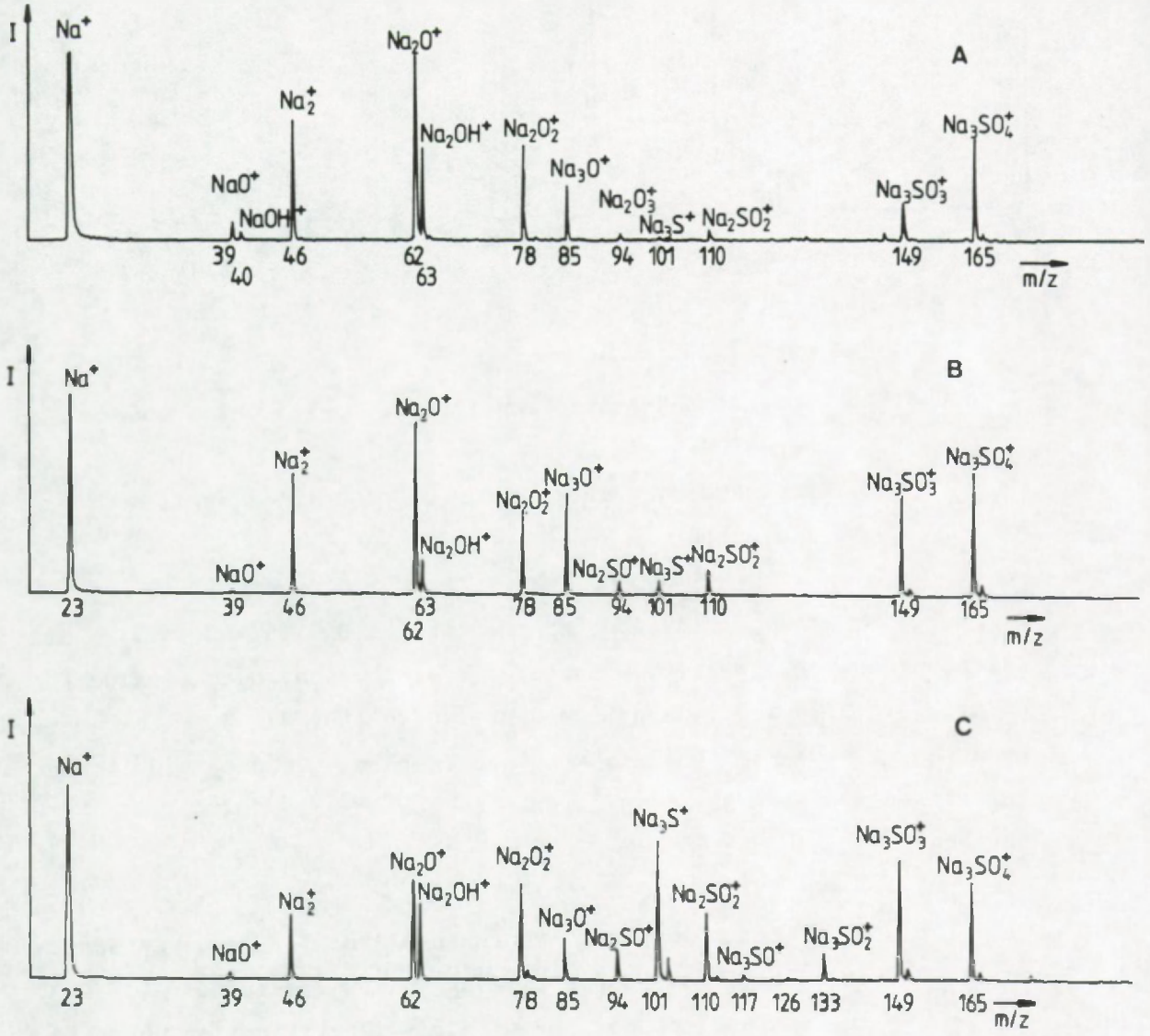

Figure 5.7: Typical LAMMA-spectra, in the positive ion mode, of:
(a) Na_2SO_4, (b) Na_2SO_3 and (c) $Na_2S_2O_3$
For each mass peak, the most plausible ion is indicated

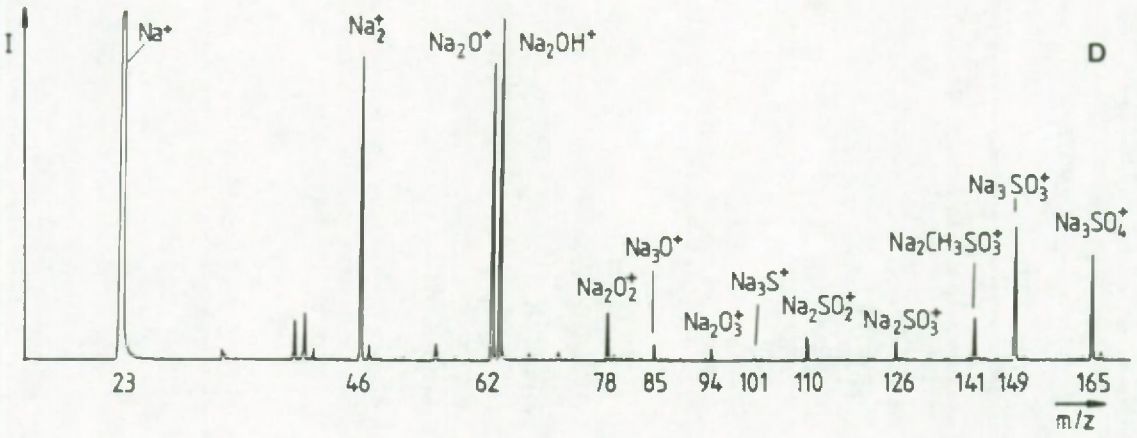

Figure 5.7.d: Typical LAMMA-spectrum, in the positive ion mode, of $NaCH_3SO_3$
For each mass peak, the most plausible ion is indicated

The low mass cluster ions of the type $Na_2O_n^+$ (n = 0 to 3), are fitted reasonably well by a Gaussian distribution, with a value for G^+ equal to 1.28 ± 0.04 and γ^+ = 0.96 ± 0.06 (for $Na_2S_2O_3$ the mass peak at m/z = 94 had to be disregarded because significant interference of the Na_2SO^+-cluster ion on the $Na_2O_3^+$-cluster is obvious).

The $Na_2O_n^+$-ions are not representative for a given sodium sulfur-oxy-salt (e.g. for Na_2CO_3 similar values are found: G^+ = 1.25 and γ^+ = 0.93) and cannot be used for identification purposes. Identical results were obtained for K-oxy-salts.

While thus the distributions of the sodium oxide ions are equivalent, the intensities of cluster ions as $(Na_3S)^+$ (m/z = 101), $(Na_2SO_2)^+$ (m/z = 110), $(Na_3SO_3)^+$ (m/z = 149) and $(Na_3SO_4)^+$ (m/z = 165) in a given spectrum appear to be very representative of the anion stoichiometry and to yield an unambiguous identification

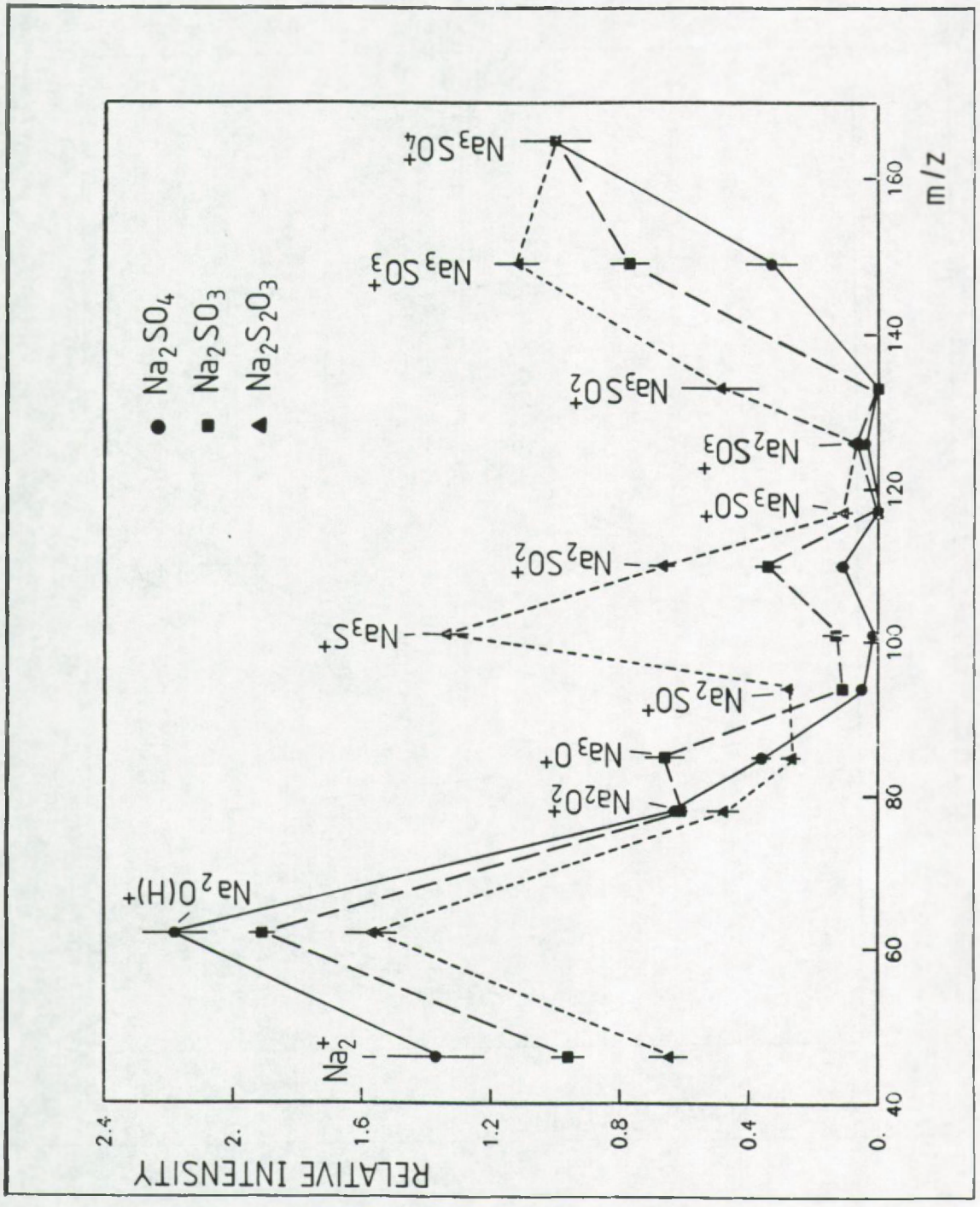

Figure 5.8a: Cluster ion intensities as a function of m/z for Na_2SO_4, Na_2SO_3 and $Na_2S_2O_3$. The intensities are the average of six measurements; they have been normalized to the m/z = 165 mass peak; the error bars represent the standard deviation of the mean.

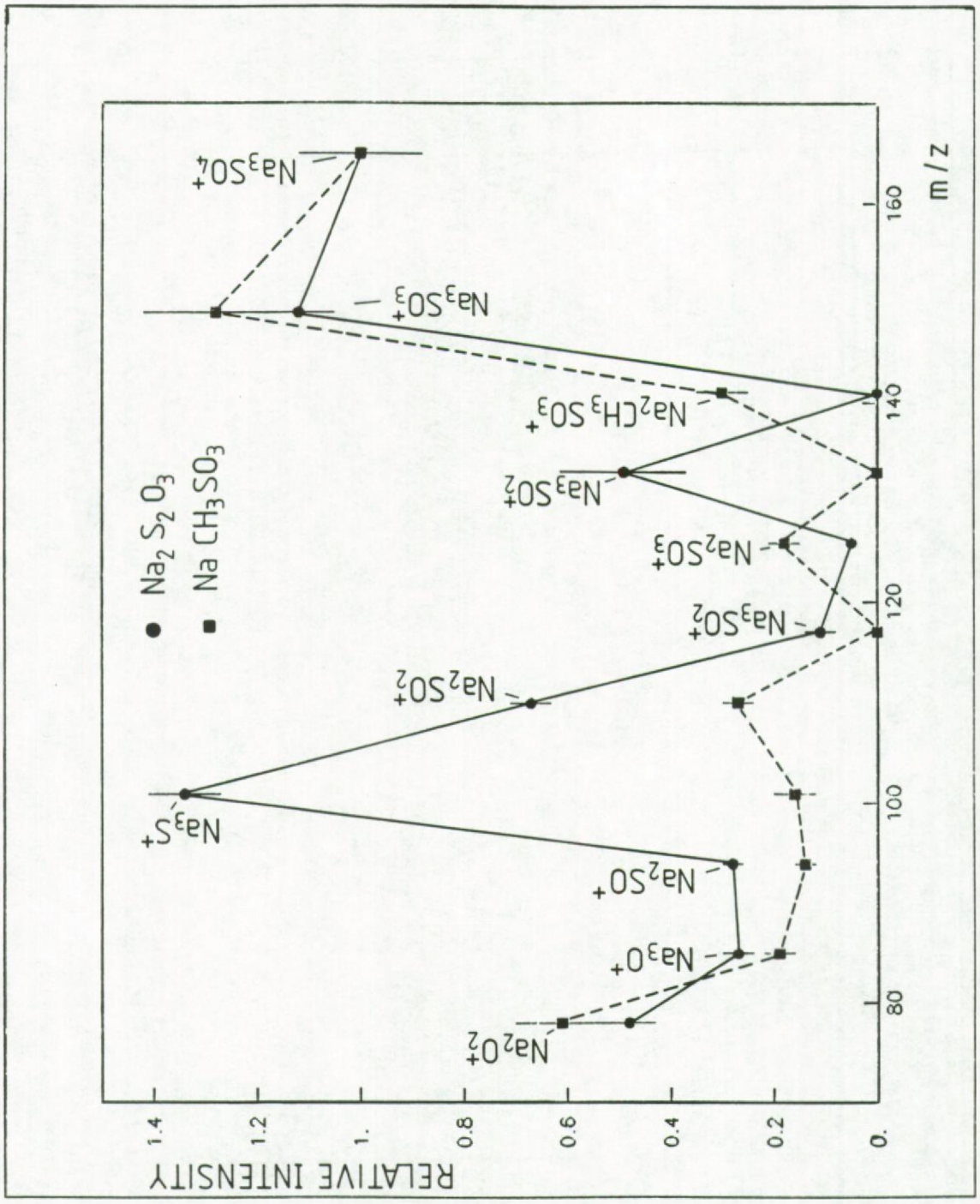

Figure 5.8b: Cluster ion intensities as a function of m/z for $NaCH_3SO_3$ and $Na_2S_2O_3$. The intensities are the average of six measurements; they have been normalized to the m/z = 165 mass peak; the error bars represent the standard deviation of the mean

criterion. Measurement of the $(Na_3SO_3)^+$ (m/z = 149) to $(Na_3SO_4)^+$ (m/z = 165) ratio as a function of the laser excitation energy (Table 5.6) showed that the laser energy is not a critical parameter, whose variability could confuse the identification. Also in this higher mass range the interference of other cluster ions is less probable than for the masses below m/z = 100 where fragment ions abundantly occur. Further confirmation of the salt speciation can even be provided by the intensity of the cluster ions $(Na_3S)^+$ (m/z = 101) and $(Na_2SO_2)^+$ (m/z = 110) that show an increasing intensity with increasing S to O ratio in the compound.

Table 5.6: Influence of the laser energy on the ratio R of the $Na_3SO_3^+$ to $Na_3SO_4^+$-cluster ion intensity for Na_2SO_4, Na_2SO_3 and $Na_2S_2O_3$

Laser Energy (in μJ)	$R(Na_2SO_4)$	$R(Na_2SO_3)$	$R(Na_2S_2O_3)$
0.7	0.28 ± 0.04*	0.84 ± 0.03	1.38 ± 0.07
1.0	0.23 ± 0.03	0.65 ± 0.05	1.10 ± 0.05
2.0	0.28 ± 0.03		1.05 ± 0.03
2.3	0.24 ± 0.02	0.76 ± 0.06	1.03 ± 0.03
3.9	0.10 ± 0.04	0.74 ± 0.06	

* standard deviation on the average

5.3.2 Conclusion

Laser microprobe mass spectrometry allows fast determination of alkali sulfur-oxy-anions on a microscopic size level. The intensity ratio of the $Na_2SO_3^+$ and $Na_3SO_4^+$ ions, which is not critically affected by the laser energy, is most indicative for the type of salt.

In marine coastal air, where high sodium and sulfur

concentrations are found in the air particulate, LAMMA provides a useful method for determining the sulfur-anions in single aerosol particles.

5.4 THE IDENTIFICATION OF NITROGEN SPECIES IN SINGLE MICROMETER-SIZE PARTICLES.

Nitrogen compounds are an important constituent of the atmosphere in both the gas and particlulate phase. In atmospheric chemistry the chemical transformation and interrelationship between the different airborne nitrogen compounds are intensively investigated.

5.4.1 Cluster ion distributions of $NaNO_3$ and $NaNO_2$

-Positive ion mode

In the positive mode spectra of $NaNO_3$ and $NaNO_2$ the following clusters could be identified (Figure 5.9):

Na_n^+ : n = 1, 2	m/z = 23, 46
$Na_2O_n^+$: n = 1, 2	m/z = 62, 78
$Na_3O_n^+$: n = 1, 2	m/z = 85, 101
$Na_4O_n^+$: n = 2, 3	m/z = 124, 140
$Na_2NO_2^+$	m/z = 92

Clusters containing both sodium, nitrogen and oxygen are also abundantly present and show the following systematic structure:

$NaNO_3.Na_n^+$: n = 1, 2	m/z = 108, 131
$NaNO_3.Na_2O_n^+$: n = 1, 2	m/z = 147, 163
$NaNO_3.Na_3O_n^+$: n = (1), 2	m/z = (170), 186
$NaNO_3.Na_4O_n^+$: n = 2, 3	m/z = 209, 225
$NaNO_3.Na_2NO_2^+$	m/z = 154

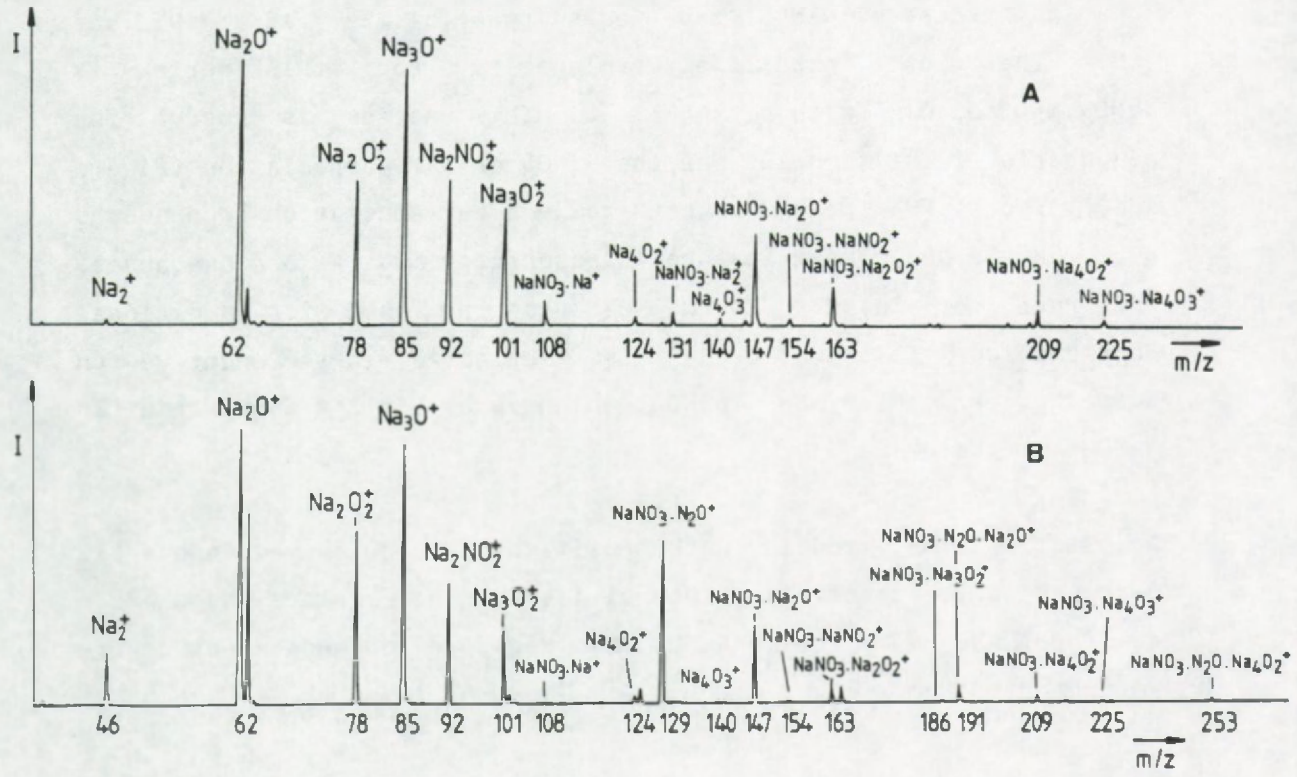

Figure 5.9: Typical LAMMA-spectra, in the positive ion mode of (a) $NaNO_3$ and (b) $NaNO_2$. For each mass peak the most plausible ion is indicated.

Since the mass of 2 sodium atoms equals the mass of NO_2, namely 46 daltons, other atom associations are possible. However, with respect to valence balance for the overall cluster, the most plausible interpretation is given. The use of dots for the cluster ion description does not serve as a structural interpretation but facilitates a systematic ordening of the clusters. It is striking that the second series of the complex clusters can be interpreted as being a combination of the first series of lower mass clusters and $NaNO_3$. Only the $NaNO_3.Na_3O^+$-cluster was not detected in the spectrum. The cluster at m/z = 85 was not interpreted as $NaNO_3^+$ because Na_3O^+ (that has the same nominal mass) appears in the mass spectra of various sodium-oxy-salts as Na_2SO_4, Na_2SO_3, $Na_2S_2O_3$, $NaCH_3SO_3$, Na_2CO_3 etc.

In the case of $NaNO_2$, mass peaks appear at m/z = 129, 191 and 253. The most plausible explanation for this series is $NaNO_3.N_2O.(Na_2O)_n^+$ with n = 0, 1, 2. This series is useful for diagnostic identification of the $NaNO_3$ or $NaNO_2$ speciation (Figure 5.10). The $Na_2NO_2^+$ peak does not show a clear speciation dependence but the $Na_2NO_3^+$ peak is more intense for $NaNO_3$. As a consequence, the ratio of $Na_2NO_2^+$ to $Na_2NO_3^+$ can be used for additional confirmation. This ratio is also reflected in the negative ion distribution for the NO_2^- to NO_3^- which is higher for $NaNO_2$ than for $NaNO_3$ (see below).

Static SIMS studies in the positive ion mode showed an overall decrease in the cluster ion intensities for the clusters above m/z = 46 for $NaNO_2$ compared to $NaNO_3$ (7). Negative ion mode spectra were not reported.

Negative ion mode

The clusters appearing in the negative ion mode spectra can be identified as outlined below (Figure 5.11):

O_n^-	: n = 1, 2	m/e = 16, 32
NO_n^-	: n = 2, 3	m/e = 46, 62
$NaNO_3^-$ or $NaNO_2.O^-$		m/e = 85
$NaNO_3.O^-$		m/e = 101
$NaNO_3.NO_n^-$	: n = 1, 2, 3	m/e = 115, 131, 147

The relative intensities of the cluster ions and their standard deviation of the mean calculated from a set of six spectra are represented in Figure 5.12. The intensity of the NO_3^--cluster at m/z = 62 was set equal to 1 as the reference peak. The NO_2^- to NO_3^- ratio is 6.7 for $NaNO_2$ and 2.1 for $NaNO_3$. The same tendency is observed for the $Na_2NO_2.NO_2^-$ (or $NaNO_3.NO^-$) cluster (m/z = 115) with a relative intensity of 5.4 for the $NaNO_2$ salt and 1.4 for $NaNO_3$. These relative peak intensities can be used to differentiate between sodium nitrate and sodium nitrite.

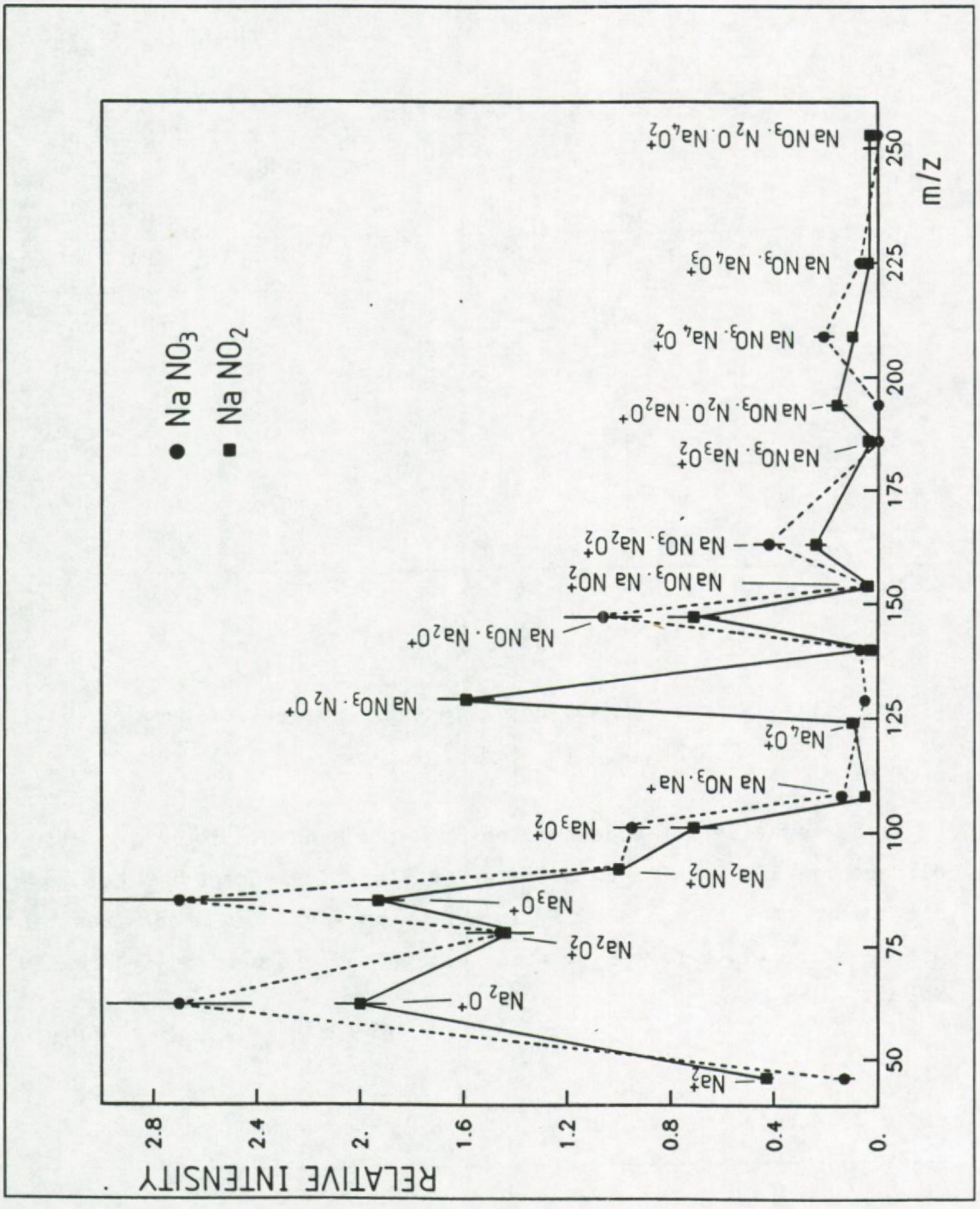

Figure 5.10: Positive cluster ion intensities as a function of m/z for $NaNO_3$ and $NaNO_2$. The intensities are the average of sixfold measurements; they have been normalized to the m/z = 92 mass peak; the error bars represent the standard deviation of the mean

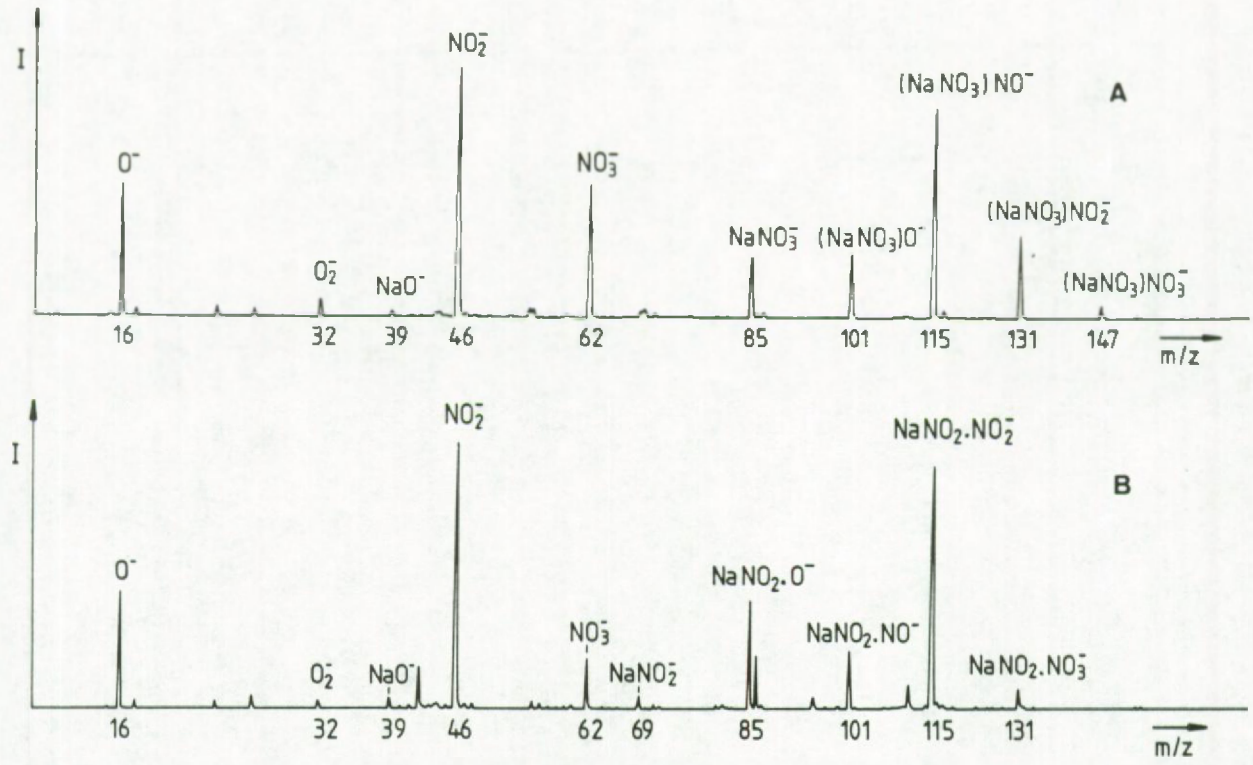

Figure 5.11: Typical LAMMA-spectra in the negative ion mode of (a) $NaNO_3$ and (b) $NaNO_2$.

The negative ion mode spectra are more useful for speciation differentiation between nitrate and nitrite because the most diagnostic peak at m/z = 129 in the positive ion mode can in practice be interfered by the cationized form of Na_2CO_3 namely $Na_3CO_3^+$ (see below).

5.4.2 Cluster ion distributions of $(NH_4)_2SO_4$, NH_4NO_3 and NH_4Cl

The uptake of gaseous ammonia by atmospheric acids, (e.g. HNO_3, H_2SO_4, HCl) either in the gaseous phase or adsorbed on particle surfaces is the major pathway for the neutralization of these acids. Direct detection on the microscopic size level of the salt speciation is also here a useful tool to investigate the atmospheric

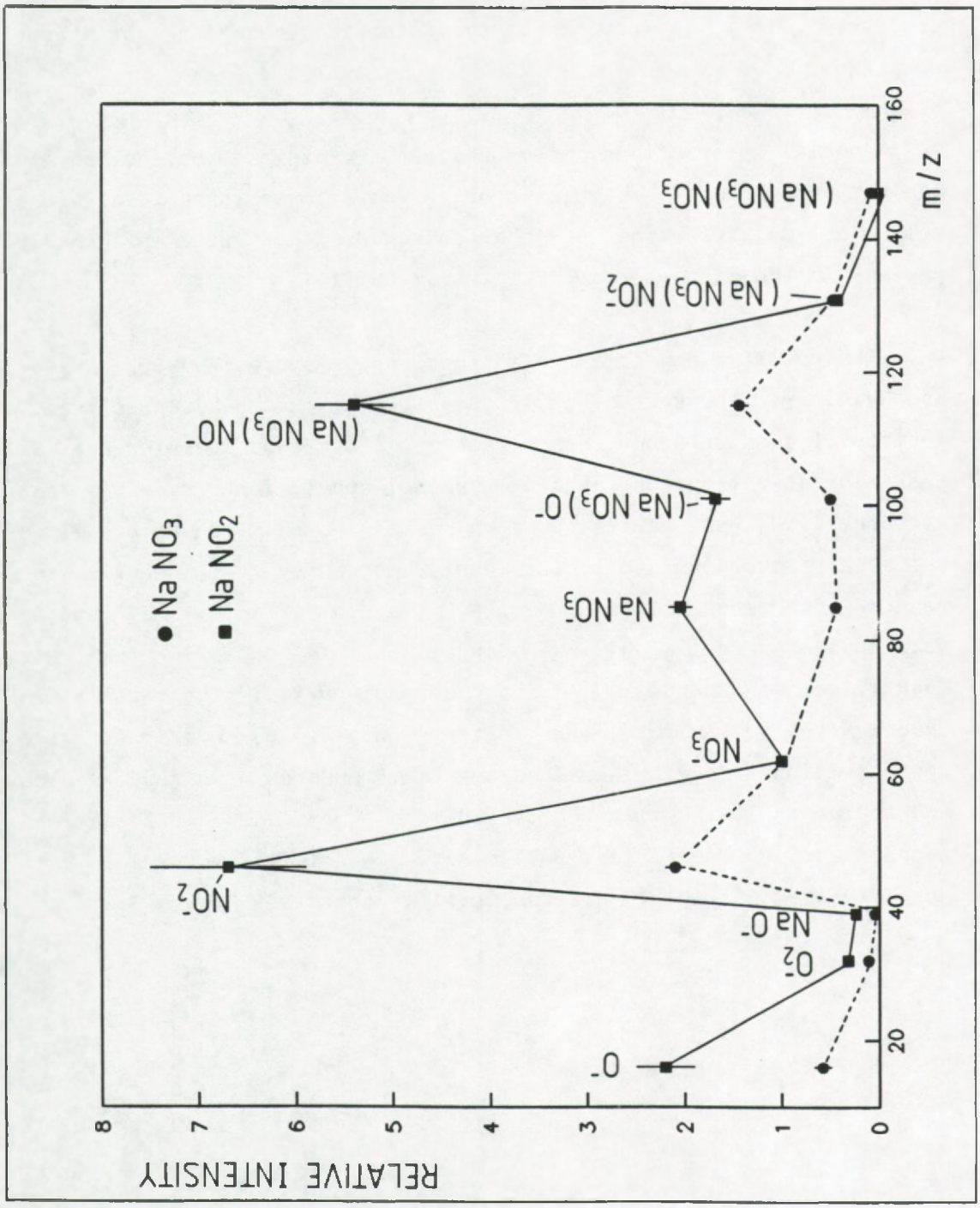

Figure 5.12: Negative ion intensities as a function of m/z for $NaNO_3$ and $NaNO_2$. The intensities are the average of six measurements; they have been normalized to the m/z = 92 mass peak. the error bars represent the standard deviation of the mean.

processes that govern the transformation reactions of these compounds.

Special precautions with respect to sample collection in ambient air and to sample storage have to be taken to assure a reliable identification of the compounds that were originally present in the airborne particulate matter (19).

The positive and negative ion mode spectra of $(NH_4)_2SO_4$, NH_4NO_3 and NH_4Cl are represented in Figure 5.13a and b, respectively. Further discussion about these spectra can be found in reference 19. LAMMA investigations on ambient aerosol particles revealed that airborne $(NH_4)_2SO_4$ particles often contain Na an K. Therefore mixed sulfates of ammonium and sodium were prepared by the nebulization method of aqueous solutions. For a mixture of 67 mole % NH_4^+ and 33 mole % Na^+, an additional mass peak at m/z = 143 appeared that was identified as $Na_2HSO_4^+$. Ambient aerosol particles of these mixed ammonium-sodium sulfate type often contain Pb over a wide concentration range. Therefore several standards of mixed ammonium and sodium sulfates were prepared that contained well defined amounts of Pb to determine the detection limit for LAMMA in this specific salt matrix of environmental interest (see Figure 3.2).

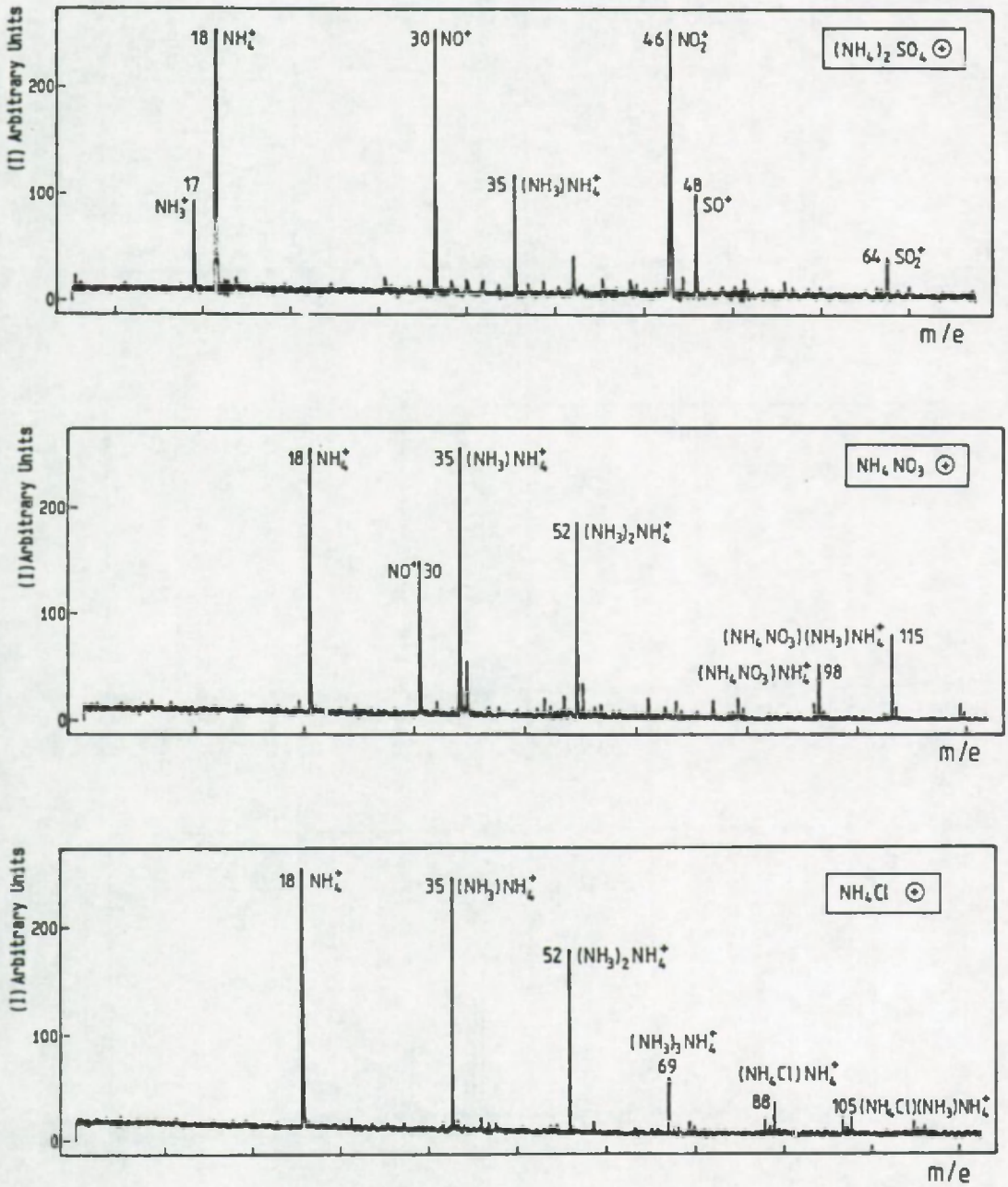

Figure 5.13a: Positive ion mode spectra of $(NH_4)_2SO_4$, NH_4NO_3 and NH_4Cl (19).

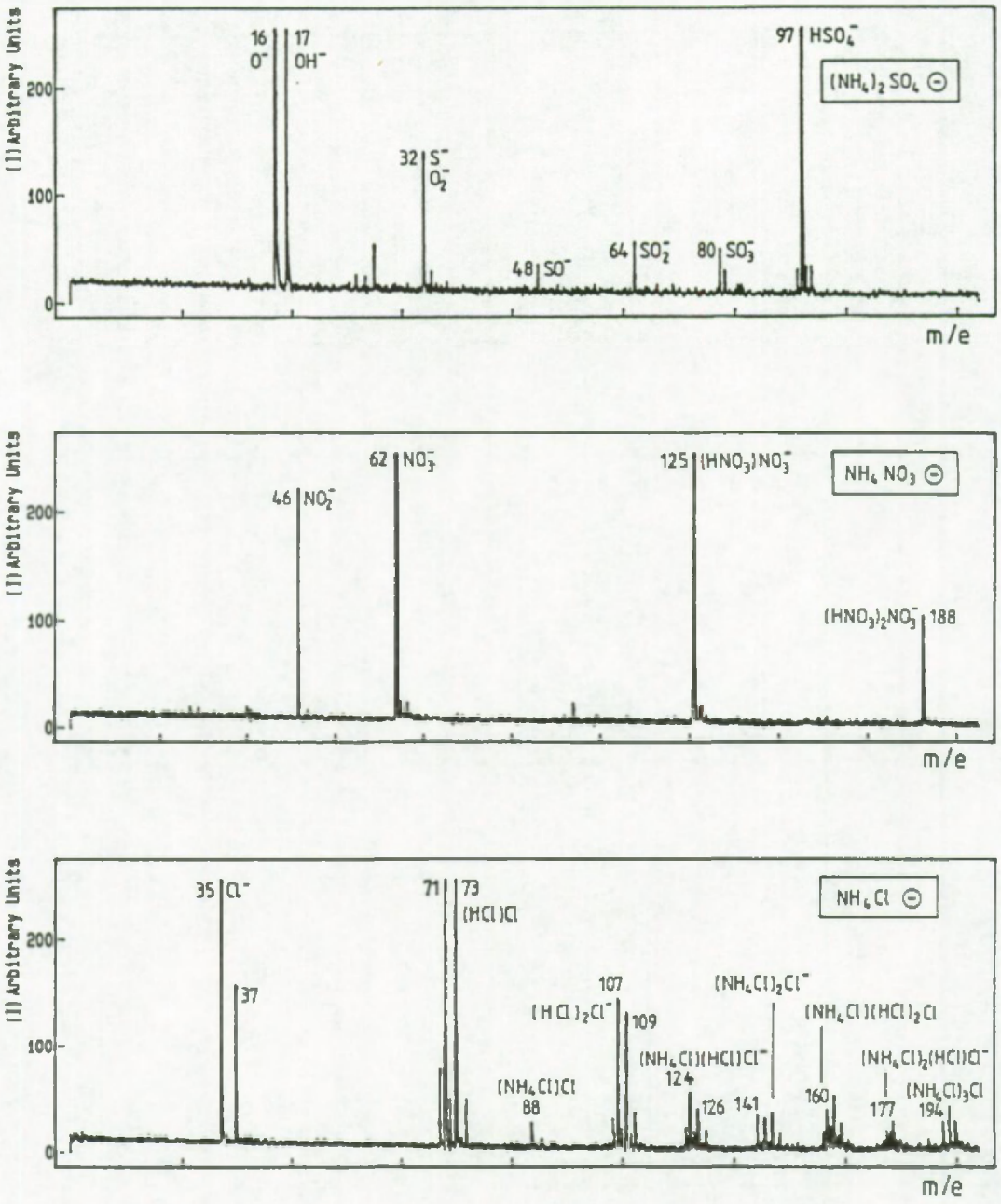

Figure 5.13b: Negative ion mode spectra of $(NH_4)_2SO_4$, NH_4NO_3 and NH_4Cl (19).

5.5.CLUSTER ION DISTRIBUTION OF Na_2CO_3 AND $Na_2CO_3.10H_2O$

Reference spectra of Na_2CO_3 and $Na_2CO_3.10H_2O$ are shown in Figure 5.14. In addition to the Na_n^+ (n = 1, 2), $Na_2O_n^+$ (n = 1, 2) and $Na_3O_n^+$ (n = 1, 2) clusters, a diagnostic mass peak at m/z = 129 indicated the presence of carbonate. This peak can be interpreted as the cationized form of Na_2CO_3. In the case of the hydrated salt, the hydrogen content of the particle is reflected in the intensity of the Na_2OH-mass peak at m/z = 63 and in the cluster series $Na_3O_2H_n^+$ with n = 0, 1, 2. It was found rather remarkable that this series of clusters is accompanied by a mass peak at m/z = 145 with the composition $Na_3CO_4^+$. The relationship between these two peaks can be recognized by inspection of spectrum 5.14a and b. Confirmation for the identification of the 145 mass peak was gained by writing the chemical formula of the structure in the following way :

$Na_3CO_3^+$ (m/z = 129) or $CO_2.Na_3O^+$ with Na_3O^+ at m/z = 85

$Na_3CO_4^+$ (m/z = 145) or $CO_2.Na_3O_2^+$ with $Na_3O_2^+$ at mz = 101

The observation that specific clusters show a similar behaviour with respect to intensity, when comparing consecutive spectra recorded for the same compound, often point to a structural relationship, that can be exploited to ease the cluster identification.

In the negative mode spectra the CO_n^- (n = 3, 4) and $NaCO_n^-$ (n = 3, 4) peaks are characteristic for Na_2CO_3 (Figure 5.14c) . The unfavourable oxygen to carbon ratio in CO_4^- is difficult to accept from conventional charge balance calculations taking an oxidation state of -2 for oxygen. Therefore a more reasonable interpretation for the oxygen valence is $CO_2.O_2^-$: CO_2 as a structural fragment was was also recognized in the positive ion mode and O_2^- shows up in the negative mode spectrum at m/z = 32. It is emphasized once more that these cluster ion interpretations do not serve as a proof for the real structure but that they are used to enable systematic description of the cluster ions observed.

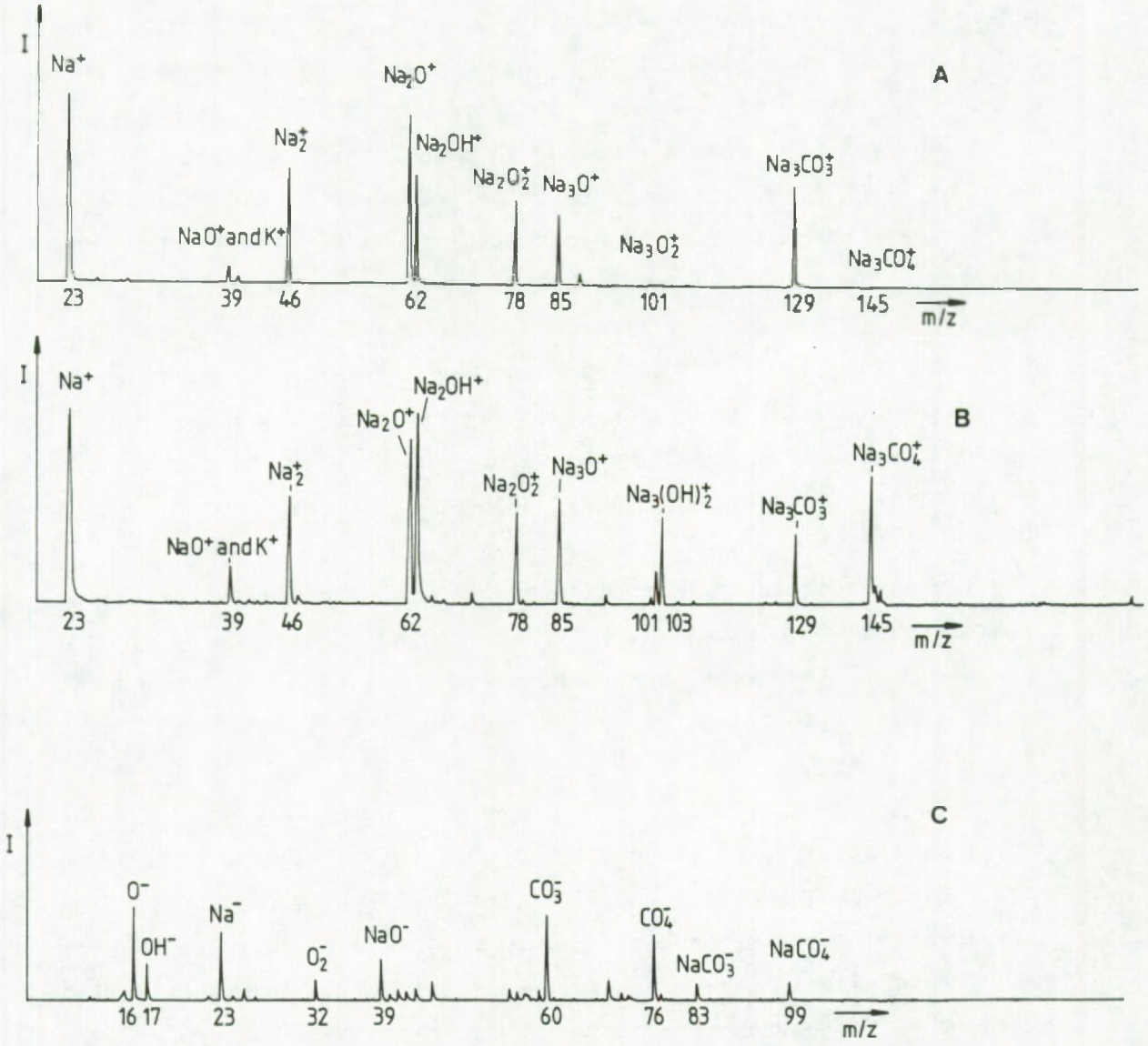

Figure 5.14: (a) and (b) Typical positive mode LAMMA-spectra of Na_2CO_3 and $Na_2CO_3.10H_2O$

(c) Typical negative mode LAMMA-spectrum of $NaCO_3.10H_2O$

5.6 CONCENTRATION DEPENDENCE OF THE CLUSTER ION DISTRIBUTION OF HOMOGENEOUS ALKALI-HALIDE PARTICULATES

5.6.1 Introduction

Alkali-halide salts were extensively used in fundamental studies with the aim of learning more about the mechanism of ion production in various instrumental techniques using a wide variety of excitation sources as electron impact on alkali-halide vapors (20), spark source mass spectrometry (21), field desorption mass spectrometry (22), secondary ion mass spectrometry (23-26), electron induced sputtering (27), photoionization and photoelectron spectroscopy (28) and laser microprobe mass spectrometry (29-32).

Jöst et al. (30) reported that the ion formation rates in LAMMA of alkali halide solids are incompatible with the assumption of a quasi-equilibrium phase transition, but should be explained in terms of non-adiabatic rate processes. The light absorption of the transparent halide crystal is assumed to be initiated by multiphoton absorption-free electron production and the further energy transfer could be maintained by rapid polaron Joule heating (33,34).

In most of the instrumental studies mentioned above, mixtures of alkali-halides were prepared either by grinding the two compounds simultaneously in an agate mortar or by spotting an aqueous solution of the alkali halide mixture onto the sample support. For most, halides, these procedures are not optimal to obtain homogeneous mixtures of the salts, that are required for the study, as was recognized by most of the investigators: for the ground mixture, complete mixing at the submicron size level is very difficult to achieve, while for the evaporation of the aqueous solution fractional crystalization can result in phase segregation. The LAMMA measurements described below, however, were performed on mixtures of KCl and KBr. These particular compounds are completely miscible in the solid state (35), so that homogeneous standards can be prepared.

5.6.2 Experimental

Carefully weighed amounts of KCl and KBr were ground in an agate mortar and were quantitatively transferred into a crucible. The crucible was put into an oven with a temperature of 850°C, well above the melting point of KBr (734°C) and KCl (770°C). Rapid cooling of the liquid solution upon removal of the crucible from the oven resulted in the immediate formation of a semi-transparent glassy compound. The homogeneous solid was ground in an agate mortar. The micrometer-size particles were mounted on a Formvar coated electron microscope grid by contacting the grid with the ground material. The chemical composition of the standard samples is shown in Table 5.7. Positive and negative ion mode spectra were recorded for every standard at several laser irradiances.

Table 5.7: Composition of the KCl/KBr-standard mixtures

Mixture number	Weight KCl (gram)	Weight KBr (gram)	Mol% KCl	Mol% KBr
#1	0.0927	1.0092	12.8	87.2
#2	0.2409	0.8673	30.7	69.3
#3	0.3747	0.6186	49.2	50.8
#4	0.5153	0.3609	69.5	30.5

5.6.3 Results and discussion

The intensities of the cluster ions for the 4 standards were normalized to the sum of the intensities of either the K_2X^+ or K_3X^+ clusters (with X = Cl, Br) as shown in Table 5.8. The spectra were recorded at a laser energy of 2.2 μJ. The % Cl in the distributions can be calculated from the normalized intensities by making the sum of the intensity of the $K_3Cl_2^+$-cluster and one half of the intensity of the K_3ClBr^+-clusters. However it was observed that for homogeneous mixtures the distribution of Cl and Br can be described by simple binomial statistics, according to the following formula:

$$I(2,m) = \frac{2!\ p^m.q^{2-m}}{m!\ (2-m)!} \qquad \text{(eq. 5.7)}$$

with m = 0, 1, 2

p: normalized intensity of Cl in the clusters
q: normalized intensity of Br in the clusters

For every cluster a value for p can be calculated as shown in Table 5.9. From Table 5.7 and Table 5.9 it can be concluded that the positive cluster ions have a higher Cl-content compared to the solid particulates from which they were generated. For the negative ions, a different behaviour is observed. Table 5.10 shows the normalized intensities of the KX_2^--clusters (with X = Cl, Br). Table 5.11 represents the % Cl in the clusters, calculated as outlined above. When the experimental values of the % Cl are plotted against the stoichiometric concentration in the particles, a fairly linear relationship is observed, which can be described by :

$I = (1.04 \pm 0.04)C - (2 \pm 3)$ with $r = 0.993$

I : % Cl in KX_2^- as calculated from the negative cluster intensities
C : % Cl in the solid particles

Table 5.8: Relative intensity distribution of the K_2X^+ and $K_3X_2^+$ cluster ions (X = Cl, Br) and the standard deviation of the mean for the KCl/KBr standard mixtures of Table 5.7

Relative intensities ± S.D.

Mixture no.	#1	#2	#3	#4
Ion				
K_2Cl^+	0.22 ± 0.04	0.487 ± 0.006	0.60 ± 0.01	0.75 ± 0.02
K_2Br^+	0.78 ± 0.04	0.513 ± 0.006	0.40 ± 0.01	0.25 ± 0.02
$K_3Cl_2^+$	0.015 ± 0.005	0.20 ± 0.01	0.44 ± 0.01	0.73 ± 0.02
K_3ClBr^+	0.25 ± 0.03	0.50 ± 0.01	0.43 ± 0.01	0.25 ± 0.02
$K_3Br_2^+$	0.73 ± 0.04	0.30 ± 0.01	0.13 ± 0.01	0.015 ± 0.003

By combining the results of Table 5.9 with those of Table 5.11, Figure 5.15 can be constructed which represents the % Cl calculated from the negative clusters by the binomial distribution as a function of the % Cl calculated from the positive clusters by the same method and vice versa. It illustrates the Cl- enrichments in the positive ion mode $K_3X_2^+$-clusters relative to the negative mode KX_2^--clusters. The theoretically expected cluster ion distribution calculated from the p-values in Table 5.11 can be compared to the experimentally observed intensities. The data for the KX_2^--clusters are plotted in Figure 5.16. It is clear that the cluster ion intensities of the negative ions can straightforwardly be correlated to the % Cl in the individual particles. Therefore the Cl/Br-ratio in a sample has to be measured in the negative ion mode rather than the positive ion mode. Preferential sputtering as observed in prolonged irradiation in SIMS-studies (26) does not occur because the particles were evaporated in a single laser shot. The measurements of the cluster ion distribution in the range from 2 to

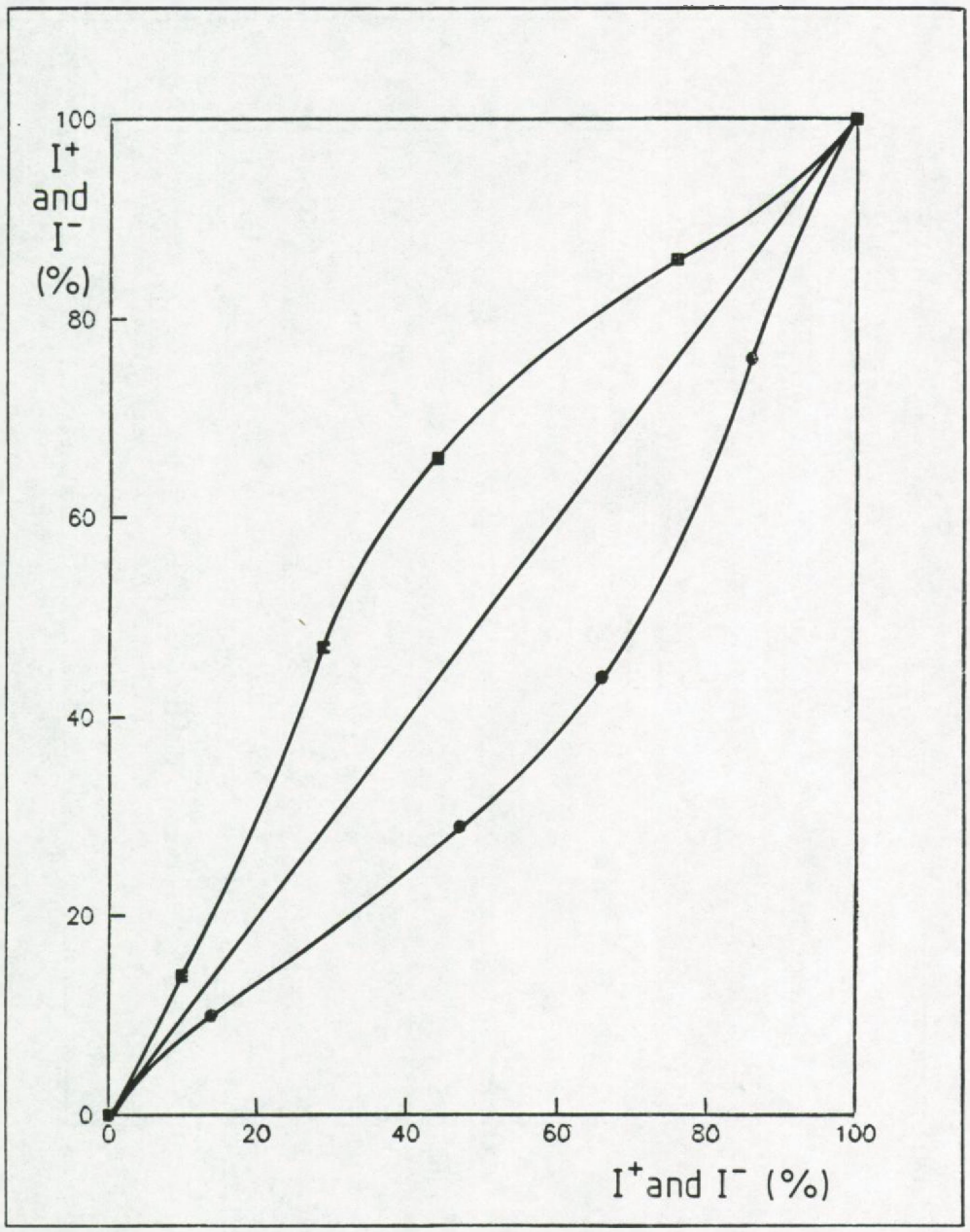

Figure 5.15: Cl-composition of the $K_3X_2^+$-ions (I^+ in %) as a function of the Cl-composition of the KX_2^--ions (I^- in %), which is directly related to the Cl-content of the standard (upper curve). The inverse relationship is presented in the lower curve.

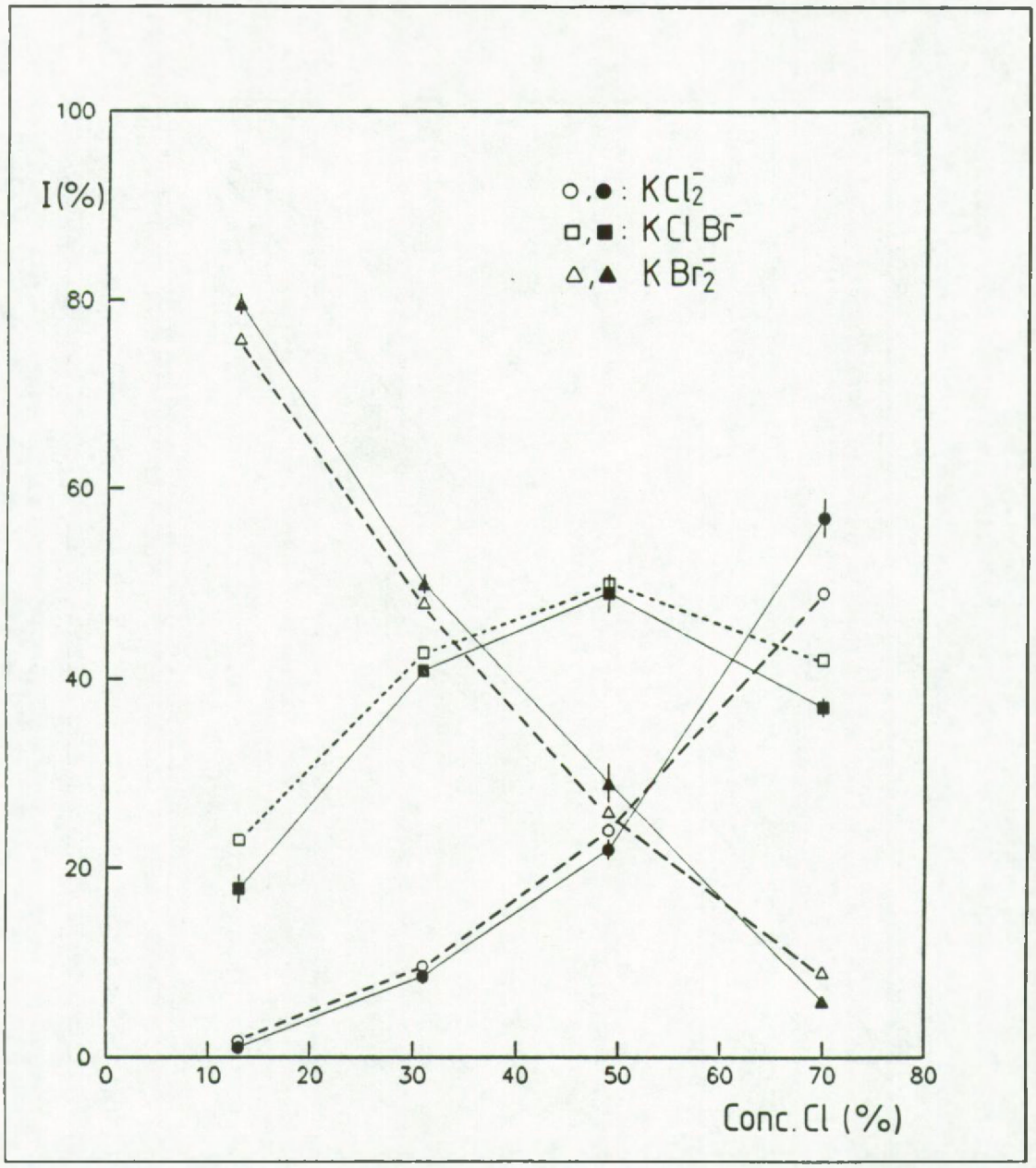

Figure 5.16: Comparison of the experimental intensity distribution of the KX_2^--cluster ions (I in %)(filled symbols), with the predicted values according to a binomial distribution (open symbols). The % molar concentration of Cl in the particles was used as p-value (eq 5.7).

Table 5.9: Comparison of the % Cl-composition of the cluster ions calculated according to the binomial distribution (p-value) and calculated from the relative ion intensities of K_2X^+ and $K_3X_2^+$.

	% Cl-composition			
Mixture no.	#1	#2	#3	#4
Ion				
K_2Cl^+	p = 0.22	p = 0.49	p = 0.60	p = 0.75
K_2Br^+				
$K_3Cl_2^+$	0.12	0.45	0.66	0.85
K_3ClBr^+	0.15	0.50	0.69	0.85
$K_3Br_2^+$	0.15	0.45	0.64	0.88
$\langle p \rangle \pm S_{\langle p \rangle}$	0.14 ± 0.01	0.47 ± 0.02	0.66 ± 0.02	0.86 ± 0.01
%Cl in $K_3X_2^+$	0.14	0.45	0.66	0.86

Table 5.10: Relative intensity distribution of the KX_2^--cluster ions (X = Cl, Br) and the standard deviation of the mean for the KCl/KBr standard mixtures of table 5.7

		% Cl-composition		
Mixture no.	#1	#2	#3	#4
Ion				
KCl_2^-	0.010 ± 0.002	0.085 ± 0.007	0.22 ± 0.01	0.57 ± 0.02
$KClBr^-$	0.178 ± 0.015	0.409 ± 0.005	0.49 ± 0.02	0.37 ± 0.01
KBr_2^-	0.796 ± 0.010	0.50 ± 0.01	0.29 ± 0.02	0.059± 0.005

Table 5.11: Comparison of the % Cl-composition of the cluster ions calculated according to the binomial distribution (p-value) and calculated from the relative ion intensities of KX_2^- (X = Cl, Br).

	% Cl-composition			
Mixture no.	#1	#2	#3	#4
Ion				
KCl_2^-	0.10	0.29	0.47	0.76
$KClBr^-$	0.10	0.29	0.43	0.75
KBr_2^-	0.11	0.29	0.46	0.76
$\langle p \rangle \pm s_{\langle p \rangle}$	0.10 ± 0.01	0.29 ± 0.01	0.45 ± 0.02	0.76 ± 0.01
%Cl in KX_2^-	0.10	0.29	0.46	0.76

7 μJ showed some minor shifts in the relative intensity ratios that were close to the experimental uncertainty on the data.

The same method can be used to estimate for example the sodium to potassium ratio in a single particle. Sodium and potassium are very sensitive elements in LAMMA, what often results in overflow for the elemental ion signals. In these cases the distribution of sodium and potassium over the members of a specific cluster type can be used to estimate their ratio in the sample. This is illustrated in Table 5.12 that shows the experimental intensities of the $M_3Cl_2^+$-clusters (M = Na, K) measured for a homogeneous NaCl/KCl mixture of 68 mol % of Na. The cluster intensities calculated for 38 % Na content of the clusters are listed between brackets. The cluster ions are relatively enriched in potassium compared to sodium. A shift in the same direction was observed for the elemental ions (see Table 3.4). By convention these shifts are expressed as a relative

sensitivity factor, which in this specific case is equal to 3.5. These factors are matrix dependent and have to be determined from suitable reference standards.

Table 5.12: Experimental intensities of the $M_3Cl_2^+$-clusters (M = Na, K), measured for a homogeneous NaCl/KCl-mixture of 68 mol % of Na. The predicted cluster ion intensities 38 % Na were calculated according to a binomial law.

Ion	Intensity (%)	
	Measured	Calculated
$Na_3Cl_2^+$	0.07 ± 0.05	0.06
$Na_2KCl_2^+$	0.24 ± 0.02	0.27
$NaK_2Cl_2^+$	0.43 ± 0.03	0.44
$K_3Cl_2^+$	0.26 ± 0.04	0.24

For homogeneous samples, the distribution of alkali metals and halides over the clusters can thus be interpreted by simple binomial statistics. If clear deviations from these distributions are observed, as in the case of the $^{12}C/^{13}C$-foils (discussed in chapter 4), they have to be attributed to the heterogeneous nature of the sample.

5.7 CONCLUSION

The capabilities of LAMMA for inorganic speciation have been demonstrated by some examples for pure salts. Now the question arises whether the method has any relevance for practical applications because several analytical procedures are available to determine the stoichiometry of a compound. The decisive factor that makes LAMMA an interesting approach in this field is the microscopic

resolution offered by the technique, so that individual particles can be analyzed in a heterogeneous and complex particulate sample. Airborne particulate matter has a high internal complexity because of the various sources that can contribute to it and because of the numerous transformation reactions that can alter the chemical composition; therefore it constitutes a very interesting research field for the application of the LAMMA-technique. Many possible atmospheric reactions were studied on a laboratory scale but the verification on and extrapolation to real atmospheric systems is largely impeded by the fact that all the reactions are simultaneously going on in ambient air and that particles with different chemical composition, and as a consequence different reactive behaviour, are present in the atmosphere.

Despite the complex nature of the airborne particulate matter, many individual aerosol particles can, to a first approximation (i.e. when the surface layer is left out of the discussion), be regarded as rather homogeneous in matrix composition. As a consequence, they can be correlated to the source material from which they were generated. Fractionation or so-called enrichment phenomena can, of course, result from the aerosol generation mechanism itself. The same fingerprinting procedure as outlined for the pure compounds can also be used to fingerprint particulates of a mixed chemical composition as will be demostrated extensively in the applications, outlined in later chapters. If suitable reference standards can be prepared, as it is e.g. the case for water soluble aerosols using the nebulization technique, a reliable interpretation of the spectra can be given.

5.8. References

1. J.D. Ganjei, R.J. Colton, and J.S. Murday, Int. J. Mass. Spectrom. Ion Phys., 37, 49 (1081).

2. E. De Pauw and J. Marien, Int. J. Mass Spectrom. Ion Phys., 38, 11 (1981).

3. C. Plog, L. Wiedmann, and A. Benninghoven, Surface Science, 67, 565 (1977).

4. E. Michiels, A. Celis, and R. Gijbels, in Microbeam Analysis-1982, ed. by K.F.J. Heinrich, San Francisco Press, San Francisco, 1982, p. 383.

5. C. Duval, Inorganic Thermogravimetric Analysis, Elsevier Publishing Company, Amsterdam, 1963.

6. E. Michiels, Ph.D. Thesis, University of Antwerp (UIA), Antwerp, Belgium, 1985.

7. E. Michiels, A. Celis, and R. Gijbels in Microbeam Analysis-1984, ed. by K.J.F. Heinrich, San Francisco Press, San Francisco, 1982, p. 27.

8. E. Michiels and R. Gijbels, Anal. Chem., 56, 1115 (1984).

9. E.K. Bigg, A. Ono and J.A. Williams, Atmos. Environ., 8, 1 (1974).

10. Y. Mamane and R.G. De Pena, Atmos. Environ., 12, 69 (1978).

11. G.P. Ayers, Atmos. Environ., 12, 1613 (1978).

12. R.J. Ferek, A.L. Lazrus and J.W. Winchester, Atmos. Environ., 17, 1545 (1983).

13. R. Kaufmann, P. Wieser, R. Wurster, Scanning Electron Microsc., II, 607-622 (1980).

14. H. Seiler, U. Haas, I. Rentschler, H. Schreiber, P. Wieser, P. Wurster, R. Optik, 58, 145-157 (1981).

15. J. Marien and E. De Pauw, Bull. Soc. Chim. Belg., 88, 115 (1979).

16. J. Marien and E. De Pauw, Int. J. Mass Spectrom. and Ion Phys., 43, 233 (1982).

17. J. Marien and E. De Pauw, Anal. Chem., 57, 362 (1985).

18. M.O. Andreae, in The Role of Air-Sea Exchange in Geochemical Cycling, ed. by P. Buat-Ménard, NATO ASI Series, series C: Mathematical and Physical Sciences Vol. 185, D. Reidel Publishing Company, Dordrecht, 1986, p. 331.

19. Ph. Otten, F. Bruynseels, and R. Van Grieken, Proceedings of the Third International LMMS Workshop, ed. by F. Adams and L. Van Vaeck, 1986, p. 159.

20. J. Berkowitz and W.A. Chupka, J. Chem. Phys., 29, 653 (1958).

21. C.E. Rechsteiner jr., R.P. Buck, and L. Pedersen, J. Chem. Phys., 65, 1659 (1976).

22. C.E. Rechsteiner, Jr., T.L. Youngless, M.M. Bursey, and R.P. Buck, Int. J. Mass Spectrom. Ion Phys., 28, 401 (1978).

23. J.A. Taylor and J.W. Rabalais, Surface Science, 74, 229 (1978).

24. F. Honda, G.M. Lancaster, Y. Fukuda, and J.W. Rabalais, J. Chem. Phys., 69, 4931 (1978).

25. F. Honda, Y. Fukuda, and J.W. Rabalais, J. Chem. Phys., 70, 4834 (1979).

26. X.B. Cox, III, R.W. Linton, and M.M. Bursey, Int. J. Mass Spectrom. Ion Proc., 55, 281 (1983/1984).

27. A. Friedenberg and Y. Shapira, J. Phys. C : Solid State Phys., 15, 4763 (1982).

28. J. Berkowitz, C.H. Batson, and G.L. Goodman, in Metal Bonding and Interactions in High Temperature Systems, ed. by J.L. Gole and W.C. Stwalley, ACS Symposium Series, No. 179, 1982, p. 275.

29. F. Bruynseels, M.Sc. Thesis, University of Antwerp (1981).

30. B. Jöst, B. Schueler, and F.R. Krueger, Z. Naturforsch, 37a, 18 (1982).

31. F. Bruynseels, IWONL-report (1983).

32. E. Michiels and R. Gijbels, Mikrochim. Acta, III, 277 (1983)

33. P.J. Kelly, D.S. Ritchie, P.F. Braunlich, A. Schmid, and G.W. Bryant, IEEEJ. Quantum Electron., QE-17, 2027 (1981).

34. P.F. Braunlich, G. Brost, A. Schmid, and P.J. Kelly, IEEEJ. Quantum Electron., QE-17, 2034 (1981).

35. J.A. Bouwstra and H.A.J. Oonk, CAL PHAD, 6, 11 (1982).

CHAPTER 6. LAMMA-STUDY OF THE MICROSTRUCTURE OF AEROSOLS

6.1 INTRODUCTION

In ambient air, aerosols are subject to interactions with both the surrounding gases and with the other airborne particles. This can lead to a rather complex structure of the aerosol particle surface, the so-called microstructure of an aerosol particle. The term microstructure refers to the topographical composition of a single particle; it considers e.g. the presence and type of multilayers or agglomerates that might occur on a primary particle core as illustrated in Figures 6.1a and and b.

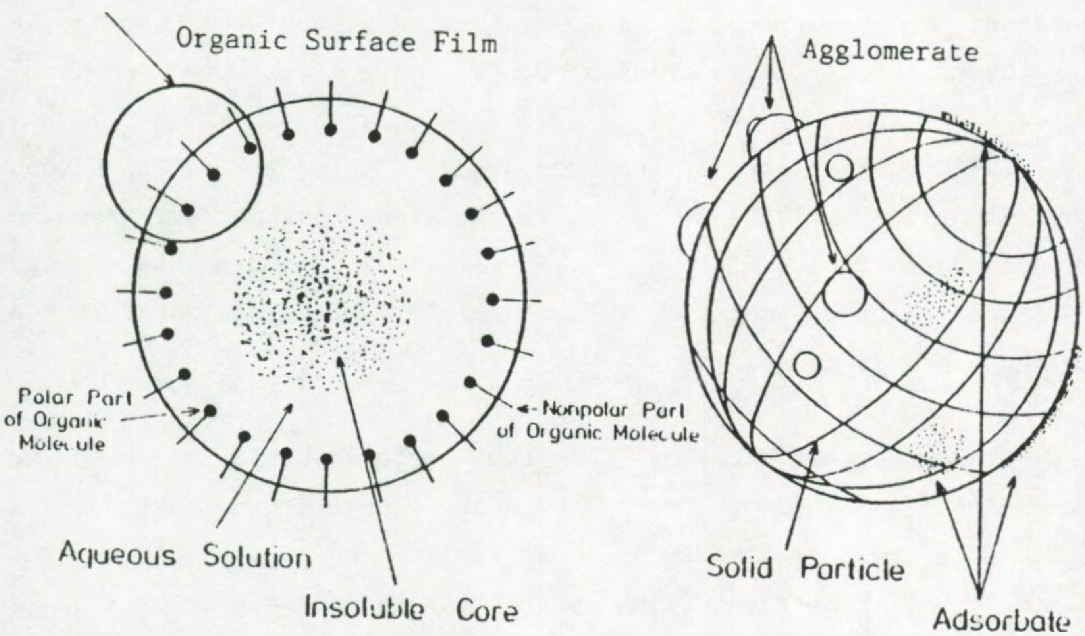

Figure 6.1: Schematic representation of the microstructure of particles
(a) hygroscopic particle
(b) solid particle

During the multiple evaporation and recondensation of fog and rain droplets in the atmospheric aerosol-water vapour circulation system, organic molecules are enriched on the droplet surface (Figure 6.1a). This organic surface layer can influence the optical characteristics of the aerosols but also the sink mechanism for reactive gases as H_2S, SO_2 and NO_x in the aqueous particle phase. It was also recognized that ammonia neutralization of acidic aerosol may be affected by a surface coating of organic material present in contaminated air. In heavily polluted regions the carbon to sulfate ratio may reach a value of 1.0 according to Appel et al. (1). If only a part of this organic material (like fatty acids or alcohols) exists together with acidic sulfates forming a non-permeable film, the sink mechanism for acids may be strongly influenced. If acidic aerosol is emitted together with unburned fuels, e.g. of a starting engine, we have to expect a very high concentration of hydrocarbons at the outlet of the exhaust. These organic vapours will mainly condense on the particulate material forming an organic layer on the surface of the particles or droplets (2).

Solid particulates as they are produced in e.g. power plants can also be active in the uptake of gaseous polynuclear aromatic hydrocarbons (PAH) : fly-ash and PAH are simultaneously emitted and condensation of the gases onto the particle surface can occur in the colder zones of the chimney.

Therefore, the knowledge of the microstructure of airborne particles is of major interest because it governs the particle-gas phase interaction mechanism and reactivity and also because the toxicity of substances like e.g. PAH by particle inhalation is largely influenced by the bioavailability on the particle surface. Moreover, further research about the heterogeneous gas phase-particle interactions in the atmosphere will improve our understanding of atmospheric chemistry.

6.2 MICROENCAPSULATION OF AMMONIUM HYDROGENSULFATE AEROSOLS WITH HEXADECANOL

In a laboratory study, artificially generated ammonium hydrogen sulfate particles were coated in their airborne state with n-hexadecanol (NHD). NHD has been chosen because of its well known properties in retarding the evaporation of water droplets (3).

6.2.1 Experimental

The coating experiments were carried out by a technique developed by Niessner (4). The experimental set-up is shown in Figure 6.2. To obtain different supersaturations of n-hexadecanol, a thermostated aerosol mixer was constructed similar to the magnifier-device of Kogan and Burnasheva (5). The mixer consists of a heated nozzle (A) and an annular slit (B) through which the organic vapour enters the mixer and joins the aerosol stream producing a mixture which is supersaturated to an extent controlled by temperature and flow rates. The primary aerosol is generated by use of a Collison-type nebulizer followed by a diffusion dryer. Pressurized nitrogen was used to nebulize the salt solution. Condensation of organic vapour takes place during mixing and is finished in the next 10-20 cm of subsequent tubing. Through a by-pass a low level (<700 ppbv) of ammonia gas can eventually be injected to study the influence of the coating on the ammonia uptake by the aerosol. After passing a mixing section, a part of the aerosol is sampled on Formvar coated grids mounted on the 5-stages of a Battelle-type cascade impactor.

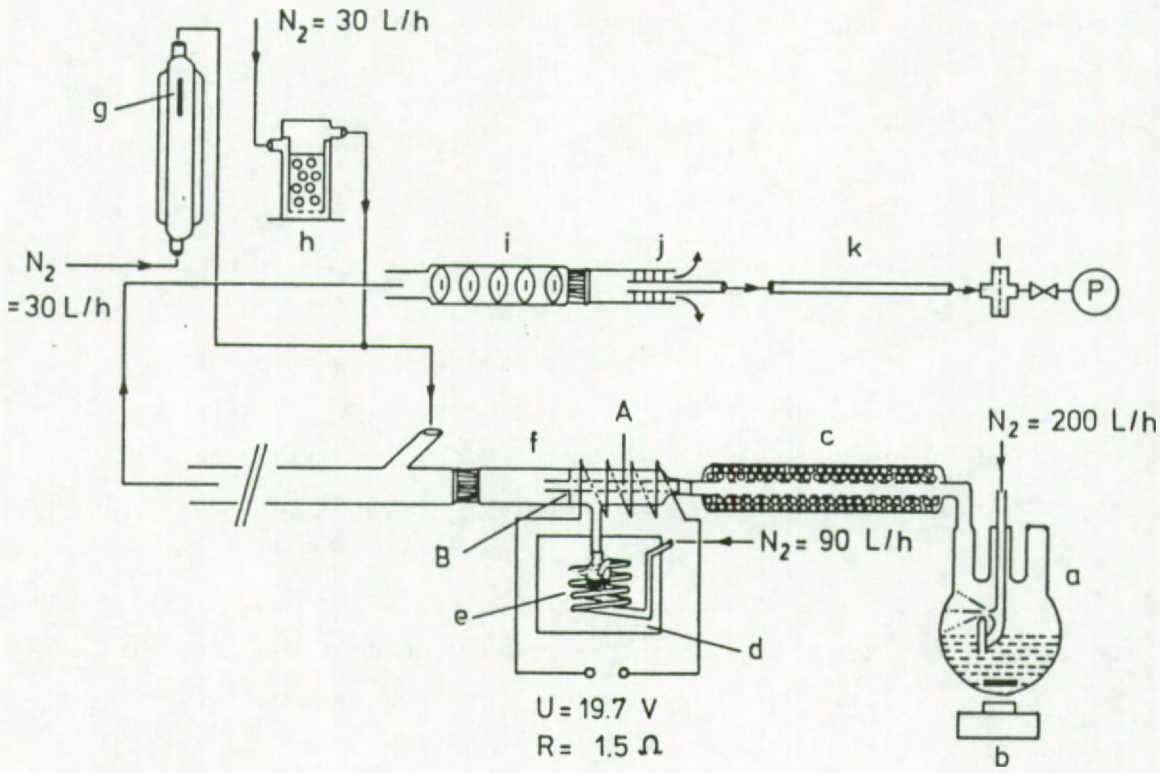

Figure 6.2: Schematic diagram of the experimental set-up used to coat aerosol particles with n-hexadecanol (4). (a) Collision - atomizer; (b) Magnetic stirrer; (c) Diffusion dryer, filled with silicagel; (d) Thermostated oil bath; (e) Boiler with 20 ml flask and 1 g n-hexadecanol; (f) Thermostated mixing nozzle; (g) Permeation tube, filled with NH_3; (h) Humidifier; (i) Mixing chamber; (j) Sample flow splitter; (k) Citric acid denuder; (l) Filter holder.

6.2.2 Results and discussion

Since no molecular or quasi-molecular ion can be observed for n-hexadecanol, the detection of selective desorption of the alcohol was not possible. A positive and negative mode spectrum of a n-hexadecanol coated aerosol particle is shown in Figures 6.3b and c.

A negative mode spectrum of pure NH_4HSO_4 is shown in Figure 6.3a. The presence of an organic substance can only be inferred from the pattern of the carbon chain C_n^- (n = 2 to 5). The hydrogen-rich sulfate can be identified by the intense HSO_4^--signal at m/z = 97. The mass signal at m/z = 18 indicates the presence of ammonium in the spectrum. Several peaks can be assigned to the alcohol, namely:

$(C_nH_{2n-1})^-$: m/z = 27, 41, 55, 69
$(C_nH_{2n+1})^+$: m/z = 29, 43, 57, 71
$(C_nH_{2n+1}O)^+$: m/z = 45, 73

In this specific case no direct information on the microstructure can be obtained. This illustrates the importance of model systems to assess the capabilities of LAMMA for specific purposes. However, the spectra recorded for the n-hexadecanol coated NH_4HSO_4 particles are strikingly similar to the fingerprint spectra of ambient aerosol particles frequently detected in the submicrometer size range. This means that the airborne organic matter is indeed incorporated in the fine mode ammonium sulfate and that the inhibition of neutralization of the airborne sulfates by an organic surface film as shown in Figure 6.1a certainly needs further research. Laboratory studies, carried out by Niessner et al. (4) with the instrumental setup shown in Figure 6.2, are in agreement with these observations. With a slightly modified set-up compared to Figure 6.2, where a La-Mer generator was used to generate pure sulfuric acid aerosols, an efficient microencapsulation of pure sulfuric acid

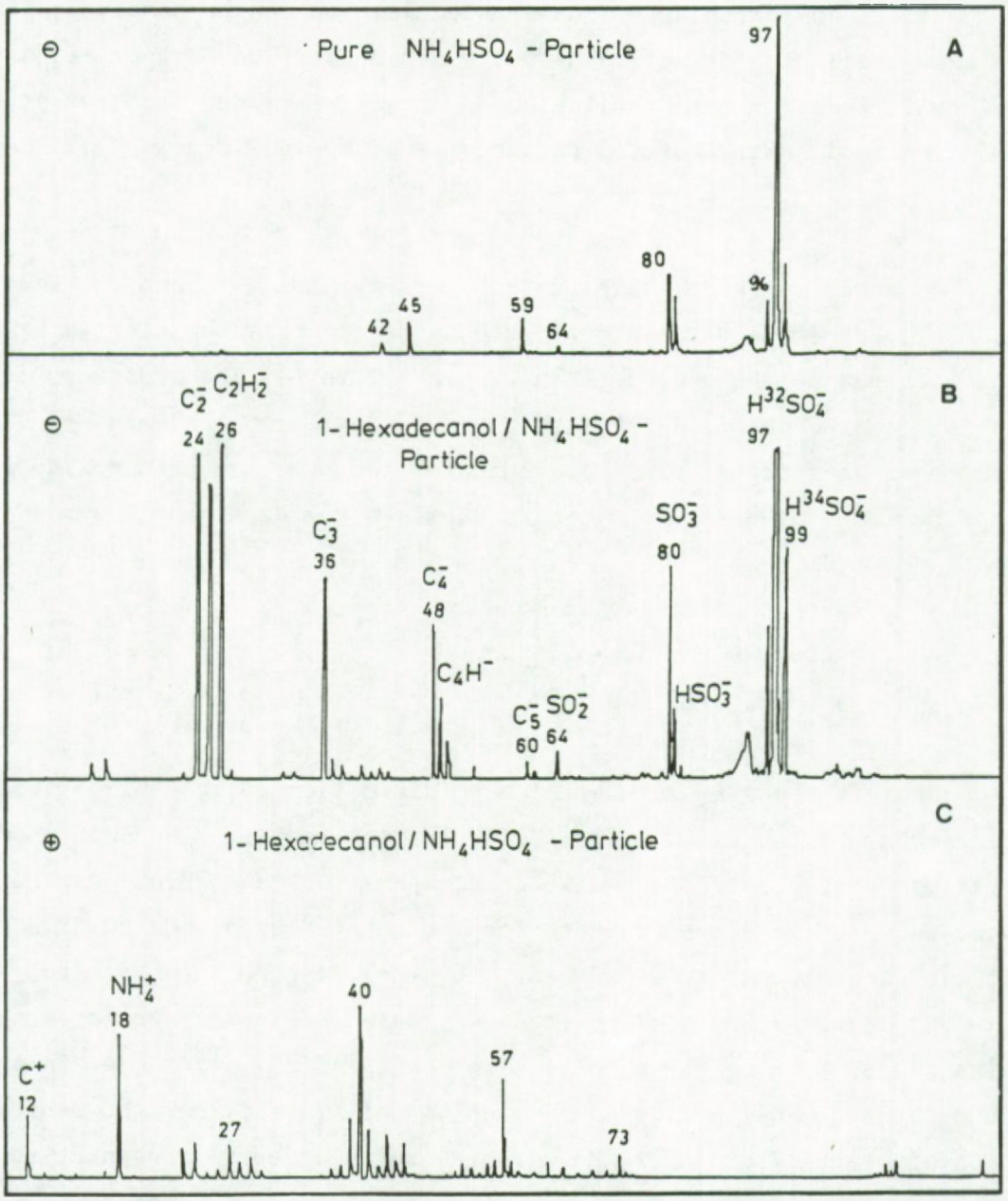

Figure 6.3: a) Negative mode spectrum of a pure NH_4HSO_4-particle
b) and c) negative and positive mode spectrum of
NH_4HSO_4-particle coated with n-hexadecanol.

aerosol was achieved (4). Sulfuric acid samples could not be analyzed in LAMMA because the particles are not stable in the vacuum of the sample chamber.

6.3 THE INVESTIGATION OF HETEROGENEOUS REACTIONS OF PAH ON PARTICLE SURFACES

One of the most interesting topics of today is the behaviour and life time of surface enriched polycyclic aromatic hydrocarbons (PAH) under various atmospheric conditions. Many of the PAH compounds and their derivatives are potent mutagens and ubiquitous air pollutants (6,7). Since the PAH are usually found associated with airborne particulate matter and are presumably adsorbed on the particle surface (see Figure 6.1b), PAH reactions with e.g. O_3 and NO_2 as well as photochemical reactions will occur at the particle/atmosphere interface. The intention of the present study was to demonstrate the usefulness of the LAMMA in studying heterogeneous gas-phase reactions of PAH, artificially deposited on micrometer-size particulate substrates.

6.3.1 Experimental

The PAH/NaCl-system was chosen because of the similarity of the PAH-emission situation : a primary thermodynamically stable particle acts as a condensation nucleus in a PAH-supersaturated exhaust gas stream. From in-situ photoemission studies of garage aerosols or burner aerosols (8) it is known that condensed higher PAH are non-uniformly enriched at particle surfaces. One explanation for this finding might be the fact, that once the PAH is deposited at an irregularity of a particle surface the further growth of the PAH-deposit continues at the same place. The PAH/NaCl-system is also advantageous for LAMMA. at low laser energy, PAH give rise to intense molecular ion peaks which can easily be identified (9),

while (complicating) recombination reactions between NaCl and PAH are not observed.

Aerosol generation

The experimental set-up for the production of artificially PAH-coated particles is given in Figure 6.4 (4). A Collison atomizer was employed for production of NaCl-condensation nuclei. A small vessel in a temperature controlled oil bath contains the PAH. Nitrogen, which is heated up by leading it through a spiral type glass tube, enters the vessel and takes up PAH-vapour. The gas is then mixed with NaCl aerosol in a heated ring-gap mixing nozzle. In the following cooling section the vapour condenses on the primary particles, thus forming an agglomerate, whose thickness depends on the amount of vapour available and thus on the temperature of the oil bath.

The primary NaCl-aerosol had a concentration around $5x10^4$ cm^{-3} and a median diameter of 0.1 - 0.2 μm. After the coating procedure an increase of diameter between 5 and around 100 % was observed depending on the PAH-supersaturation. As a typical example anthracene coated NaCl-particles are shown in Figure 6.5. The anthracene cristallization typically starts at the edge of a particle.

The relative humidity in the set-up was kept close to 0 %. After passing the condensation section the coated particles were mixed with reactive gases. Bromine and NO_2 were delivered from a permeation system (10) with known permeation rates. Ozone as a reactive gas was generated by use of a Welsbach O_2-discharge unit. The ozone concentration was determined by iodometric analysis (11). The mixture of the reactive gas and the coated aerosol was conducted through a plastic chamber (60 l) allowing a residence time of about 10 minutes. From this a known sample volume was drawn.

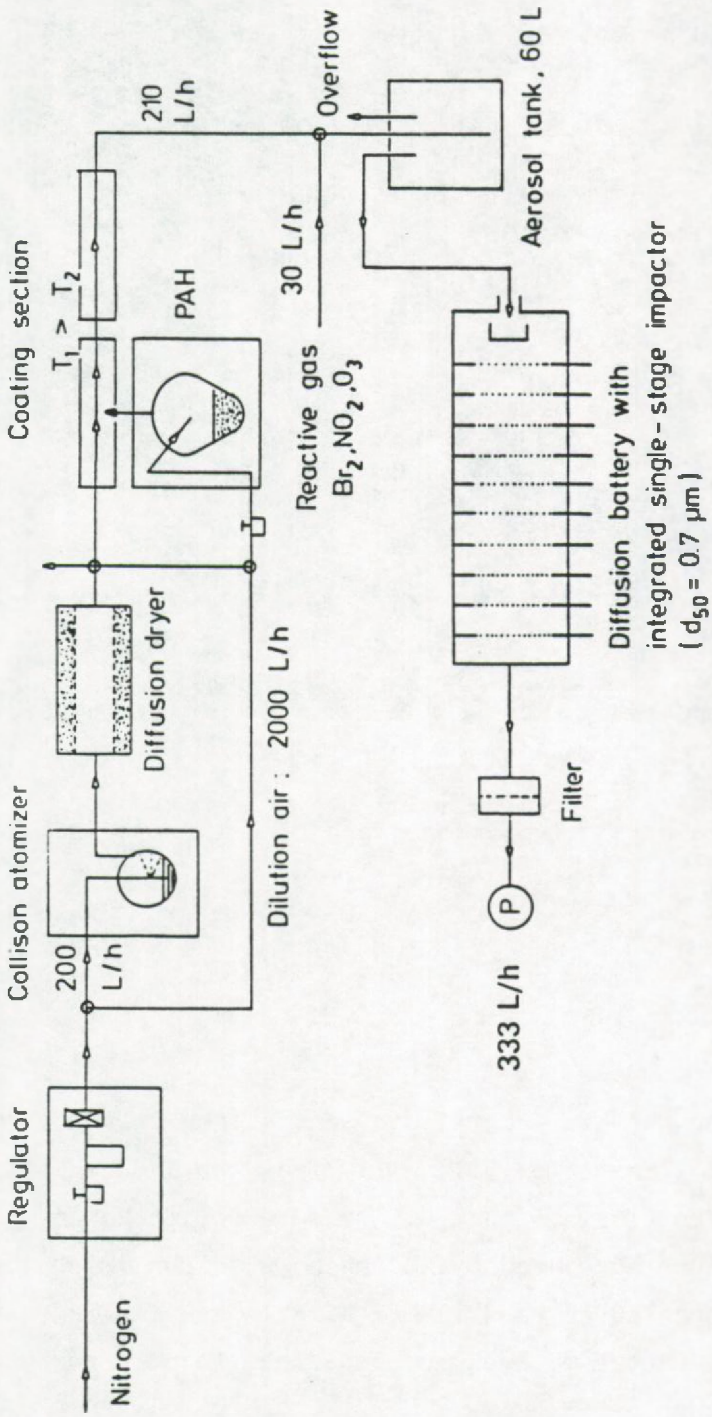

Figure 6.4: Experimental set-up for PAH-coated aerosol particles and subsequent reaction with Br_2, NO_2 and O_3.

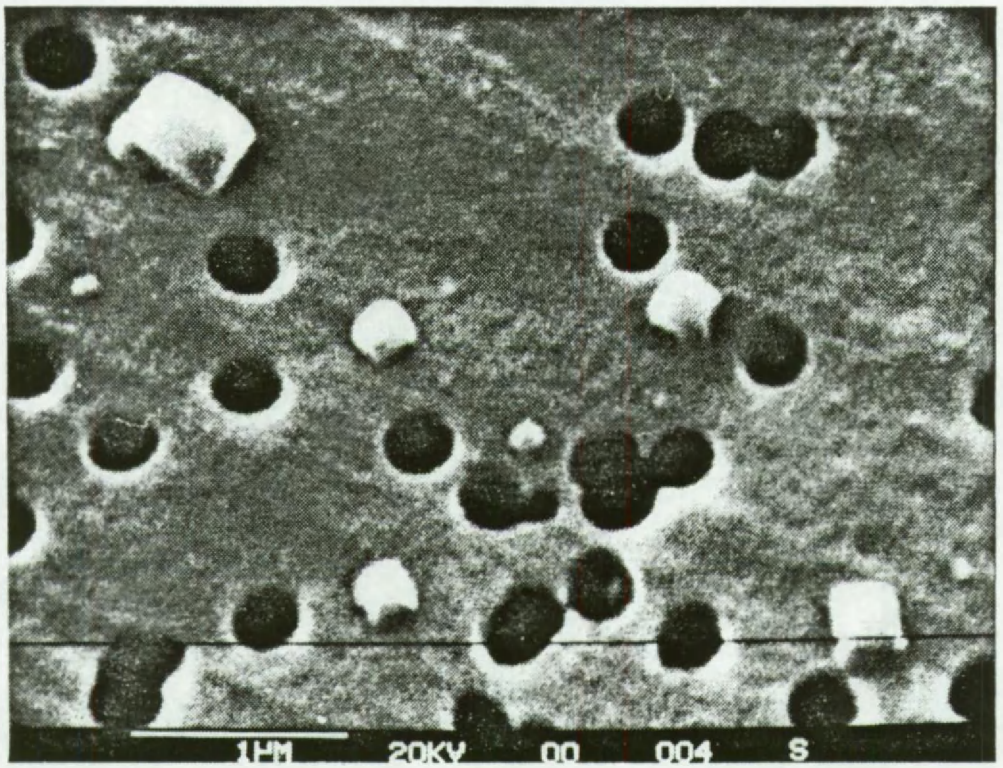

Figure 6.5: Electron micrograph of anthracene-coated NaCl particles on a Nuclepore filter.

Sampling procedure

For LAMMA analysis a one-stage impactor with an effective cut-off diameter of 0.7 μm (12) was applied as sampling instrument. Particles larger than 0.7 μm were collected on <100 nm thick foils of Formvar supported by 300 mesh electron microscope grids which were mounted on Parafilm backings. The sampling time was restricted to ten minutes to avoid overloading; this corresponded to a sampled air volume of 55.5 l.

In order to obtain the average PAH-content of the aerosols parallel samples were drawn using glass fibre filters (Whatman GFC). The filters were extracted for 10 min. by a known volume of n-heptane under assistance of an ultrasonic bath. After the

extraction, the filter and extract were subjected to a centrifugation procedure for 3 min. at 15,000 rpm. An aliquot of the supernatant extract was transferred for fluorimetric analysis.

Fluorimetric analysis

Fluorimetric analysis was performed by a Zeiss PMQ II with fluorimetric device ZFM4. Excitation and emission wavelengths according to Jurgensen et al. (13) were applied. Calibration standards of the PAH under study were prepared in n-heptane and stored in a dark and cool place.

6.3.2 Results and discussion

Fluorimetric analyses of the coated aerosols were carried out before and after the exposure to the reactive gases, in order to assess whether a heterogeneous gas-phase reaction took place or not. The decision for a reaction between PAH and reactive gas was based on a statistical treatment of the data at a 95 %-confidence level. The results are compiled in Table 6.1. As can be seen the amount of fluoranthene and chrysene was not altered by the attack of ozone. A bromination reaction under the applied experimental conditions was observed only in the case of anthracene and perylene. No influence of nitrogen dioxide on any PAH under study was observed. Considering the PAH used and data like the first ionization potential or aromaticity index (see Table 6.2), one can expect a high reactivity of anthracene and perylene as predicted by Nielsen (14). Although a high NO_2-concentration was applied, no difference between the NO_2-treated and untreated aerosol was found. This seems to corroborate the conclusion of Grosjean et al. (15) that a fast conversion of PAH only takes place in the presence of an acid. Similar results were obtained by Pitts (6) and Nielsen (14). On the other hand, Sine (16) reported a reaction between NO_2 and pyrene for carbon black as a carrier for the PAH.

Table 6.1: Results of fluorimetric analysis (n = 6) of aerosols before and after exposure to reactive gases.

PAH	PAH-concentration of aerosol (in $\mu g/m^3$ ± S.D. per meas.)		reaction (p = 0.95)
	Exposure to O_3 (3.32 mg/m^3)		
	Before	After	
Anthracene	393 ± 13	253 ± 25	Yes
Perylene	45.5 ± 4.5	2.8 ± 0.5	Yes
Phenanthrene	12.1 ± 1.6	7.3 ± 1.6	Yes
Pyrene	94.8 ± 5.1	57.1 ± 5.0	Yes
Fluoranthrene	3.8 ± 1.1	4.3 ± 0.4	No
Chrysene	33.8 ± 1.1	31.2 ± 1.9	No
	Exposure to Br_2 (187 $\mu g/m^3$)		
	Before	After	
Anthracene	9.5 ± 2.2	1.1 ± 0.6	Yes
Perylene	7.0 ± 0.1	5.2 ± 0.3	Yes
Phenanthrene	2.3 ± 0.2	2.1 ± 0.6	No
Pyrene	17.9 ± 1.4	17.7 ± 1.1	No
Fluoranthrene	0.4 ± 0.1	0.4 ± 0.1	No
Chrysene	61.6 ± 6.7	57.3 ± 4.9	No
	Exposure to NO_2 (1.79 mg/m^3)		
	Before	After	
Anthracene	140 ± 6	147 ± 2	No
Perylene	0.5 ± 0.1	0.5 ± 0.1	No
Phenanthrene	6.5 ± 1.3	5.3 ± 6.1	No
Pyrene	5.5 ± 0.6	6.1 ± 0.5	No
Fluoranthrene	11.9 ± 0.9	11.5 ± 1.2	No
Chrysene	85.4 ± 8.1	80.7 ± 5.9	No

LAMMA was applied to the aerosol samples drawn in parallel. One advantage of LAMMA in the desorption mode is the possibility of progressively analysing the surface layers of a particle in repetitive laser shots. This is demonstrated in Figure 6.6. First only the molecular ion of the PAH is observed. After three low-energy shots, a fourth pulse at higher power onto the same particle reveals the thermodynamically stable particle core. All coatings of the PAH used in this study were observed in the mass spectra, by occurrence of their molecular ions.

In agreement with the results obtained by fluorimetric analysis, no reaction products were found by LAMMA for the NO_2-experiments. Also for the bromination study no reaction products were observed, but possibly some reaction products might have volatilized in the vacuum of the instrument before the analysis. Additionnally, brominated compounds characteristically have a lower specific sensitivity in LAMMA (17).

The ozone-PAH experiments yielded similar reactivities as found by fluorimetry except for perylene.

The mass spectra found before and after O_3 treatment of the anthracene-coated particles are given in Figure 6.7. Also shown for comparison are the mass spectra of anthrachinone enriched onto NaCl-particles. The mass peaks at m/z = 180 and 152 are due to single and double loss of CO (M = 28) from the anthrachinone molecule (M = 208). While in electron impact mass spectrometry, anthrachinone yields a molecular ion mass peak at m/z = 208, in the LAMMA-spectrum a quasi molecular ion at m/z = 209 of $(M+H)^+$ shows up (17). The interpretation of the spectra in Figure 6.7, is consistent with the following reaction.

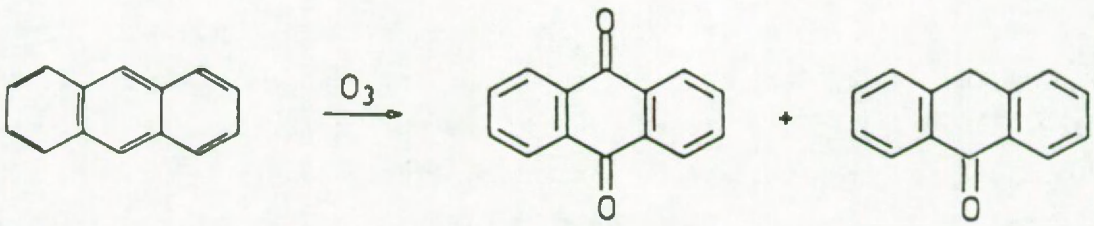

Anthrachinone and anthrone (M = 194) are thus the main products of the ozonisation reaction. This is in agreement with findings of several groups, e.g. (18). The mass peak at m/z = 193 can be due to the loss of a hydrogen radical from anthrone, the peak at m/z = 165 is due to °CHO-loss.

Phenanthrene/NaCl aerosols sometimes show a complete conversion of phenanthrene by O_3 as seen in Figure 6.8. On some particles we found also unreacted phenanthrene. The reaction seems to be the following :

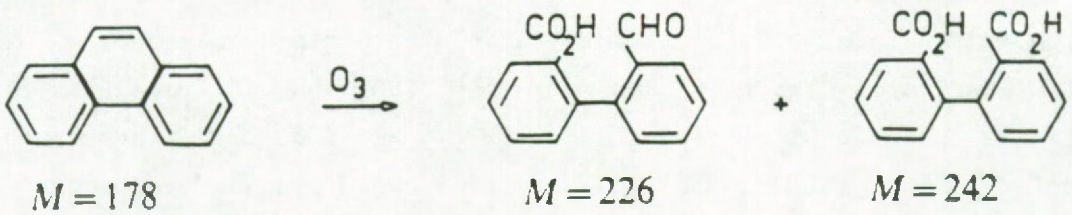

The mass peaks at m/z = 225 and 241 are due to H^+-loss from the acids.

LAMMA-spectra for the pyrene/NaCl particles are shown in Figure 6.9. The mass peaks at m/z = 218, 234 and 250 are due to incorporation of oxygen atoms in the pyrene molecule (m/z = 202).

Table 6.2: Aromaticity index and ionization potential for the considered PAH.

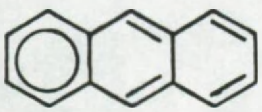

Aromaticity Index : 0.71
Ionization Potential : 7.47 eV

Anthracene

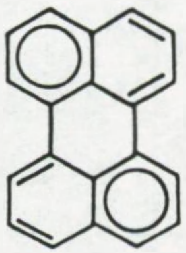

AI : 0.83
IP : 7.00 eV

Perylene

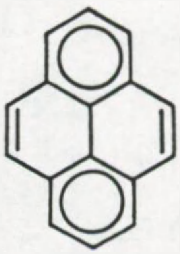

AI : 1.25
IP : 7.45

Pyrene

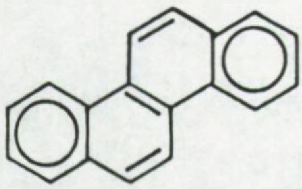

Chrysene

AI : 0.93
IP : 7.60 eV

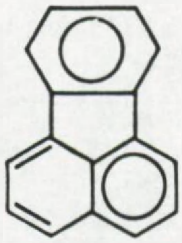

Fluoranthene

AI : 1.25
IP : 7.80 eV

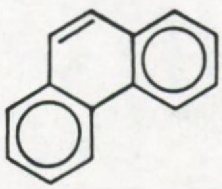

Phenanthrene

AI : 1.43
IP : 7.86 eV

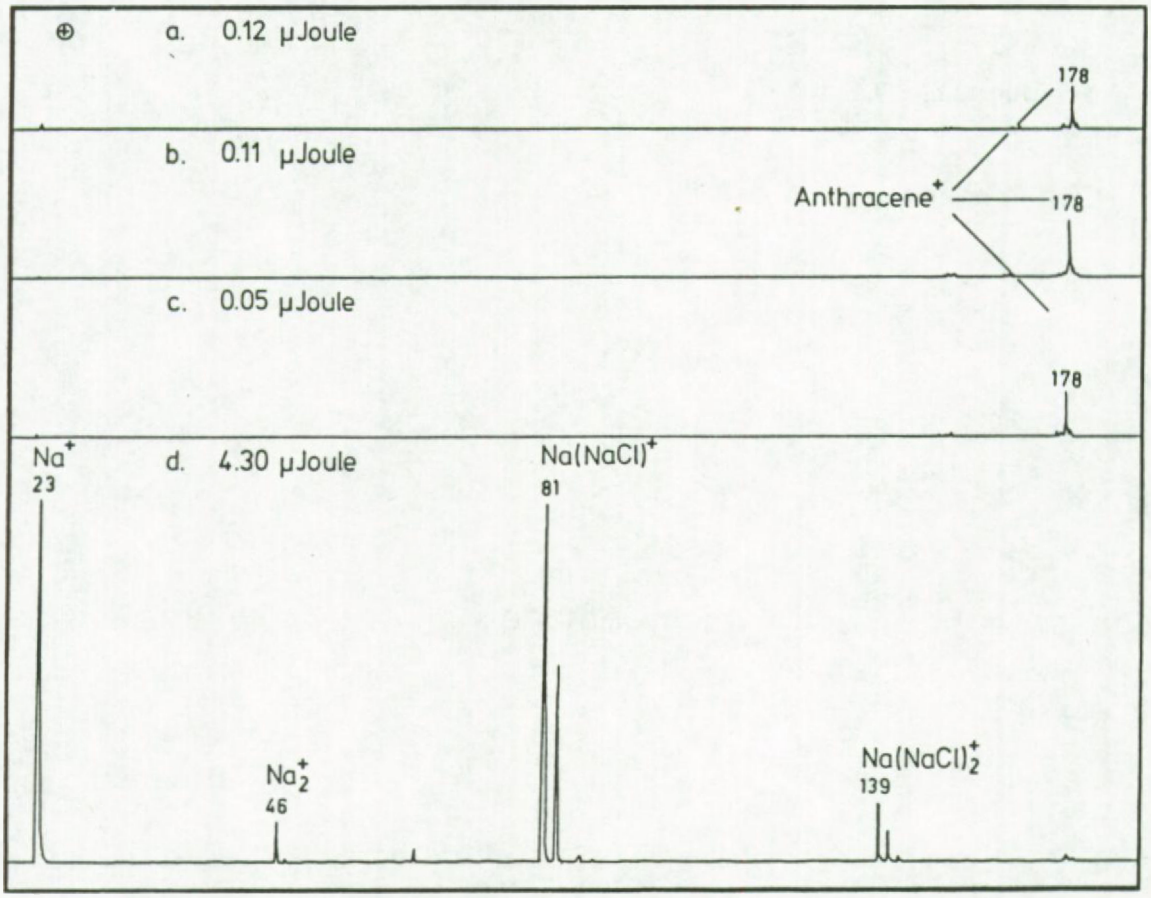

Figure 6.6: LAMMA-spectra of subsequent laser shots on an anthracene-coated NaCl-particle.

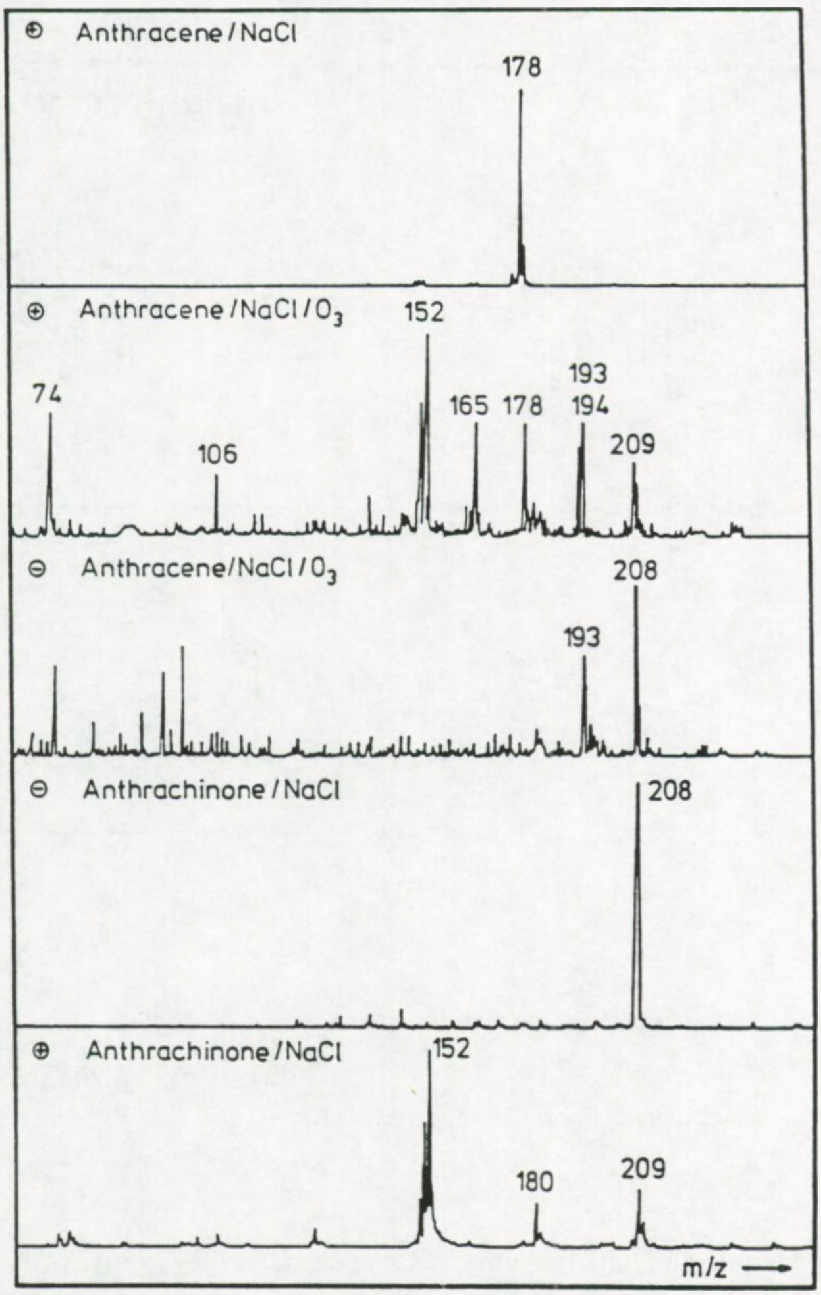

Figure 6.7: LAMMA-spectra of an untreated anthracene-coated NaCl-particle (in the positive ion mode), of anthracene/NaCl-particles after reaction with O_3 (in positive and negative ion mode) and of anthrachinone coated NaCl-particles (in the positive and negative ion mode).

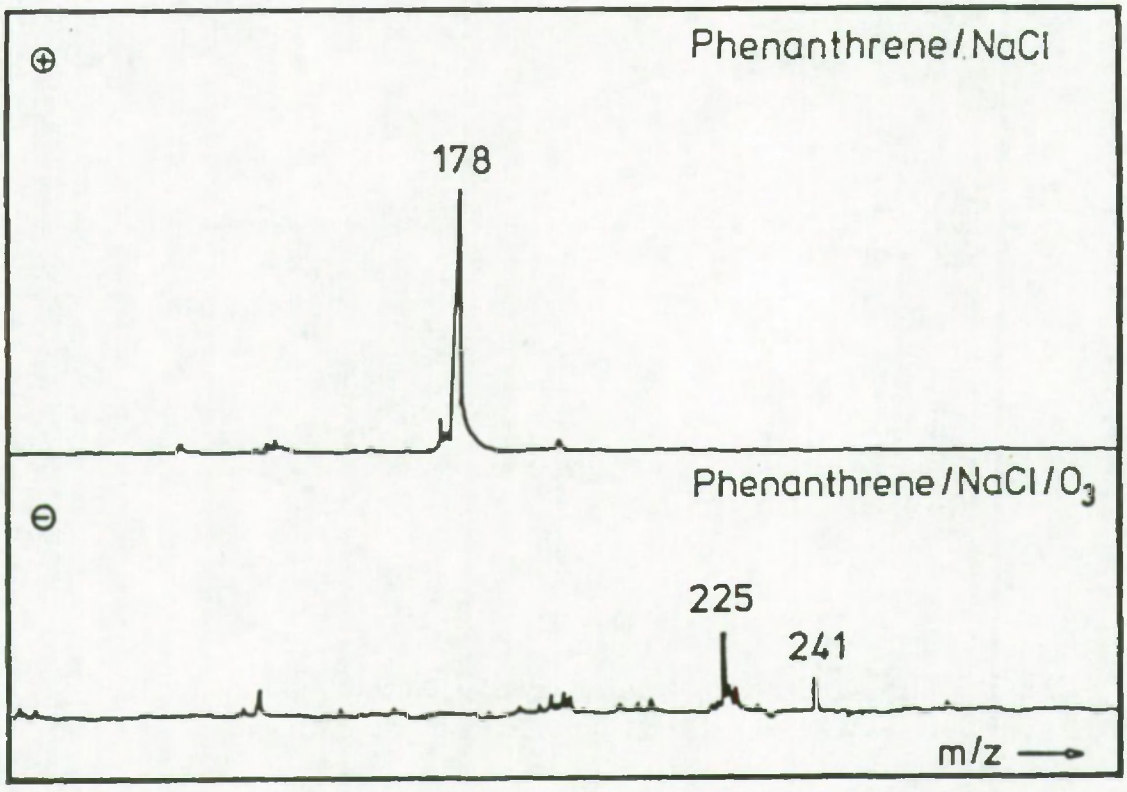

Figure 6.8: LAMMA-spectra of phenanthrene-coated NaCl-particles before and after exposure to O_3, in the positive and negative ion mode respectively.

A detailed and unambiguous structural interpretation is not possible at present.

For the most reactive PAH in our study, perylene, no reaction product, could be observed by LAMMA after exposure to O_3. However, the fact that also no molecular ion was detected anymore in these mass spectra, strongly indicated that an efficient transformation of perylene had taken place.

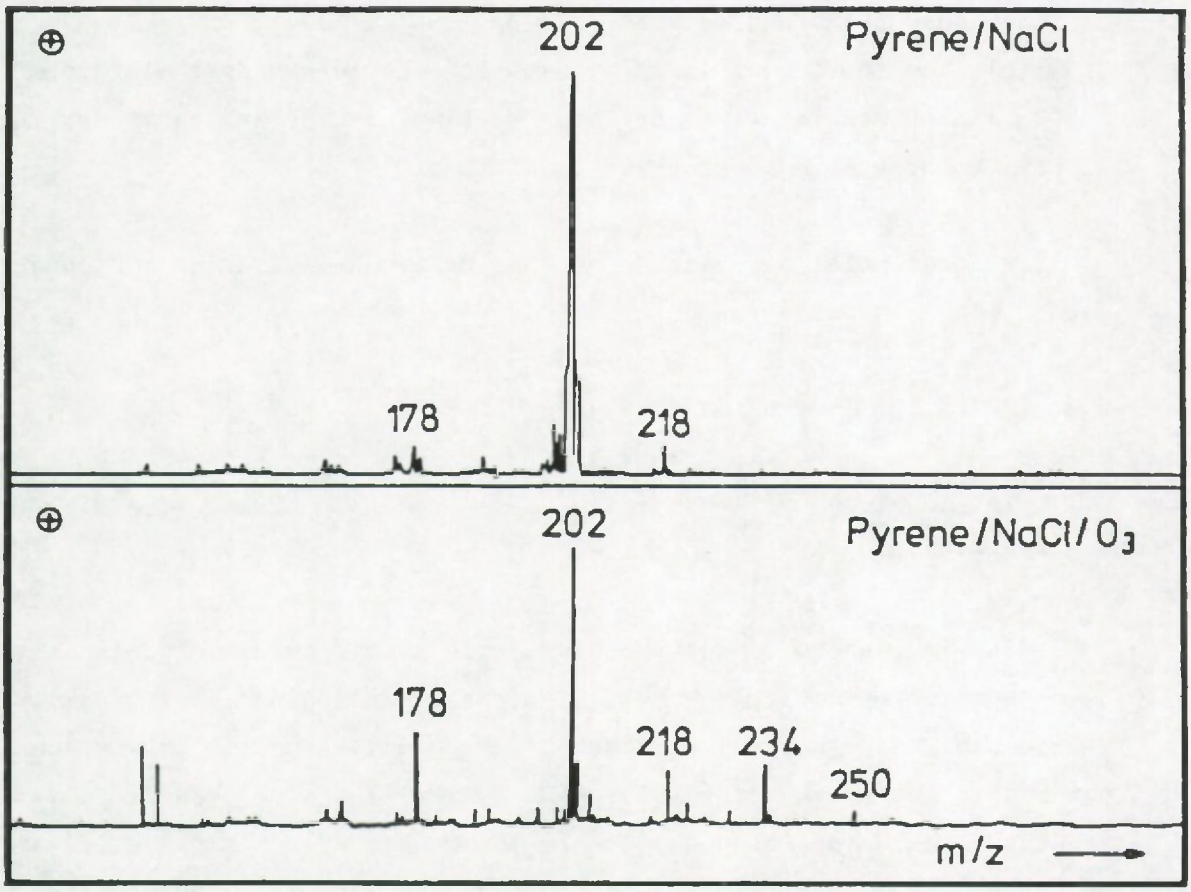

Figure 6.9: LAMMA-spectra (in the positive and negative ion mode) of pyrene-coated NaCl-particles before and after exposure

6.3.3 Conclusion

The following conclusions are possible from the results presented above:

1. By the application of soft consecutive laser pulses (<0.2 μJoule) microstructure description of aerosol particles is possible. For a system like PAH/NaCl, it is further possible to study gas-phase reactions and identify some reaction products at the femtogram-level.
2. In case of weakly-bound reaction products, thermodynamically unstable products, or complex mixtures of structurally similar

compounds, LAMMA analysis is not applicable.

3. Within the short reaction time used for the aerosol/gas mixture O_3 is more reactive than Br_2 or NO_2. Fluoranthene and chrysene seem to be stable under these conditions.

Further studies are planned on the behaviour of PAH enriched onto diesel exhaust aerosol.

6.4. THE INTERACTION OF GASEOUS HNO_3 WITH THE SEASALT AEROSOL

6.4.1 Introduction

The presence of nitrate in coarse mode coastal aerosols has been reported by several research workers including Junge (19), Savoie and Prospero (20), Harrison and Pio (21). A possible reaction pathway is the uptake of gaseous HNO_3 by the seasalt aerosol. This reaction could be of considerable importance as a removal process for HNO_3 from the atmosphere, especially in polluted marine environments as coastal zones and seas surrounded by industrialized countries as e.g. the North Sea. The uptake of of gaseous nitrate by coarse mode aerosols followed by wet and dry deposition of the particles constitutes an effective mechanism for nitrate deposition to the sea surface. Moreover it was already pointed out that nitrate-controlled enhancement of marine primary production can be induced by rainfall in coastal and near-urban regions (22).

With laser microprobe mass analysis it became possible to detect the nitrate enrichments in individual seasalt particles (23). A special sample collection technique has to be used to remove gaseous HNO_3 before the collection of the aerosols, because enhanced particulate nitrate production can result from HNO_3 uptake by the previously impacted aerosol particulates (23-25).

6.4.2 Experimental

Marine aerosols were collected by means of a 5-stage single-orifice Battelle-type cascade impactor. The principle of the impactor is illustrated in Figure 6.10 (26). The aerosol stream is drawn into the impactor by a pump, passes through a single orifice and impinges upon the first plate. Particles in the aerosol stream having a large enough inertia will impact upon the plate, and smaller particles will make the turn into the next stage. The orifice of the 5 successive impaction stages are carefully designed so that the aerosol is separated in the following fractions: > 4 μm, 2-1 μm, 1-0.5 μm and 0.5-0.25 μm equivalent aerodynamic diameter when operating at a flow rate of 1.2 l/min. The aerosols are deposited on thin Formvar films supported by electron microscope grids. The grids were mounted onto Mylar foils. Particles smaller than 0.25 μm diameter which pass through the fifth stage are collected on a back-up filter (0.4 μm pore size Nuclepore filter).

The samples were collected during periods of 10 minutes at various coastal locations in both the Northern and Southern Hemisphere. The loaded electron microscope grids were mounted in the LAMMA-instrument. Single aerosol particles in the micrometric range can be totally evaporized by a single laser pulse of the focussed Nd-YAG laser. If desired the laser power can be attenuated drastically by means of an optical filter sequence. When LAMMA is used in the laser desorption mode, a low laser energy (! 0.2 μJ) is applied to an aerosol particle. This can result in the selective excitation and analysis of the surface material. The spectrum recorded for the second laser pulse on the same particle allows the analysis of the core material. For the $NaCl/NaNO_3$ systems this analysis procedure was tested on laboratory generated aerosol standards.

Sodium chloride aerosols were produced by the pneumatic nebulization of an aqueous 0.1 M NaCl solution. The airborne

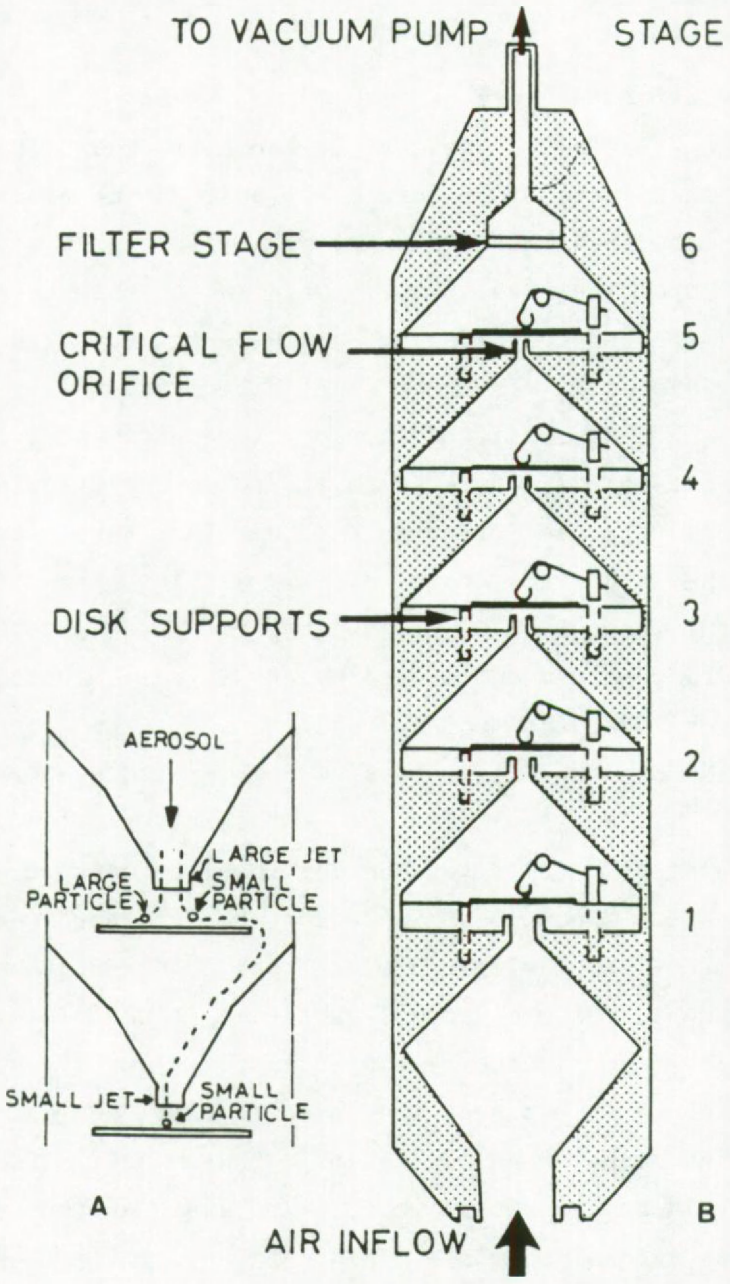

Figure 6.10: a) Schematic representation of the principle of size differential impaction of particles using a series of orifices of successively smaller diameter.
b) Five stage cascade impactor as used in the present project. Calibrated flow rate was 1.2 l/min. (26)

particulates are dried during their passage through a diffusion dryer (see Figure 6.2). The aerosols were collected with the cascade impactor. According to the particle size distribution measured with the automated EPMA the aerosol contained 240 particles per cm^3 in the size range of 1-2 μm diameter.

The HNO_3 test atmosphere was produced by diffusion of the HNO_3 vapour through a capillary from a thermostated solution (10). After dilution with N_2 the gaseous HNO_3 was passed over the NaCl particles already collected in the impactor. Other reference samples were prepared by direct nebulization of a NaCl-$NaNO_3$ mixture, and by the interaction of gaseous HNO_3 with NaCl droplets. All the samples were analyzed with LAMMA in the desorption mode (23,25) .

6.4.3 Results and discussion

Figure 6.11a shows a negative mode LAMMA-spectrum as is often found for the surface layer of 1-4 μm aerodynamic diameter coastal aerosol particles. The cluster ion distribution is identical to the one recorded for pure $NaNO_3$ (see section 5.4). Figure 6.11b shows the LAMMA-spectrum of the core material of the same particle as in Figure 6.11a. In this spectrum the typical seasalt derived ions Cl^-, $NaCl^-$ and $NaCl_2^-$ are predominant.

Identical spectra were recorded on all the laboratory generated aerosol standards. This clearly indicates the capibility of LAMMA to assess $NaNO_3$-enrichments in individual marine aerosols in a very convenient way.

The interpretation of the results in terms of mechanistic pathways needs further explanation. During the sampling in ambient air in coastal regions, relative humidities are frequently higher than 70 %. This means that the hygroscopic seasalt aerosols are present in a liquid or at least semi-liquid state. If the aerosols are impacted on the collection surface, crystallization of the salt

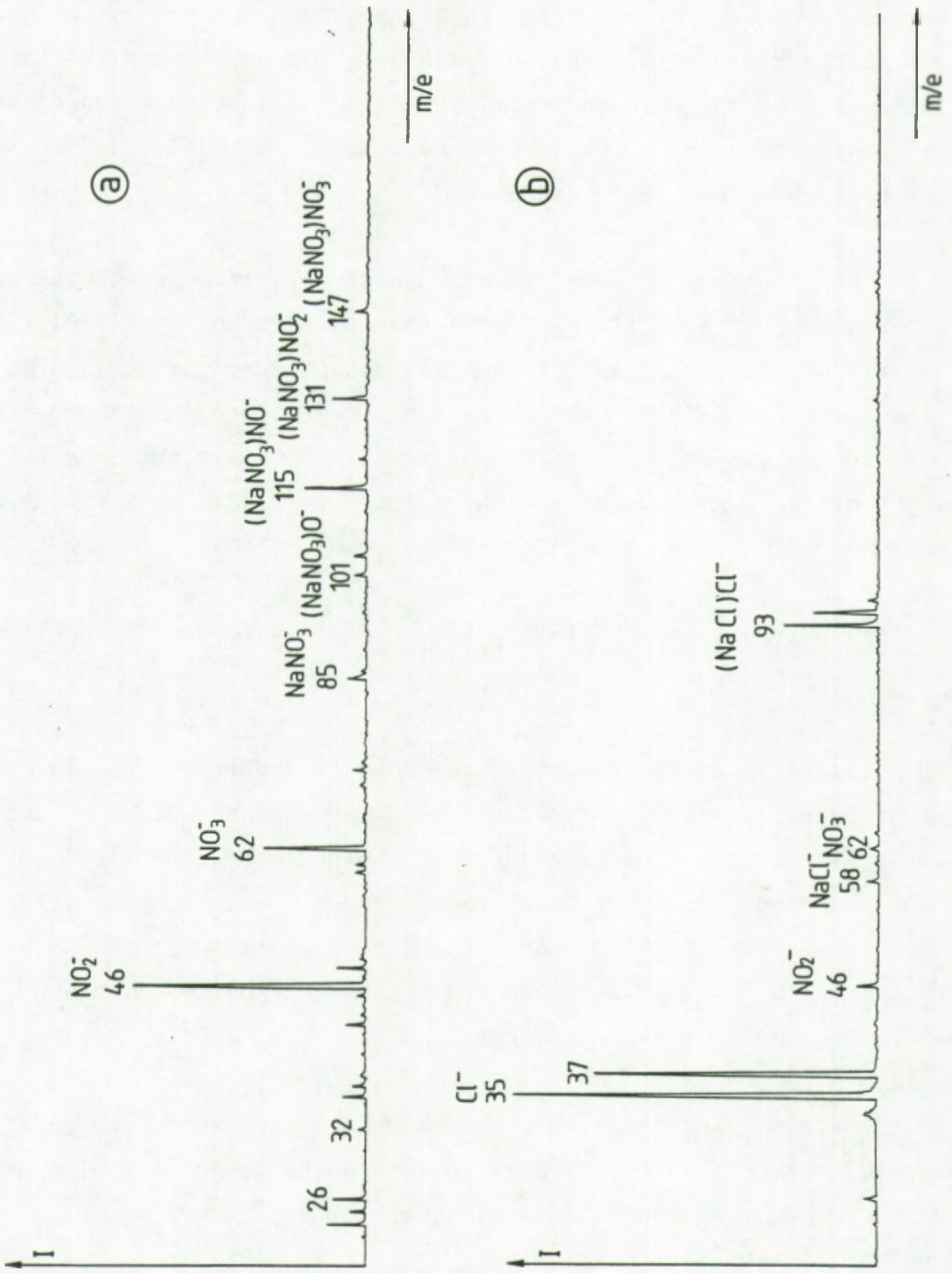

Figure 6.11: Negative-mode LAMMA-spectra of (a) the surface layer and (b) the core, of a 1-4 μm diameter marine aerosol particle, showing surface enrichment of $NaNO_3$ (the $^{35}Cl^-$ peak in spectrum (b) is in overflow).

mixture will occur. As a consequence the aerosol particles cannot be sampled in the impactor without a disturbance of their true airborne state. In both the ambient and laboratory generated aerosols, $NaNO_3$ could be preferentially desorbed from the particles and adittional measurements on the reference standards showed that LAMMA is more sensitive for NaCl detection than for $NaNO_3$ (25). Thus, preferential desorption of $NaNO_3$ can be excluded and the results have to be interpreted as a surface enrichment of $NaNO_3$. This surface enrichment on the other hand cannot be interpreted as being representative for the particles "in the airborne state" on the basis of the LAMMA results as such, for the reason explained above.

An enhancement of particulate nitrate production could possibly result from the interaction of the sampled marine aerosol with the HNO_3 gas in the passing air stream. For short term samplings, where the gas phase is in "equilibrium" with the aerosols, no serious implications are to be expected. Moreover aluminium impactors as used in the present study are known to be efficient scavengers for HNO_3 themselves (27). For a quantitative assessment by long term samplings, however, the use of a NaF-coated denuder for the adsorption of the HNO_3-gas previously to aerosol collection is highly recommendable (28).

In a comparative study of impactor samples collected for 10 minutes at the Belgian coast both with and without denuder, $NaNO_3$-enrichments could be observed by LAMMA in the desorption mode in all samples and no quantitative differences could be inferred from the LAMMA-measurements.

6.4.4 Conclusion

By laser microprobe mass analysis the uptake of gaseous HNO_3 by individual marine aerosol particles can straightforwardly be detected and the speculations from indirect observations are proven on the basis of individual particle analysis. The elevated concentrations frequently detected in combination with the laboratory studies on the interaction of HNO_3-vapour with NaCl-particulates confirm the rapid uptake of HNO_3 by the marine aerosol.

The application of the analysis technique on ambient aerosol samples will be demonstrated in the following chapter.

6.5 REFERENCES

1. B.R. Appel, E.L. Kothey, E.M. Hoffer and J.J. Wesolowski, in The Character and Origin of Smog Aerosols,ed. by G.M. Hidy, P.K. Meuller, D. Grosjean, B.R. Appel and J.J. Wesolowski, John Wiley and Sons, New York, 1980, p.315.

2. D.B. Kittelson and D.F. Dolan, in Generation of Aerosols and Facilities for Exposure Experiments, ed. by K. Willeke, Ann Arbor Science, 1980, p.337.

3. W.M. Mansfield, Nature, 175, 247 (1955)

4. R. Niessner, Sci. Total Environ., 36, 353 (1984).

5. Y.I. Kogan and Z.A. Burnasheva, Russian Journal of Physical Chemistry, 34, 1240 (1960).

6. J.N. Pitts Jr., Phil. Trans. R. Soc. Lond. A, 290, 551 (1979).

7. J.N. Pitts.,Jr, K.A. Van Cauwenberghe, D. Grosjean, J.P. Schmidt D.R. Fitch, W.L. Belser, G.B. Knudson, P.M. Hynds, Science, 207, 763 (1980).

8. H. Burtsher, R. Niessner and A. Schmidt-Ott, Aerosols, Science Technology, and Industrial Applications of Airborne Particles, ed. B.Y.H. Liu, D.Y.H. Pui and H. Fissan, Elsevier, New York, Amsterdam, Oxford, (1984), pp. 436 - 438.

9. T. Mauney, F. Adams, and M.R. Sine, Sci. Total Environ., 36, 215 (1984).

10. A. Teckentrup and D. Klockow, Anal. Chem.,50, 1728 (1978).

11. VDI-Richtlinie 2468, Blatt 1; Verein Deutscher Ingenieure, Düsseldorf, F.R.G.

12. R. Niessner, D. Klockow, H. Fissan and F. Kapitza J. Aerosol Sci., 13, 223 (1982).

13. A. Jurgensen, e.l. Inman and D.J. Winefordner, Anal. Chem. Acta., 131, 187 (1981).

14. T. Nielsen, Environ. Sci. Technol. 18, 157 (1984).

15. D. Grosjean, K. Fung and J. Harrison, Environ. Sci. Technol., 17, 673 (1983).

16. M.R. Sine "The Formation of Particles emmited from Oil Shale Retorting". Dissertation, Department of Chemistry, Fort Collins, Colorado, U.S.A., pp. 247, (1983).

17. L. Van Vaeck, personal communication.

18. K. Nikolaon, P. Masclet and G. Mouvier, Sci. Total Environ., 32, 103 (1984).

19. C.E. Junge, Tellus, 8, 127 (1956).

20. D.L. Savoie and J.M. Prospero, Geophys. Res. Letters, 9, 1207 (1980).

21. R.M. Harrison and C.A. Pio, Atmos. Environ., 17, 1733 (1983).

22. H.W. Paerl, Nature, 315, 747 (1985).

23. F.J. Bruynseels and R.E. Van Grieken, Atmos. Environ., 19, 1969 (1985).

24. Ph. Otten, F. Bruynseels, and R. Van Grieken, Proceedings of the Workshop on "Aerosols and Acid Deposition" of the Concerted Action COST 611, ECN Petten, The Netherlands, 9 - 10 December 1985, 67 - 71.

25. Ph. Otten, F. Bruynseels, and R. Van Grieken, Bull. Soc. Chim. Belg., 95, 447 (1986).

26. H.J. Annegarn, R.E. Van Grieken, P. Van Espen, F. von Blottnitz, J.P.F. Sellschop, and J.W. Winchester, Madoqua, II, 107 (1978).

27. S. V. Hering, Proceedings of the Second International Aerosol Conference, West Berlin, Germany, 22 -26 September 1986, 515 (1986).

28. J. Slanina, L. Lamsen-Doornenbal, W. Lingerak, W. Meilof, D. Klockow and R. Niessner, Int. J. Environ. Anal. Chem., 9, 59 (1981).

CHAPTER 7. CHEMICAL CHARACTERIZATION OF INDIVIDUAL AEROSOL PARTICLES FROM REMOTE AND POLLUTED AREAS

7.1 CHARACTERIZATION OF INDIVIDUAL PARTICLE TYPES IN COASTAL AIR

7.1.1 Introduction

The LAMMA-technique has been applied to a set of samples collected with a cascade impactor on a transect from a beach site under constant influence of steady clean onshore trade winds, towards and through a very heavily polluted industrialized area. The aim was to evaluate the general potential of this single particle analysis technique to remote and polluted marine aerosol studies, to find out to what extent information about the chemical diversity of individual particles is obtained, and to contribute to answers concerning sources, transport processes and physico-chemical interaction processes that influence the chemical composition of the airborne particulate matter.

7.1.2 Experimental

Sampling sites

The samples were taken near the Brazilian coast, in the state of Bahia, north of the city of Salvador, under stable landinward wind from the East (Figure 7.1). The sample inlet of the cascade impactor was held at 2 m above the ground. The sites were:

#1) a beach location, about 20 m from the waterline of the Atlantic ocean, 20 km northeast of Salvador.

#2) a hill with low vegetation, 10 km from the coast and 15 km north of the beach location.

#3) a residential area, 30 km from the Ocean, 20 km downwind from

site # 2, and downwind from a zone with tropical vegetation but also downwind from cement and metallurgy plants.

#4) a strongly polluted site 10 km more to the north, 20 km from the coast, in the center of a large industrial complex including petrochemical, fertilizer and metallurgical plants.

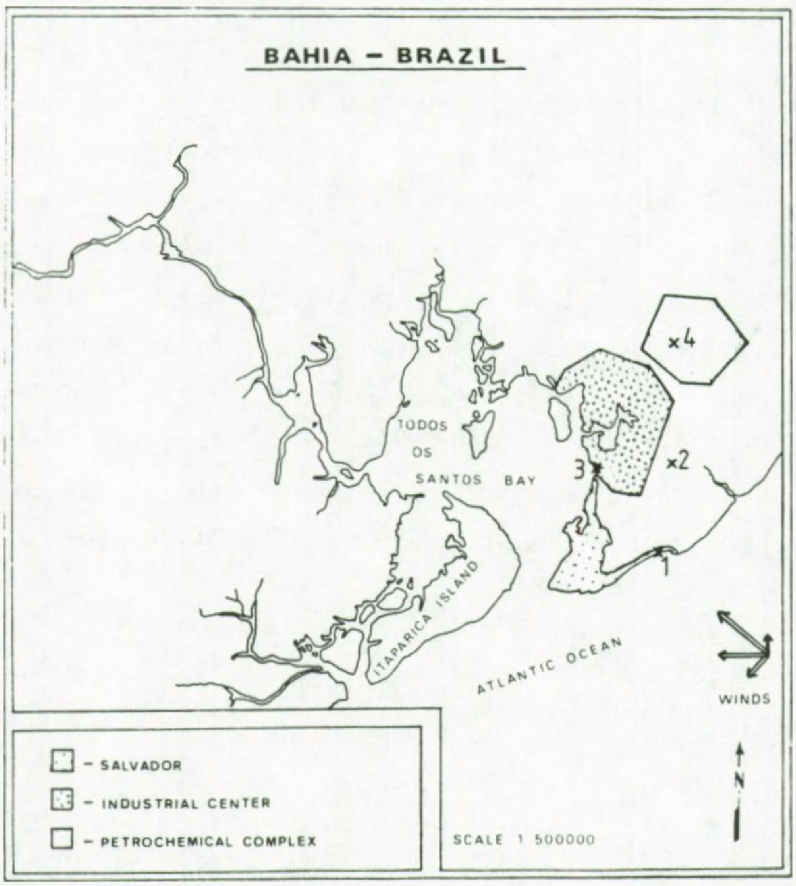

Figure 7.1: Map of the sampling area in Bahia; the sampling locations are indicated and numbered from 1 to 4.

Sample collection and preparation

Atmospheric aerosol particles were sampled by means of a five-stage single-orifice Battelle-type cascade impactor (see section 6.4) , operated at a flow rate of 1.2 l/min. The equivalent aerodynamic diameter ranges for the particles collected at the different stages are: > 4 μm, 4-2 μm, 2-1 μm, 0.5-0.25 μm for stages 1 to 5, respectively.

The particles were deposited on a thin foil of Formvar, supported by 300 mesh electron microscope (EM) grids, which were mounted on Mylar backings. The sampling time was restricted to ten minutes; experience has shown that, with the experimental system used, much longer collection times in marine environments lead to overloading what results in unwanted particle-particle interactions.

In the laboratory the Mylar backing was removed from the EM-grids to yield suitable targets for LAMMA-analysis. The loaded EM-grids were mounted in the LAMMA sample chamber and for each stage 50 - 100 particles were randomly selected for LAMMA-analysis.

7.1.3 Results

In order to characterize the different types of aerosol particles, the LAMMA-spectra were classified according to the major elemental and cluster ion peaks, that are characteristic for a given sampling site and associated with specific particle size ranges. The positive and negative LAMMA-spectra of nearly all particles could each be classified as belonging to one of six specific particle types.

In Table 7.1 the distribution of the mass spectral types over the different impactor stages is shown for the four sampling sites. A representative spectrum of each type is shown in Figures 7.1 and 7.2.

Table 7.1: Comoosition, as inferred from LAMMA-analysis, and size distribution of different particle types at the four locations (+ = present).

SAMPLE SITE	# 1: BEACH					# 2: INLAND					# 3: INLAND					# 4: INDUSTRIAL AREA				
PARTICLE TYPE \ SIZE RANGE (μm)	>4	4-2	2-1	1-0.5	0.5-0.25	>4	4-2	2-1	0.5-0.25		>4	4-2	2-1	1-0.5	0.5-0.25	>4	4-2	2-1	1-0.5	0.5-0.25
#P1)Sea salt particles	+	+	+			+	+	+			+	+	+			+				
#P2)Sea salt particles rich in $NaNO_3$			+				+	+				+	+				+	+		
#P3)Ca-rich particles	+	+		+	+							+		+						
#P4)Na,Mg,Al,Si, K, Ca, Ti,Fe-rich particles				+	+														+	
#P5)Particles containing some elements such as Al, Si,Ti,V,Mn Fe,Co,Sr,Ba																			+	
#P6)Particles also yielding positive mass peaks at m/e= 18,30,42,44,56,86,88, 100									+					+	+				+	+
#N1)Sea salt particles	+	+	+			+	+	+			+	+	+			+				
#N2)Sea salt particles rich in $NaNO_3$			+				+	+				+	+				+	+		
#N3)SO_n^--rich particles	+	+										+								
#N4)HSO_4^--rich particles containing organic material.				+	+				+					+	+				+	
#N5)Particles containing PO_n^- and NO_n^--anions																			+	
#N6)Particles containing HSO_4^-,NO_n^--anions and organic material																				+

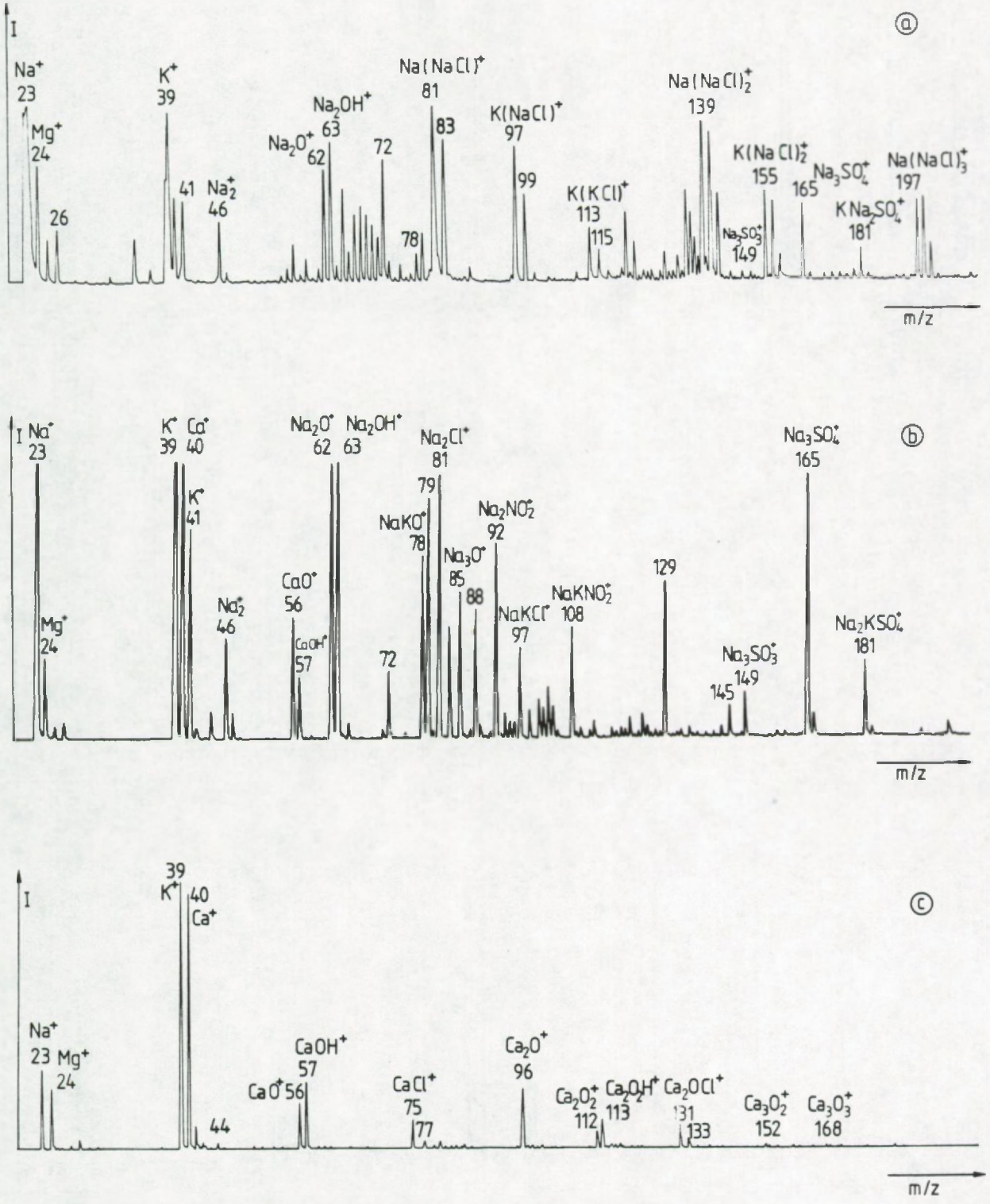

Figure 7.1a to c: Positive LAMMA-spectra of the type P1 to P3 respectively. The corresponding particle types are indicated in Table 7.1.

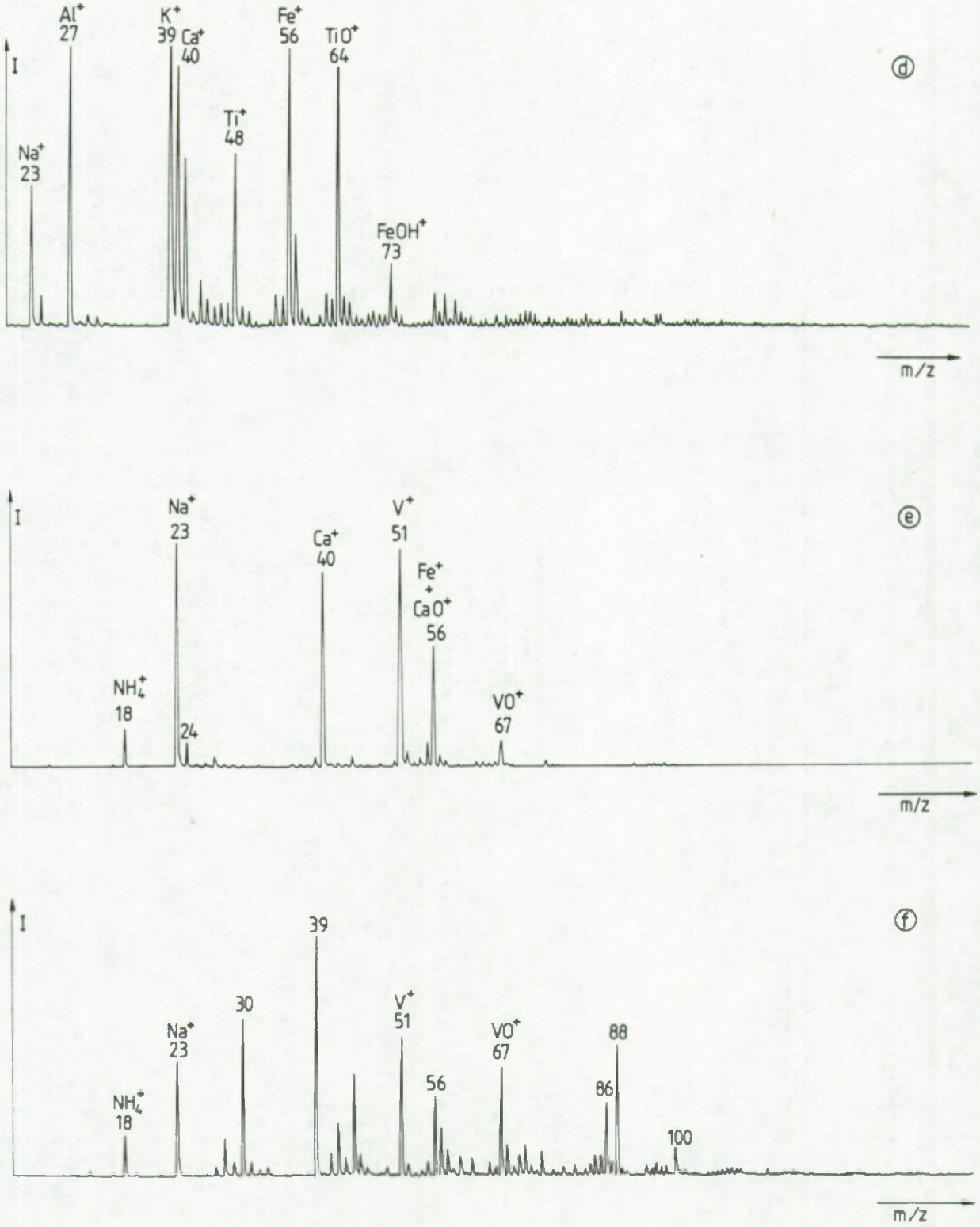

Figure 7.1d to f: Positive LAMMA-spectra of the type P4 to P6 respectively. The corresponding particle types are indicated in Table 7.1.

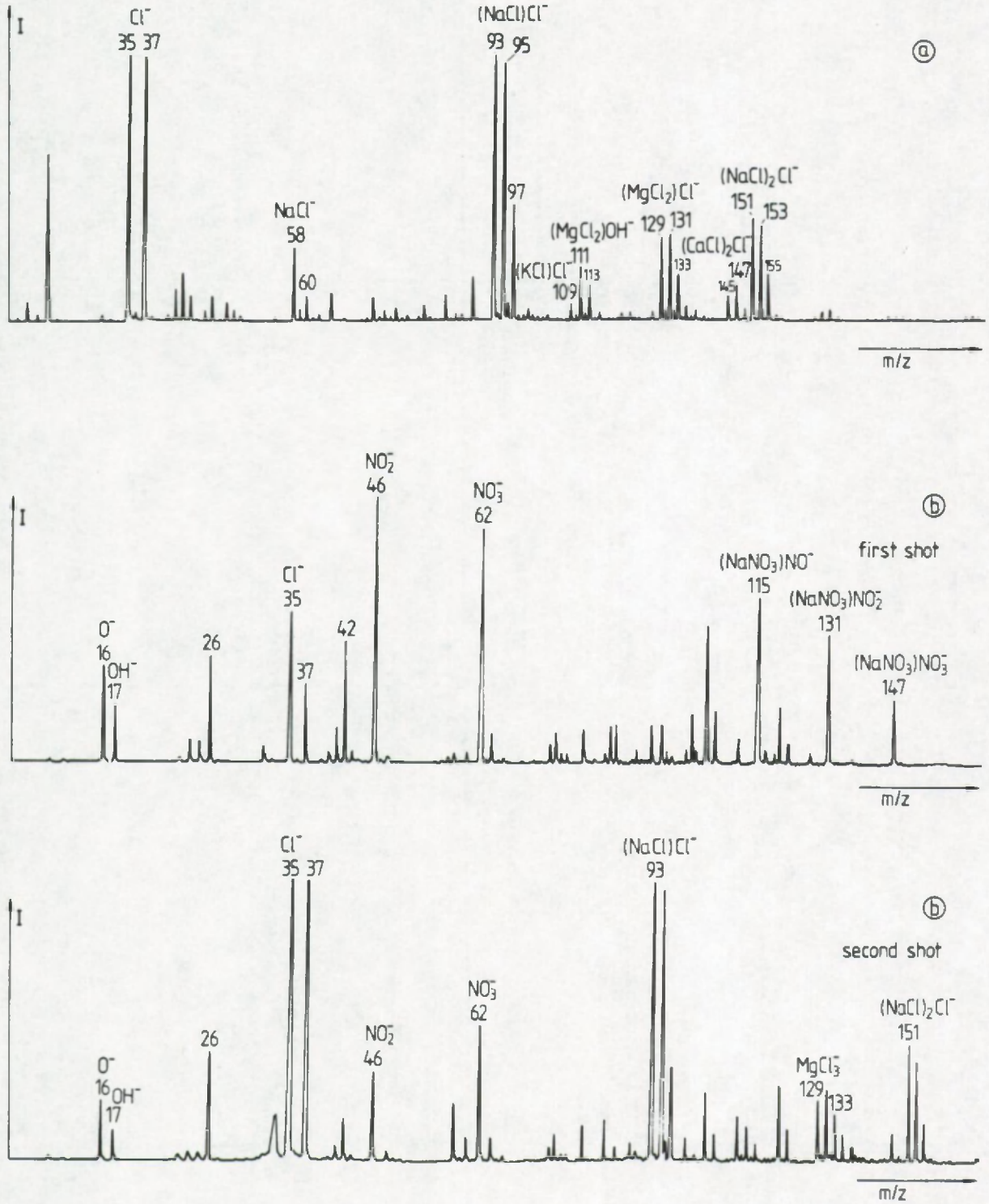

Figure 7.2a and b: Negative LAMMA-spectra of the type N1 to N2 respectively. The corresponding particle types are indicated in Table 7.1.

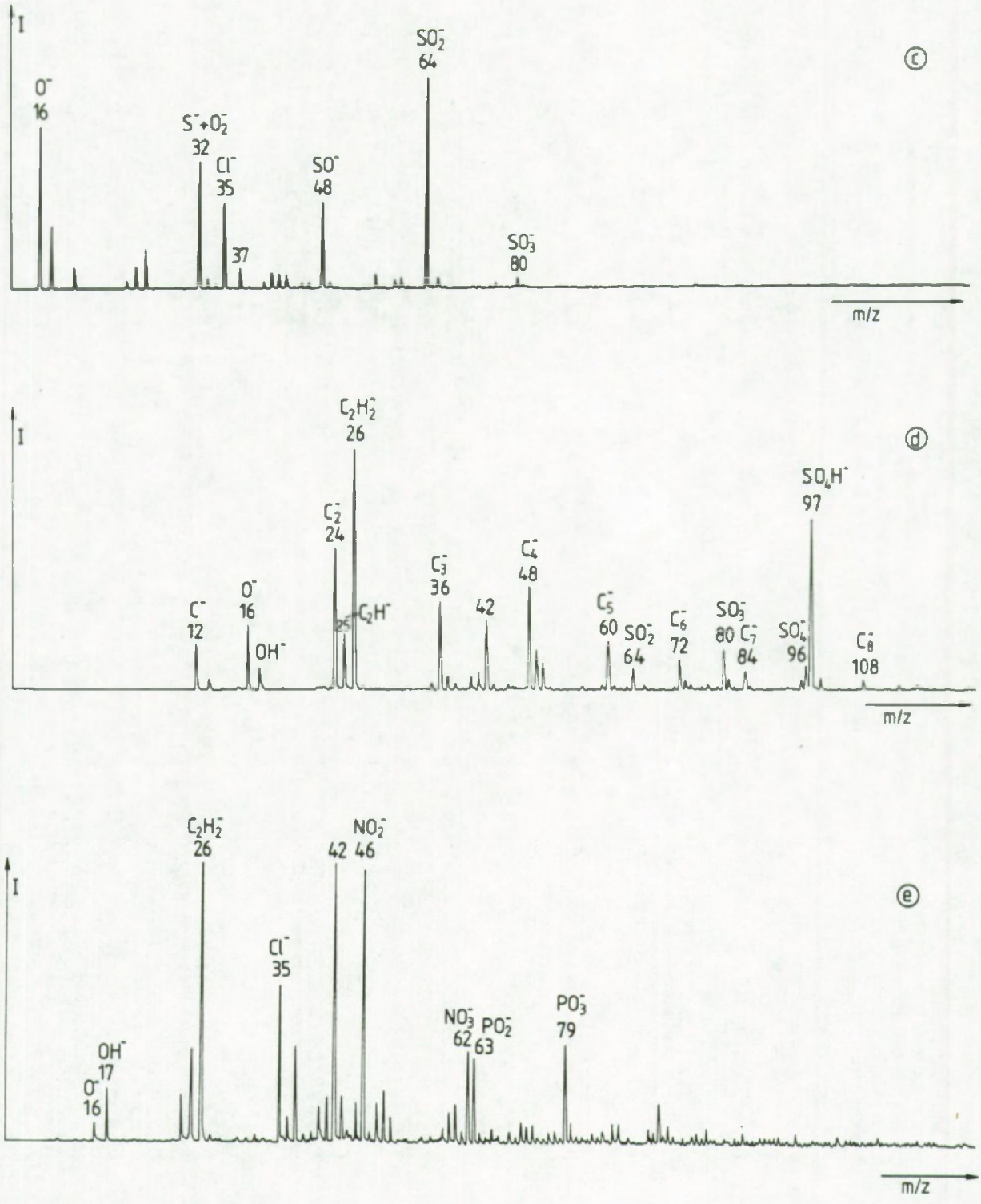

Figure 7.2c to e: Negative mode LAMMA-spectra of the types N3 to N5 respectively. The corresponding particle types are indicated in Table 7.1.

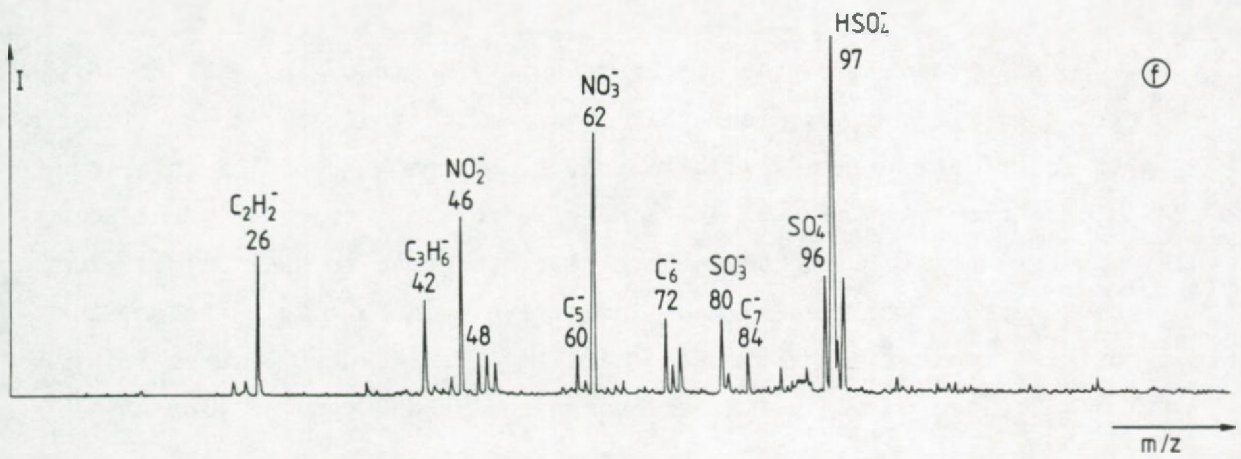

Figure 7.2f: Negative LAMMA-spectrum of the type N6. The corresponding particle type is indicated in Table 7.1.

Impactor stage 4 from site # 2 was not suitable for LAMMA-analysis because the background Formvar foil was too thick to yield suitable spectra. This was attributed to an incorrect preparation of the supporting foil. Electron probe X-ray microanalysis on this sample revealed the presence of sulfur-rich particles.

7.1.4 Discussion

The seasalt particles, formed by direct particle production by the oceans, through the mechanism of bubble bursting (1), are, as expected for a coastal region, abundantly present in the giant particles (> 1 μm). The major mass peaks in their positive mode LAMMA-spectra (Figure 7.1a) are identified as Na- and K-chlorides ($M_nCl_{n-1}^+$ with M = Na and or K. The intensity ratio of the cluster

ions at m/z = 149 ($Na_3SO_3^+$) and m/z = 165 ($Na_3SO_4^+$) is typical for alkali sulfates (see section 5.3). The negative LAMMA-spectra are dominated by $M_{n-1}Cl_n^-$ (M = Na, K), $MgCl_3^-$, $(MgCl_2)OH^-$ and $CaCl_3^-$ (Figure 7.2.a).

When applying the laser desorption mode to the seasalt particles, it becomes clear that a significant fraction of these particles are coated with a layer of $NaNO_3$ devoid of chloride. Spectra proving that LAMMA can give direct evidence for such coatings on sampled aerosols have been discussed in section 6.4. The negative mode spectra are most indicative (Figure 7.2b), though the positive mode spectra can also give important clues (Figures 7.1b). The mass peak at m/z = 129 is interpreted as $Na_3CO_3^+$ (section 5.5). The positive mode spectra also show the presence of sulfate in the same aerosol particle. Also the intensity of the sulfate clusters relative to the chloride clusters are systematically more intense in these aerosols, compared to the pure seasalt particles. This can also be explained by the uptake of gaseous acidic sulfates as will be exlained more thoroughly in the next section 7.2.

With respect to the nitrogen cycle, several authors have already shown that the homogeneous gas phase condensation of HNO_3 is rather improbable under normal atmospheric conditions and that particulate nitrate is formed by a heterogeneous reaction between HNO_3-vapour and the atmospheric particulate matter, resulting in the release of HCl from seasalt (2-8). Only a minor fraction of the 1-2 μm seasalt particles are found to be rich in $NaNO_3$ in the sample taken at the beach location; inland the NaCl-$NaNO_3$ particles become predominant in the 1-4 μm size range and, in the industrialized area, pure seasalt particles are not observed in this size range at all. The drastic abundance difference of $NaNO_3$-rich particles between the beach site and the industrialized area samples gives direct indication for a very fast gas-to-particle conversion of a fraction of the seasalt towards sodium nitrate in polluted air. It is not surprising that the $NaNO_3$-enrichments are first detected in the smallest seasalt particles because of their larger

surface-to-volume ratio compared to the bigger aerosol particles. This is consistent with a heterogeneous gas phase-particle transformation process governing the nitrate concentrations in the individual aerosol particles.

The positive spectra of the Ca-rich particles as shown in Figures 7.1c can result from various Ca-compounds as e.g. $CaSO_4$, $CaCO_3$ and CaO: indeed these all yield predominantly $Ca(CaO)_n^+$, $(CaO)_n^+$ and $(CaO)_nH^+$ mass peaks (see section 5.2). In some cases the negative mode spectra reveal the presence of the sulfate ion by the SO_n^--distribution (n = 0 to 3) (Figure 7.2c) and identify the particles as $CaSO_4$. Besides the $CaSO_4$-particles, EPMA shows the presence of $CaCO_3$ by an intense Ca-signal in the X-ray spectrum and the absence of other elememts with Z > 11. Microanalyses on aerosols, sampled under clean as well as polluted conditions, also confirm the presence of $CaSO_4$-particles. They can eventually be formed by e.g. differential crystallization of seaspray droplets and subsequent breakup of the particles, or from the reaction of acid gases with $CaCO_3$.

Type #P4 spectra (Figure 7.1d) are derived from particles which contain typical crustal elements but whose size distribution does not plead for local soil dispersion as their source. EPMA measurements on the 0.5-0.25 μm stage of sample #1 showed particles rich in Al, Si, Fe and S, all with a non-crystalline aspect, and predominantly particles rich in Al and Si and less S and Fe in the 1-0.5 μm size particles (in addition to the Ca-compound particles). In view of the presence of S and the fact that the only negative spectrum type seen for $\leq$ 1 μm particles at the beach is #N4, it is likely then that the spectra of type #P4 and #N4 are derived at least partially from the same particles. In mass spectra #N4 (Figure 7.2d) wich are frequently seen and are related to different particle types, the peaks at m/z = 64, 80, 96 and 97 are always found and they correspond to SO_2^-, SO_3^-, SO_4^- and HSO_4^-, respectively. This cluster ion pattern is typical for sulfur compounds such as $(NH_4)_2SO_4$ and NH_4HSO_4 (see sections 5.4 and 6.2) . The abundance of

C_n^--cluster ions is typical for carbonaceous material in these particles. They are therefore identified as fly ash like particles associated with carbonaceous material and sulfate, either derived from the common charcoal fires on the beach or related to the diurnal wind directions in the coastal regions.

The heterogeneous group #P5 (Figure 7.1e) gathers diverse spectra which exhibit mass peaks from a combination of the following elements: Al, Si, Ca, Ti, V, Mn, Fe, Co, Ba and NH_4^+. Because of the high variability in composition and the unusual metal enrichments, the corresponding particles are classified as pollution particles from the industrial complex and the local metallurgy. The negative mode type #N5 (Figure 7.2e) and #N4 LAMMA-spectra might be derived from the particles yielding type #P5 positive spectra . Indeed spectra #P5 and #N5 are both only seen for 1-0.5 μm particles in the industrial zone. The mass peaks in #N5 do not point to soot or sulfur compounds but to phosphorus and nitrogen oxy-salts. Since #N5 spectra are seen much less frequently than #P5 spectra, since EPMA showed transition elements such as Ti, V, Mn, Fe, and Co to occur together with S and since all #P5 spectra contained a strong NH_4^--signal, confirming the presence of $(NH_4)_2SO_4$ or NH_4HSO_4 also demonstrated by #N4 spectra, it can be assumed that spectra #P5 and some of the #N4 spectra result from the same particles formed by combustion processes and that they reacted with sulfur compounds either during their emission or in the atmosphere.

Group #P6 refers to particles, which in addition to crustal elements or V, yield positive mass peaks at m/z = 18, 30, 42, 44, 56, 86, 88 and 100 (Figure 7.1f). These particles are found in the smallest size-range and their relative abundance increases inland and in the industrial area. Most of the observed peaks could be interpreted as originating from organic N-compounds such as amines. Indeed the electron impact mass fragments of amines include: $CH_2{=}NH_2^+$ (m/z = 30), $C_2H_4^+$ (m/z = 42), $C_2H_6N^+$ (m/z = 44), $C_5H_{12}N^+$ (m/z = 86), $C_4H_{14}N^+$ (m/z = 100). Amines can be released into the atmosphere by decomposition of proteins of biogenic origin or by the

combustion of polyamides or they could be emitted by the amine-producing industry near site #4. The occurrence of type #P6 spectra as a function of particle size and sampling location suggests that they are related to some of the negative spectra #N4, #N5 and #N6 (Figure 7.2f). The latter spectra are only seen for the smallest size range and show HSO_4^-, carbonaceous clusters and NO_n^- anions. The simultaneous detection of HSO_4^- and NO_n^- in one spectrum is rather remarkable and will be discussed in some detail. It is generally believed that NO_3^- volatilization should occur in the presence of acidic sulfate (9). This could indicate that both anions are neutralized by e.g. ammonium, or that they are present as an amine salt. Another, though rather speculative possibility is that both anions are separated by an organic surface coating, similar to the model system in section 6.2. The possibility that two separate aerosol particles are evaporated in one single laser shot so that the recorded spectrum is actually a superposition of two individual particle spectra is highly unprobable because the NO_n^--mass signals were never observed on their own i.e. as a specific particle type. The sample under consideration is the only one in which up to now, NO_n^--anions were detected with LAMMA in the 0.5 to 0.25 μm size range (pure submicrometer NH_4NO_3-particles are unstable under vacuum).

7.1.5 Conclusion

LAMMA has shown that the formation of particulate nitrate is actually occuring in coastal areas with their high atmospheric sea salt load, and that polluted air enfavours this production mechanism. In the accumulation mode particles, sulfur is present in compounds such as NH_4HSO_4 or $(NH_4)SO_4$, containing significant quantities of carbonaceous material. Besides inorganic nitrogen as NH_4^+ and NO_n^-, organic N-compounds (probably amines) were also detected in the industrial area.

7.2 CHARACTERIZATION OF NORTH SEA AEROSOLS BY INDIVIDUAL PARTICLE ANALYSIS

7.2.1 Introduction

It has been shown that atmospheric input of particulate matter to the North Sea by wet and dry deposition processes is of significant importance as a pathway for the pollution emitted by the surrounding industrialized countries (10). Table 7.2 gives a survey of the estimated yearly input of anthropogenic pollutants into the North Sea by atmospheric and river transport, direct discharges and dumping. It can be seen that the atmospheric input constitutes the major pollution source for metals such as Zn, Pb and Cu but also for PAH, hexachlorohexanes and PCB. Studies for the estimation of deposition fluxes from the atmosphere to the sea have used of a variety of analytical techniques for the analysis of the bulk chemical composition of air and rain water samples but micro-analytical techniques have rarely be invoked. The microanalytical techniques used for single particle analysis in this study are LAMMA and electron probe X-ray microanalysis (EPMA).

EPMA has been used for many years now in microanalytical studies. The development of suitable software for automated particle analysis and of data processing routines by multivariate analysis highly reduces the analysis time necessary to characterize an aerosol sample based on individual particle analysis measurements.

In the present study EPMA was employed to identify the major elements of individual aerosol particles, collected on Nuclepore filters. The particles were classified according to their matrix composition by hierarchical clustering methods resulting in the assessment of the abundances for the different particle types, that can be correlated with their source of emission or their formation mechanism.

Table 7.2: Inputs of polutants to the North sea (525000km^2) (10 and references therein).

Substance	Atmospheric input (1975-1982) t/yr*	Via Rivers t/yr	Direct discharges t/yr	Amounts dumped t/yr	Total t/yr
As	220 - 270	123	133	75	300 - 1100
Cd	110 - 900	1600	2300	2080	7400 - 19500
Cu	1400 - 13500	1900	1800	60	3800 - 5200
Cr	70 - 1400	26	32	38	<100 - 110
Hg	< 36	1430	560	10	2400 - 5600
Ni	360 - 3600	2400	2200	4200	12400 - 21800
Pb	3600 - 13000	16500	5700	7400	36800 -107100
Zn	7200 - 77500				
Fe	92600				
Mn	3100				
Polycyclic aromatic hydrocarbons (PAH's)	100 - 1500	50			150 - 1500
VOCl(1)		750			
EOCl(2)		450			
DOCl(3)		6600			
Hexachlorobutadiene		20			
Chlorobenzene		70			
Chlorotoluene		70			
Dichlorobenzene		260			
Dichlorotoluene		60			
Trichlorobenzene		60			
Hexachlorobenzene		4			
Hexachlorocyclohexane					
(α-HCH)	10 - 100	1			13 - 100
(γ-HCH)		1.5			
Chlorinated phenols		370			
PCB's	10 - 200				

(1) Volatile organic chlorine
(2) Extractable organic chlorine
(3) Dissolved organic chlorine
*t/yr: ton per year

LAMMA-measurements on simultaneously collected impactor samples revealed additional data about the low Z-elements (Z<11) and about the speciation of elements such as S and N. Because of the favourable detection limits in LAMMA, trace elements were also detected. The interpretation of the LAMMA-data is based on an attentive inspection of the mass spectra and the comparison with reference spectra of standard samples.

7.2.2 Sampling

Aerosols and rain water samples were collected on board the research vessel "Belgica" during a cruise in the Southern Bight of the North Sea from 12 to 16 December 1984. Atmospheric aerosols were collected by filtration onto a 47 mm diameter Nuclepore filter with a pore size of 0.4 and 8 μm in cascade geometry, at a flow rate of 12 l/min. Table 7.3 gives a survey of the sampling periods for the filters. The sampling was carried out in the mast on the fore deck

Table 7.3: Sampling periods of the aerosol collections by filtration om 0.4 and 8.0 μm pore size Nuclepore filters in December 1984.

Sample number	Date		Effective sampling period (hours)
	from	to	
#0	1123.27*	1209.29	10
#1	1209.58	1308.20	18
#2	1410.33	1507.30	13
#3**	1509.50	1607.18	5.7
#4	1519.47	1607.18	7.4

* 1123.27 = 11 December 1984, 11.27 p.m.

** Collection of rain water from 1515.15 to 1515.48

of the ship at an altitude of 11 m above the sea surface (Figure 7.3). Special precautions with respect to wind speed and wind direction relative to the ship were made to avoid local contamination from the vessel. The power to the pump was cut off during unfavourable sampling conditions so that the effective sampling period is always shorter than the total period of filter exposure.

During the collection of sample #3, it started to rain after 4.5 hours. It rained for 33 minutes and the precipitation was collected in a 33 cm diameter polyethylene funnel and flask. For the analysis of the rain water suspension, 5 ml of rain was filtered on a 0.4 μm pore size Nuclepore filter of 25 mm diameter. During and after the rain shower, aerosol sampling was continued. The filter inlet of the filtration unit was shielded off to avoid the collection of rain water droplets during the precipitation event. At selected times a total of 10 additional samples were collected with a low volume (1.2 l/min) cascade impactor for a period of 10 minutes. In the latter case, the aerosol particles were directly impacted on a 100 nm thick Formvar foil supported by 300 mesh electron microscope grids, which were mounted on the 5 stages of the single-orifice Battelle-type cascade impactor. The 10 minute low volume cascade impactor samples have the advantage of offering very good time resolution for the observation of chemical changes and transformations of the atmospheric aerosol. Moreover they only collect air that was " in equilibrium" with the aerosols in contrast to long term sampling where e.g. artifact nitrate formation or sulfate neutralization could be enhanced when pure seasalt particles sampled at an earlier stage are brought into contact with polluted air masses containing elevated NO_x, SO_2 and ammonia concentrations.

The two dimensional back trajectories for 3 to 4 days of the sampled air masses are shown in Figures 7.4 to 7.8. The sampling site is indicated with an arrow. For sample #0 the air masses spent about 50 hours over the southern part of Great Britain and also

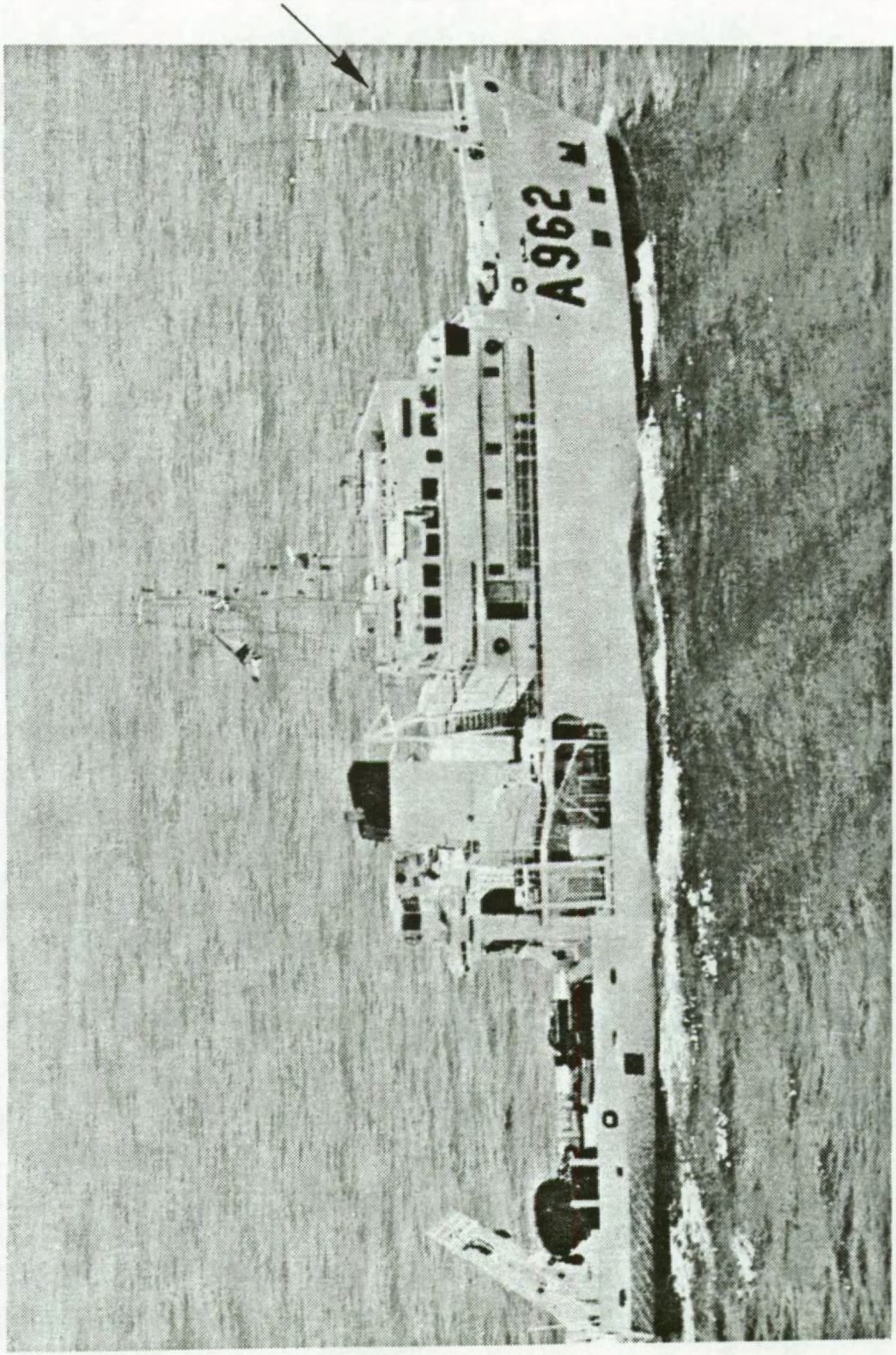

Figure 7.3: Side-view of the oceanographic ship "Belgica". The location for the aerosol sampling is indicated with an arrow.

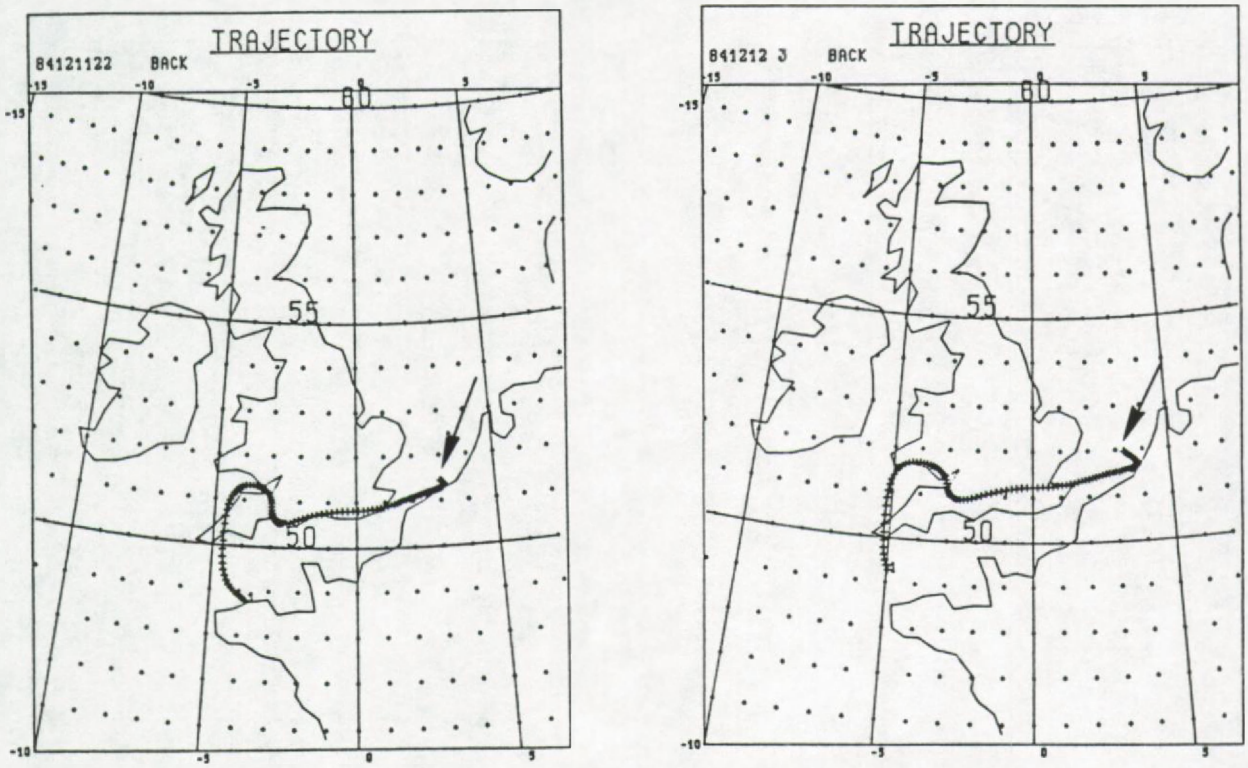

Figure 7.4: Air mass back trajectories of sample #0 (the arrow indicates the sampling site).

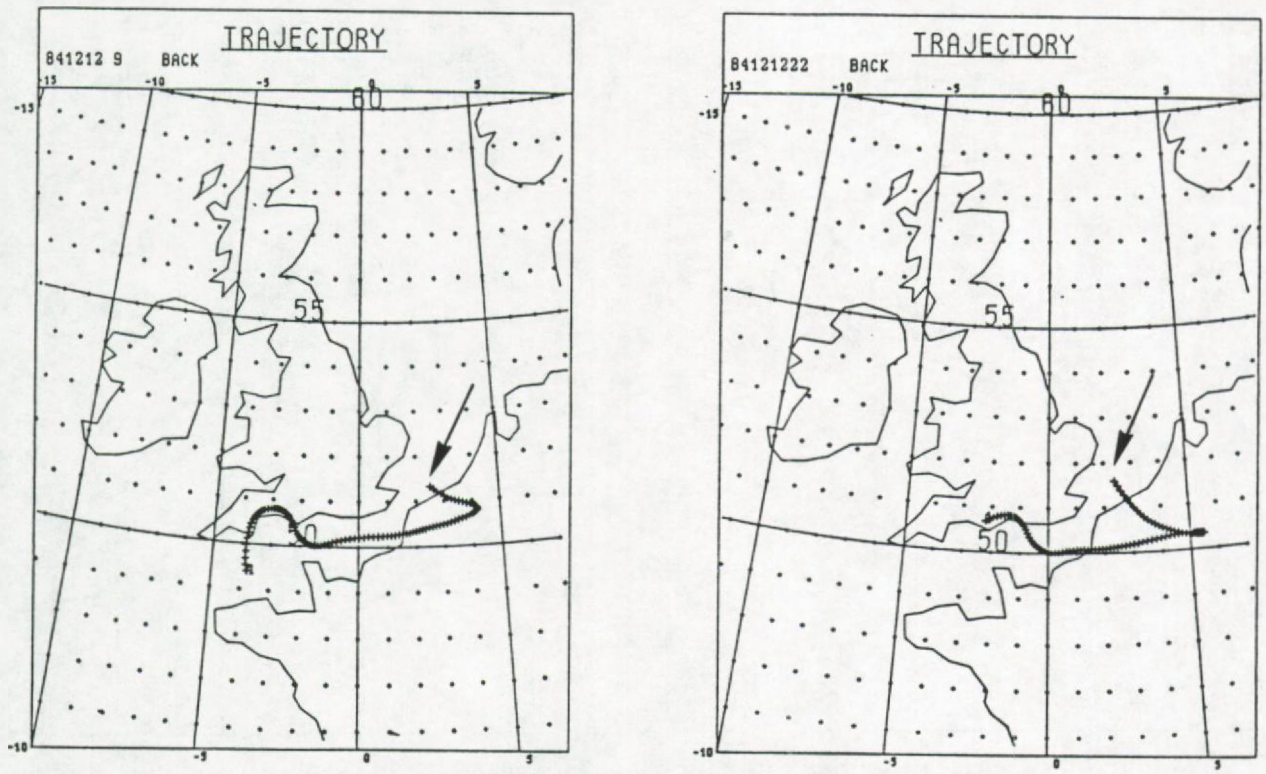

Figure 7.5: Air mass back trajectories of sample #1 (the arrow indicates the sampling site).

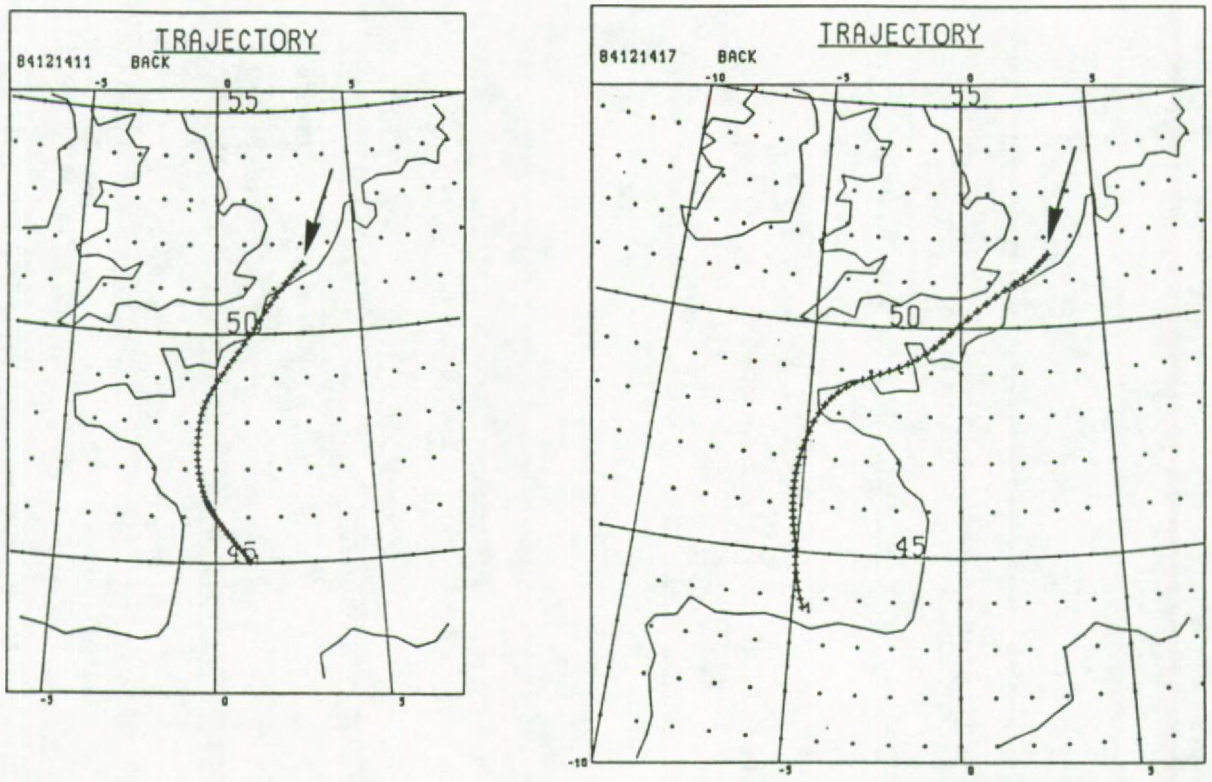

Figure 7.6: Air mass back trajectories of sample #2 (the arrow indicates the sampling site).

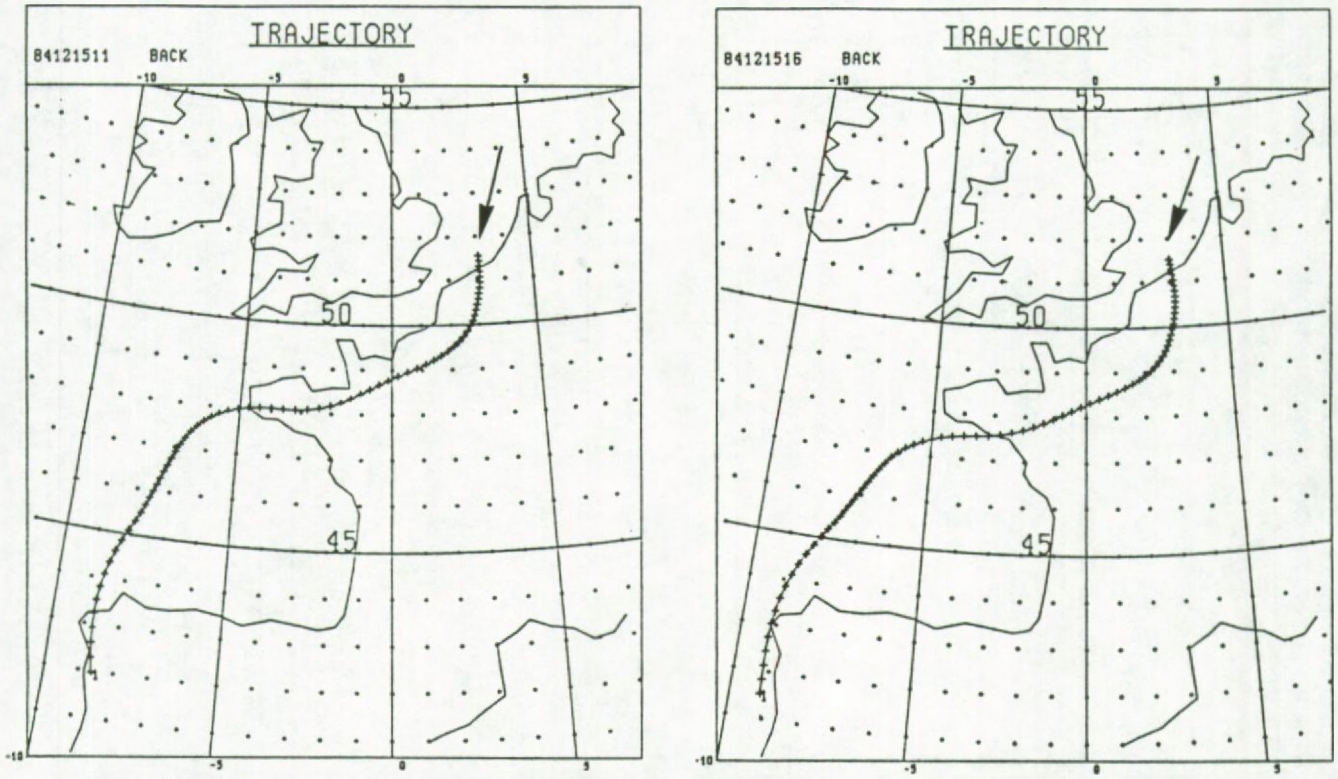

Figure 7.7: Air mass back trajectories of sample #3 (the arrow indicates the sampling site).

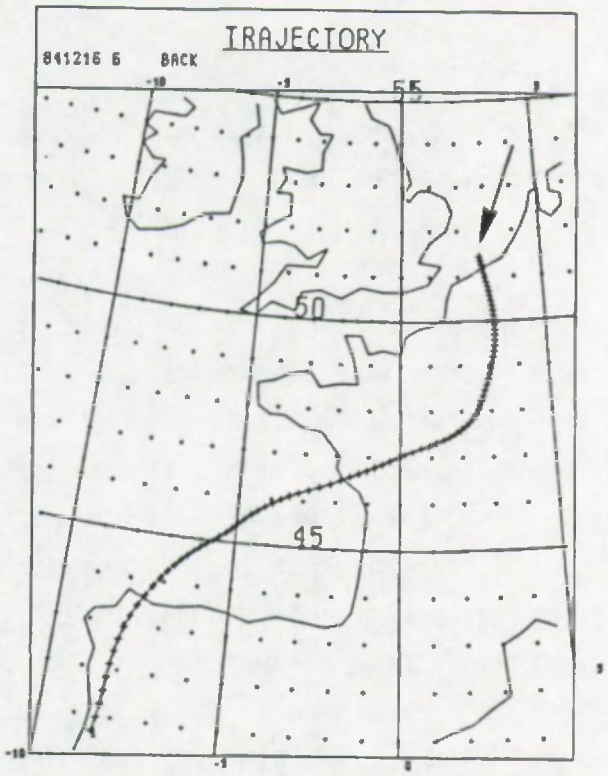

Figure 7.8: Air mass back trajectory of sample #4 (the arrow indicates the sampling site).

passed over the London area. The air mass sampled #1 originated from the southern tip of Great Britain, crossed the channel and travelled over France and Belgium. Aerosol sample #2 was collected during wind speeds of 7 Beaufort so that a considerable contribution from direct aerosol production by the sea can be expected. For sample #3 and #4 the trajectories show that the air coming from the Iberian Peninsula crosses the Gulf of Biscay and traveled close to the coast line at the beginning of the sampling period and gradually shifted more landinward over France. The wind speed decreased from 5 to 4 Beaufort during the last sampling periods.

7.2.3 Analysis

The sampling times of both filtration and impactor samples were optimized to obtain an appropriate loading on the collection surface to allow single aerosol particle analysis by the microanalytical techniques. Overloading has to be avoided because it deteriorates

the possibility of single particle analysis and can result in the formation of secondary compounds as a consequence of recrystallization on the impaction surface (11).

The EPMA-measurements on the loaded Nuclepore filters were performed by H. Storms with a JXA-733 Superprobe of JEOL, (Tokyo, Japan) used at an electron energy of 20 keV and a beam current of ca. 1 nA. The instrument is equipped with a TN-2000 system of Tracor Northern (Middleton ,USA) that allows a fully automatic analysis of a preset number of particles. Morphological data as average diameter and a shape factor are obtained, while compositional information is derived from an energy dispersive X-ray spectrum that is accumulated for each particle. For each sample about 500 particles were analyzed in this way. To reduce the data set, hierarchical cluster analysis was performed on each sample with the DPP-software package (12), so that particles with a chemically similar composition are classified in a "particle type" . Relative X-ray peak intensities were used as a measure of element abundance.

X-Ray Fluorescence (XRF) in the secondary-target energy-dispersive mode, was used for the determination of the total atmospheric loading for 11 elements, including metals as V, Fe, Ni, Cu, Zn and Pb. The characteristic X-rays for all the elements were simultaneously measured by a Si(Li) detector and stored in a multichannel recorder. The spectra were transferred to a magnetic tape for spectrum evaluation and quantification (13).

The Formvar coated EM-grids of the low volume cascade impactor were analyzed with the LAMMA-500 instrument.

7.2.4 Results and discussion

The atmospheric loading (ng/m^3) for the number of elements (as inferred from XRF-data) is represented in Table 7.4. The particles in both the atmosphere and the rain water were classified according to morphology and major chemical composition on the basis of the EPMA data. The percent abundance of the different groups in the aerosol samples and for the suspended matter in the rain water is listed in Table 7.5. The concentration of particles with a diameter larger than 0.5 μm in the air (per m^3) and in the rain water (per l) has been estimated by extrapolation from the number of particles per cm^2 of filter area and the volume of sampled air and rain respectively. These data were used for the calculation of the washout factors for the suspended matter in the rain water.

Table 7.4: Concentrations of selected elements in the North Sea aerosol samples collected in December 1984.

Concentration in ng/m^3

Sample number	#0	#1	#2	#4
Element				
S	4600	1650	600	1510
Cl	800	620	1350	≤200
K	310	310	190	270
Ca	250	450	120	140
V	70	32	18	30
Fe	470	720	300	740
Ni	15	7	≤5	≤5
Cu	33	8	≤6	≤5
Zn	180	180	32	80
Br	130	40	10	34
Pb	210	150	40	140

The atmospheric aerosol

Both the XRF-measurements (Table 7.4) and the EPMA-clustering (Table 7.5) data clearly demonstrate the strong dependence of the chemical composition of the airborne particulate matter on the meteorological conditions and the back trajectory of the air masses. Sample #1 is largely dominated by the anthropogenic and continental influence from both the United Kingdom and the European mainland. For aerosol sample #2 a higher influence of the marine environment on the aerosol composition can be expected because of the longer residence time over the Southern Bight of the North Sea and the strong S.W.-wind up to 7 Beaufort. For sample #3 and 4 the residence time over the European continent increases from 34 hours at the beginning of the collection of sample #3 to 49 hours at the end of the sampling period of #4. This is also clearly reflected in the relative abundance of the natural versus anthropogenic sources that contribute to the aerosol composition. In sample #3, more than 40 % of the aerosols are sea derived and have an average (dry) diameter of 1.9 μm. Nearly 7 % were seasalt particles with a clear relative depletion of Cl and enrichment in S. LAMMA-measurements on a 10 minute cascade impactor sample taken the day before on December 14 at 5.20 p.m. during the sampling period of #2 in which 60 % of the particles were identified as seasalt by EPMA. showed that the aerosols under consideration had no or only very slight nitrate enrichments. They were of recent formation. generated by breaking waves at wind speeds of 6 to 7 Beaufort, However in at least 80 % of the seasalt particles sampled on December 15 at 9.50 a.m. evidence for nitrate enrichment was found. The analysis of a cascade impactor sample. collected at 11.20 a.m. the same day, showed 95 % transformed seasalt particles that consisted of a mixture of $NaNO_3$, Na_2SO_4 and NaCl. Typical positive and negative mode LAMMA-spectra of untransformed and highly transformed seasalt particles are shown in Figures 7.7 and 7.8.

Table 7.5: Percent abundance of the particle types in sample #1 to #4.

Particle type	Particle abundance in %				
	Aerosol samples				Particulate matter in the rainwater sample
	#1	#2	#3	#4	
Seasalt	-	60	33	-	dissolved
Aged seasalt	2	10	7	-	dissolved
Mixture of seasalt and aluminosilicates	-	2	11	-	partly dissolved
Carbonaceous S-rich particles	19	4	7	34	dissolved
Aluminosilicates	47	1	22.5	11	41
Spherical iron oxide	8	10	5	35	< 1
Ca-rich particles	20	9	7	15	dissolved
SiO_2*	4	-	4	1.5	54
Al-rich**	-	-	2.5	1	dissolved
Miscellaneous	-	4	-	2.5	4

*: Al was not detectable

**: Si was not detectable

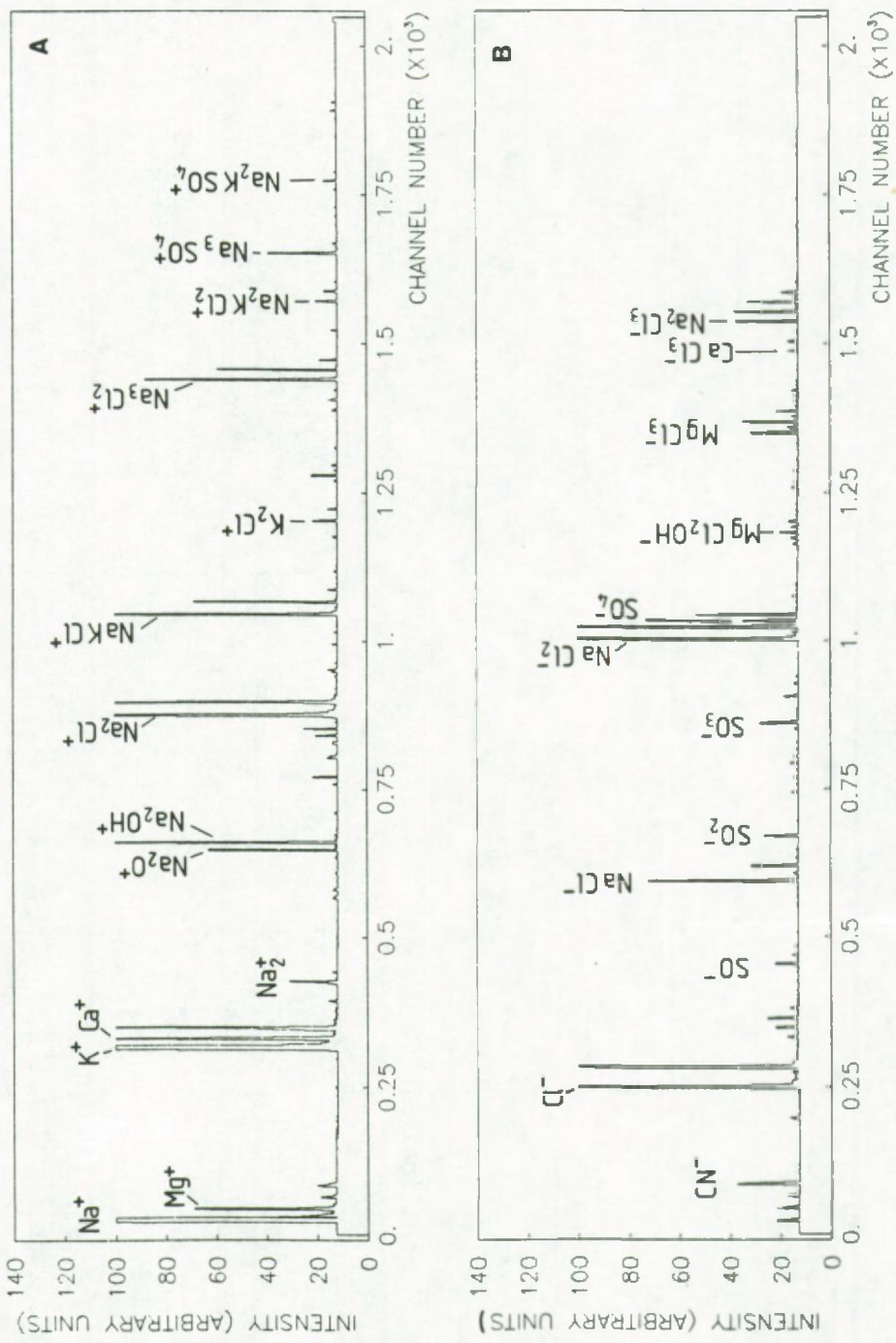

Figure 7.7: Positive (a) and negative (b) mode LAMMA-spectra of untransformed seasalt particles.

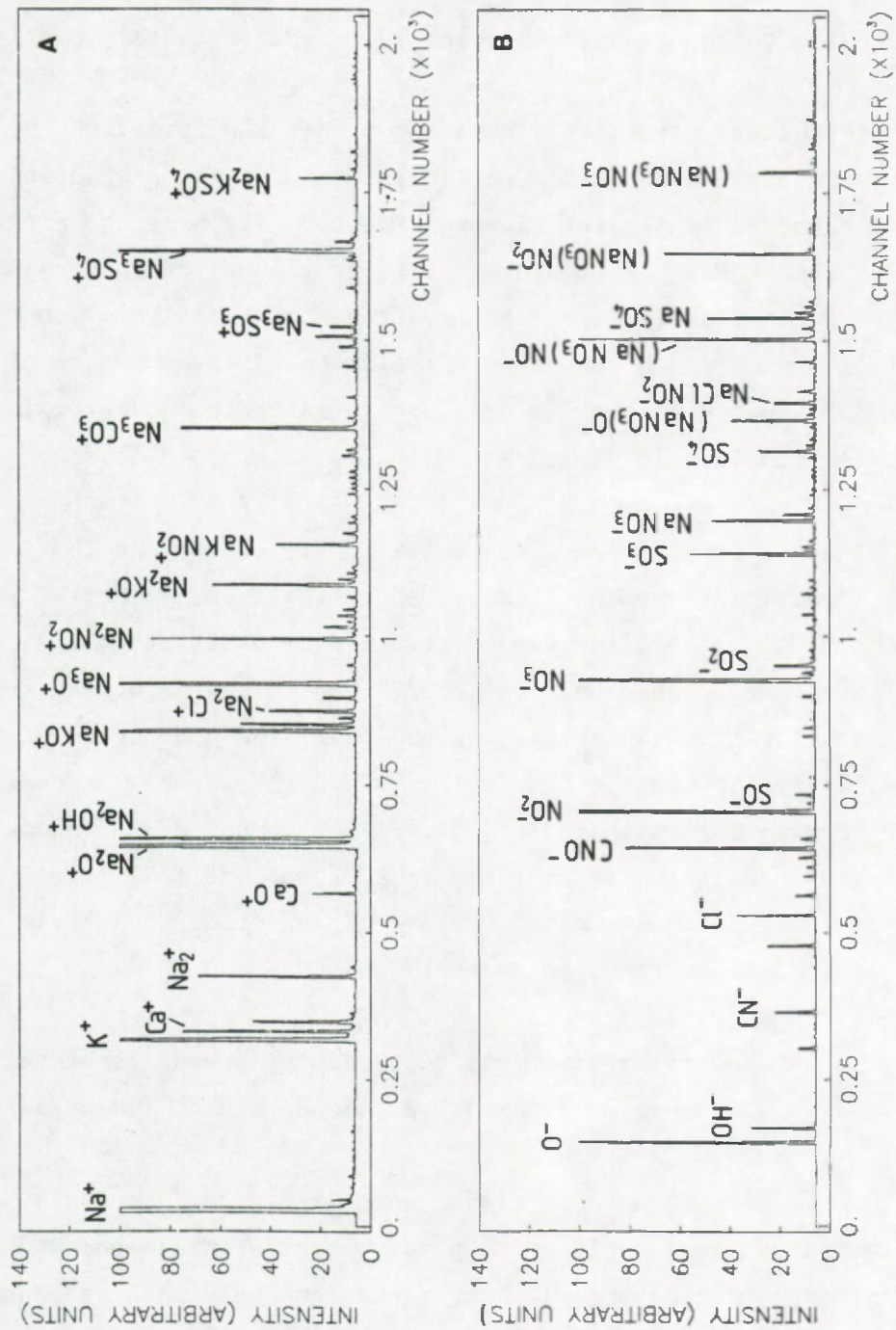

Figure 7.8: Positive (a) and negative (b) mode LAMMA-spectra of highly transformed seasalt particles.

By bulk X-ray powder diffraction measurements on samples collected in the UK. Harrison et al. (14) found evidence for the presence of Na_2SO_4, $NaNO_3$ and $Na_2SO_4.2H_2O$, which were also attributed to halogen displacement reactions in seasalt particles.

Laboratory experiments have shown that the formation of $NaNO_3$ on micrometer size NaCl particles sampled by impaction can be enhanced by the uptake of gaseous HNO_3 from the passing air stream (15). When a NaF-coated denuder for the removal of gaseous HNO_3 was placed before the inlet of the impactor, LAMMA-analyses on seasalt particles sampled in coastal air still showed the presence of $NaNO_3$. Thus, artifact $NaNO_3$ formation alone is insufficient to explain the $NaNO_3$-enrichments in marine aerosols (see section 6.4).

Because of the size differentiated collection and the extremely low impaction surface loadings for the 10 minutes sample, interaction between the fine particle mode H_2SO_4 and the seasalt in the coarse mode can be neglected. Mechanisms proposed for the sulfate formation on seasalt aerosols are the scavenging of SO_3 gas produced by atmospheric oxidation of SO_2 or the scavenging of H_2SO_4-containing particulates (16) or even the production of sulfuric acid in the seasalt aerosols themselves (17). The reaction should result in a displacement of chloride by sulfate and the release of HCl in the atmosphere (5,18).

In the aerosol samples collected during prevailing continental influence (#1 and 4) pure seasalt particles are no longer detected.

The formation of mixed seasalt/mineral aerosols can be explained by cloud coalescence processes between mineral and seasalt containing particles (19). This mechanism could also be responsible for the sulfate enrichments in seasalt containing droplets.

In the air sample #4 for which the collection started 3 hours after the rain event pure seasalt is virtually absent; this can probably be explained in part by wash out and rain out processes. In

addition, the air masses sampled in this period were more influenced by the European continent and collected closer to the coast line than for sample #3. Also for sample #1 that was collected under a prevailing continental influence on the air masses, not more then 2 % of the particles was identified as being sea-derived.

In all the samples, particles are found which consist of elements with atomic number Z < 11 (this includes e.g. H, C, N and O) and bearly detectable elements with Z > 11, except for S. The abundance of this particle type clearly reflects the continental and anthropogenic influence on the airborne particulate matter: they have a higher abundance during land-derived air masses nl. 19 % and 34 % for sample #1 and 4, respectively and a lower abundance in the relative marine air nl. 4 % and 7 % in sample #2 and 3, respectively. This particle type incorporates the carbonaceous aerosols such as e.g. soot, and S-compounds as e.g. $(NH_4)_2SO_4$ and NH_4HSO_4, and mixtures of both, as was inferred from the LAMMA-results. Positive and negative mode LAMMA-spectra of such mixed carbonaceous and S-rich particles abundantly detected in the 0.5-1 μm size range of the impactor samples, are shown in Figure 7.9. Comparison with reference spectra of standard samples pointed out that these particles largely consist of ammonium sulfates, Na and K and carbonaceous material. Lead and vanadium, two elements for which LAMMA has very good detection limits down to 30 ppm in individual aerosol particles (see section 3.6), are nearly always present. Also Fe and Mn can frequently be detected in these particles. These aerosols are probably the result of the oxidation of SO_2 dissolved in water droplets, a process known to be catalyzed by Fe^{3+} and Mn^{2+} (20-23). The relative humidity during sampling was close to 100 %. Also soot is known to catalyze the SO_2 oxidation (24), especially near combustion sources, where both SO_2 and soot concentrations are highest. This is consistent with the lead and vanadium content of the aerosols. Although the sodium in these particles could be of marine origin, the V, Pb and the organic matter are probably pollution derived and this can also be assumed for the SO_2 and the NH_3, active in the neutralisation of the sulfates as the SO_2

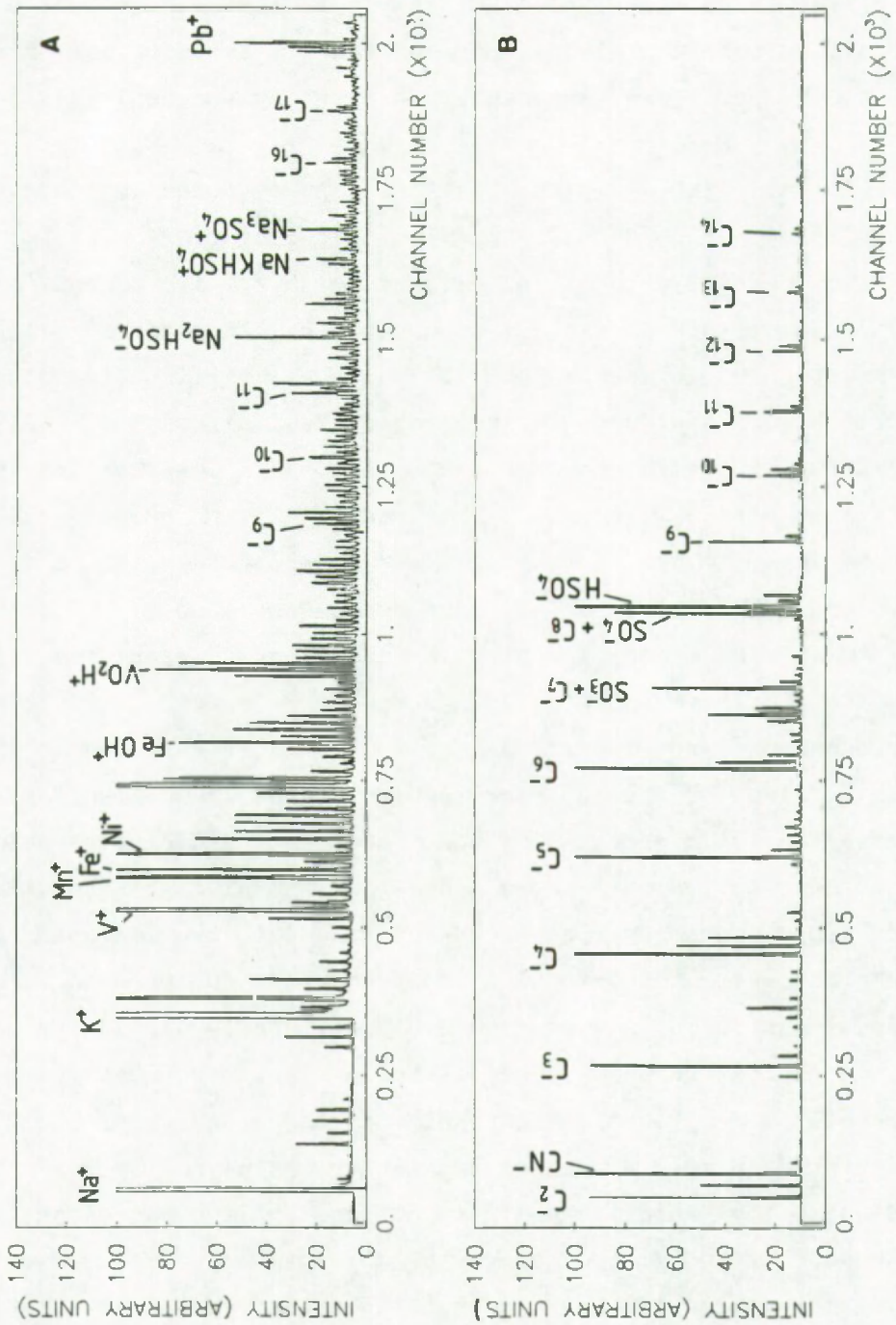

Figure 7.9: Positive (a) and negative (b) LAMMA-spectra of the S-rich carbonaceous particles.

oxidation proceeds. The chemical complexity of these particles indicates that several atmospheric interaction processes can be involved in their formation.

The aluminosilicates with an abundance of 22.5 % in sample #3 and 11 % in sample #4, can be divided into spherical fly-ash particles and particles of irregular shape. The spherical aluminosilicates, provided by high temperature combustion processes, constitute 80 % of the aluminosilicate group in sample #3 and 60 % in sample #4. The fly-ash particles have a rather uniform chemical composition. From the EPMA-data and using a ZAF-correction specific for particles (25), the following average composition was calculated for this group : 25.1 % Si, 18.4 % Al, 5.5 % K, 3.0 % Fe, 0.9 % S, 0.4 % Ca, 46.7 % O. These data are in close agreement with the results reported by Kaufherr and Lichtmann (26) for fly-ash particles sampled in the U.S. Positive mode LAMMA-spectra of these spherical aluminosilicates show the presence of Na, Mg, Al, Si, K, Ca, Ti, Fe and trace elements as V, Ga, Rb, Cs, Ba, Pb, etc. were also detected (Figure 7.10a). In the negative ion mode spectra the mass peak at m/z = 97 HSO_4^- points to the presence of a sulfate species such as $(NH_4)_2SO_4$ or NH_4HSO_4 (Figure 7.10b). The intensity of HSO_4^--peak was highly variable from one particle to another. The other mass peaks in the negative ion mode are related to the matrix of the aluminosilicate. In some cases a typical pattern of peaks could be detected by applying low energy shots to the spherical aluminosilicate particles. The resulting mass spectrum is interpreted as a fingerprint for the desorption of polynuclear aromatic hydrocarbons (PAH). The set of detected ions largely coincides with the ones reported by Mauney (27) for an oil shale retort soot sample. The peaks in Figure 7.11 are assigned to the following compounds (only one of the possible isomers is listed):

m/z = 252 benzo(a)pyrene, perylene, benzo(k)fluoranthene

m/z = 276 anthanthrene, dibenzo(ah)anthracene, benzo(ghi)perylene

m/z = 300 coronene

m/z = 326 dibenzo(a,ghi)perylene

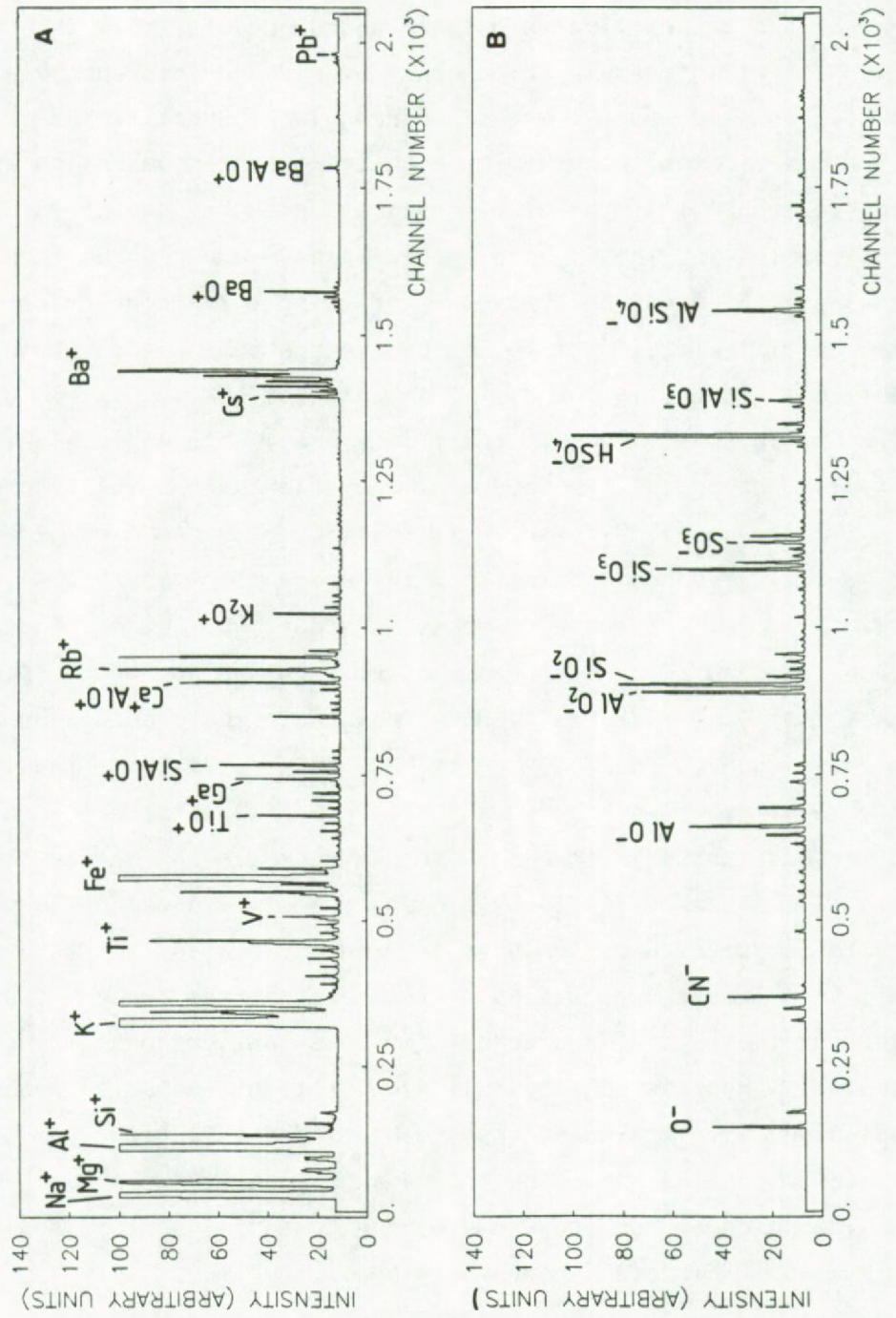

Figure 7.10: Positive (a) and negative (b) mode LAMMA-spectra of the spherical aluminosilicate particles.

m/z = 350 benzo(a)coronene
m/z = 362 benzo(a)thiophene
m/z = 374 dibenzonapthocoronene
m/z = 424 benzonapthocoronene
m/z = 448 benzo(a)ovalene
m/z = 472 dibenzo(a,bc)ovalene
m/z = 496 circumanthracene
m/z = 520 circumpyrene
m/z = 546 benzo(a)circumanthracene
m/z = 570 dibenzo(a,bc)circumanthracene
m/z = 594 circumtetracene

The irregularly shaped aluminosilicate component can originate from low temperature burning processes or eolian transport of mineral dust, Also SiO_2 and Al-bearing particles can be both of continental or anthropogenic origin, The relative abundance of the spherical aluminosilicates, the SiO_2 and Al-bearing particle groups in sample #3 and 4 is fairly similar, what may indicate that they were emitted by the same source or by geographically related ones.

The spherical iron oxide particles have an abundance ranging from 5 to 10 % in sample #1 to 3, and represent up to 35 % of the particles in sample #4. The spherical aluminosilicates were most abundant in sample #3. Since the ratio of spherical iron oxide particles to spherical aluminosilicates is not constant, the aerosols are probably emitted by different pollution sources. Beside Fe, the spherical iron oxide particles also contain Mn and Zn in concentrations around 5 % by weight. They are probably related to the metallurgical activity located on the French coast in the region of Dunkerque, Northern France.

Calcium-bearing particles (with and without S) are present in all aerosol samples. $CaSO_4$ can be produced by fractional crystallisation of marine aerosols (19). The relative humidity during sampling was 100 % so that all seasalt was present in droplets. Therefore fractional crystallization of these individual droplets occured on the impaction surface and resulted in a halite

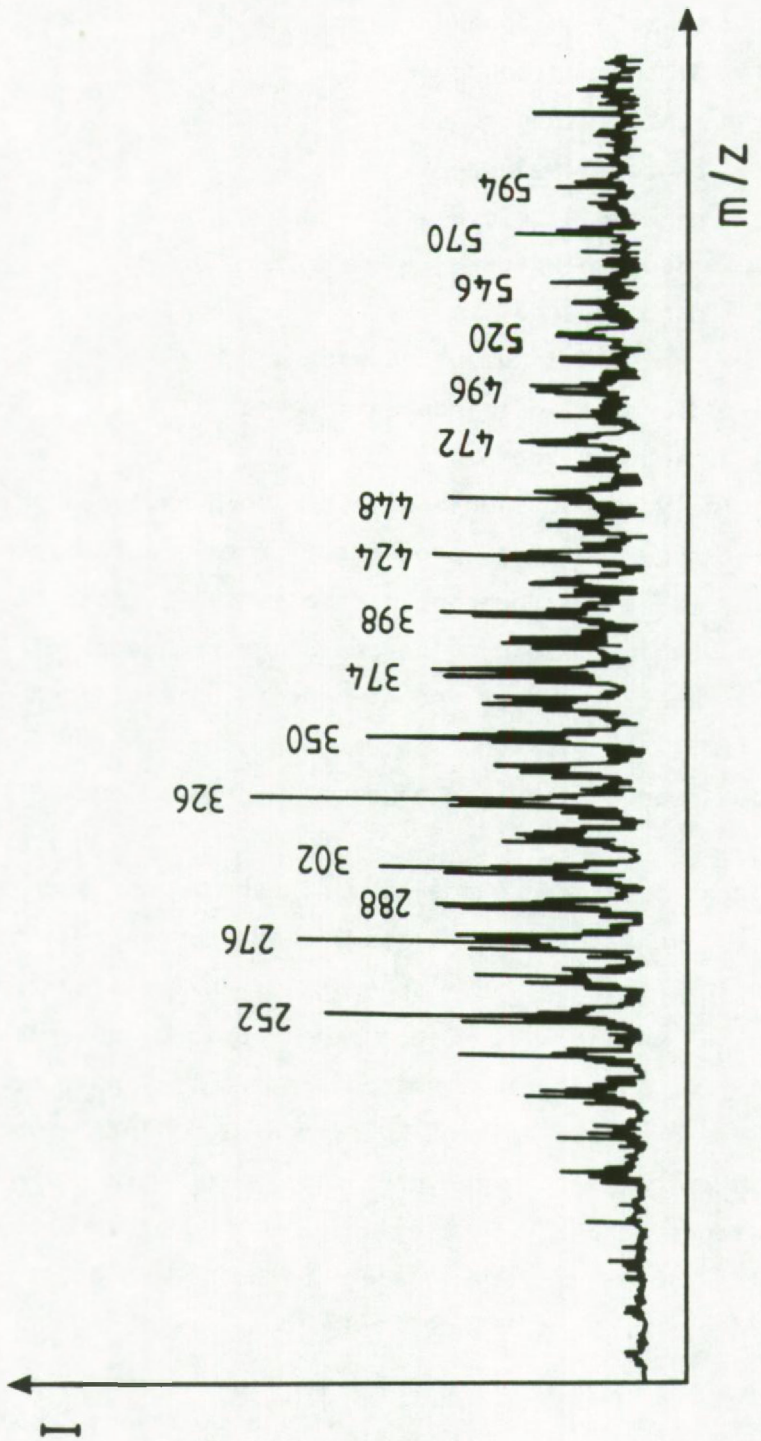

Figure 7.11: Positive mode LAMMA-spectrum of PAH desorbed from a fly-ash particle.

(NaCl) crystal and a second solid phase of Na, K, Mg sulfates and chlorides as expected from the seawater evaporation sequence. The calcium carbonate and the gypsum ($CaSO_4.2H_2O$) accounts for 1 % and 3 %, respectively, of the total dissolved material and they were not detected as discrete phases in the crystallized aerosols. Individual $CaSO_4$-particles, however, containing Cl as a minor component were detected by both EPMA and LAMMA-observations (Figure 7.12a). This indicates that at least a part of these $CaSO_4$-particles are of marine origin. The mechanism by which they "lost" their other crystalline phases remains unsolved. Also the interaction of airborne $CaCO_3$ either from marine or biogenic origin with SO_2 or H_2SO_4 could explain the formation of $CaSO_4$. Another important source for $CaSO_4$-particles above the North Sea are the combustion processes and eolian transport from the continent. These sources are the most important for the North Sea, because the highest abundance of Ca-rich particles are found in the continental samples #1 and 4. Figure 7.12b shows a LAMMA-spectrum of this type of $CaSO_4$-particles. Beside the $CaSO_4$-cluster peaks (section 5.1), they show an intense Al-signal and related cluster peaks as $CaAlO^+$ and $FeAlO^+$. The mass peaks at m/z = 59, 75 and 115 indicate the presence of Co in this sample. $Ca_3(PO_4)_2$-particles were also detected and they contained either Co or Pb as minor elements (Figure 7.12c).

Suspended matter in the rain

The seasalt particles, and the S-rich and Ca-rich aerosol particle groups dissolved in the rain water and disappeared in the particulate fraction. The major group (54 %) was identified as SiO_2. Also the aluminosilicate components with spherical and irregular shape are very abundant 16 % and 24 % respectively. Also the Al-bearing groups dissappeared in the rain water as would be expected for e.g. the soluble Al_2O_3. The ratio of the spherical aluminosilicates to the SiO_2-particle group is different from the ratio in the aerosol samples (Table 7.5). Leaching of Al from the aluminosilicates could be one explanation for this concentration difference, and indeed, in some rain water samples an $Al(OH)_3$

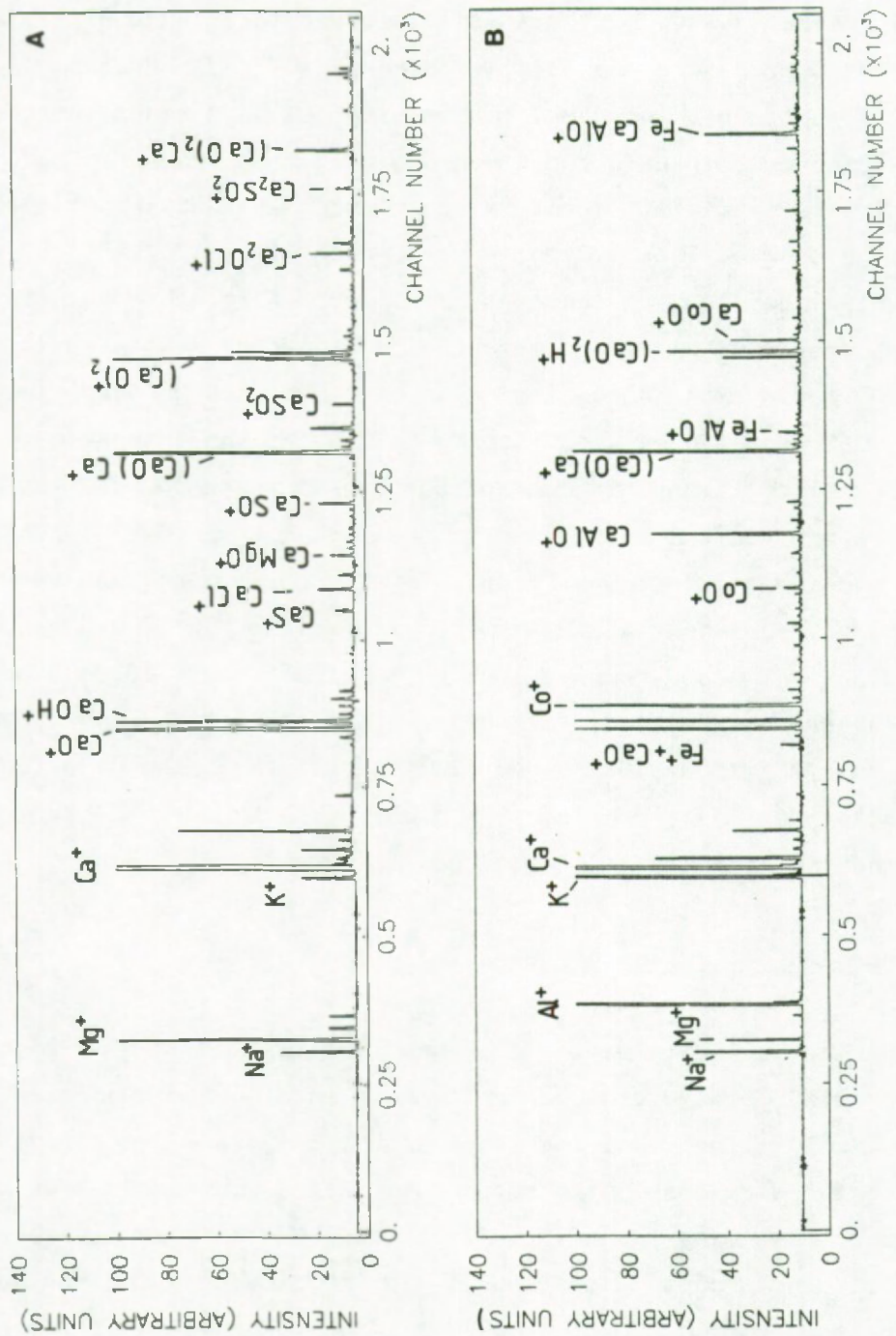

Figure 7.12a and b: Positive mode LAMMA-spectra of Ca-rich particles

a) $CaSO_4$ with Cl

b) $CaSO_4$ with Al, Fe and Co.

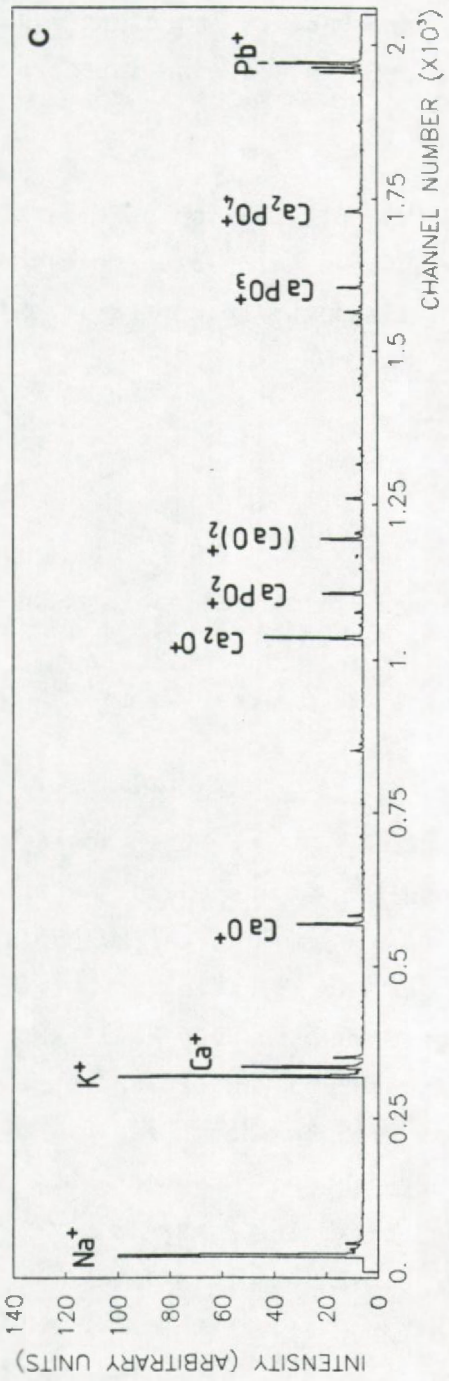

Figure 7.12c: Positive mode LAMMA-spectrum of a Ca_3PO_4-particle

precipitate was observed covering the whole Nuclepore filter. Nevertheless, the complete dissolution of the Al-content from the aluminosilicates seems unprobable. Therefore the difference in abundance in rain and air samples was also interpreted on the basis of different scavenging ratios.

Scavenging ratios (W) of the insoluble particle types in the size range of 0.5 to 5.5 μm were calculated from the particle number concentrations in sample #1 and the concentrations in the rain water by the formula (28),

$$W = K \rho C^{-1}$$

with K = the particle number concentration in rain (per cm^3)
ρ = the density of air (0.0012 g/cm^3)
C = the particle number concentration in air (per cm^3)

Because the cut-off diameter at the inlet of the aerosol sampling device is around 10 μm the scavenging ratios were calculated only for aerosols and suspended material in the rain water between 5.5 μm to 0.5 μm diameter aerosols. The results are shown in Table 7.6. The scavenging ratios for the aluminosilicates are in the same range of 500 to 2000 as is the value reported by Uematsu et al. (28) for the North Pacific and by Cause (29) for the United Kingdom. The high washout factor of 10500 for the SiO_2-particles could be caused by a non-uniform vertical concentration of these particles, namely higher SiO_2 particle concentrations at higher elevations relative to the aerosol sampling height (long range transport). The concentration of Al in the dissolved phase as a result of the dissolution of the Al-bearing particles was estimated to be about 80 μg/l of Al. The low scavenging ratio ($\leq$ 170) for the spherical iron oxide particles could indicate that they were present in higher concentrations at lower heights where the aerosol sampling was carried out (nearby emission in the coastal region as indicated above).

Table 7.6: Scavenging ratios for the insoluble particles ($0.5 \leq d \leq 5.5\ \mu$) in the rain water.

	Aluminosilicates		SiO_2	Fe-oxide
Particle type:	Spherical	Irregular		
Scavenging Ratio	610	1,600	10,500	≤ 170

7.3 LAMMA-STUDY OF AEROSOL SAMPLES COLLECTED DURING THE AMAZON BOUNDARY LAYER EXPERIMENT

7.3.1 Introduction

The Amazon Boundary Layer Experiment (ABLE-2A) refers to a sampling campaign organized in the context of the Global Tropospheric Experiment (GTE) (30). The GTE is a longterm project executed the U.S. National Aeronautics and Space Administration (NASA), with the aim to investigate the dynamics of the chemical and physical processes that take place in the earth's atmosphere.

The design and execution of the sampling of ABLE-2A was a collaboration of U.S. and Brazilian scientists, sponsored by NASA and the Instituto Nacional de Pesquisas Espaciais (INPE) while a small fraction of the analysis and interpretation was done at UIA. The experiment focused on assessing the role of biosphere-atmosphere interactions on the chemistry of the troposphere over relatively pristine tropical forests and wetlands in order to learn more about the role of the tropics in global atmospheric chemistry.

The first mission of the ABLE-program was carried out during the early phase of the Amazonian dry season because it provides the

best opportunities for characterizing the chemistry of the undisturbed (non-precipitating) atmospheric boundary layer over tropical forests and wetlands. A general outline on the scope of the ABLE-2A experiment can be found elsewhere (30).

7.3.2 Sampling

Aerosol sampling was carried out both from ground based stations as by aircraft flights by Dr. P. Artaxo and coworkers during ABLE-2A in July-August 1985 (31).

The sampling site, named Bacia Modelo Tower, is situated in a reservation park about 70 km north of the city of Manaus, Brazil. The sampling equipment was installed on top of a 45 m high tower, at about 15 m above the forest canopy. The sampling area is very difficult to access, so that almost no local anthropogenic contributions are to be expected. The sampled air passed through areas with only primary forests for at least 200 km. During the dry season long range transported aerosol from vegetation burning in the southern part of Para state (32) about 300 to 400 km away, can possibly be received at the sampling site. On the Bacia Modelo Tower, the aerosols were collected with a 10-stage Battelle-type cascade impactor (cut-off diameters of 16, 8, 4, 2, 1, 0.5, 0.25, 0.12, 0.06 μm and a backup filter), operated at a flow rate of 1 l/min. Formvar-coated electron microscope grids were mounted on each stage. Since an electric power line was not available, battery operated vacuum pumps were used. The sampling campaign was carried out from July 11 to August 5, 1985. The impactor sample for LAMMA-analysis discussed below, was sampled on July 13, 1985 from 11.58 a.m. to 12.13 p.m.

The second aerosol sample discussed in this section, was collected during a flight of the NASA Lockheed Electra aircraft. The aim of this particular flight was to study the chemistry and

dynamics of the atmospheric boundary layer during fair weather conditions. Besides the aerosol sampling, in situ measurements of CO_2, CO, CH_4, non-methane hydrocarbons (NMHC), NO, N_2O, O_3, DMS and meteorological parameters were conducted during most flights. The stages with cut-off diameters of 0.5 and 0.25 μm were removed from the impactor to allow a higher flow rate of 2.6 l/min. Sampling was carried out on July 19, 1985 during a flight path shown in Figure 7.13 and on July 23, during a flight from Manaus to Belem. A total air volume of 3.3 m^3 was sampled. Because of the variation in altitude during the flight, the total mass of sampled air is difficult to assess. Also the cut-off characteristics can be significantly influenced by this effect. Therefore the particle size was controlled by optical observations in the light microscope.

The loaded electron microscope grids were analyzed in the LAMMA-instrument for the determination of the chemical composition of the individual aerosol particles. From the impactor sampled at Bacia Modelo Tower, 150 spectra of individual aerosols were recorded. For the aerosol sample collected during the aircraft flight, 100 submicron aerosol particles were analyzed. The goal of the study was to get a first idea about the elements and compounds that are detectable by LAMMA in these samples. Further work will focus on the combined interpretation of LAMMA-, EPMA- and PIXE-measurements on simultaneously collected samples, to obtain as much information as possible on the atmospheric aerosol composition.

7.3.3 Results and Discussion

The sample collected at the Bacia Modelo Tower

In the cascade impactor collected in Bacia Modelo Tower at least 7 different types of particles could be detected. In the coarse mode aerosol, large particles can be found that are released by mechanical abrasion of the leaves, due to wind action (33).

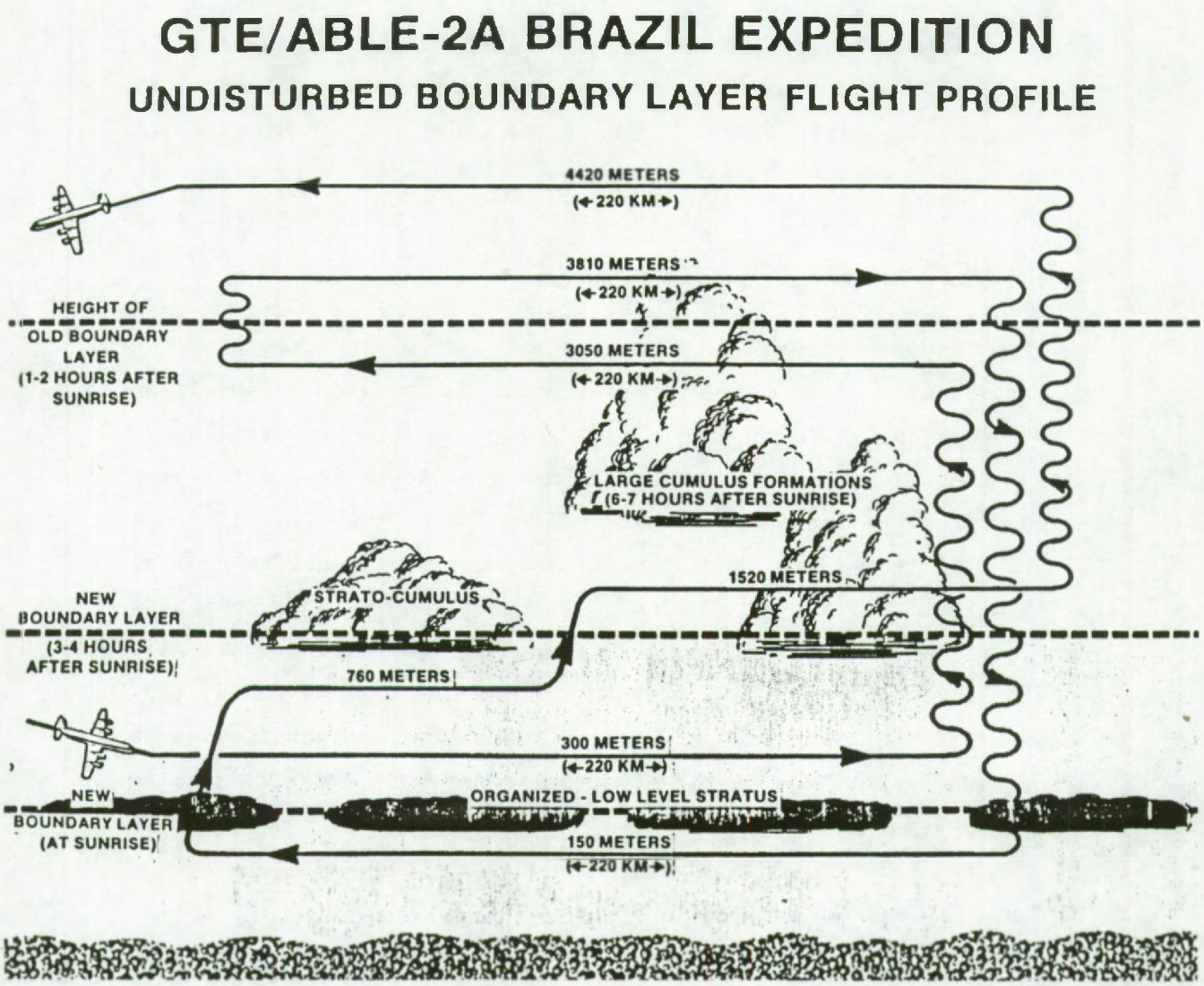

Figure 7.13: Flight profiles flown during ABLE-2A. Undisturbed boundary layer (30).

Positive and negative mode spectra of these leaf fragments are shown in Figure 7.14a to c. The numerous mass peaks in the positive mode mass spectrum originating from the organic material show the following systematic structure:

$(C_nH_{2n-1})^+$ at m/z = 27, 41, 55, 69, 83, 97,...

$(C_nH_{2n+1})^+$ at m/z = 29, 43, 57, 71, 85, 99,...

$(C_nH_{2n+1}O)^+$ at m/z = 31, 45, 59, 73, 87, 101,...

In the negative ion mode spectrum the following series of peaks were identified:

$(C_nH_{2n-1})^-$ at m/z = 41, 55, 69, 83, 97, 111, 125,...

$(C_nH_{2n-1}O)^-$ at m/z = 43, 57, 71, 85, 99, 113, 127,...

$(C_nH_{2n+1}O)^-$ at m/z = 45, 59, 73, 87, 101, 115, 129,...

These mass peaks are the result of the fragmentation of hydrocarbons and terpenes, and the oxygen-containing ions are formed by the fragmentation of oxygenated compounds as e.g. alcohols, esters, etc. Since the spectrum is a superposition of many different organic compounds, and because of the fragmentation behaviour of long chain hydrocarbons, a detailed structural interpretation of the spectra is not possible. Besides the organics, also inorganic elements such as Na, Mg, K, Ca and Cu could be identified. The chemical composition of the pieces of leave is not uniform, as can be seen from Figure 7.14a and b that were recorded from different areas on the same leaf fragment.

The second and most abundant particle type accounts for about 50 % of the number of particles. Positive and negative mode fingerprint spectra are shown in Figures 7.15a and b. The mass spectrum of these particles was compared with reference spectra of

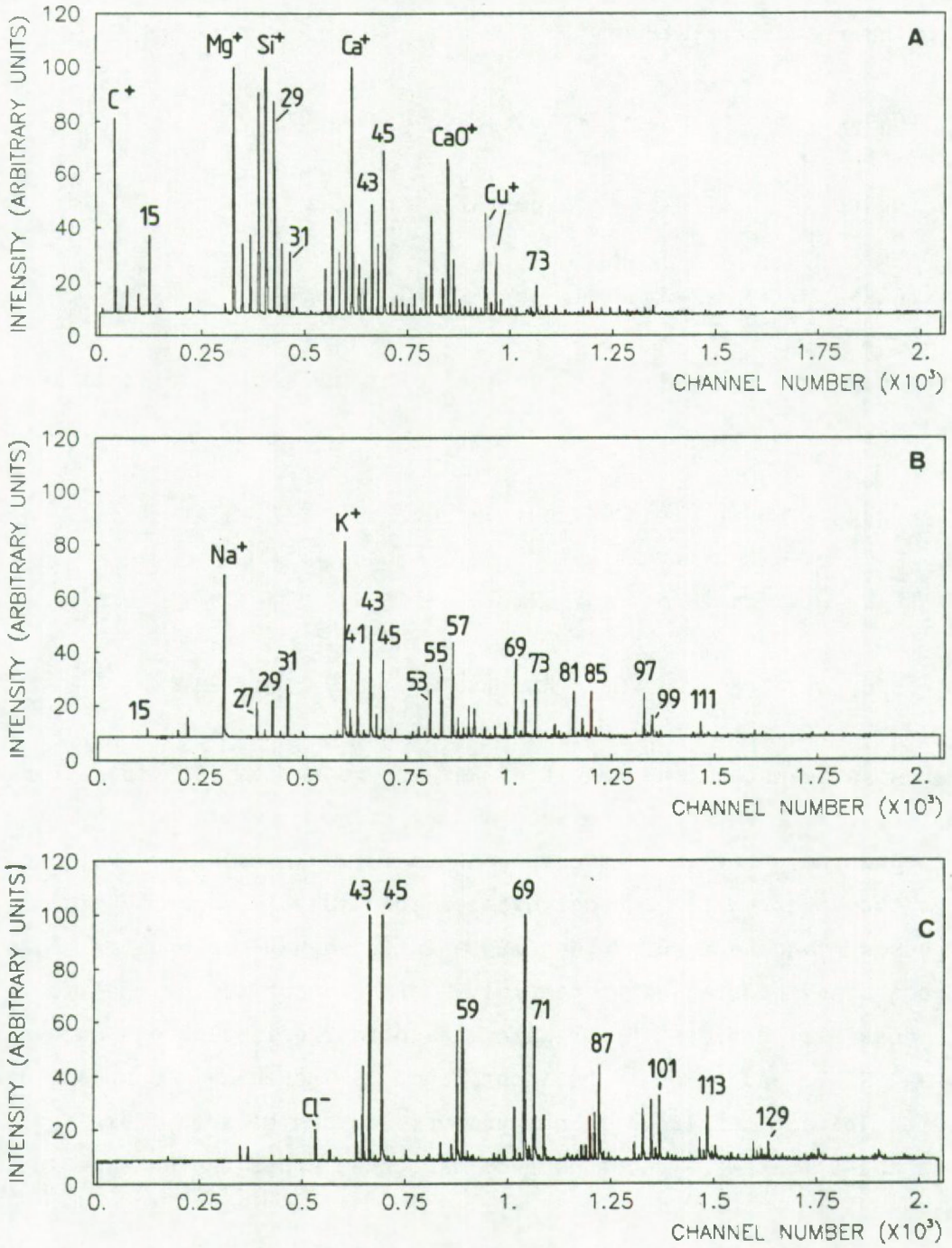

Figure 7.14a to c: Positive (a and b) and negative (c) mode LAMMA-spectra of a leaf fragment.

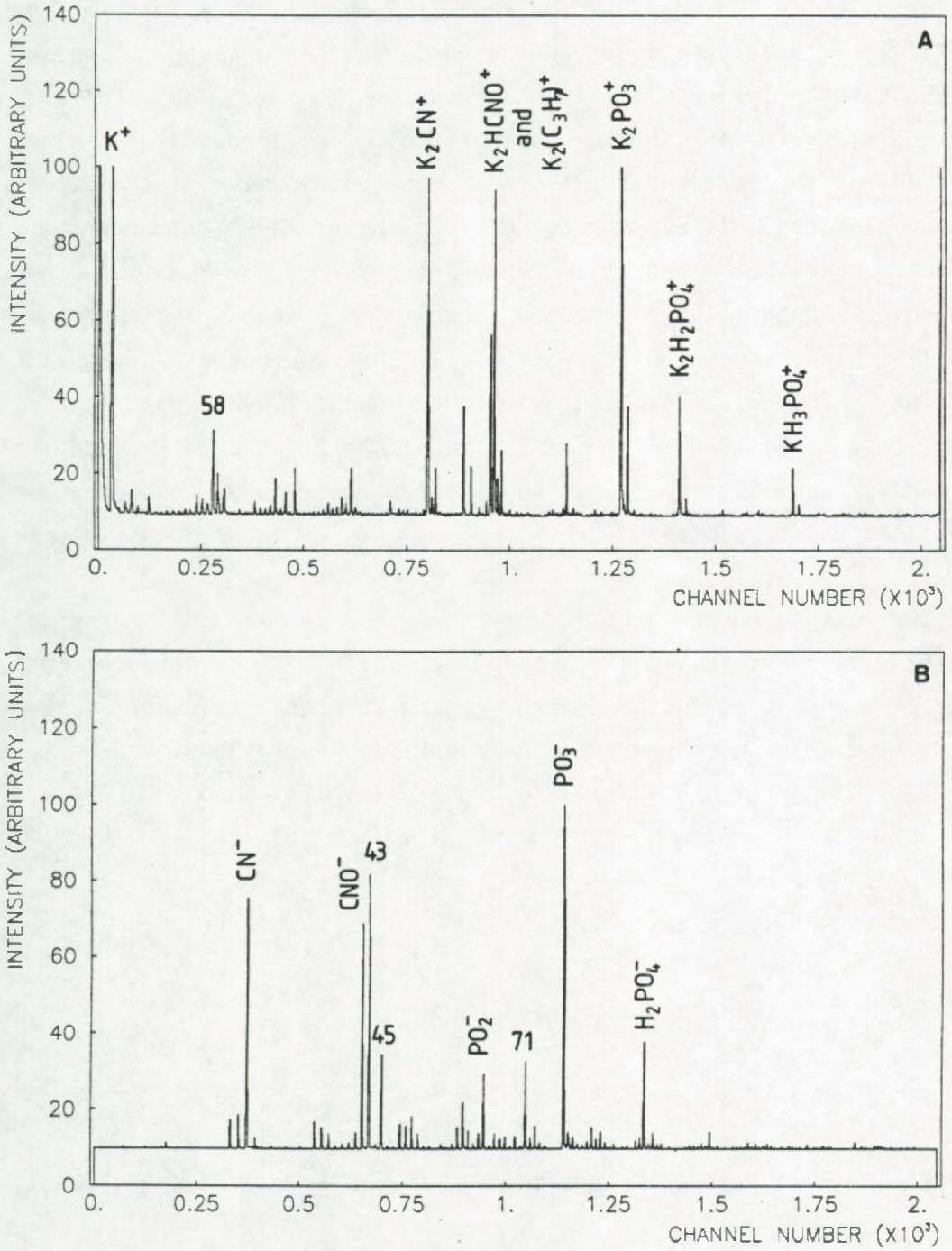

Figure 7.15a and b: Positive (a) and negative(b) mode LAMMA-spectra of the most abundant particle type found in the sample of Bacia Modelo Tower.

K_3PO_4, K_2HPO_4 and KH_2PO_4. The positive mode peaks at m/z = 141, 157, 175 and 213 were identified as $K_2PO_2^+$, $K_2PO_3^+$, $K_2H_2PO_4^+$ and $K_3HPO_4^+$, respectively. In the negative ion mode, the mass peaks at m/z = 63 (PO_2^-), m/z = 79 (PO_3^-) were detected for all reference compounds, but the $H_2PO_4^-$-cluster was only observed for KH_2PO_4. The positive mode clusters, seen in the spectra of the aerosols were also recorded for the reference salts. Although the relative intensities of the clusters most closely correlate with the KH_2PO_4 fingerprint, the spectra are not identical. This allows to assume that the phosphate group in the unknown sample is probably linked to an organic chain (as e.g. in phospholipids). The presence of an organic fraction is clearly indicated by clusters such as $C_3H_7^-$ (m/z = 43), $C_2H_5O^-$ (m/z = 45), $C_5H_{11}^-$ (m/z = 71), etc. The presence of K and P in aerosol samples collected above forested areas was assigned to aerosol emission by plants (33).

The third important particle type was identified as being a mixture of several salts including sulfates, carbonates and chlorides, and it also contains an organic fraction (Figures 7.16a and b). The major mass peaks can be classified as follows:

M_2^+ at m/z = 46, 62, 78 with M = Na, K

M_2CN^+ at m/z = 72, 88, 104

$M_2C_3H_7^+$ at m/z = 89, 105, 121

M_2O^+ at m/z = 62, 78, 94

M_2OH^+ at m/z = 63, 79, 94

M_2Cl^+ at m/z = 81, 97, 113

$M_3SO_4^+$ at m/z = 165, 181, 197, 213

$M_3CO_3^+$ at m/z = 129, 145, 161

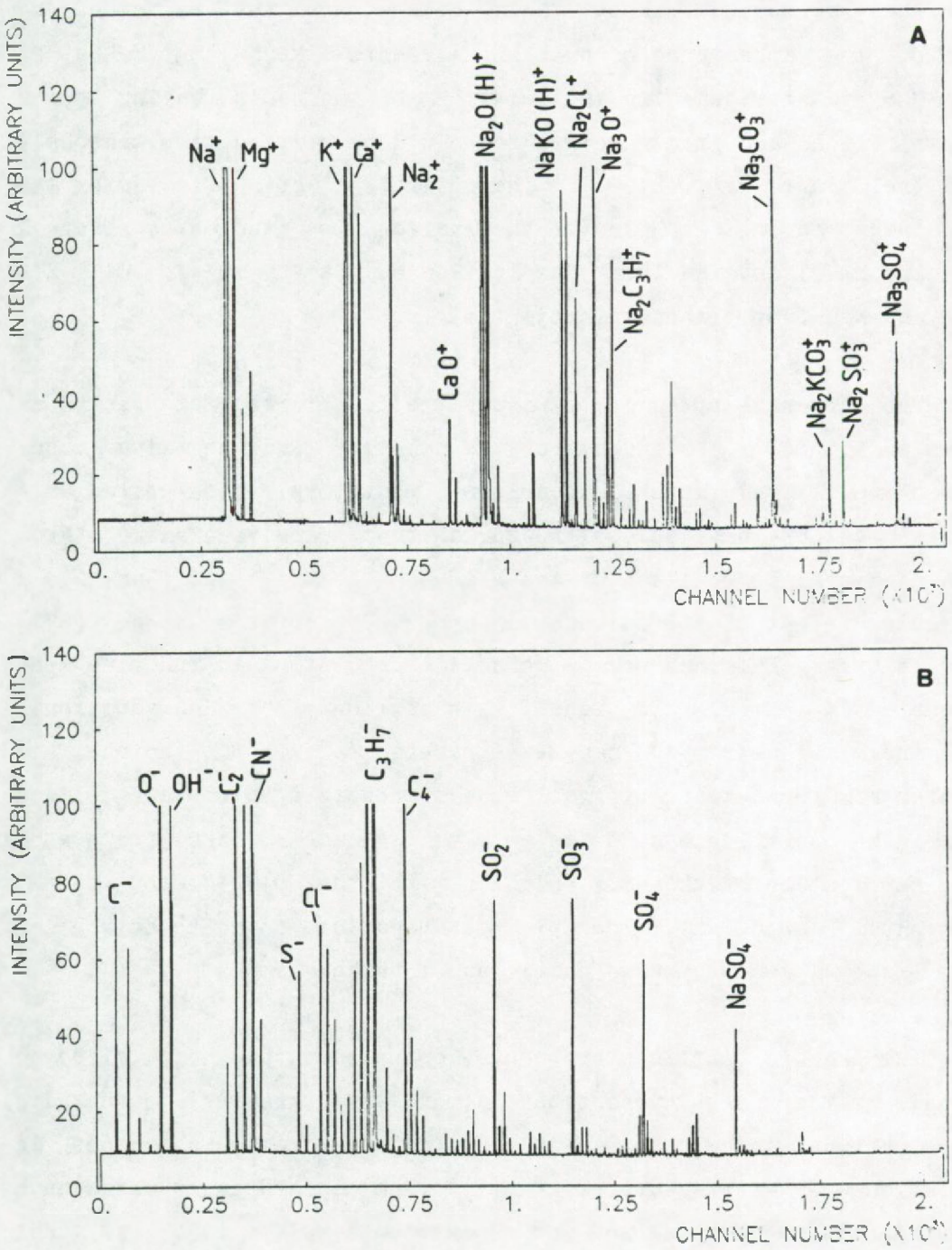

Figure 7.16: Positive (a) and negative (b) mode LAMMA-spectra of aerosol particles that can be related to plant transpiration.

Inorganic elements such as Na, Mg, K, and Ca are abundantly present. Also these aerosols are most likely related to the emissions by plants. The appearance of nutrient elements like Na, Mg, K, Ca, Cl and SO_4^{2-} is attributed to the emission of aerosols during plant transpiration and these elements could be emitted simultaneously with the plant wax (34,35). The migration of salts into the atmosphere during crop plant transpiration, was studied by Nemeruyk (36) and he discovered the transpiration of Ca^{2+}, SO_4^{2+}, Cl, K^+, Mg^{2+} and Na^+ from plants in ambient air.

The fourth type of aerosols yielded fingerprint spectra as shown in Figures 7.17a and b. for the positive and negative mode, respectively. Their major component was tentatively interpreted as a sulfate salt of an organic nitrogen compound, namely an amine. From the elemental composition of the mass peak at m/z = 112 ($C_7H_{14}N^+$) a molecular weight of 113 daltons is proposed for the amine (37). Sulfate salts of amines were also detected by LAMMA in the fine mode aerosol, sampled in Bahia, Brazil (see section 7.2). An additional mass peak at m/z = 95 can be attributed to a $CH_3SO_3^-$-anion. This cluster was found to be typical for a sulfonate species (see section 4.3). The negative mass peaks at m/z = 141 and 155 are interpreted as a combination of the HSO_4^--cluster with the $C_2H_6N^-$ and $C_3H_8N^-$ fragments respectively. The origin of vanadium, found to be present as a trace element in these particles, in unknown.

The organic fractions frequently detected in biogenic airborne organic matter are hydrocarbons (wax and terpenes), carboxylic acids, ketones and alcohols (38). Data about amino-compounds in aerosols are very scare, but amines, amides and amino acids have been identified in total and wet deposition samples (39), so that their occurrence in the atmosphere is obvious. The formation of organic ammonium salts could be important for the neutralization of the airborne sulfuric acid in addition to the neutralization by ammonia. The detection of the methane sulfonic acid species is consistent with the finding that also land plants can produce dimethylsulfide (DMS) (40). The reaction pathway for the oxidation

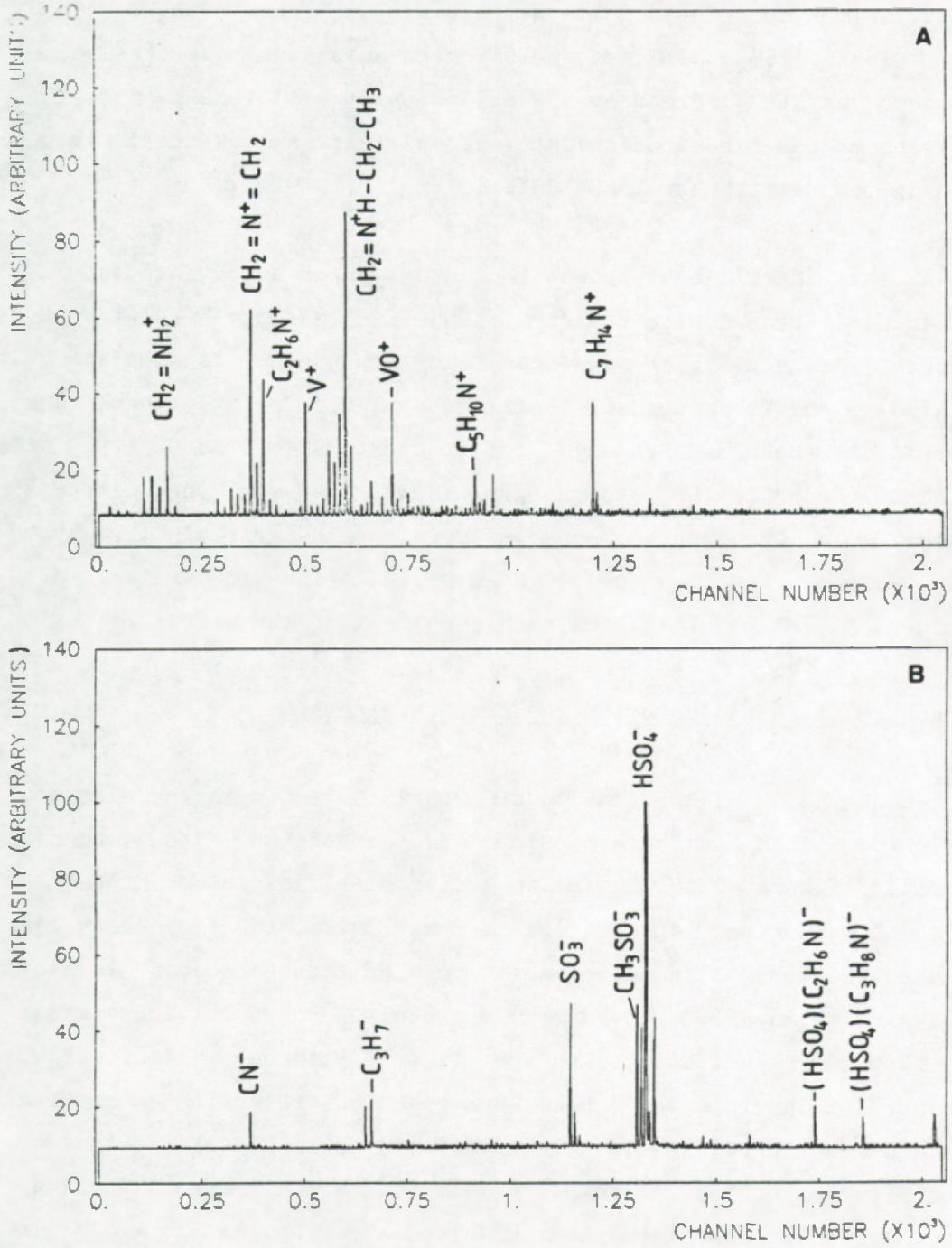

Figure 7.17a and b: Positive (a) and negative (b) mode LAMMA-spectra of a particle type assigned to a sulfate and sulfonate salt of an amine.

of DMS by OH- and NO_3-radicals results in the formation of dimethylsulfoxide (CH_3SOCH_3), methanesulfonic acid (CH_3SO_3H) and sulfur dioxide (SO_2). If methanesulfonic acid exhibits the same behaviour as H_2SO_4 formed by SO_2 oxidation it will take part in the formation of the fine mode sulfate aerosol (excess sulfate), which is in agreement with the LAMMA-data.

Another particle type was characterized as an organic matrix, containing inorganic elements such as Na, K, Ca together with Cu (Figures 7.18a and b). The enrichments of trace elements such as Cu, but also Zn and Pb in aerosols emitted by higher plants, has been reported by Beauford et al. (41). Clusters of the C_n^--type as abundantly found in the spectra are indicative for the nitrogen content of the carbonaceous material. Clusters of the type $(C_nH_{2n-1})^+$ and $(C_nH_{2n+1})^+$ and $(C_nH_{2n+1}O)^+$ as discussed earlier, are also present and point to the organic content of the sample.

The sample collected on board the Electra aircraft

About 80 % of the fine mode aerosols detected in the aircraft sample contained sulfates, chlorides, carbonates and organic material (Figure 7.19a), similar to the particles shown in Figures 7.15a and b. However, in addition to these salts, trace elements as Pb and Cr were also detected in some of these aerosols. In fact about 25 % of the fine mode aerosols contained Pb as a trace element and they were not associated specifically with one particle type. This could point to a gas phase condensation formation mechanism that is not specifically selective for a certain particle type. A minor fraction of these aerosols also contained nitrogen-oxy-salts. Other aerosols contained Cu but also Zn and Pb (Figure 7.19b) in agreement with the results of Beauford et al.(41), as mentioned earlier. In addition to these elements also Cr could be detected in the same particles.

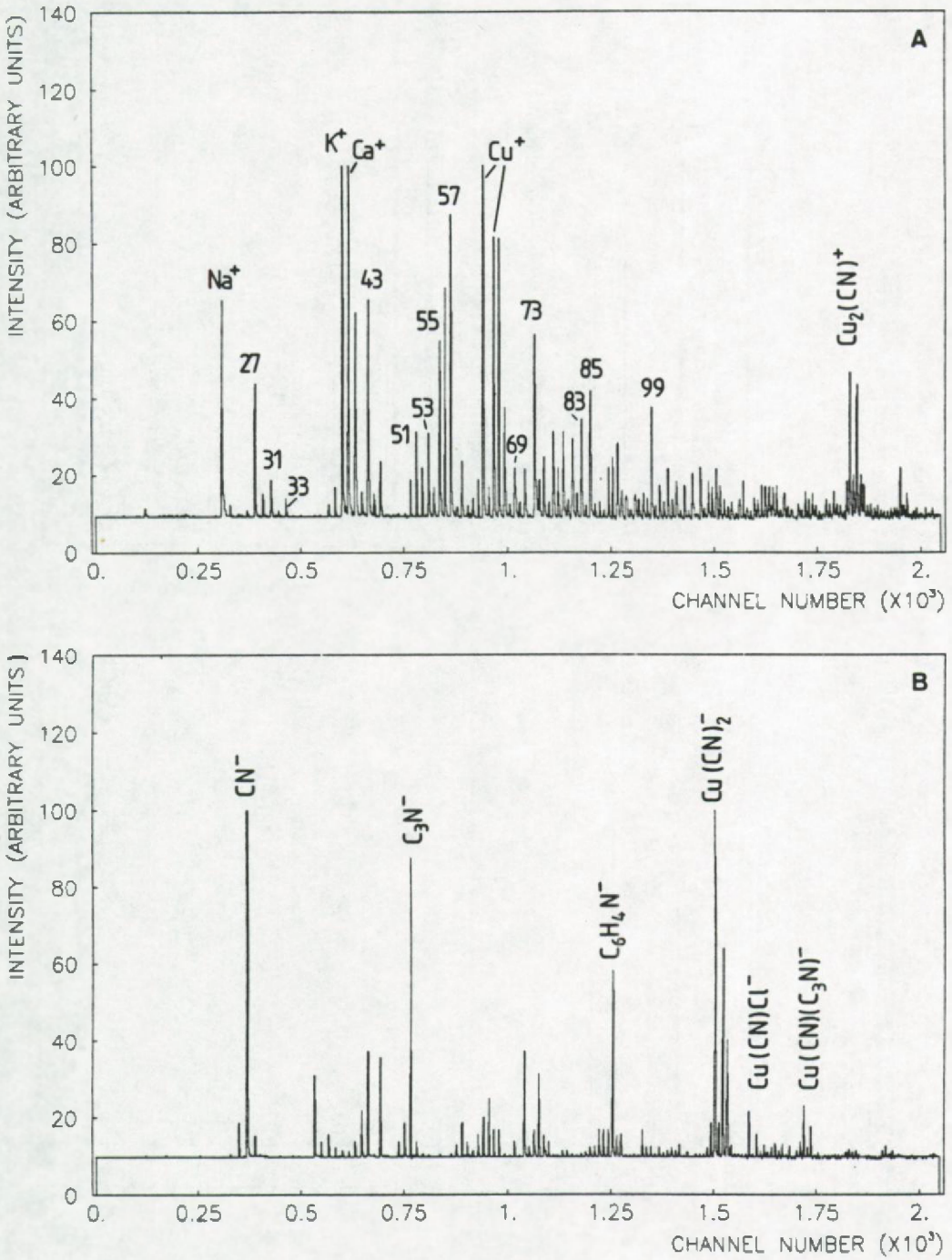

Figure 7.18: Positive (a) and negative (b) mode LAMMA-spectra of aerosol particles that are highly enriched in Cu.

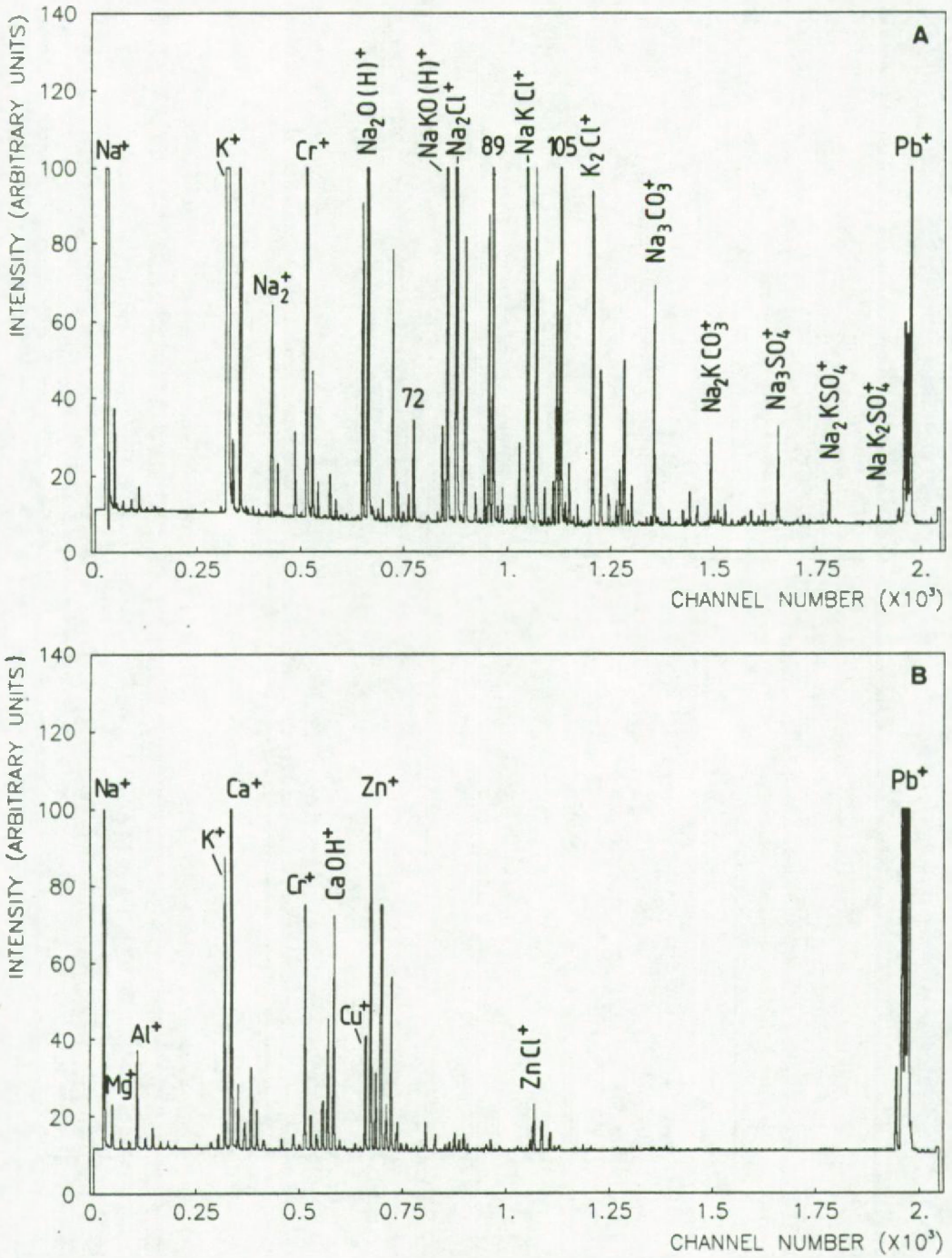

Figure 7.19a and b: Positive mode LAMMA-spectra illustrating the presence of elements such as Cr, Pb, Cu and Zn in the Amazon Basin aerosol.

The K- and P-rich phosphate particles (Figures 7.20), similar to the type of Figures 7.15a and b for the ground based sampling, revealed some molecular fragement peaks that point to the molecular species $C_4H_9NO_2$. The fragmentation pattern is consistent with an organic molecule having both a carboxyl group and an amine function, what points to an aminobutyric acid as being the most plausible identification for the unknown molecule (42).

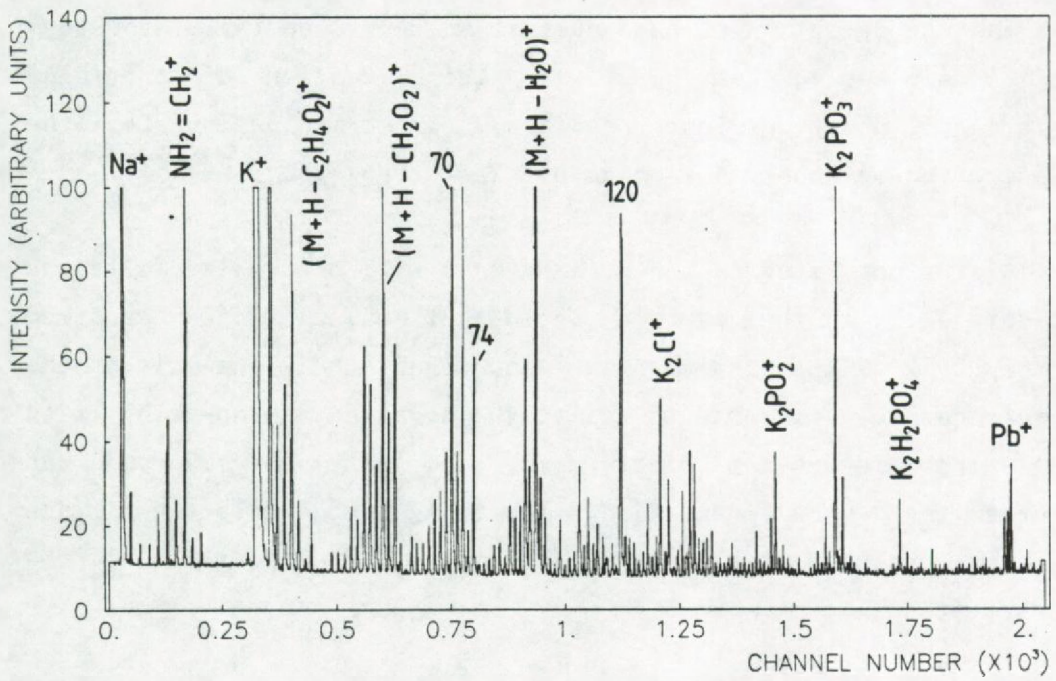

Figure 7.20: Positive mode LAMMA-spectrum of the K- and P-rich particles that also point to the presence of a $C_4H_9NO_2$-molecule.

7.3.4 Conclusion

The results clearly demonstrate the power of LAMMA for the simultaneous detection of trace elements and the fingerprinting of organic molecules, together with the speciation of the matrix composition of the individual aerosol particulates. Since one spectrum is a superposition of the fingerprints of many individual chemical identities, the interpretation of the spectra is not always straightforward.

Interesting data about the correlation of plant related material with trace elements such as Cr, Cu, Zn and Pb have been found and the detection of some organic molecules on the micrometer-size level became feasible. Also the detection of particles consisting of plant nutrients provides a direct indication for the release of these chemical species by plant transpiration.

In further studies the LAMMA-data will be combined with the EPMA-data and with the source apportionment calculations performed on the bulk PIXE-measurements. Also organic bulk analysis of the aerosols has to be invoked to assist the organic microprobing with LAMMA. The preparation of standard model systems of compounds and mixtures that were identified, including the detected trace elements, can be very helpful in improving and refining the interpretation.

7.4 REFERENCES

1. D.C. Blanchard, in Air-Sea Exchange of Gases and Particles, ed. by P.S. Liss and W.G.N. Slinn, D. Reidel Publishing Company, Dordrecht, 1983, p. 407.

2. C.S. Kiang, D. Stauffer, V.A. Mohnen, J. Bricard, and D. Vigla, Atmos. Envir., 7, 1279 (1973).

3. C.E. Junge, Air Chemistry and Radioactivity (Academic Press, New York, London , 1963).

4. R.D. Cadle, in Chemistry of the Lower Atmosphere, ed. by S.I Rasool, Plenum Press, New York, 1973, p. 69.

5. C.S. Martens, J.J. Wesolowsky, R.C. Harris, and R. Kaifer, J. Geophys. Res., 78 8778 (1973).

6. D.L. Savoie and J.M. Prospero, Geophys. Res. Lett., 10, 1207 (1982).

7. R.M. Harrison and C.A. Pio, Atmos. Environ., 17 1733 (1983)

8. R.M. Harrison and C.A. Pio, Environ. Sci. Technol.17, 167 (1983).

9. R.J Ferek, A.L. Lazrus, and J.W Winchester, Atmos. Environ., 17, 1545 (1983).

10. J. Broeckx, in Onze Noordzee, kostbaar internationaal erfgoed Staatssekretariaat voor leefmilieu, Colloquium Oostende, 22 november 1986, p.125.

11. H. Storms, P. Van Dyck, R. Van Grieken, and W. Maenhaut, J. Trace and Microprobe Techn., 1, 79 (1982).

12. P. Vanespen, Anal. Chim. Acta, 165, 31 (1984).

13. P. Van Dyck, Ph.D. Thesis, University of Antwerp (UIA), Antwerp Belgium 1983.

14. R.M. Harrison and W.T. Sturges, Atmos. Environ., 18, 1829 (1984).

15. Ph. Otten, F. Bruynseels, and R. Van Grieken, Bull. Soc. Chim. Chim. Belg., 95, 447 (1986).

16. E. Erikson, Tellus, 12, 63 (1960).

17. D.R. Hitchcock, L.L. Spiller, and W.E. Willson, Atmos. Environ., 14, 165 (1980).

18. S.L. Clegg and P. Brimblecombe, Atmos. Environ., 19, 465 (1985).

19. M.O. Andreae, J.C. Charlson, F. Bruynseels, H. Storms, R. Van Grieken, and W. Maenhaut, Science, 232, 1620 (1986).

20. M.T. Kleinman, R.F. Phalen, R. Mannix, M. Azizian, and Walters, Atmos. Environ., 19, 607 (1985).

21. F.J. Kaplan, D.M. Himmelblau, and C. Kanaoka, Atmos. Environ., 15, 763 (1981).

22. L.A. Barrie and H.W. Georgii, Atmos. Environ., 10, 743 (1976).

23. P. Brimblecombe and D.J. Spedding, Atmos. Environ., 8, 937 (1976).

24. T. Novakov, S.G. Chang, and A.B. Harker, Science, 186, 259 (1974).

25. H. Storms, S. Török, and R. Van Grieken, Anal. Chem., submitted (1987).

26. N. Kaufherr and D. Lichtman, Environ. Sci. Technol., 18, 544 (1984).

27. T. Mauney, F. Adams, and M.R. Sine, Sci. Total Environ., 36, 2151 (1984).

28. M. Uematsu, R.A. Duce, and J.M. Prospero, J. Atmos. Chem., 3, 123 (1985).

29. P.A. Cause, AERE-R8869, United Kingdom Atomic Energy Authority, AERE, Oxfordshire, England (1977).

30. R.C. Harris, S.C. Wofsy, M. Garstang, L.C.B. Molion, R.J. Mc Neal, J.M. Hoell, R.J. Bendura, S.M. Beck, R.L. Navarro, J.T.Riley, and R.L. Snell, Journal of Geophysical Research, 1986, submitted.

31. P. Artaxo, H. Storms, F. Bruynseels, R. Van Grieken and W. Maenhaut, Journal of Geophysical Research, 1986, submitted.

32. A.W. Setzer and M.C. Preira, Eos Transactions, 67, 246 (1986).

33. W. Beauford, J. Barber, A.R. Barringer, Science, 195, 571 (1977).

34. E.R.J. Wils, A.G. Hulst, J.C. Hartog, Chemosphere, 11, 1087 (1982).

35. B.R.T. Simoneit, Sci. Tot. Environ., 36, 61 (1984).

36. G.E. Nemeruyk, Soviet Plant Physiol., 17, 560 (1970)

37. L. Van Vaeck, private communication (1986).

38. B.R.T. Simoneit, M.A. Mazurek, CRC Critical Reviews in Environmental Control, 11, p219.

39. M.A. Mazurek and B.R.T. Simoneit, CRC CRitical Reviews in Environmental Control, vol.16, 1986, p.1

40. M.O. Andreae, in the Role of Air-Sea Exchange in Geochemical Cycling, ed. by P. Buat-Ménard, NATO ASI Series, D. Reidel Publisching Company, Dordrecht, 1986, p.331

41. W. Beauford, J. Barber and A.R. Barringer, Nature, 256, 35 (1975).

42. C.D. Parker and D.M. Hercules, Anal. Chem., 57, 698 (1985).

CHAPTER 8 A SURVEY OF THE APPLICATIONS OF LAMMA IN ENVIRONMENTAL RESEARCH

Most of the applications of LAMMA in environmental research make use of the single particle analysis capabilities for the investigation of ambient aerosols, asbestos fibers, fly ash and dust of industrial origin. Another important field of application is the study of geological samples.

The major advantages offered by LAMMA in these research fields are on one side its capability for simultaneous detection of nearly every element of the periodic system with a favourable detection limit, and, on the other side, its potential for the fingerprinting of organic compounds and for the speciation of inorganic constituents, all on a microscopic scale. In what follows, a survey of the LAMMA applications in environmental research is given, with a brief comment about results obtained. Special attention is drawn to review papers that deal with the same subject (1-4).

8.1 APPLICATIONS IN AEROSOL RESEARCH

The analytical techniques most frequently used provide accurate data about the bulk chemical composition of airborne particulate matter, but do not give information about the internal heterogeneity. Especially in the study of airborne particulate matter, such information is useful for detailed interpretation of the data with respect to the origin and formation mechanism of the individual particles (e.g. marine, continental or pollution derived) and their behaviour during transport, i.e. the physico-chemical interactions with the transporting medium (e.g. gas-to-particle conversion) or with other particulates (e.g. coagulation processes). Microprobe techniques such as LAMMA can be helpful in the study of these phenomena because they allow the analysis of individual aerosol particles for their organic and inorganic composition.

Moreover, other relevant data concerning trace elements and the dispersion of a chemical component within a single particle, e.g. enrichment at the particle surface, can be assessed. When combined with the particle size distribution, these data can lead to a better understanding of atmospheric chemistry, which is necessary for the determination of the effects of particle inhalation on human health.

The airborne particlulate matter can be devided into the so-called natural background aerosol (e.g. soil erosion, sea spray, biological and volcanic emissions) and man-made pollution (e.g. fly ash and dust produced by industrial activities).

For the sample preparation of particulate matter collected in bulk, e.g. steel furnace dust (5), oil shale retort (6), fly ash (9) and refinery source emissions (10), the particles are usually dispersed on a polymer film (e.g. Formvar or Pioloform) by bringing the filmed grid into contact with the bulk sample. This sample preparation procedure is not advisable for aerosol particles because the formation of agglomerates changes the particle size distribution and can result in the chemical transformation of reactive components that were originally distributed over specific particle types. The particles would not retain their identity, so that individual particle analysis is no longer meaningful. Therefore, the aerosols are often directly sampled from the air with impactors (11-14). The collection substrate must be sufficiently thin to allow perforation by the laser, e.g. Formvar films. If the filmed grids are mounted on the impaction surfaces, size-fractionated aerosol samples are obtained and no further sample manipulation is needed for the analysis. The sampling time must be optimized to assure an appropriate loading on the impaction surface, i.e. the particles have to be spatially separated from each other, so that particle-particle interactions are negligible. Since the particle number and particle size distribution is largely dependent on the sampling area, previous and simultaneous monitoring of these parameters by a particle counter can prevent the necessity to

collect several samples with different collection times in order to have at least one sample with convenient loading for single particle analysis.

For the transparant Formvar films inspection of the sample loading can also rather easily be controlled by a careful observation in an optical or electron microscope. In the case of hygroscopic particles, the lateral impaction area of the individual aerosol particulates is clearly defined by a residual mark of the evaporated water content. Special problems arise for the fine mode aerosol that often contains acidic components as H_2SO_4. The Formvar film or the Cu-grid are attacked by this chemically aggresive species. This can result in a partial or even total destruction of the film and the appearance of intense Cu-signals in the spectra.

A new development in laser induced mass spectrometry is the in flight analysis of the individual aerosols in their airborne state. In this case collection of the particulates on an impaction surface is no longer needed and the aerosols can be mass spectrometrically analyzed with a minimal disturbance of their "real airborne state" (15-16).

A general procedure for quantification in LAMMA-analysis is not available at present. For water soluble compounds, however, suitable mixed salt standards for quantification purposes can easily be prepared by the nebulization of aqueous solutions (17). The flexibility of this system allows the generation of a wide spectrun of standards that are relevant to aerosol research. In many cases, a valuable interpretation is possible for qualitative and semi-quantitative data based on the comparison of the unknown spectra with fingerprint spectra of the reference standards.

The first LAMMA-studie on atmospheric aerosols were reported by Wieser et al. (13, 18-20) and Kaufmann et al. (3,12). Ambient aerosol particles in the giant and large size range were sampled with inertial impaction devices. Individual aerosol particles were

analyzed with LAMMA for their major and minor elemental composition. The spectra showed the occurrence of trace contaminants and the first preliminary investigations on the chemical state of sulfur and nitrogen were reported. Seiler et al. (21) described the differences in the spectra for solid Si-rich aerosols and vacuum-dried S-rich particles.

Adams et al. (14) and Surkyn et al. (22) used the LAMMA instrument for aerosol source identification. It was possible to explain the anomalous enrichment of Na as $NaNO_3$ and Ca as $CaSO_4$ in aerosols collected in remote continental regions of the southern hemisphere.

Bruynseels et al. (11,23) applied the LAMMA-technique to study a set of samples collected with a low volume cascade impactor on a trajectory from a beach site, towards and through a heavily polluted industrial area. Six types of both positive and negative mass spectra with different inorganic and organic signals could be distinguished in the different particle size ranges. It allowed to retrieve different types of chemical composition and to evaluate the influence of the different sources, e.g. sea spray, soil erosion and anthropogenic pollution. LAMMA was also used to study the speciation and distribution of sulfur and nitrogen in individual aerosol particles as a function of particle size and origin and for the detection of sulfate and nitrate layers on individual marine aerosols (24,25).

In a combined study with LAMMA and EPMA, Bruynseels et al. (26, 27, section 7.2) characterized the airborne particulate matter sampled above the North Sea from air masses of different origin as determined by air mass back trajectory analysis. The combination of the results of both analytical tools has considerable advantages because they can provide complementary analytical data. EPMA was used to identify the matrix elements of individual aerosol particles collected on Nuclepore filters. The application of multivariate clustering methods on the data set revealed the percentage of

abundance for the different particle types, that can be correlated with their source of emission or their "history" during their atmospheric residence time. In principle this can also be done on the basis of the LAMMA-results but because of the higher speed and better reproducibility of the EPMA-data, this technique is generally recommmended for routine measurements conserning the inorganic elemental (Z > 11) composition of aerosols. A comparison between both analytical techniques, that clearly illustrates the complementary nature of both methods, is shown in Table 8.1.

Table 8.1: Comparison if the analytical features of LAMMA and EPMA.

Analytical features of Laser Microprobe Mass Analysis.

Advantages	Disadvantages
-advantageous detection limits down to ppm-level	-poor visual resolution (>0.5 μm)
-multi-element analysis from H to U	-semi-quantitative results are only achievable when good reference standards can be prepared
-in selected cases inorganic speciation and organic fingerprint and also surface layer analysis are feasible	-limited mass resolution
-positive and negative mode spectra can be recorded LAMMA	-loss of volatile products in the vacuum (10^{-4} Pa) of the sample chamber
	-destructive

Analytical features of automated Electron-Probe X-Ray Microanalysis

Advantages	Disadvantages
-detailed morphological information	-limited sensitivity
-many elements simultaneously	-the sample has to be made electrically conductive
-rapid analysis of a large population of particles	-elements with Z<11 (e.g. C, N, O) are not detected
-reasonable accuracy achievable by particle adapted ZAF-correction	
-non-destructive	

LAMMA-measurements on simultaneously collected impactor samples provided additional data on the low-Z and trace elements, the speciation of elememts such as S and N and the organic content of the particles.

Artificial PAH-coated particles, generated in the laboratory by gas phase condensation of PAH (anthracene, perylene, phenanthrene pyrene and chrysene),prepared in the laboratory of Dr. Niessner, were also investigated (28, section 5.2). After mixing of the PAH-coated aerosols with gases such as O_3, NO_2 and Br_2, subsequent LAMMA-analysis yielded information about the chemical reactivity of the PAH with the trace gases and the reaction products formed.

The residual particles formed after dispersion and drying of rain water samples were analyzed by Kühme (29) to study the scavenging of trace substances from the atmosphere as well as their relative solubility.

Denoyer et al. (7,8) used LAMMA for the characterization of

caol and fly ash that was collected in bulk with an electrostatic precipitator and mounted on a Formvar-coated grid by touching the grid to the bulk fly ash. The mass spectra of the oil fly ash provided data on the chemical composition such as their carbonaceous nature, the presence of S- and V-compounds and trace elements. On the basis of their LAMMA spectra, the coal fly ash particles were classified into three particle types: two types of aluminosilicates showing a statistically meaningful difference in the $^{54}Fe/^{44}Ca$-intensity ratio and carbonaceous particles containing PAH. In a multi-instrumental study of fly ash particles with respect to their morphology and surface enrichment of trace elements, Gay et al. (9) used the laser microprobe for the detection of trace elements and anions in the individual particles. Van Craen et al. (5) investigated the surface and possible leaching characteristics of steel furnace dust with predominantly with SIMS and to a lower extent with LAMMA. The negative spectra from both techniques provided information from which the chemical form of certain elements such as Fe, S and P could be inferred. Soot from an experimental oil shale retort has been examined by Mauney et al. (6), who showed that LAMMA can detect a wide molecular range of PAH, simultaneously with a multi-element inorganic analysis of individual particles with a 1 to 10 μm diameter.

Duta et al. (10) reported on the characterization of refinery emissions and ambient refinery samples. The source emissions were described as V-containing carbonaceous particles and La-containing aluminosilicate particles.

Verdun and Muller (30) used LAMMA for desorption studies of PAH, adsorbed from toluene solutions onto activated coal, silicagel and asbestos.

8.2 APPLICATIONS IN ASBESTOS STUDIES

It is well known that fine respirable asbestos fibers and man-made mineral fibers are biologically active in producing lung fibrosis, cancer and other diseases. Although the particle geometry is of primary importance for the carcinogenic effect, such chemical properties as the leachability of specific elements and the surface adsoption of pollutants can be of considerable pathogenic importance.

LAMMA-analysis of asbestos fibers relies on their light microscopical (visual) detection and on the ability to distinguish asbestos from non-asbestos fibers and to discriminate different asbestos varieties on the basis of the mass spectra obtained. Spurny et al. (31) utilized the possibility to differentiate between the serpentines and the amphibole classes of fibers and also between amosite and crocidolite on the basis of the fingerprint LAMMA spectra. De Waele et al. (32,33) systematically studied the LAMMA fingerprint spectra of the 5 UICC (International Union against Cancer) asbestos standards and pointed out that especially the positive-ion mode spectra are indicative for the different asbestos varieties. The same authors (34) also described the striking difference in spectral appearance between chrysotile originating from Zimbabwe and the variety mined in Canada. The laser desorption fingerprint spectra, indicative for the surface material of the asbestos fiber, showed an elemental peak of Fe at least a factor of 10 more intense in the Canadian chrysotile. This could be explained by the presence of magnetite micro-crystallites as surface impurities in the Canadian asbestos.

The asbestos fibers were treated with several organic products such as benzidine, benzo(a)pyrene, aliphatic alkylammonium salts, N,N-dimethylaniline (DMA) and ortho-phenylene diamine (OPDA) (33, 35-38). De Waele et al. also reported the detection of organic surface contaminants such as phthalate plasticizers originating from

the storage in polyethylene bags with a detection limit of 500 µg/g and a shot-to-shot reproducibility of ca. 20 %. LAMMA was also used for the characterization of chemically modified fiber surfaces, such as triethyloxyoctylsilane-coated chrysotile fibers (40),organosilane grafted sepiolite fibers and chrysophosphate fibers (32).

Spurny et al. (31, 41-44) studied UICC-asbestos standards and glass fibers before and after treatment with acids and bases, blood sera and animal tissues. They observed a chemical instability of the fibers in leaching experiments, e.g. for the elements Mg, Fe and Si in chrysotile and Na, K, Ca and Zn in a man-made mineral fiber.

8.3 APPLICATIONS TO GEOLOGICAL SAMPLES

Dutta et Talmi (45) applied LAMMA to optically distinct regions of a coal surface. The edge regions of polished sections of the coal samples were investigated. Since coal is a heterogeneous mixture, several model compounds such as clays, polyethylene, polystyrene and phenoxy resin were also studied. By comparison with these model compounds, they determined areas on the coal surface that were carbonaceous in nature other that were clay-like. They also identified aromatic polymers with oxygen groups. From their study of the edge regions of small chips of coal and shale samples, Vanderborgh and Jones (46) concluded that rapid heating, as by high-power laser irradiation, selectively directs energy into the hydrocarbons that are firmly sorbed onto a polymeric matrix and that the majority of the molecular species are neutral compounds that react with the available positive and negative ions to form detectable charged clusters. The results emphasize the formation of metallic cation adducts in the positive spectra and Cl-adducts in the negative spectra.

Henstra et al. (47-49) analyzed compounds from thin sections of soils developed in weathered granite. LAMMA-spectra of secondary

Ti-compounds and other constituents were obtained. The characteristic analytical possibilities of the Ion Microprobe Mass Analyzer (IMMA), EPMA and LAMMA were compared.

Weinke et al. (50) investigated troilite (stoichiometric iron sulphide, FeS, of meteoritic origin) and pyrite of terrestrial origin. The trace element content was calculated by a method using the LTE-model and results were compared with those obtained by other instrumental techniques, such as neutron activation analysis, EPMA and SIMS.

Freund et al. (51) reported the detection of atomic carbon in arcfusion grown MgO and CaO single crystals. Similar measurements were done on synthetic forsterite and natural olivines (52) and led to the conclusion that these minerals can take up atomic carbon in the solid solution.

Osmium-containing specimens from different deposits were analyzed by Englert and Herpers (52). The samples were prepared by spreading the powders on filmed grids or by fixing larger fragments between two grids. They found isotopic anomalies for ^{187}Os (daughter of the long-lived radionuclide ^{187}Re) corresponding to the sample's age and the ^{187}Re content of the ores from which the Os was separated. In a combined LAMMA and analytical EM study of Zr-deposits, Steel et al. (54) measured the content of the trace elements U, Th and Pb, as well as the relative abundance of the Pb-isotopes.

8.4 REFERENCES

1. E. Michiels, L. Van Vaeck, and R. Gijbels, Scanning Electron Microsc.,III,1111 (1984).

2. A.H. Verbueken, F.J. Bruynseels, and R.E. Van Grieken, Biomed. Mass Spectrom., 12, 438 (1985).

3. R. Kaufmann, P. Wieser, and R. Wurster, Scanning Electron Microsc., II, 607 (1980).

4. R. Kaufmann and P. Wieser, in Modern Methods of Fine Particle Characterization, Vol. II, ed. by I. Beddow and A. Vetter, CRC Press, Boca Raton, 1982, p.199.

5. M.J. Van Craen, E.A. Denoyer, D.F.S. Natusch, and F. Adams, Environ. Sci. Technol., 17, 435 (1983).

6. T. Mauney, F. Adams, and M.R. Sine, Sci. Total Environ., 36, 215 (1984).

7. E. Denoyer, T. Mauney, D.F.S. Natusch, and F.Adams, in Microbeam Analysis-1981, ed. by K.F.J. Heinrich, San Francisco Press, San Francisco, 1982, p.191.

8. E. Denoyer, D.F.S. Natusch, P. Surkyn, and F.C Adams, Environ. Sci. Technol., 17, 457 (1983).

9. A.J. Gay, A.P. von Rosenstiel, and P.J. van Duin, in Microbeam Analysis-1981, ed. by R.H. Geiss, San Francisco Press, San Francisco, 1981, p.229.

10. P.K. Dutta, D.C. Rigano, R.A. Hofstader, E. Denoyer, D.F.S. Natusch, and F. Adams, Anal. Chem., 56, 302 (1984).

11. F. Bruynseels, H. Storms, T. Tavares, and R. Van Grieken, Int. J. Environ. Anal. Chem., 23, 1 (1985).

12. R. Kaufmann, and P. Wieser, in Characterization of Particles, ed. by K.F.J. Heinrich, NBS Spec. Publ. 533, Washington, 1980, p.199

13. P. Wieser, R. Wurster and L. Phillips, in Aerosols in the Mining and Industrial Work Environment, Vol. 3, ed. by V.A. Marple and B.Y.H. Liu, Ann Arbor Science, Michigan, 1983, p.1169.

14. F. Adams, P. Bloch, D.F.S. Natusch, and P. Surkyn, in Proceedings of the International Conference on Environmental Pollution, Thessaloniki, Greece, Sept. 21-25, 1981, p.122.

15. M.P. Sinha, and S.K. Friedlander, in Aerosols: Formation and Reactivity, Proceedings of the 2nd Int. Aersol Conf. Berlin, Sept. 22-26, 1986, p.875.

16. R. Kaufmann, personal communication.

17. Ph. Otten, F. Bruynseels, and R. Van Grieken, Anal. Chim. Acta (1986), submitted

18. P.Wieser, R. Wurster, and H. Seiler, Atmos. Environ., 14, 485 (1980).

19. P. Wieser, R. Wurster, and U. Haas, Fres. Z. Anal. Chem., 308, 260 (1081).

20. P.Wieser, R. Wurster, and H. Seiler, Scanning Electron Microsc., III, 56 (1980).

21. H. Seiler, U. Haas, I. Rentschler, H. Schreiber, P. Wieser, and R. Wurster, Optik, 58, 145 (1981).

22. P. Surkyn, J. De Waele, and F. Adams, Int. J. Environ. Anal. Chem., 13, 257 (1983).

23. F. Bruynseels, H. Storms, and R. Van Grieken, J. Physique, 45, C2-785 (1984)

24. F. Bruynseels and R. Van Grieken, Atmos. Environ., 19, 1969 (1985).

25. Ph. Otten, F. Bruynseels, and R. Van Grieken, Bull. Soc. Chim. Belg., 95, 447 (1986).

26. F. Bruynseels, H. Storms, and R. Van Grieken, in Proceedings of the International Conference on Heavy Metals in the Environment, Vol. 1, ed. by T.D. Lekkas, Athens, Greece, Sept. 10-13, 1985, p.189

27. F. Bruynseels, H. Storms, R. Van Grieken, and L. Van der Auwera, Atmos. Environ., 1986, submitted.

28. R. Niessner, D. Klockow, F. Bruynseels and R. Van Grieken, Int. J. Environ. Anal. Chem., 22, 281 (1985).

29. H. Kühme, Meteorol. Rundsch., 36, 119 (1983).

30. F. Verdun, and J.F. Muller, J. Physique, 45, C2-819 (1984).

31. K.R. Spurny, J. Schörmann, and R. Kaufmann, Fres. Z. Anal. Chem., 308, 274 (1981)

32. J.K. de Waele and F.C. Adams, Scanning Electron Microsc., III, 935 (1985).

33. J. De Waele, P. Van Espen, E. Vansant, and F. Adams, in Microbeam Analysis-1982, ed. by K.F.J. Heinrich, San Francisco Press, San Francisco, 1982, p.371.

34. J.K. De Waele, M.J. Luys, E.F. Vansant, and F.C. Adams, J. Trace and Microprobe Tech., 2, 87 (1984).

35. J. De Waele, E.F. Vansant, P. Van Espen, and F.C. Adams, Anal. Chem., 55, 671 (1983).

36. J.K. De Waele, I. Verhaert, E.F. Vansant, and F.C. Adams, Surface and Interface Analysis, 5, 186 (1983).

37. J.K. De Waele, E.F. Vansant, and F.C. Adams, Mikrochim. Acta, III, 367 (1983).

38. J. K. De Waele, E.F. Vansant, and F.C. Adams, Anal. Chim. Acta, 161, 37 (1984).

39. J.K. De Waele, J.J. Gijbels, E.F. Vansant, and F.C. Adams, Anal. Chem., 55, 2255 (1983).

40. J.K. De Waele, I.M. Swenters, and F.C. Adams, Spectrochim. Acta, 40B, 795 (1985).

41. K. Spurny, Sci. Total Environ., 23, 239 (1982).

42. K. Spurny, Environ. Health Perspectives, 51, 343 (1983).

43. K. Spurny, F. Pott, W. Stöber, H. Opiela, J. Schörmann, and G. Weiss, Am. Ind. Hyg. Assoc. J., 44, 833 (1983).

44. K. Spurny, Sci. Total Environ., 30, 147 (1983).

45. P.K. Dutta and Y. Talmi, Fuel, 61, 1241 (1982).

46. N.E. Vanderborgh, and C.E.R. Jones, Anal. Chem., 55, 527 (1983).

47. S. Henstra, E.B.A. Bisdom, A. Jongerius, H.J. Heinen, and S. Meier, Beitr. electronenmikroskop. Direktabb. Oberfl., 13, 63 (1980).

48. E.B.A. Bisdom, S. Henstra, A. Jongerius, H.J. Heinen, and S. Meier, Neth. J. Agric. Sci., 29, 23 (1981).

49. S. Henstra, E.B.A. Bisdom, A. Jongerius, H.J. Heinen, and S. Meier, Fres. Z. Anal. Chem., 309, 280 (1981).

50. H.H. Weinke, E. Michiels, and R. Gijbels, Int. J. Mass Spectrom. Ion Phys., 47, 43 (1983).

51. F. Freund, H. Wengeler, H. Kathrein, and H.J. Heinen, Mat. Res. Bull., 15, 1019 (1980).

52. F.Freund, H. Kathrein, H. Wengeler, R. Knobel, and H.J. Heinen, Geochim. Cosmochim. Acta, 44, 1319 (1980).

53. P. Englert and U. Herpers, Inorg. Nucl. Chem. Lett., 16, 37 (1980).

54. E.B. Steel, D.S. Simons, J.A. Small, and D.E. Newbury, in Microbeam Analysis-1984, San Francisco Press, San Francisco, 1984, p.27.

SUMMARY AND CONCLUSIONS

It is generally recognized that there is a need for the further development of microanalytical techniques to elucidate questions that arise in the field of particulate sample analysis as e.g. in aerosol research. An exhaustive interpretation of bulk measurements seldomly allows eludication of the chemical composition of the sample on a microscopic level and it is this information that is required for reliable aerosol particle source identification, and for studies concerning the dynamic behaviour of aerosols in a chemically reactive environment.

With the introduction of the commercial laser microprobe mass analyser (LAMMA-500 instrument, manufactured by Leybold Heraeus, Köln, F.R.G.) the expectations ran high because the obtained results were very encouraging when compared to other instrumental alternatives. Especially the very low detection limits (down to the ppm range) that became achievable for a very minute material consumption ($< 10^{-12}$ g) were very remarkable. However, the difficulties encountered in the quantification of the results readily limited the applicability of the method to specific highly elaborated analyses. Certainly in the field of individual aerosol particle analysis, for which numerous aerosol particles have to be analyzed, in order to obtain statistically meaningful results, the destructive nature of the method coupled to a shot-to-shot reproducibility of 10 to 30 % for single elemental signals, makes it difficult to obtain reliable quantitative data for ambient aerosols. This is also aggravated by the possible non-uniformity and inherent natural variability of the trace element concentrations of individual aerosol particles, that is superimposed on the uncertainty of the analytical method itself.

An interesting field of applications for LAMMA is the determination of inorganic and organic species on a microscopic level. The cluster ions observed in the LAMMA-spectra are the result

of the interaction process of the 15 ns laser pulse with the chemical compounds of the particle. Knowlegde about the relative importance of direct (i.e. intact) fragment emission from the original chemical structure, compared to recombination reactions between cluster fragments eases the interpretation of the spectral data. From the study of $^{12}C/^{13}C$ bilayer samples it could be concluded that for energies above twice the threshold for sample perforation, the mechanisms of both direct fragment emission and the formation of recombination clusters, are active in the generation of the charged cluster ions, and their relative importance could be inferred. For laser excitation energies close to the threshold for sample perforation, preferential ion extraction from the side of the sample that is faced towards the mass spectometer was observed. This geometry effect for ion extraction increases with decreasing laser irradiance and it can facilitate the use of LAMMA-500 as a surface selective analysis technique, certainly in the cases where the threshold for sample perforation is not exceeded. The depth resolution in the so-called laser desorption mode, is estimated to be around 20 nm or better.

A number of chemical species that are relevant for atmospheric research were investigated with LAMMA. The composition and relative intensities of the cluster ions are examined in order to find the relationship between the mass spectral pattern and the original compound stoichiometry, and to contribute to the understanding of the laws that govern ion formation under laser irradiation. The study includes Ca-salts such as $CaSO_4$, $CaSO_4.2H_2O$, $CaCO_3$ and CaO. Special attention was paid to the S-salts $NaSO_4$, $NaSO_3$, $Na_2S_2O_3$, $NaCH_3SO_3$, K_2SO_4, $MgSO_4$, $CuSO_4$, NH_4HSO_4... but also the N-compounds ($NaNO_3$, $NaNO_2$, $(NH_4)_2SO_4$....). The development of a convenient method for the chemical S- and N-speciation in individual micrometer-size particles can contribute in solving the current discussion concerning the origin and fate of the natural and anthropogenic S- and N-compounds and their impact on the atmospheric S- and N-cycles, nowadays generally refered to as the acid rain problem.

The capability of LAMMA for the surface selective analysis of aerosol particles was investigated for three different model systems that are of direct interest in actual research concerning the heterogeneous gas/particle interaction mechanisms. The study of the microstructure of airborne particles is of major interest because it governs the chemical reactivity between a particle and the gas phase. Also the toxicity of substances like e.g. polynuclear aromatic hydrocarbons (PAH) by particle inhalation is largely influenced by the bioavailability on the particle surface. The investigations on laboratory generated NH_4HSO_4-aerosols coated with n-hexadecanol were not successful as far as the selective desorption of the coating material is concerned. The results for the PAH-coated aerosols, however, were very interesting. All PAH (anthracene, perylene, phenanthrene, pyrene, fluoranthene, chrysene and anthracinone) could be gently desorbed from the carrier-particle in absolute amounts around 10^{-15} g. The PAH-coated particles were also subjected to the interaction with gaseous components including O_3, Br_2 and NO_2. For the reaction with ozone, the oxidation products observed could be correlated with specific reaction mechanisms. O_3 was more reactive than Br_2 and NO_2, while fluoranthene and chrysene seemed to be stable under the experimental conditions used. The third model system dealt with the interaction between gaseous HNO_3 and seasalt aerosol. It was shown that LAMMA offers a powerful and fast method for the detection of nitrate enrichments in individual marine aerosol particles, provided that special precautions are made to eliminate HNO_3-interaction with the aerosols already collected in the impaction device.

The LAMMA-technique was also applied for the individual particle characterization of ambient aerosols, sampled in three environmentally different areas. The first set of samples were collected in Salvador, Brazil and had the aim to study the changes in chemical composition of the atmospheric aerosol during a transect from a rather remote beach site towards and through a heavily industrialized area as a result of the steady on-shore trade winds. The study pointed out that the formation of particulate nitrate on

seasalt particles is actually occuring in coastal areas with their high atmospheric seasalt load, and that polluted air enhances this production mechanism. In the accumulation mode particles, sulfur is present as ammonium sulfates, together with significant quantities of carbonaceous particles. Besides inorganic nitrogen (NH_4^+ and NO_n^-), organic nitrogen compounds were also detected in the industrialized area.

A second study focused on the aerosol source identification for airborne particulate matter sampled above the North Sea under various wind directions. The aerosol sampling was carried out on board the oceanographic ship Belgica. The project was initiated to study the importance of the atmospheric input of particulate matter by wet and dry deposition processes, as a pathway to the North Sea for the pollutants emitted by the surrounding industrialized countries. By the combination of the LAMMA-results with those of automated electron microprobe measurements, considerable improvement was gained for a more detailed interpretation of the data. Some of the particle types that could be identified are for instance, seasalt with and without nitrate and sulfate enrichments, aerosols consisting of a mixture of seasalt and aluminosilicates, spherical aluminosilicates produced by combustion sources, carbonaceous S-rich particles, spherical iron oxide particles, different types of Ca-rich particles.... Trace elements (e.g V, Mn, Ni, Pb, Ga, Rb, Cs, Co) but also a wide range of PAH could be detected in the individual aerosol particles.

In a third case study, aerosol samples were analysed that had been collected both from a ground based station and by aircraft flights in the Amazon basin during the Atmospheric Boundary Layer Experiment (ABLE-2A) executed by the U.S. National Aeronautics and Space Administration (NASA) in July and August 1985. The experiment focused on assessing the role of biosphere-atmosphere interactions on the chemistry of the troposphere over relatively pristine tropical forests and wetlands in order to learn more about the role of the tropics in global atmospheric chemistry. Interesting data

about the correlation of plant derived material with trace elements, such as Cr, Cu, Zn and Pb, have been found and the detection of some organic molecules on the micrometer-size level became feasible. Also the detection of particles consisting of plant nutrients provides a direct indication for the release of these chemical species by plant transpiration.

Most of the studies cited above clearly demonstrated the possibilities offered by LAMMA in the field of aerosol research. Nevertheless several improvements, both in the instrumental set-up and for the data interpretation, are recommendable to really exploit the full capabilities of the method. As an alternative for the aerosol collection on substrates using impaction devices, another alternative for sampling can be proposed namely, the in-flight analysis of airborne particles. This instrumental approach has been followed for several years already by Sinha et al. (1,2). Their experimental set-up makes use of a particle beam generator, a differential pumping system, a resistively heated rhenium filamemt and a focal plane mass spectrograph. Although this instrumental configuration is important because of the concept as such, it is certainly not the best nor the final version that will be built. In addition to a particle beam (produced by an aerosol expanding into the vacuum through a capillary nozzle) one could think of the introduction of the photoelectric charging technique, that is based on the charging of particles suspended in a gas by the emission of photoelectrons upon irradiation with a ultraviolet lamp, as described by Burtscher et al. (3-5). Photoelectric charging may be used for the determination of the particle size and yields information on chemical and surface properties (3). Moreover, it can also be used for the guidance of the particle by an electric field, so that is can be directed to the focal plane of the laser beam. The combination of this sampling device with the versatile laser ionisation source coupled to a time-of-flight mass spectrometer could be much more successful for the in-flight analysis of aerosols.

For the interpretation of the spectral data, on the other hand, one could think of the development of an expert system to recognize fingerprint spectra and to assign them to reference spectra of standard compounds. This could also provide a series of possible identifications for the different mass signals that can be checked in more detail by the LAMMA-user. Research about further automation of the data reduction is necessary, because at the moment it is the most time-consuming task in the whole procedure of LAMMA-analysis of particles with unknown chemical composition. Up to now, it was most convenient for the operator to rely on his visual memory to recognize the fingerprint patterns of the different particle types. The spectra presented in the former chapters can serve as the onset to a reference basis for the interpretation of the mass spectral data of airborne particles.

In spite of the specific limitations of the LAMMA-technique, interesting results were found, that would be very difficult, or even unpossible, to obtain with other instrumental techniques.

SAMENVATTING EN BESLUIT

Algemeen wordt de noodzaak erkend voor een verdere ontwikkeling van micro-analytische technieken die kunnen bijdragen tot het onderzoek van stalen bestaande uit partikels zoals bijvoorbeeld in aerosol studies. Een diepgaande interpretatie van de gegevens bekomen door bulkanalyse is zelden toereikend om tot een grondige interpretatie te komen betreffende de samenstelling op microscopische schaal. Nochtans is het deze informatie die vereist is om een eenduidig verband te leggen tussen een aerosol deeltje en zijn emissiebron, alsook voor de studie aangaande het dynamisch gedrag van aerosolen in een chemisch reactieve omgeving.

Toen de laser microprobe massa analysator (LAMMA-500, vervaardigd door Leybold Heraeus, Keulen, West-Duitsland) op de markt werd gebracht, waren de verwachtingen zeer hoog gespannen door de veelbelovende resultaten die reeds werden verkregen. Vooral de uitzonderlijk lage detectielimieten (tot het ppm-niveau) die werden gehaald voor een zeer gering materiaal verbruik ($<10^{-12}$ g) waren zeer gunstig in vergelijking met andere beschikbare instrumentele alternatieven. De problemen in verband met de kwantificatie van de resultaten zorgde er al vrij vlug voor dat de toepasbaarheid van de methode werd beperkt tot een aantal zeer specifieke en grondig uitgewerkte analyses. Zeker in het gebied van individuele deeltjes analyse, waarbij een relatief groot aantal aerosoldeeltjes dient te worden geanalyseerd om tot statistisch betekenisvolle resultaten te komen, wordt het vergaren van betrouwbare kwantitatieve gegevens bemoeilijkt door het destructief karakter van de techniek en de eerder beperkte reproduceerbaarheid van de massa-signalen voor elementen (10-30 %). Daarenboven wordt dit probleem nog versherpt door de mogelijke inhomogeniteit en natuurlijke variabiliteit van de concentraties aan sporenelementen tussen de individuele aerosoldeeltjes onderling, wat zich nog eens superponeert op de onzekerheid van de analytische methode zelf.

Een interessant toepassingsgebied voor LAMMA is de anorganische

en organische speciatie van verbindingen op microscopische schaal. De klusterionen (dit zijn ionen opgebouwd uit verschillende elementen) worden gevormd door het interaktieproces tussen de 15 ns durende laserpuls en de chemische componenten van het deeltje. Voor de interpretatie van de spektra is een beter inzicht vereist aangaande de relatieve belangrijkheid van de emissie van intakte fragmentionen, die dus rechtstreeks gevormd worden uit de originele chemische verbindingen, in vergelijking met rekombinatiereakties tussen klusterfragmenten. Uit de studie van een gelaagd monster bestaande uit een ^{12}C- en een ^{13}C-laag kon worden afgeleid dat voor bestralingsenergieën groter dan 2X de drempelwaarde nodig voor de perforatie van het monster, zowel het mechanisme van direkte fragmentionenemissie als de vorming van gerekombineerde klusters werkzaam zijn in de produktie van de geladen ionen. De relative belangrijkheid van beide mechanismen werd bestudeerd in funktie van de laserintensiteit. Bij lage laserbestralingsenergieën (in de buurt van de drempelwaarde nodig voor de perforatie van het monster) werd een preferentiële ionenextraktie vastgesteld voor de ionen die afkomstig zijn van de zijde van het monster dat naar de opening van de massaspektrometer is gekeerd. Dit geometrie-effect dat zich manifesteert bij de ionenextraktie neemt in belangrijkheid toe voor lagere excitatie-energieën en maakt het mogelijk om met het LAMMA-500 instrument een oppervlaktegevoelige analyse uit te voeren, zeker voor deze gevallen waarbij de drempelenergie voor de perforatie van het monster niet werd overschreden. De diepte-resolutie in de zogenaamde laserdesorptie mode, werd geschat rond 20 nm of lager.

Een aantal chemische verbindingen die van belang zijn voor atmosferisch onderzoek werden met LAMMA onderzocht. De samenstelling en relatieve intensiteiten van de klusterionen werden bestudeerd met als doel een verband te leggen tussen het massaspectrometrisch patroon en de chemische structuur van de geanalyzeerde verbinding. Zo werden ondermeer Ca-zouten bestudeerd zoals $CaSO_4$, $CaSO_4.2H_2O$, $CaCO_3$ em CaO. Er werd ook speciale aandacht besteed aan de S-verbindingen ($NaSO_4$, $NaSO_3$, $Na_2S_2O_3$, $NaCH_3SO_3$, K_2SO_4, $MgSO_4$,

$CuSO_4$, NH_4HSO_4...) en de N-verbindingen ($NaNO_3$, $NaNO_2$, $(NH_4)_2SO_4$...). De ontwikkeling van een geschikte methode voor de chemische speciatie van S- en N-verbindingen in individuele microscopische kleine aerosol deeltjes kan nuttig zijn in het onderzoek naar de oorsprong en het gedrag van de natuurlijke en anthropogene S- en N-verbindingen en hun invloed op de atmosferische S- en N-cycli. Deze problematiek wordt in de gebruikstaal omschreven als het verschijnsel "zure regen".

De mogelijkheden van LAMMA voor de oppervlaktestudie van aerosol deeltjes werd onderzocht voor drie verschillende modelsystemen die van praktisch belang zijn voor atmosferisch onderzoek in verband met de heterogene gas-deeltjes interactie-mechanismen. De studie van de mikrostruktuur van aerosoldeeltjes is belangrijk omdat het bepalend is voor de chemische reaktiviteit van de deeltjes met de gasfase. Bovendien is de toxicitiet van de chemische componenten zoals bijvoorbeeld polyaromatische koolwaterstoffen (PAK) in hoge mate afhangkelijk van de biologische beschikbaarheid aan het oppervlak van het deeltje. De analyse van in n-hexadecanol ingekapselde NH_4HSO_4-aerosolen was niet erg succesvol wat betreft de selektieve desorptie van de oppervlaktelaag. Voor de met PAK-bedekte aerosolen daarentegen werden wel goede resultaten bekomen. Al de polyaromaten (antraceen, peryleen, fenantreen, pyreen, fluoranteen en chryseen) konden selectief van de drageraerosolen worden gedesorbeerd in absolute hoeveelheden tot 10^{-15} g. Vervolgens werden de bedekte deeltjes in de aerosolfase in kontakt gebracht met gasvormige componenten zoals O_3, Br_2 en NO_2. De produkten onstaan door de interaktie van de PAK met ozon, konden aan de hand van de LAMMA-spektra in verband worden gebracht met specifieke reaktie mechanismen. Ozon was reaktiever dan Br_2 en NO_2, terwijl fluoranteen en chryseen stabiel waren voor de uitgeteste experimentele voorwaarden. Het derde model systeem behandelde de interaktie tussen gasvormig HNO_3 en zeezoutaerosol. Er werd aangetoond dat LAMMA een zeer interessante techniek is voor de snelle detectie van nitraataanrijkingen in mariene aerosoldeeltjes op voorwaarde dat bepaalde voorzorgen worden genomen om de reaktie

van HNO_3 met de reeds geïmpakteerde aerosolen te vermijden.

De LAMMA-techniek werd eveneens aangewend voor de chemische karakterisatie van individuele aerosoldeetjes die werden gekollekteerd in drie gebieden waarvoor duidelijke verschillen wat betreft de aerosolsamenstelling kon worden verwacht. De eerste groep luchtstalen werd bemonsterd in Salvador (Brazilië) en had tot doel om de veranderingen in chemische samenstelling van de aerosolen te bestuderen wanneer deze zich van een vrij ongepollueerde strandzone naar een sterk geïndustrializeerd gebied begeven, onder invloed van een overheersend landinwaartse wind. De vorming van nitraat-aanrijkingen in het zeezoutaerosol dat door gepollueerde lucht nog wordt verhoogd, werd experimenteel aangetoond. In de fijne deeltjes-fraktie werd S aangetroffen onder de vorm van sulfaat tesamen met belangrijke hoeveelheden aan organisch materiaal. Naast de anorganische stikstofverbindingen (NH_4^+ en NO_n^-) werden in het industriegebied ook de aanwezigheid van organische stikstofmolekulen aangetoond

Een tweede studie naar de identificatie van de emissiebronnen van aerosoldeeltjes werd uitgevoerd op luchtstalen gekollekteerd boven de Noordzee bij verschillende windrichtingen. De bemonstering gebeurde aan boord van het oceanografisch schip Belgica. Het projekt werd opgezet om de atmosferische bijdrage tot de Noordzee pollutie ten gevolge van droge en natte depositie van polluenten, geëmiteerd door de omliggende geïndustrialiseerde landen te bestuderen. Door kombinatie van de LAMMA-resultaten met deze van geautomatiseerde elektronenmikroprobe metingen, werd een meer gedetaileerde interpretatie van de gegevens mogelijk. De deeltjestypen die konden worden geïdentificeerd omvatten ondermeer zeezout met en zonder nitraat- en sulfaataanrijkingen, aerosolen bestaande uit een mengsel van aluminosilikaten en zeezout, sferische aluminosilikaten afkomstig van verbrandingsprocessen, koolstofrijke zwavelhoudende deeltjes.... Sporenelementen (bijvoorbeeld V, Mn, Ni, Pb, Ga, Rb, Cs en Co), maar ook polyaromaten konden worden geïdentificeerd in individuele aerosoldeeltjes.

Een derde onderzoek betrof de analyze van luchtstalen die werden gekollekteerd op een grondstation en aan boord van de Lockheed Electra tijdens vluchten boven het Amazone gebied. De bemonsteringen werden uitgevoerd tijdens de periode juli-augustus 1985 in het kader van het "Atmospheric Boundary Layer Experiment (ABLE-2A)", een projekt van de "National Aeronautics ad Space Administration (NASA)". Er werd onderzoek verricht naar de rol van biosfeer-atmosfeer interakties op de chemie van de troposfeer over relatief afgelegen tropische wouden en moerassen, om een beter inzicht te verwerven in hun invloed op de chemische samenstelling van de atmosfeer op wereldschaal. Er werden interessante gegevens verkregen over de aanrijking van sporenelementen zoals Cr, Cu, Zn and Pb in aerosolen geëmitteerd door de planten en er werd een belangrijke organische fraktie in deze aerosolen gedetecteerd. De aerosolen bestaande uit plantnutriënten geven een direkte aanwijzing voor de emissie van deze verbindingen door zogenaamde transpiratie door de plantengroei.

De meeste van de hierboven vermelde studies hebben de mogelijkheden van LAMMA op het gebied van aerosol onderzoek duidelijk aangetoond. Desalniettemin kunnen nog een aantal verbeteringen worden aangebracht zowel aan de instrumentele kant, als wat betreft de gegevensverwerking om de de mogelijkheden van het instrument ten volle te benutten. In de plaats van de kollektie van aerosolen of substraten door middel van impaktoren, bestaat er een interessant alternatief namelijk, de analyse van deeltjes in de aerosol fase zelf. Deze instrumentele aanpak word reeds verscheidene jaren gevolgd door Sinha (1,2) en medewerkers. Hun instrumentele opstelling maakt gebruik van een deeltjesbundelgenerator, een differentiële pompeenheid, een resistief verwarmd rheniumfilament en een massaspectrometer. Alhoewel deze instrumentele configuratie belangrijk is omwille van het concept als dusdanig, is het zeker niet de beste noch de laatste versie die zal worden ontworpen. Naast de deeltjesbundelgenerator waarbij het aerosol expandeert in het vacuum door een capillair, zou het nuttig kunnen zijn om de techniek

van foto-elektrische oplading in te bouwen. Deze methode, ontwikkeld door Burtscher en medewerkers (3-5), biedt de mogelijkheid om deeltjes gesuspendeerd in een gasfase te voorzien van een elektrische lading, door ze te bestrallen met UV-licht. De foto-elektrische oplading laat toe de deeltjesgrootte te bepalen en te selekteren en verschaft bovendien informatie over chemische en oppervlakte-eigenschappen (3). Bovendien kan de elektrische lading geïnduceed op de deeltjes handig aangewend worden om ze in een gewenste baan te sturen door middel van een elektrisch veld, zodat ze eventueel naar het focaal vlak van de laserbundel kunnen worden gedirigeerd. De kombinatie van een dusdanig bemonsteringssysteeem met de veelzijdige laserionisatiebron, gekoppeld aan een vluchttijdmassaspektrometer, zou interessante mogelijkheden kunnen bieden voor de analyse van deeltjes in de aerosolfase.

Voor de interpretatie van de spektra zou de ontwikkeling van een expertsysteem om karakteristieke spektra te herkennen ze te correleren met de referentie-spektra van standaarden, zeer goede diensten kunnen bewijzen. Het programma zou ook een aantal mogelijke identificaties kunnen vooropstellen voor specifieke massasignalen, die dan door de LAMMA-gebruiker nader kunnen worden onderzocht. Omdat de interpretatie van de spektrale gegevens voor onbekende aerosoldeeltjes het meeste tijd vergt in de gehele procedure van de LAMMA-analyse, is verder onderzoek naar de automatisatie van de gegevensverwerking noodzakelijk. Totnogtoe wordt veelal gebruik gemaakt van het visuele geheugen van de operator voor de herkenning van de typische massaspektra voor verschillende deeltjes. De spektra opgenomen in dit werk kunnen een aanzet zijn tot een referentiebasis voor de interpretatie van de massa spektra van aerosoldeeltjes.

Niettegenstaande de specifieke beperkingen van de LAMMA-techniek, werden voor een aantal gerichte onderzoeksprojecten interessante resultaten bekomen, die met andere technieken zeer moeilijk, zoniet onmogelijk, kunnen worden behaald.

REFERENCES

1. M.P. Sinha, C.E. Giffin, D.D. Norris, T.J. Estes, V.J. Vilker, and S.K. Friedlander, J. Colloid Interf. Sci., 87, 104 (1981).

2. M.P. Sinha and S.K. Friedlander, in Aerosols: formation and reactivity, Proceedings of the 2nd Int. Aerosol Conf., Berlin, Sept. 22-26, 1986, 875.

3. H. Burtscher, L. Scherrer, H.C. Siegmann, A. Schmidt-Ott, and B. Federer, J. Appl. Phys., 53, 5 (1982).

4. H. Burtscher and A. Schmidt-Ott, J. Aerosol Sci., 17, 4 (1986).

5. H. Burtscher, A. Schmidt-Ott and, H.C. Siegmann, in Aerosols: formation and reactivity, Proceedings of the 2nd Int. Aerosol Conf., Berlin, Sept 22-26, 1986, 935.

APPENDIX

LIST OF PUBLICATIONS

1. F.J. Bruynseels and R.E. Van Grieken, Molecular ion distributions in laser microprobe mass spectrometry of calcium oxide and calcium salts, Spectrochim. Acta, 38B, 853 (1983).

2. F. Bruynseels and R. Van Grieken, Laser microprobe massa analyse van microscopische partikels, VCV Tijdingen, Dag der jongeren, K.U.L., 20 april 1983.

3. F. Bruynseels, H. Storms, and R. Van Grieken, LAMMA and electron microprobe analysis of atmospheric aerosols, J. Physique, 45, C2, 785 (1984).

4. H. Storms, F. Bruynseels, and R. Van Grieken, Report to the Commission of the European Communities, Joint Research Center Karlsruhe, Development of methods for the analysis of trace amounts of rare earth oxides in combustion particles by laser microprobe mass analysis, 1984, pp26.

5. F.J. Bruynseels and R.E. Van Grieken, Laser mass spectrometric identification of sulfur species in single micrometer-size particles, Anal. Chem., 56, 871 (1984).

6. F. Bruynseels and R.E. Van Grieken, Speciation and distribution of sulfur and nitrogen in individual aerosol particles measured by LAMMA, in Proceedings of the SCOPE-symposium on "Acid deposition and the sulfur cycle", ed. by O.L.J. Vanderborght, Brussels, Belgium, June 6, 1984, 85.

7. F. Bruynseels amd R. Van Grieken, Direct detection of sulfate and nitrate layers on sampled marine aerosols by laser microprobe mass analysis, Atmos. Environ., 19, 1969 (1985).

8. R. Niessner, D. Klockow, F. Bruynseels, and R. Van Grieken, Investigation of heterogeneous reactions of PAH's on particle surfaces using laser microprobe mass analysis, Int. J. Environ. Anal. Chem., 22, 281 (1985).

9. F. Bruynseels, H. Storms, and R. Van Grieken, Chemical characterization of individual aerosol particles from remote and polluted marine air, in Proceedings "Progress in Belgian Oceanographic Research", ed. by R. Van Grieken and R. Wollast, Brussels, Belgium, March 1985, 178.

10. F. Bruynseels, H. Storms, T. Tavares, and R. Van Grieken, Characterization of individual particle types in coastal air by laser microprobe mass analysis, Int. J. Environ. Anal. Chem., 23, 1 (1985).

11. A.H. Verbueken, F.J. Bruynseels, and R.E. Van Grieken, Laser microprobe mass analysis: a review of applications in the life sciences, Biomed. Mass Spectrom., 12, 438 (1985).

12. F. Bruynseels, H. Storms, and R. Van Grieken, Chemical characterization of airborne particulate matter sampled above the North Sea, in Proceedings of the International Conference - Heavy Metals in the Environment, Athens, Greece, September 10-13, 1985, 189.

13. Ph. Otten, F. Bruynseels, and R. Van Grieken, Reaction of marine aerosols with HNO_3 vapour studied by single particle analysis, in Proceedings of the workshop on "Aerosols and acid deposition", Petten, The Netherlands, December 9-10 1985, 67.

14. Ph. Otten, F. Bruynseels, and R. Van Grieken, Nitric acid interaction with marine aerosols sampled by impaction, Bull. Soc. Chim. Belg., 95, 447 (1986).

15. M.O. Andreae, R.J. Charlson, F. Bruynseels, H. Storms, R. Van Grieken, and W. Maenhaut, Internal mixture of seasalt, silicates and excess sulfate in marine aerosols, Science, 232, 1620 (1986).

16. F. Bruynseels and R. Van Grieken, Recombination reactions and geometry effects in laser microprobe mass analysis studied with $^{12}C/^{13}C$ bilayers, in Third international laser microprobe mass spectrometry workshop 1986, ed. by F. Adams and L. Van Vaeck, , Antwerp, Belgium, August 26-27, 1986, 31.

17. Ph. Otten, F. Bruynseels, and R. Van Grieken, LAMMA analysis of inorganic ammonium compounds in individual marine aerosol particles, in Third International laser microprobe mass spectrometry workshop 1986, ed. by F. Adams and L. Van Vaeck, , Antwerp, Belgium, August 26-27, 1986, 159.

18. F. Bruynseels and R. Van Grieken, Recombination reactions and geometry effects in laser microprobe mass analysis studied with $^{12}C/^{13}C$ bilayers, Int. J. Mass Spectrom. Ion Proc., in press. (1987).

19. Ph. Otten, F. Bruynseels and R. Van Grieken, LAMMA analysis of inorganic ammonium compounds in individual marine aerosols particles, Anal. Chim. Acta, in press (1987).

20. P. Artaxo, H. Storms, F. Bruynseels, R. Van Grieken, and W. Maenhaut, Composition and sources of aerosols from the Amazon basin, J. Geophys. Res., in press (1987).

21. F. Bruynseels, H. Storms, R. Van Grieken, and L. Van der Auwera, Characterization of North Sea aerosols based on individual particle analysis, Atmos. Environ., submitted (1987).

22. A.H. Verbueken, F.J. Bruynseels, R.E. Van Grieken, and F.C. Adams, Laser microprobe mass spectrometry, in Inorganic Mass Spectrometry, Chapter 6, ed. by F.C. Adams, R. Gijbels, and R. Van Grieken, J. Wiley and Sons, submitted, 103 pg.(1987).

23. H. Storms, P. Artaxo, F. Bruynseels, and R. Van Grieken, Individual particle analysis by automated EPMA for the improvement of source apportionment studies for remote aerosols, in Microbeam Analysis-1987, in preparation (1987).

24. F. Bruynseels, P. Artaxo, H. Storms, and R. Van Grieken, LAMMA-study of aerosol samples collected in the Amazon basin, in Microbeam Analysis-1987, in preparation (1987).

25. R.W. Linton, I.H. Musselman, F.J. Bruynseels, and D.S. Simons, Inorganic cluster ion formation in the laser microprobe in Microbeam Analysis-1987, in preperation (1987).

26. R. Van Grieken, A. Verbueken, F. Bruynseels, D. Vandeputte, C. Goossenaerts, L. Leysen, Ph. Otten, and L. Wouters, Laser microprobe mass analysis: characteristics and applications, Proceedings of the "Analytiktreffen 1986", ed. by K. Dittrich, Neubrandenburg, DDR, Sept 15-19, 1986, in press.